A.I.K.E.F.: An Adaptive Hybrid Model with Application to Fossil Fields at Titan and Mercury's Double Magnetopause

Von der Fakultät für Elektrotechnik, Informationstechnik, Physik
der Technischen Universität Carolo-Wilhelmina
zu Braunschweig
zur Erlangung des Grades eines
Doktors der Naturwissenschaften
(Dr.rer.nat.)
genehmigte
Dissertation

von Joachim Müller
aus Oldenburg

Bibliografische Information der Deutschen Nationalbibliothek

Die Deutsche Nationalbibliothek verzeichnet diese Publikation in der Deutschen Nationalbibliografie; detaillierte bibliografische Daten sind im Internet über `http://dnb.d-nb.de` abrufbar.

1. Referentin oder Referent: Prof. Dr. Uwe Motschmann
2. Referentin oder Referent: Prof. Dr. Karl-Heinz Glaßmeier
eingereicht am: 30.09.2011
mündliche Prüfung (Disputation) am: 24.11.2011
Druckjahr: 2012

Vorveröffentlichungen der Dissertation

Teilergebnisse aus dieser Arbeit wurden mit Genehmigung der Fakultät für Elektrotechnik, Informationstechnik, Physik, vertreten durch den Mentor der Arbeit, in folgenden Beiträgen vorab veröffentlicht:

Publikationen

- Müller, J., Simon, S., Wang, Y. C., Motschmann, U., Heyner, D., Schüle, J., Ip, W. H., Kleindienst, G., Pringle, G. J., Origin of Mercury's Double Magnetopause: 3D Hybrid Simulation Study with A.I.K.E.F., *ICARUS*, 2012, doi:10.1016/j.icarus.2011.12.028

- Müller, J., Simon, S., Motschmann, U., Schüle, J., Glassmeier, K. H., Pringle, G. J., A.I.K.E.F.: Adaptive hybrid model for space plasma simulations, *Computer Physics Communications*, Vol. 182, Seiten 946-966, 2011

- Müller, J., Simon, S., Motschmann, U., Glassmeier, K. H., Saur, J., Schüle, J., Pringle, G. J., Magnetic field fossilization and tail reconfiguration in Titan's plasma environment during a magnetopause passage: 3D adaptive hybrid code simulations, *Planetary Space Science*, Vol. 58, Seiten 1526-1546, 2010

- Müller, J., Simon, S., Motschmann, U., Schüle, J., Particle-Refinement for Adaptive Particle-in-Cell Codes with an Optimized Reduction of Numerical Noise by modified Refinement Triggering, eingereicht bei *Journal of Computational Physics*, 2011

Tagungsbeiträge

- Müller, J., Simon, S., Motschmann, U., Glassmeier, K.-H., Saur, J. A.I.K.E.F. - An Adaptive Hybrid Model with Application to Fossil Fields at Titan and Mercury's Double Magnetopause (eingeladener Vortrag), *Oberseminar des Instituts für Geophysik der Universität Köln*, Köln, 21. Juni 2011

- Müller, J., Simon, S., Motschmann, U., Glassmeier, K.-H., Saur, J. A.I.K.E.F. - Adaptive hybrid model with application to a Magnetopause Passage of Titan (Vortrag), *European Geosciences Union General Assembly (EGU)*, Wien, 02. - 07. Mai 2010

- Müller, J., Simon, S., Motschmann, U., Schüle, J., Glassmeier, K.-H., A.I.K.E.F. An adaptive hybrid model with application to fossil magnetic fields in Titan's Ionosphere (Vortrag), *The International Max-Planck Research School (IMPRS) on Physical Processes in the Solar System and Beyond*, May-Planck-Institut für Sonnensystemforschung, Katlenburg-Lindau, 24. Februar 2010

- Müller, J., Simon, S., Motschmann, U., Glassmeier, K.-H., A.I.K.E.F. - An adaptive hybrid model for planetary plasma environment studies (Poster), *American Geophysical Union Fall Meeting (AGU)*, San Francisco, 14. - 18. Dezember 2009

- Müller, J., Pringle, G. J., Motschmann, U., Schüle, J., A.I.K.E.F. - Adaptive Ion Kinetic Electron Fluid Model for space plasma simulations (Vortrag), *HPC-Europa2 Transnational Access Meeting (TAM)*, Montpellier, 14. - 16. Oktober 2009

- Müller, J., Simon, S., Motschmann, U., Schüle, J., A.I.K.E.F. - A hybrid block-AMR hybrid model (Poster), *The 9th International School for Space Simulations (ISSS)*, Saint-Quentin-en-Yvelines, 03. - 10. Juli 2009

- Müller, J., Simon, S., Motschmann, U., Schüle, J., Glassmeier, K.-H., A.I.K.E.F. Adaptive Ion Kinetic Electron Fluid Simulation Model (Vortrag), *The International Max-Planck Research School (IMPRS) on Physical Processes in the Solar System and Beyond*, May-Planck-Institut für Sonnensystemforschung, Katlenburg-Lindau, 11. Februar 2009

- Müller, J., Simon, S., Motschmann, U., Schüle, J., Glassmeier, K.-H., Induction processes at Mercury (Vortrag), *Committee on Space Research Scientific Assembly (COSPAR)*, Montreal, 13. - 20. Juli 2008

- Müller, J., Simon, S., Motschmann, U., Schüle, J., Glassmeier, K.-H., Adaptive mesh refinement applied to Plasma Simulation Codes (Vortrag), *The International Max-Planck Research School (IMPRS) on Physical Processes in the Solar System and Beyond*, May-Planck-Institut für Sonnensystemforschung, Katlenburg-Lindau, 13. Februar 2008

- Müller, J., Simon, S., Bagdonat, T., Motschmann, U., Glassmeier, K.-H., Self consistent hybrid simulation of Mercury's plasma environment (Vortrag), *European Planetary Science Congress*, Potsdam, 20. - 24. August 2007

- Müller, J., Simon, S., Bagdonat, T., Grosser, J., Glassmeier, K.-H., Motschmann, U. Hybrid-Simulation von Merkurs Plasmaumgebung unter Einfluss planetarer Induktionseffekte (Vortrag), *71. Jahrestagung der Deutschen Physikalischen Gesellschaft*, Regensburg, 26. - 30. März 2007

Contents

1 Introduction

On August 3$^{\mathrm{rd}}$, 2004 the launch of the NASA probe MESSENGER (MErcury Surface, Space ENvironment, GEochemistry and Ranging) was successfully initiated. The probe is targeted to investigate several properties of planet Mercury, which of all planets in the solar system is closest to the sun. After three flybys in 2008 and 2009, MESSENGER entered its designated orbital phase in March 2011. The magnetic field measurements that have been collected until the time of this writing show several interesting features, where the most unexpected signature is the so called "Double Magnetopause" (Slavin et al. 2008). Such a double current sheet had never been observed before, neither at Earth nor in any other planetary magnetosphere. According to widely accepted textbooks, a single current sheet would be expected instead. A trusted explanation for the origin of the double current sheet is missing to the present day. From the few one-dimensional measurements it is hardly possible to understand the involved physics.

Fortunately, three-dimensional plasma simulations have become an important tool within the past ten years to gain a deeper insight and to place spacecraft data within the context of the full 3D interaction scenario. A wide range of numerical plasma models is available to capture the space plasma processes. Which method to choose depends on the particular problem. Basically three self-consistent plasma models exist to describe the plasma flow around obstacles that are exposed to a magnetized plasma: Magnetohydrodynamics (MHD) that describe the plasma as a conducting fluid, full particle models that describe both, the electrons and ions kinetically and finally the hybrid approach that treats the electrons as a fluid, whereas a completely kinetic approach is retained to cover ion dynamics.

When dealing with obstacles like planet Mercury whose size is comparable to the scale of the ion gyro-motion, a hybrid model is the most convenient choice. Many other obstacles within the solar system require the application of this approach as well, such as Mars, Venus, several Saturnian moons, asteroids and comets. Due to the kinetic description of the ions, the hybrid model accounts for non-Maxwellian distribution functions, cycloidal pickup motion or velocity shear between distinct ion species. From the numerical point of view it can be categorized as a particle-mesh code. The particles interact with the electron fluid and electromagnetic fields defined on the nodes of the numerical mesh. While the number of particles per unit volume defines the resolution in velocity space, the spatial scale of resolvable plasma processes is limited by the resolution of the numerical mesh.

Several hybrid models are available that perform a spatial discretization by using a static Cartesian mesh (eg. Modolo and Chanteur (2008), Trávníček et al. (2010) or Omidi et al. (2002)). However, there are at least two models which take advantage of more sophisticated mesh types that adapt spatially to the given geometry. The hybrid model by Kallio and Janhunen (2003) uses hierarchical meshes while the hybrid model of Bagdonat and Motschmann (2002) applies curvilinear meshes, but both mesh types are static in time. The latter model has been successfully applied to numerous scenarios such as comets (Bagdonat and Motschmann 2002, Gortsas et al. 2010, Wiehle et al. 2011a), asteroids (Simon et al. 2006a), Mars (Bößwetter et al. 2004) and several Saturnian moons such as Titan (Simon et al. 2006b), Rhea (Roussos et al. 2008) and Enceladus (Kriegel et al. 2009). The curvilinear shape of the numerical mesh improves the resolution in critical regions, such as the ionosphere of an obstacle. However, due to several numerical approximations accuracy is decreased whenever the curvilinear coordinate system deviates strongly from a Cartesian system which in turn limits the gain of resolution (Bagdonat 2005).

This resolution deficiency introduces inaccuracy whenever localized small-scale features are of interest. For instance fossil fields at Titan are strongly localized (Neubauer et al. 2006, Bertucci et al. 2008) and require high resolution just for certain regions close to the obstacle's surface. Modeling efficiently the fine structure of shocks of ionospheric obstacles and its related shocklets (Bagdonat and Motschmann 2002, Bößwetter et al. 2004) introduces an even greater challenge, as firstly the region is strongly localized and secondly develops with time. In particular modelling the Hermean magnetosphere is most challenging when small structures such as the double current sheet shall be taken into account. The reason are the significantly different scales: the width of the current sheets, on the one hand, and the width of the magnetosphere, on the other differ by nearly a factor of thousand.

Increasing the global resolution usually is not an option, as Hybrid codes (or in general particle-mesh-codes) are extremely expensive in both, memory consumption and computation time. As memory consumption grows with a power of three and computation time by at least a power of four when increasing the mesh resolution, more sophisticated methods are required to increase the resolution. One of these methods is referred to as Adaptive Mesh Refinement (AMR).

The idea behind AMR is to specify a coarse mesh before starting a simulation run and then to locally refine the mesh in regions where small scale structures evolve. This self-refinement usually is guided by strong local gradients in physical quantities like densities, currents or electromagnetic fields. It ensures that fine-scale structures are well resolved and avoids spending disproportional computational resources on calculating large-scale structures or even undisturbed solar wind flow, which would be the case when a uniform mesh is applied. To the authors' knowledge, there is no adaptive hybrid simulation code in space plasma physics to the present day.

The objective of this thesis is therefore to develop an adaptive hybrid model which we call A.I.K.E.F. *(**A**daptive **I**on-**K**inetic **E**lectron-**F**luid)* and its application to the plasma environments of planet Mercury and the Saturnian moon Titan. We will briefly introduce the basic hybrid equations in chapter 2. Since several ways exist on how to implement the adaptive mesh refinement, we will discuss the most common AMR techniques in chapter

3 and substantiate why we chose to use the method called “Hybrid-Block-AMR”. For clarification we shall point out that the term “Hybrid” of the AMR method does not relate to the term “Hybrid” of the physical method in any way. This chapter also includes a detailed description of the code’s parallelization and analysis of its scaling behavior. In view on future code development we provide a detailed explanation on the implementation in chapter 4. During and after the implementation of A.I.K.E.F., the code has been intensively tested. The most important tests are presented in chapter 5, including a first comparison of Mercury simulation results with MESSENGER observations.

Chapter 6 is subject to a detailed discussion on Mercury’s plasma environment. The A.I.K.E.F. simulation model enabled the application of high resolution meshes, such that we succeeded in capturing the double current sheet which had been observed during the MESSENGER flybys. Based on our simulation results, we give a potential explanation for the origin of the so called “Double Magnetopause”. A completely different obstacle is analysed in chapter 7, that is the Saturnian moon Titan. In contrast to planet Mercury, Titan does not possess an intrinsic magnetic field but a highly conducting ionosphere. During Titan’s excursion through Saturn’s magnetopause so called “fossil fields” that were memorized in Titan’s ionosphere have been detected by the Cassini spacecraft. Even though the involved physics are rather well understood, the time scale of their survival is still under debate. The A.I.K.E.F. simulation code is the first hybrid model that succeeded in capturing the fossil fields. Based on these results, we estimate a time-scale for their survival and analyse the complex tail reversal during a magnetopause passage. The most important results are summarized in chapter 8 and an outlook is given.

2 Hybrid Model

The hybrid approximation treats the electrons as a fluid while the ions are modeled kinetically. A detailed derivation of the equations is given in several references, such as Matthews (1994), Bagdonat (2005) or Simon (2007a). Thus, we only provide the final equations and name the limits of validity that must be accounted for in section 2.1. The idea behind dimensionless equations and values is shown in section 2.2. In contrast to full particle models, Gauss's law is not considered when deriving the hybrid equations and is not exactly fulfilled. The introduced error is discussed in section 2.3.

2.1 Equations

The electron fluid approximation limits the application of hybrid models to scenarios where the investigated

1. time scales are larger than the electron gyration period
2. spatial scales are larger than the electron gyration radius
3. spatial scales are larger than the Debye length

If the conditions above hold it can be shown that the electron mass and displacement currents in Ampère's law can be neglected and quasi-neutrality can be assumed for the plasma (Bagdonat and Motschmann 2002):

1. $m_e = 0$ mass-less electrons
2. $\rho_i \approx -\rho_e$ quasi neutrality
3. $\underline{j} = \frac{1}{\mu_0}\nabla \times \underline{B}$ Darwin Approximation (Bagdonat 2005)

where m_e is the electron mass, ρ_e and ρ_i are the electron and ion charge density, respectively. Considering the above approximations, an explicit equation for the electric field can be derived from the electron momentum equation:

$$\underline{E} = -\underline{u}_i \times \underline{B} + \frac{(\nabla \times \underline{B}) \times \underline{B}}{\mu_0 \rho_i} - \frac{\nabla p_e}{\rho_i} + \frac{\eta}{\mu_0}\nabla \times \underline{B} \quad , \tag{2.1}$$

where $\underline{u}_i$ is the mean ion velocity, p_e the electron pressure and η the plasma resistivity that may arise from particle-wave scattering. While $\underline{u}_i$ and ρ_i can be directly derived from the individual ion quantities which will be described in section 3.5, an adiabatic equation of state is assumed for the electron pressure:

$$p_e = p_{e0} \left(\frac{n_e}{n_{e0}} \right)^{\kappa} , \tag{2.2}$$

where p_{e0} and n_{e0} are initial electron pressure and density and $\kappa = (f+2)/f$ is the adiabatic exponent. We chose the number of degrees of freedom $f = 2$ to account for the two-dimensional thermodynamic coupling that acts only perpendicular to the magnetic field (Bagdonat 2005). The application of Faraday's law to equation 2.1 yields a time evolution equation for the magnetic field:

$$\frac{\partial \underline{B}}{\partial t} = \nabla \times \left(\underline{u}_i \times \underline{B} \right) - \nabla \times \left(\frac{(\nabla \times \underline{B}) \times \underline{B}}{\mu_0 \rho_i} \right) - \nabla \times \left(\frac{\eta}{\mu_0} \nabla \times \underline{B} \right) \tag{2.3}$$

Since the ions are treated kinetically, the equation of motion has to be solved for each ion:

$$\frac{d\underline{v}_i}{dt} = \frac{q_i}{m_i} \left(\underline{E}' + \underline{v}_i \times \underline{B} \right) \tag{2.4}$$

and

$$\frac{d\underline{x}_i}{dt} = \underline{v}_i \quad , \tag{2.5}$$

where q_i and m_i are the ion's charge and mass, respectively. The vectors $\underline{E}'$ and $\underline{B}$ are the electric and magnetic field at the ion position $\underline{x}_i$ and are needed to advance the ion velocity $\underline{v}_i$. The use of $\underline{E}'$ is required for conservation of momentum (Bagdonat 2005):

$$\underline{E}' = \underline{E} - \eta \nabla \times \underline{B} \tag{2.6}$$

In some scenarios, solid obstacles are present, such as planets, moons or asteroids. Any ion that hits the surface of the solid obstacle is removed from the simulation. The ion velocity and inverse ion density are set to zero inside the obstacle in order to eliminate the convective and Hall term in equation 2.1. An arbitrary resistivity profile can be specified for the obstacle. Hence, the magnetic field can propagate through the obstacle by means of diffusion.

2.2 Normalization

In order to eliminate natural constants such as μ_0 and to avoid unwanted round-off errors, all equations and quantities of the simulation are normalized to background values:

$$A^* = \frac{A}{A_0}, \tag{2.7}$$

where A^* is the normalized quantity that is used within the simulation, A is the physical quantity in SI units and A_0 is the background value in SI units.

Typically the background magnetic field B_0, the background ion number density n_{i0} and mass m_{i0} are chosen corresponding to the respective scenario. Any further normalization quantities can be derived from these, as shown in table 2.1. In this particular example the employed background values relate to the undisturbed solar wind at planet Mercury (Milillo et al. 2005).

Quantity	Symbol	Value
Magnetic field	B_0	21 nT
Density	n_0	$32\,\mathrm{cm}^{-3}$
Mass	m_0	m_{proton}
Charge	q_0	e
Time	$t_0 = \Omega_{g,i}^{-1}$	0.5 s
Length	$x_0 = c/\omega_{p,i}$	40.3 km
Velocity	$v_0 = x_0/t_0$	$80.9\,\mathrm{km\,s}^{-1}$
Conductivity	$\sigma_0 = t_0/(\mu_0 x_0^2)$	$2.4 \cdot 10^{-4}\,\mathrm{S\,m}$
Magnetic moment	$M_0 = 4\pi B_0 r_0^3/\mu_0$	$1.4 \cdot 10^{13}\,\mathrm{Am}^2$

Table 2.1: The Table provides an example for normalization values for the undisturbed solar wind at planet Mercury. The background values are taken from Milillo et al. (2005).

2.3 Violation of Charge Neutrality

As argued in section 2.1, charge neutrality is assumed to derive equation 2.1 for the electric field, i.e. $\rho_i + \rho_e = 0$. However, in general the divergence of the electric field does not vanish. Hence, Gauss's law yields a charge that is different from zero which obviously conflicts with the assumption of charge neutrality. In the following we will estimate the error that is introduced:

Gauss's law reads:

$$\nabla \cdot \underline{E} = \frac{\rho_c}{\epsilon_0} \tag{2.8}$$

where ρ_c is the sum of ion and electron charge density $\rho_c = \rho_i + \rho_e$ and $\epsilon_0 = (\mu_0 c^2)^{-1}$ the permittivity of free space. Like any other hybrid equation Gauss's law can be normalized as follows:

$$\begin{aligned}
& \nabla \cdot \underline{E} = \frac{\rho_c}{\epsilon_0} && (2.9)\\
\Leftrightarrow\ & \frac{E_0}{x_0}\ \nabla^* \cdot \underline{E}^* = \frac{\rho_c^*}{\epsilon_0}\ \rho_{c,0} && (2.10)\\
\Leftrightarrow\ & \epsilon_0\ \frac{v_0 B_0}{x_0}\ \nabla^* \cdot \underline{E}^* = \rho_c^*\ q_0 n_0 && (2.11)\\
\Leftrightarrow\ & \frac{1}{\mu_0 c^2}\ \frac{q_0 B_0^2}{m_0}\ \nabla^* \cdot \underline{E}^* = \rho_c^*\ q_0 n_0 && (2.12)\\
\Leftrightarrow\ & \frac{1}{c^2}\ \frac{B_0^2}{\mu_0 m_0 n_0}\ \nabla^* \cdot \underline{E}^* = \rho_c^* && (2.13)\\
\Leftrightarrow\ & \left(\frac{v_0}{c}\right)^2\ \nabla^* \cdot \underline{E}^* = \rho_c^* && (2.14)
\end{aligned}$$

where $x_0 = v_0 m_0/(q_0 B_0) = c/\omega_{p,i}$ is the inertia length of the normalization species with charge q_0, mass m_0 and corresponding Alfvén speed $v_0 = B_0/\sqrt{\mu_0 m_0 n_0}$.

In typical hybrid simulations (e.g. on the plasma environment of Mercury and Titan) the normalized divergence of the electric field turns out to be of order one, $\nabla^* \cdot \underline{E}^* \approx \mathcal{O}(1)$. As the Alfvén speed is about $v_0 = 10^5 \mathrm{m/s}$ and the speed of light $c = 3 \cdot 10^8 \mathrm{m/s}$ Gauss's law yields a normalized charge density that is of order $\rho_c \approx \mathcal{O}(10^{-7})$ that is seven orders of magnitudes smaller than the normalized ion charge density $\rho_i \approx \mathcal{O}(1)$. Hence, the approximation $\rho_e = \rho_c - \rho_i \approx -\rho_i$ only affects the seventh decimal place and thus the introduced error can be considered negligible.

3 Application of Hybrid-Block-AMR to the Hybrid Model

For quite some time, hybird models have been used to study space plasma interactions in astrophysics (Leroy et al. 1982, Winske and Leroy 1985, Motschmann et al. 1992). The particular hybrid schema that we use was designed by Matthews (1994) for two-dimensional staggered Cartesian meshes. The essential difference to other hybrid schemas was the application of the "Cyclic leapfrog" and "Current advancement Method ", as described in section 3.3. Based on this schema, Bagdonat and Motschmann (2001) developed a simulation code with the application to three dimensional un-staggered curvilinear meshes. The concept behind the application of this schema to three dimensional un-staggered adaptive meshes and its efficient parallelization is described throughout this chapter. A more compact version is given by Müller et al. (2011a).

3.1 Strategies for Adaptive Mesh Refinement (AMR)

Long since, AMR has been used in numerical simulations and several strategies exist to refine the numerical mesh. An early method proposed by Simpson (1978) is to merge additional mesh nodes into coarser meshes in order to enhance the local resolution. However, Berger and Oliger (1984) pointed out that this strategy compromises the local uniformity of the mesh which substantially slows down the integrator and prevents its efficient parallelization.

Instead, Berger and Oliger (1984) introduced a patch-based version of AMR, where a patch is a cuboid sub-mesh of arbitrary size. In a first step regions within the mesh that need to be refined are flagged. Afterwards a clustering algorithm covers the respective regions with patches of higher resolution. In order to achieve an optimal fit, patches can be translated, rotated and may overlap. Each patch can be processed highly cache efficient and individually, which enables the possibility of efficient massive parallelization. Several of today's simulation codes and packages have implemented this refinement strategy, such as CHOMBO, SAMRAI or AMRVAC (Keppens et al. 2003).

In order to further improve the mesh adaption and avoid duplication of nodes, Khokhlov (1998) proposed to refine each individual node into 2^{dim} children nodes and organize individual computational nodes directly in a fully threaded refinement tree, where *dim* is the number of dimensions. These children in turn can be successively further refined until the required resolution is reached. Even though this method creates perfectly flexible meshes, it is harder to process mesh nodes as cache-efficient as in the Patch-AMR method.

This drawback is addressed by the Block-AMR method, which is implemented in several simulation codes like the MHD simulation code BATS-R-US by Gombosi et al. (2003) or RACOON by Dreher and Grauer (2005). The idea behind Block-AMR is basically to refine entire blocks of nodes rather than single nodes and organize them into a tree structure similar to the method of Khokhlov (1998). Therefore a fixed number of nodes is grouped into a block, that can be processed highly cache-efficient. Since blocks can be processed individually, efficient massive parallelization is possible as well. An initial decomposition of the numerical mesh into blocks is provided and in case refinement is required, entire blocks are refined into 2^{dim} children blocks. In contrast to Patch-AMR, all blocks are of equal size and no sophisticated clustering algorithms are required, which simplifies strongly the implementation. However the mesh adaption is usually not as good as in the patch based method.

To keep the advantages of Block-AMR but improve its mesh adaption, a modified version of Block-AMR was introduced by van der Holst and Keppens (2007) which they referred to as *Hybrid-Block-AMR*. In contrast to the standard block AMR approach, the common rule that a block must be either entirely refined or not at all is released. Instead, each oct of the block (in 3 dimensions) can be refined individually, which strongly increases the adaption of the refined mesh. Van der Holst and Keppens (2007) carried out a comparison of ordinary Block-AMR, Hybrid-Block-AMR and Patch-AMR and showed that identical results were obtained with the different methods, but the hybrid schema turned out to be fastest with respect to the execution speed.

It is further worth noting that Hybrid-Block-AMR can create meshes identical to cell-based-AMR and ordinary Block AMR. In case base blocks of 2^{dim} mesh nodes are specified, the meshes obviously are identical to meshes created by cell-based-AMR. On the other hand it is straightforward to force refinement of entire blocks, which yields meshes identical to the ordinary Block-AMR approach.

Since the Hybrid-Block-AMR approach offers a good mesh adaption, yet inherits the advantage of cache efficiency and can efficiently be scheduled in massive parallel, we decided to apply this method to the hybrid schema of Bagdonat and Motschmann (2002). However, since the underlying data structures differ very much from the former version, the A.I.K.E.F. simulation code has been rewritten from scratch.

3.2 Refinement Tree

Prior to each simulation run the numerical mesh is decomposed into a fixed number of blocks. For instance a three-dimensional mesh consisting out of 80^3 mesh nodes is decomposed into 8^3 blocks, each in turn consisting out of 10^3 mesh nodes. These blocks are labeled “root blocks” or “L_0-blocks”. By halving the block size in each dimension, each block can be virtually subdivided into 8 parts of equal size (in three dimensions) that are referred to as *octs*. In the Hybrid-Block-AMR approach individual octs are refined rather

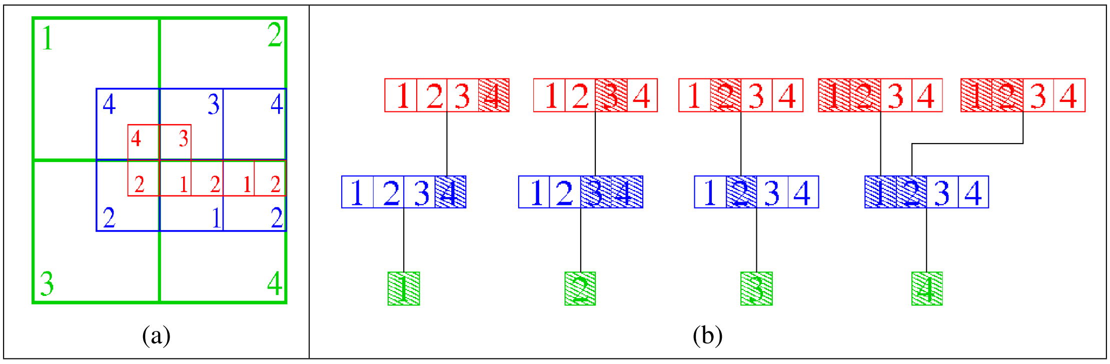

(a)

(b)

Figure 3.1: Shown is a mesh topology of the hybrid-AMR approach (a) with its corresponding refinement tree in (b). The tree of this two-dimensional example is a quad tree, i.e. each block can be assigned four potential children blocks. In three dimensions an oct tree is required. Root-blocks are colored in green, L_1-blocks in blue and L_2-blocks in red. The shaded squares represent blocks that are effectively refined, while the non-shaded squares indicate blocks that could be refined if required. The ability to refine individual quads (octs) rather than entire blocks significantly increases the mesh flexibility (see van der Holst and Keppens (2007)). In root block 2 the level one quad number 4 is refined to guarantee that the refinement level of neighboring blocks must not differ by more than one.

than entire blocks, which works as follows:

After a given time T_{Refine} it is checked for every mesh node whether a given refinement criterion is fulfilled and therefore resolution enhancement required. A criterion can be for instance when the local field strength of any physical quantity exceeds a given value. If this is the case, the respective mesh nodes are *flagged for refinement*. In case a certain number of mesh nodes inside one oct are flagged, the respective oct of the given block is refined, i.e. the oct volume is covered up by a block of half length in each dimension but equal number of mesh nodes, thereby doubling the resolution in each dimension. Therefore the new block covers precisely the oct of the underlining block (see fig. 3.1(a)). These blocks are labeled “L_1 blocks”. If further resolution enhancement is required, any oct of the L_1 block is refined in up to eight “L_2 blocks” which in turn can be further refined until the requested solution is reached.

Our implementation does not restrict the maximal level of refinement, however in practice it is limited by finite computational resources. In order to manage computational resources in a reasonable way, resolution can be decreased if not required anymore, i.e. blocks are removed. This works as follows: after a given time T_{Remove} it is checked for every mesh node whether a given removement criterion is fulfilled and therefore resolution reduction is required. If so, the respective mesh nodes are *flagged for removement*. In case a given number of mesh nodes inside one block are flagged, the block is removed. During both the refinement and removement process any oct can be refined, unless the refinement level of neighboring blocks does not differ by more than one. This rule is introduced to avoid rapid changes in resolution.

Newly refined blocks are grouped into a tree data structure. Each root block represents the root of one tree. Figure 3.1(b) shows the refinement tree which corresponds to the two-dimensional mesh topology of fig. 3.1(a). Please note that the refinement tree of this two-dimensional example is a quad tree, i.e. each block can be assigned four potential children blocks, while in three dimensions an oct tree is required. Blocks are enumerated in the following way: the upper left block is assigned number 1, upper right number 2, lower left number 3 and lower right number 4. Root-blocks are colored in green, L_1-blocks in blue and L_2-blocks in red. The shaded squares represent blocks that are effectively refined, while the non-shaded squares indicate blocks that could be refined if required.

This small mesh already illustrates quite well the advantage of Hybrid-Block-AMR over standard Block-AMR. In this case mesh nodes inside blue octs are flagged for level one refinement and mesh nodes inside red octs for level two refinement. As stated above, in standard Block-AMR a block is completely refined or not at all which means for this case that 16 blocks in level one would be refined instead of 6, even though the majority of mesh nodes are not flagged. The same applies to refinement level 2 where 20 blocks have to be created instead of 7. Even worse, due to the rule that the refinement levels of neighboring blocks must not differ by more than one, further refinement will be triggered in lower levels (not visible in this simple sketch). Beyond that, the ratio gets worse in case of three-dimensional meshes. A detailed comparison and quantitative analysis of hybrid and standard block AMR has been presented by van der Holst and Keppens (2007).

In our implementation, blocks that are covered by finer blocks (such as the green block 1 in fig. 3.1(a)) are not removed, regardless of whether they are covered partially or entirely by finer blocks. The electromagnetic fields are propagated within every level of refinement i.e. every block, independent of whether it is covered by finer blocks or not. This is required for interpolation and projection of electromagnetic fields at refinement boundaries, which will be explained in section 3.4. In contrast, particles are exclusively assigned to the highest level of refinement, i.e. to the maximal refined block at the particle's position. In the following these blocks will be referred to as "top-level-block" (TLB).

3.3 Time Integration Schema

The time integration is discussed in detail by Matthews (1994) and is shown to be of second order accuracy. Since we choose the same time step Δ_t for any level of refinement the schema doesn't need to be modified for the application to AMR which is why we simply provide a brief summary here.

The electromagnetic fields and particle positions are initialized at full time steps $\underline{E}^n$, $\underline{B}^n$ and $\underline{x}_p^n$. The charge density at full time steps ρ_i^n is gathered from the particle positions (see section 3.5). The particle velocities, on the other hand, are initialized at half time steps $\underline{v}_p^{n-1/2}$. This allows the application of a time-centered second-order accurate leap-frog schema for the particle advancement. The same second order leap-frog method is applied to the magnetic field $\underline{B}^n$ (equation 2.3) that depends on the charge density $\rho_i^{n+1/2}$

and mean ion velocity $\underline{u}_i^{n+1/2}$ at half time steps. The latter quantities are defined as

$$\rho_i^{n+1/2} = \frac{\rho_i^{n+1} + \rho_i^n}{2} \tag{3.1}$$

and

$$\underline{u}_i^{n+1/2} = \frac{(\underline{u}_i^+ + \underline{u}_i^-)}{2} \quad , \tag{3.2}$$

where $\underline{u}_i^+ = f(\underline{x}_p^{n+1}, \underline{v}_p^{n+1/2})$ and $\underline{u}_i^- = f(\underline{x}_p^n, \underline{v}_p^{n+1/2})$ are gathered from the individual particle positions and velocities. The additional quantities $\underline{u}_i^+$ and $\underline{u}_i^-$ have to be introduced since the mean ion velocity requires both, particle positions and velocities which are defined at different points in time (full and half, respectively).

Once the quantities are initialized as described above the following computational cycle is repeated until stationarity is reached. Prior to each cycle, the values for $\underline{E}^n$, $\underline{B}^n$, ρ_i^n, $\underline{x}_p^n$ and $\underline{v}_p^{n-1/2}$ are known.

(1) Advance $\underline{v}_p^{n-1/2}$ to $\underline{v}_p^{n+1/2}$ by eq. 6.3 using $\underline{E}^n$, $\underline{B}^n$ and $\underline{x}_p^n$

(2) Gather $\underline{u}_i^-$ from $\underline{x}_p^n$, $\underline{v}_p^{n+1/2}$

(3) Advance $\underline{x}_p^n$ to $\underline{x}_p^{n+1}$ by eq. 2.5 using $\underline{v}_p^{n+1/2}$

(4) Gather ρ_i^{n+1} and $\underline{u}_i^+$ from $\underline{x}_p^n$, $\underline{v}_p^{n+1/2}$

(5) Average $\rho_i^{n+1/2} = \frac{\rho_i^{n+1}+\rho_i^n}{2}$ and $\underline{u}_i^{n+1/2} = \frac{(\underline{u}_i^+ + \underline{u}_i^-)}{2}$

(6) Advance $\underline{B}^n$ to $\underline{B}^{n+1}$ by eq. 2.3 using $\rho_i^{n+1/2}$, $\underline{u}_i^{n+1/2}$

(7) Extrapolate $\underline{u}_i^{n+1/2}$ to $\underline{u}_i^{n+1}$ using the
"Current Advancement Method (CAM)" by Matthews (1994).

(8) Calculate $\underline{E}^{n+1}$ by eq. 2.1 using $\underline{B}^{n+1}$, $\underline{u}_i^{n+1}$, ρ_i^{n+1} .

After the end of the computational cycle the values for $\underline{E}^{n+1}$, $\underline{B}^{n+1}$, ρ_i^{n+1}, $\underline{x}_p^{n+1}$ and $\underline{v}_p^{n+1/2}$ are known which means the loop is closed. We shall point out that for the magnetic field advancement step (6) a cyclic leap-frog schema is used as described in Matthews (1994). The corresponding time step is smaller than the time step of the particle advancement in steps (1) and (3), which is referred to as magnetic field sub-cycling. For a usual simulation we set $\Delta t_{particle} = 7 \cdot \Delta t_{BField}$.

We add some numerical diffusion to the electromagnetic fields after each time step which we refer to as *smoothing*. This is required to stabilize the magnetic field integration. The smoothing is a 26 point stencil averaging procedure. In a first step the spatial average $\underline{b}$ of the magnetic field $\underline{B}$ at mesh node i, j, k is calculated:

$$\underline{b}_{ijk} = \sum_{a,b,c=-1}^{1} \underline{B}_{i+a,j+b,k+c} \cdot 2^{-(a^2+b^2+c^2+3)} \tag{3.3}$$

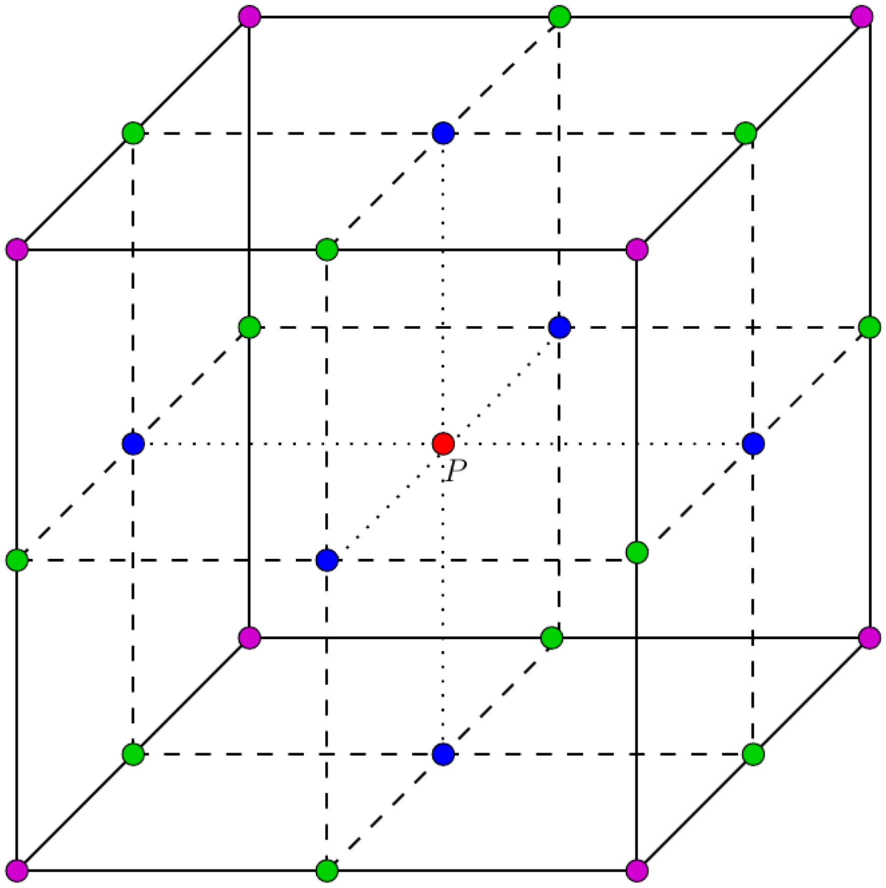

Figure 3.2: The sketch illustrates the smoothing procedure equation 3.3. In order to damp small scale fluctuations that arise from numerical noise, a weighted average is calculated after each magnetic field update for each mesh node (here exemplarily *P*) in the following way: the magnetic field values at the surrounding mesh nodes are added where the value at the respective node itself is weighted with 1/8 (red), values at blue mesh nodes are weighted with 1/16, the values at green nodes with 1/32 and the values at magenta nodes with 1/64. Afterwards, the new magnetic field value at the red mesh node is calculated corresponding to equation 3.4. The image is taken from Simon (2007b).

Afterwards the average weighted magnetic field is estimated:

$$\underline{B}_{ijk} = (1 - \alpha_s)\underline{B}_{ijk} + \alpha_s \underline{b}_{ijk} \tag{3.4}$$

where we call α_s the *smoothing parameter*. In finite differences this schema is similar to a high order Laplace operator and therefore acts similar as diffusion. This procedure is sketched in Figure 3.2. In some scenarios however, the smoothing procedure may destroys physical features such as “Fossil Fields” at Titan as will be explained in chapter 7. Thus, a more sophisticated method that generally enables the application of smaller smoothing values is discussed in section 7.4.

As mentioned in section 3.2, particles are always assigned to “Top-Level-Blocks” (TLBs).

Hence, steps (1) and (3) are exclusively carried out at TLBs. The same is valid for the gathering steps (2) and (4). However, densities and currents are projected to lower levels and non TLBs after the gathering is completed as will be explained in section 3.4. In contrast, steps (5) to (8) that relate to electromagnetic field propagation are carried out within every block of each level in order to allow field interpolation at level boundaries, as will be explained in section 3.4.

3.4 Spatial Discretization

Each mesh node inside a given block is identified by its indices i, j, k where i denotes the mesh nodes in x-direction and j and k in y- and z-direction, respectively. The standard way to calculate first and second spatial derivatives of a function f at the position of a given mesh node is derived by means of a Taylor series:

$$\left.\frac{\partial f_{[i,j,k]}}{\partial x}\right|_i = \frac{f_{[i+1,j,k]} - f_{[i-1,j,k]}}{2\Delta_x} + O(\Delta_x^2) \tag{3.5}$$

$$\left.\frac{\partial^2 f_{[i,j,k]}}{\partial x^2}\right|_i = \frac{f_{[i+1,j,k]} - 2f_{[i,j,k]} + f_{[i-1,j,k]}}{\Delta_x^2} + O(\Delta_x^2) \tag{3.6}$$

This central finite differencing schema is of second order accuracy. At the intersection of lower and higher refinement levels, the values from lower levels are linearly interpolated to higher levels. In turn, when available the values from higher levels are projected to lower levels by means of equation (3.10). This standard technique is discussed in detail by Fujimoto and Machida (2006a).

3.5 Moment Gathering and Force Interpolation

We use a “Cloud in Cell” schema in order to derive the macroscopic plasma moments such as ion charge density ρ_c and current $\underline{j}_i$. In this schema, it is assumed that the total charge, mass and momentum carried by a certain macroparticle are distributed homogeneously within the cell where it is located. This homogeneous charge cloud is then distributed to the adjacent mesh nodes according to a certain weighting schema, defining the fraction of each macroparticle quantity which is assigned to each of the eight cell corners. Furthermore, each particle is assigned an individual weight w_p, where the weight represents the number of ions inside the respective cloud. For each particle the charge

$$\Delta\rho_{i+a,j+b,k+c} = \frac{q_p w_p}{V_{cell}} \xi_a(x)\xi_b(y)\xi_c(z) \qquad (a, b, c = 0, 1) \tag{3.7}$$

and the current

$$\Delta\underline{j}_{i+a,j+b,k+c} = \frac{q_p w_p \underline{v}_p}{V_{cell}} \xi_a(x)\xi_b(y)\xi_c(z) \qquad (a, b, c = 0, 1) \tag{3.8}$$

is added to each of the eight mesh nodes of the cell in which the particle is located, where V_{cell} is the cell-volume, x, y and z define the particle position in cell coordinates that are normalized to the interval]0 : 1] and ξ is the shape function:

$$\xi_0(x) = (1 - x) \qquad \text{and} \qquad \xi_1(x) = x \tag{3.9}$$

As was described in section 3.2, particles are exclusively assigned to TLBs which is why the gathering schema can exclusively be executed inside TLBs. However, the electromagnetic field equations (2.1) and (2.3) require the densities and currents to be known at lower levels as well. One way to derive the moments in lower levels would be to temporary copy the particles to lower levels in order to enable moment gathering. However, this would be computationally extraordinary expensive. Fortunately the plasma moments at lower levels n can be derived from higher levels $n + 1$ as is explained below.

Assume a block of level n is covered by blocks of level $n + 1$. Then for each mesh node ijk of the respective block a mesh node uvw at level $n + 1$ exists that is at the identical coordinate in space. The value of any plasma moment M^n_{ijk} at level n is then derived by means of the equation:

$$M^n_{ijk} = \sum_{a,b,c=-1}^{1} M^{n+1}_{u+a,v+b,w+c} \cdot 2^{-(a^2+b^2+c^2+3)} \quad . \tag{3.10}$$

It can be shown by some straight forward algebra that this yields exactly the plasma moments that a Cloud-in-Cell schema executed inside lower levels would produce (Fujimoto and Machida 2006b).

Since electromagnetic fields are exclusively defined at mesh nodes they have to be interpolated to the particle positions in order to calculate the Lorentz force that acts on each particle. A given field A is interpolated to the particle position (x, y, z) of the cell i, j, k in the following way:

$$A_{x,y,z} = \sum_{a,b,c=0}^{1} A_{i+a,j+b,k+c} \;\; \xi_a(x)\xi_b(y)\xi_c(z) \tag{3.11}$$

This operation is basically inverse to moment gathering procedure. It can be shown that the weighting functions ξ must be identical in moment gathering and field interpolation in order to avoid self forces on the particles (Bagdonat 2005).

3.6 Particle Refinement

In particle mesh models, a certain number of particles must be present inside one cell in order to provide a reasonable resolution in velocity space. In the following we will label this number *oPiC* (optimal number of Particles in Cell) which we usually set to a value of 100. When adaptive mesh refinement is applied, particles have to be split up and merged in order to achieve this number. When particles travel across refinement boundaries from level L_n to level L_{n+1}, the volume of each cell decreases by a factor of eight (in three dimensions). Hence, the number of particles must be increased by a factor of eight to obtain the *oPiC*. This is achieved by splitting particles. On the other hand as particles travel from level L_{n+1} to level L_n the number of particles in each cell would increase by eight. In order to reduce this number particles are merged.

However, we shall point out that the value of *oPiC* may vary in space, i.e. a global value $oPiC_{global}$ is set prior to each simulation. Afterward a local value $oPiC_{local}$ is assigned to each cell as described in the following. First we set $oPiC_{local} = 8 \cdot oPiC_{global}$ inside blocks that are located adjacent to refinement boundaries of higher levels. This causes particles to be split before entering higher resolved levels which strongly reduces numerical noise. A quantitative analysis of numerical noise reduction is given in section 5.2.1. At first glance this seems to be numerically more expensive since more particles are involved. However, this is not necessarily the case, since it allows to completely avoid splitting and merging inside the highest level of refinement. This in turn is more accurate since no features inside the highest level of refinement (which are “the features of interest“) are falsified by means of particle refinement. Secondly we set $oPiC_{local} >= \rho_{local} \cdot oPiC_{global}$, where ρ_{local} is the local plasma density (as described in section 2.2 the background density equals one). This ensures that disproportional splitting or merging occurs in regions of increased plasma density (eg. inside shocks, magnetosheath or ionosphere). In summary, splitting and merging is triggered (a) by mesh refinement rather the physical features, (b) inside coarser rather than finer meshes and (c) never inside the highest level of refinement.

For the splitting of particles we apply a method similar to Kallio and Janhunen (2003). At each time step and for each cell it is tested, how much the number of particles inside the cell differs from oPiC. The smaller the number, the higher is the probability to split particles. In case a given number “minimal PiC” is under-run, the probability to split is set to one (see figure 3.3). The higher the number, the larger is the probability to merge particles. If a certain number “maximal PiC” is exceeded, the probability to merge is set to one.

For the following discussion it is instructive to label particles that exhibit a high weight value *large particles* while particles that exhibit a low weight value are labeled *small particles*. In addition we will use *weight* and *size* synonymously. If splitting is required, the largest particle of the cell is split into two particles, each of half size. The positions of the new particles are shifted by a small random distance $\Delta\underline{x}_1$ and $\Delta\underline{x}_2$ from the original particle position, where $\Delta\underline{x}_1$ and $\Delta\underline{x}_2$ are perpendicular to the particle velocity. In case one of the new positions is located outside the cell, the splitting process is canceled. The method conserves mass, momentum and kinetic energy. Since we generate $\Delta\underline{x}_1$ and $\Delta\underline{x}_2$ inde-

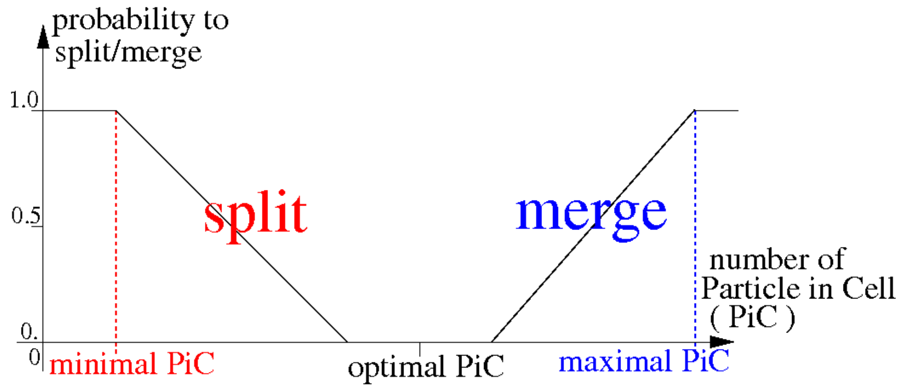

Figure 3.3: The sketch illustrates when splitting and merging is activated. The smaller the number of particles within a given cell, the higher is the probability to split particles. In case a given number “minimal PiC” is under-run, the probability to split is set to one. The higher the number, the larger is the probability to merge particles. If a certain number “maximal PiC” is exceeded, the probability to merge is set to one. This schema is adapted from Kallio and Janhunen (2003).

pendently, the center of mass is not conserved exactly for each individual split-process. However, since millions of particles are split it is statistically guaranteed that the center of mass accumulated over all particles is conserved.

Obviously shifting the two newly generated particles by $\pm\Delta\underline{x}$ from the original particle position would conserve the center of mass exactly for each individual split process. However, we found that doing so significantly increases the noise level of the plasma moments. Even worse it may result in numerical artifacts, since doing so tends to shift particles away from the cell center and accumulate them close to the cell edges. This in turn will result in lamellar shaped regions of enhanced density as particles travel into regions of higher refinement. A detailed explanation and test simulations on the different splitting strategies are given in section 5.2.1. In summary we found that overall physics are significantly better maintained when two small independent shifts $\Delta\underline{x}_1$ and $\Delta\underline{x}_2$ are generated that are perpendicular to the particle's velocity (see fig 3.4).

The method we use to merge macroparticles is adapted from Kallio and Janhunen (2003) as well. In order to conserve mass, momentum and kinetic energy, three particles are merged to two particles. In a first step two particles inside one cell are estimated that minimize the condition:

$$(w_1 + w_2)(\underline{v}_1 - \underline{v}_2)^2 \quad . \tag{3.12}$$

The third particle is found by minimizing the condition

$$w_3(\underline{v}_3 - \underline{v}_{CM}) \qquad \text{where} \qquad \underline{v}_{CM} = \frac{w_1\underline{v}_1 + w_2\underline{v}_2}{w_1 + w_2} \tag{3.13}$$

Computationally this process is of order $O(N^2)$ operations, where N is the number of particles inside the respective cell. Eq. (3.12) and (3.13) ensure that particles are selected

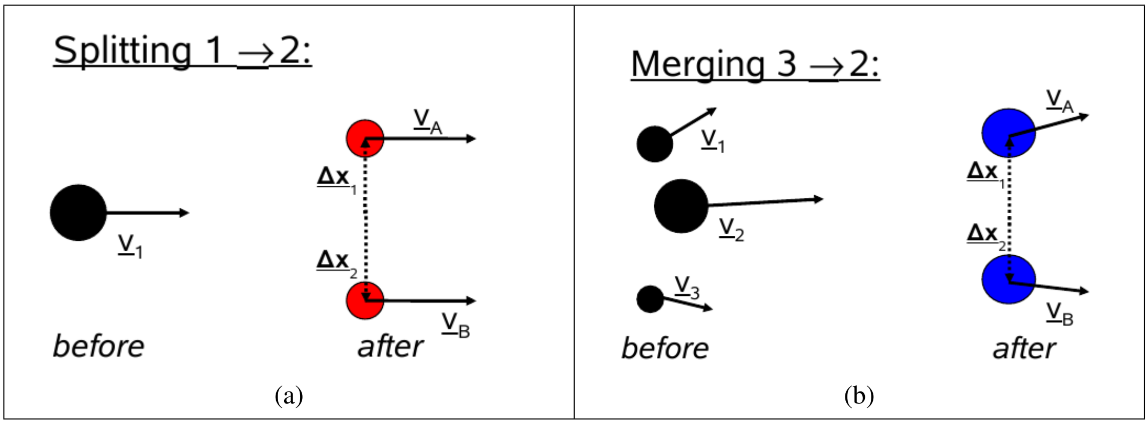

(a) (b)

Figure 3.4: The figure illustrates the method of particle splitting (a) and merging (b). The largest particle of the cell is split into two particles, each of half size. The positions of the new particles are shifted by a small random distance $\Delta \underline{x}_1$ and $\Delta \underline{x}_2$ from the original particle position, where $\Delta \underline{x}_1$ and $\Delta \underline{x}_2$ are perpendicular to the particle velocity. In order to conserve mass, momentum and kinetic energy, three particles are merged to two particles (b). This method is adapted from Kallio and Janhunen (2003). Both methods conserve mass, momentum and kinetic energy.

that are both, small and close in velocity space. Mathematically it would even be better to estimate three particles to merge at once. However, this operation would be of order $O(N^3)$ and therefore too expensive. In a second step velocities for two new particles are estimated that conserve momentum and kinetic energy. The mass is equally distributed to both particles. The new positions are calculated in the same way as in the splitting method.

In particular the merging procedure can be numerically very expensive if not implemented with great care. The number of particles inside several cells may easily reach 1000, resulting in 1000^2 = one million operations during each merging process. Especially in view of code parallelization this is unacceptable since it could never be load-balanced in an efficient way (see section 3.8). In order to accelerate the method we keep all particles weight-sorted: each cell is assigned its own particle-array. Whenever a particle leaves one cell and enters another cell, the particle is removed from the old cell's particle-array and inserted into the new cell's particle-array. In particular it is inserted before the next largest particle. This size sorting process can be efficiently implemented in C++ by means of "memmove" and "memcpy" operations. The time required for this operation is negligible. As a result the first particle of the particle-array is the smallest one and the size increases to the last particle, which is the largest one.

Hence for splitting no search operation has to be carried out. Instead the last particle of the array is chosen which is guaranteed to be the largest one. For merging, it is commonly sufficient to compare particles within the interval $[0 : N_{compare}]$ inside the cell's particle array, where we set $N_{compare} = \sqrt{N}$. On the one hand this ensures that only particles beyond the smallest are merged. On the other hand this yields a process $O((\sqrt{N})^2) = O(N)$. The effect of not considering the entire particle array for the merging procedure is discussed in section 5.2.3.

In summary the merging process, originally of order $O(N^3)$, is reduced to a process $O(N)$ and performs significantly faster than any of steps (1)-(6) listed in section 3.3. Since all operations related to particles now are of order $O(N)$, the schema can be efficiently load-balanced for parallelization. It will be argued in section 3.8, that this could not be achieved if any process related to particles would be of order $O(N^x)$ with $x \neq 1$.

3.7 Boundary Conditions

The boundaries have to be distinguished into obstacle and domain boundaries, referring to the inner and outer domain of the simulation geometry. For both of these types, conditions have to be set for the particles and electromagnetic fields. In the following we will discuss 1. particle-domain, 2. particle-obstacle, 3. field-domain and 4. field-obstacle boundary conditions.

1. Two different types of domain-boundary-conditions are used for the particles. "Inflow" conditions are specified at the upstream boundary, i.e. in every time step, each boundary cell is refilled with a particle distribution of a given bulk velocity and temperature. Particles that hit the downstream boundary are removed from the simulation which we refer to as "outflow" condition. However, in some scenarios where the thermal velocity is comparable to the bulk velocity (eg. Saturnian moons) both these condition fail at the downstream boundary: Due to the high thermal velocity outflow conditions result into a plasma depletion region while inflow condition artificially refill the plasma wake that forms behind the moon. In this case we clone the particle distribution from the ultimate plasma cell to the boundary cell which we refer to as "‘phase function cloning"’. In particular "‘phase function cloning"’ is required for modeling oppositely directed plasma streams that react very sensitive to the domain boundaries (see chapter 7, Titan’s magnetopause passage).

2. Particles that hit the obstacle’s surface are removed from the simulation in order to account for the particle-absorbing solid obstacle.

3. Two different types of field-domain-boundaries can be applied. Either the boundary value is set constant (Dirichlet-boundary-condition) or the derivative is set constant (Neumann-boundary-condition). Usually Dirichlet-conditions are specified at inflow boundaries while Neumann-conditions are specified at outflow boundaries where the field derivative is set to zero. In additional a resistive layer can be applied in order to damp waves that may be reflected at the domain boundaries.

4. The A.I.K.E.F. simulation code self-consistently includes the obstacle into the plasma environment: The obstacle is assumed to be an ohmic conductor for which a resistivity profile is specified. Equations 2.1 and 2.3 are solved within the entire geometry. Obstacle or plasma cells are exclusively distinguished by means of their coefficients $\underline{u}_i$, ρ_i and η. Within the obstacle $\underline{u}_i$ and $(\rho_i)^{-1}$ are set to zero which eliminates the convective and Hall terms in equation 2.1 while η is assigned a given profile. Hence, the magnetic field may propagate through the obstacle by means of

diffusion. This method has been successfully applied to study the plasma environment of several inert moons, e.g. Roussos et al. (2008) and Kriegel et al. (2009). Using a single equation for both regions where only the coefficients control the type of propagation process enables a continuous and self consistent coupling of obstacle and plasma regions.

3.8 Parallelization

The parallelization of fluid codes that use uniform meshes is very much straightforward. The computational domain is spatially split up into several sub-domains of equal size. This action is identical to the initial block decomposition which is inherently included in the block adaptive approach, except for that "blocks" are being labeled "sub-domains". Since the amount of work for each "sub-domain" is identical, each available CPU is assigned the same number of sub-domains which guarantees ideal load balancing.

This task becomes more challenging for particle-codes since in general the number of particles in each block strongly varies. For instance the density of particles inside ionospheres is very high compared to the background density. In contrast the particle density can be very low inside magnetospheres. Since the amount of work related to a given block depends on the number of particles inside this respective block, the amount of work per block varies strongly as well.

For this reason a reasonable load-balancing cannot be obtained by simply assigning an equal number of blocks to each CPU. Instead, in a first step each block is assigned a certain "workload", which we usually choose proportional to the number of particles inside this block. This assumption is reasonable since any function of the simulation code related to particles is of order $\mathcal{O}(N)$, where N is the number of particle. In a second step, the total workload of the entire simulation is estimated and divided by the number of CPUs, resulting in an average workload. In a third step, the blocks are distributed in such way that each CPU obtains approximately the average workload. For instance one CPU operates on a single block that includes 2 million particles while another CPU operates on two blocks that include one million particles each. The finer grained the domain decomposition is, the closer the workload for a given CPU is to the average workload.

On the other hand, the finer grained the domain decomposition is, the more communication is required which in turn slows down the computation and even may dominate over workload in case too fine grained decompositions are applied. In order to reduce the communication, blocks are not distributed arbitrarily among CPUs. Instead, all blocks of the entire computational domain are sorted along a so called "Space Filling Curve" (SFC). This method is for instance implemented by the RACOON simulation code by Dreher and Grauer (2005). For our simulation we choose a Hilbert-SFC that is visualized in fig. 3.5(f) for two dimensions. The SFC requires the number of root blocks to be a power of two in each dimension. Afterwards, the curve is subdivided into as many intervals as CPUs are available in such a way that each interval includes approximately the average workload. Finally, each CPU is assigned one interval of this curve. The shape of the curve ensures that blocks of a given interval are close in coordinate space. This in turn minimizes communication between CPUs. The steps of the block redistribution process are summarized below:

1. Sort blocks along SFC
2. Assign workload to each block
3. Estimate average workload each CPU
   (= total workload / N_{CPU}, where N_{CPU} is the number of CPUs)
4. Subdivide SFC into N_{CPU} intervals with the average workload each
5. Assign each CPU one SFC-interval

In summary the strategy explained above optimizes load-balancing and minimizes communication. In case adaptivity is used, the blocks of each refinement level are sorted along a SFC, i.e. each refinement level is assigned its individual SFC. As the number of potential blocks doubles for each dimension in higher levels of refinement, the condition that the number of blocks in each direction must equal a power of two is always met. After each refinement the blocks are redistributed in order to obtain an optimal load balancing. But even in case refinement is deactivated, blocks must be reorganized every several hundreds of time steps. This is required since the plasma processes are highly dynamical and particle numbers per block may strongly change in both, space and time. Fortunately time related to block redistribution is comparable to the time required for a single time step and therefore negligible.

The scaling of the A.I.K.E.F. simulation code is tested on up to 256 CPUs by means of two mesh types, a) uniform mesh and b) adaptive mesh. In both cases the physical parameters are chosen for the plasma environment of Mercury (see table 2.1). The simulation's coordinate frame is sketched in fig. 3.5(a). The solar wind is streaming in positive x-direction and Mercury's dipole moment is anti-parallel to the z-axis.

Simulations are run until the 3D simulation of the interaction between Mercury's magnetic field and the solar wind reaches the downstream simulation boundary, i.e. the solar wind has crossed about half of the simulation domain. The mesh refinement and corresponding CPU assignment for the adaptive mesh simulation that used 256 CPUs is visualized in fig. 3.5(b) by means of the polar cross-section. Each color refers to a certain CPU. Blocks of the same color are not scattered arbitrarily across the computational domain but close in coordinate space, i.e. these blocks are processed by the same CPU and network communication via MPI is not required. Each level of refinement is assigned an individual SFC which is why the color of parent- and children blocks differ. The simulations were carried out on HECToR at the EPCC Edinburgh. At this particular HPC-Cluster the minimal number of CPUs that must be used is two. Hence, for normalization we define the speedup of two CPUs to equal two.

We shall point out that we have tested the adaptive simulation exclusively for strong

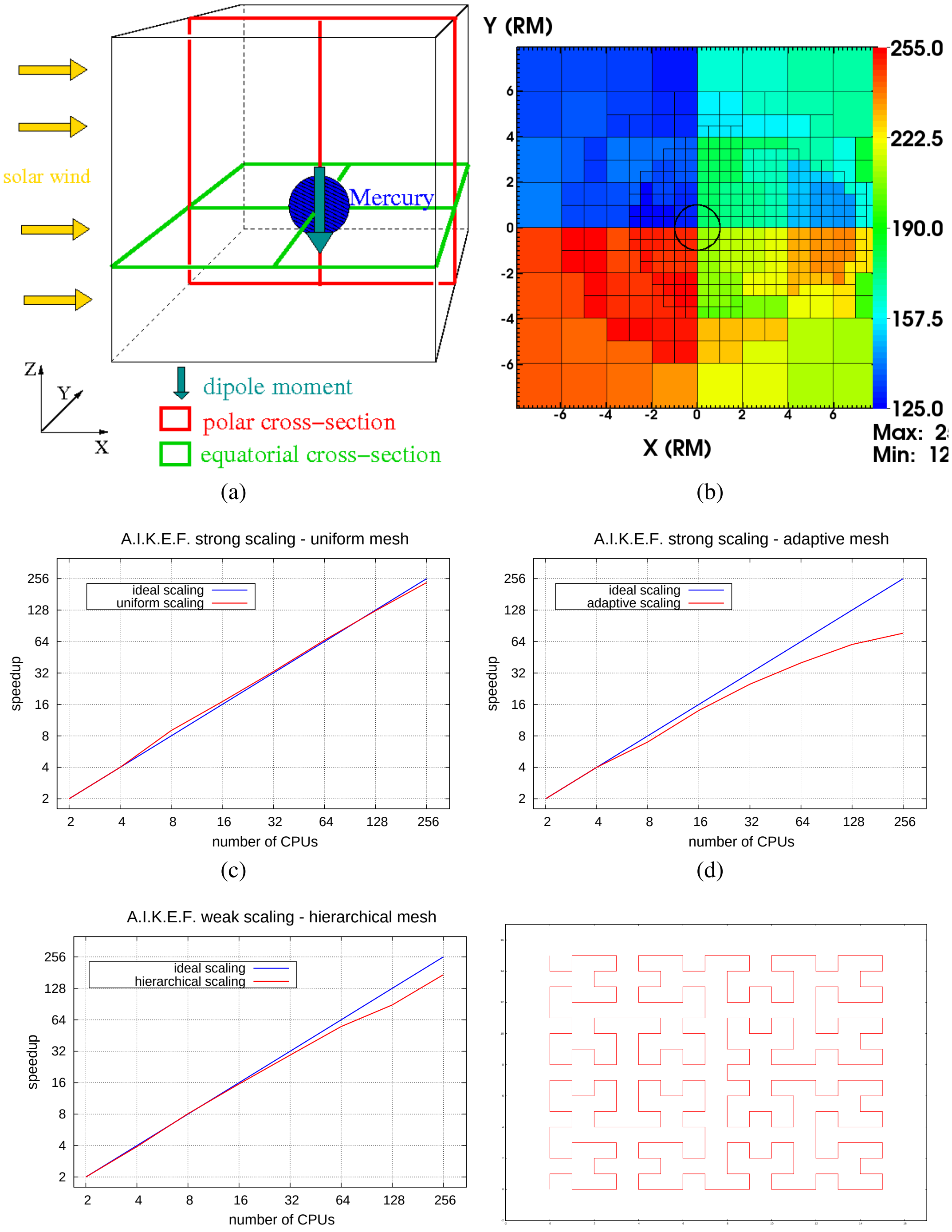

(a) (b)

(c) (d)

(e) (f)

Figure 3.5: The simulation's coordinate frame is sketched in (a). The mesh refinement and corresponding CPU assignment for the adaptive mesh simulation that used 256 CPUs is visualized in (b) by means of the polar cross-section. Strong scaling is visualized for a uniform mesh simulation (c) and an adaptive mesh simulation (d). Weak scaling for a hierarchical mesh is visualized in (e). For optimization of load balancing blocks are organized along Space Filling Curves (f).

scaling. This means that the identical program is executed several times with increasing number of CPUs. Hence, the total workload remains constant while communication increases. In contrast, the weak scaling approach doubles the problem size as the number of CPUs doubles, i.e. both workload and communication increase by the same factor which tends to scale much better. However, when AMR meshes are used, changing the problem size may result in completely different meshes. This in turn strongly affects the total workload and any estimate of speedup due to parallelization may become meaningless.

The plot of the static uniform mesh simulation fig. 3.5(c) shows that the A.I.K.E.F. code nearly scales linearly on up to 256 CPUs. At a number of 8 CPUs a slight super scaling can be observed. This effect is due to the HECToR architecture that applies nodes with 4 CPUs and 8 GB shared memory each. Since the simulation run requires approximately 7 GB memory, the execution speed is strongly memory bound. In the 8 CPUs simulation memory becomes distributed across two nodes which is why both, the number of CPUs and the bandwidth doubles compared to the 4 CPUs simulation and a speedup larger than two is obtained. When further increasing the number of CPUs, communication becomes dominant. Yet, even at 256 CPUs the speedup is 235 which corresponds to 92% of the ideal scaling value. The adaptive simulation fig. 3.5(d) scales less good than the uniform mesh simulation. The reasons for this are as follows:

First after each field or particle update ghost nodes must be exchanged (a) in between blocks of the same refinement level and (b) between parent and children blocks of different refinement levels. This inherently includes about twice as much communication compared to the uniform mesh simulation.

Second as described in section 3.3, the electromagnetic fields are propagated in each block of every level, while the particles are exclusively assigned to Top-Level-Blocks. Hence, an optimal load distribution for the electromagnetic field propagation would be to assign each CPU the identical number of blocks. In contrast, to obtain an optimal workload distribution for the particle propagation, the number of blocks for each CPU strongly varies as the number of particles in each block strongly varies. Since in general the work related to particles dominates, blocks are distributed proportional to the particle number. This in turn limits the optimal load balancing for electromagnetic field propagation and hence scalability.

Third, the uniform mesh simulation involves 512 blocks that consist of 14^3 mesh nodes each. In the adaptive simulation small blocks of 6^3 mesh nodes are used. This has to be done to obtain flexible meshes that in addition fit on a single computational node with 8 GB storage capacity. In the final setup about 5000 blocks are involved which is nearly one order of magnitude more than in the uniform mesh simulation. This requires significantly more communication which explains the reduced speedup compared to the uniform mesh simulation.

However, we shall point out that small blocks with a size of 6^3 mesh nodes have been used for this particular strong scaling test to adapt the simulation to a single computational node that is limited by 8GB memory. In general larger blocks comparable to the uniform mesh simulation are used when adaptive mesh simulations are carried out on 256 CPUs. Then communication is by far less dominant which is why this strong scaling is more of theoretical interest rather than of practical usage. However, as argued above it is not easy to set up a well-defined adaptive mesh scenario for weak scaling. Yet hierarchical meshes can be easily weak-scaled since they are static in time. Also we shall point out that an adaptive mesh simulation between the time interval $[nt_{refine} : (n+1)t_{refine}[, n = 0, 1, 2, ...$ equals a hierarchical mesh simulation since it involves identical operations. As the process of block reorganization after each t_{refine} is negligible in terms of computation time, it is reasonable to assume that an adaptive mesh will weak scale equal to a hierarchical mesh which is why we test the A.I.K.E.F. simulation code for weak scaling by means of a hierarchical mesh.

The weak scaling of a hierarchical mesh is carried out by using an identical refinement tree for each simulation and as a consequence equal number of blocks. However the number of mesh nodes of each block is doubled as the number of CPUs doubles. Hence, the workload and communication is increased by the same factor. The result is visualized in fig. 3.5(e). As can be seen the code scales linearly up to 64 CPUs. As CPUs are doubled to 128 the code does not scale linearly but continues to scale linearly as the number of CPUs increases to 256. We cannot state a definite reason for this behavior, yet secondary effects not related to parallelization might play a role. For instance the block size might exceed system cache. However, in general our tests show that the code efficiently scales up to at least 256 CPUs.

The parallelization is exclusively implemented by means of MPI-1 functions, that means in particular we resign to use MPI-2 functions such as remote memory access. The code is designed in such way that no distinguished “master-process” exists, i.e. every process is coequal. Data is written in a poor man’s parallel fashion, i.e. every MPI-process writes the data of the blocks on which it operates into an individual file. No synchronisation is required during the file output. Afterwards, the data is combined via the visualization software into a complete image. We use the VisIt[1] visualization tool (Childs et al. 2005) in combination with the Silo[2] file format.

---

[1] VisIt: https://wci.llnl.gov/codes/visit/

[2] Silo: https://wci.llnl.gov/codes/silo/

4 Implementation

When using adaptive mesh-refinement for particle-mesh simulation codes, the implementation is not as straightforward as for uniform mesh-codes, in particular when it is intended to be used on massive parallel computer clusters. It can be highly inefficient when not using a convenient concept. In the following we will discuss the implementation in detail. This is in particular to support future code development. For furhter information we refer the reader to van der Holst and Keppens (2007), Büchner et al. (2003), Lipatov (2002) and references therein.

4.1 Uniform Blocks

As described in section 3.2, the entire simulation domain is built of blocks, where each block is a uniform sub-mesh. This is also the case for uniform unrefined meshes, as the code is meant to operate in parallel where each processor handles a pre-defined number of blocks (see section 3.8). Figure 4.1 illustrates the numerical mesh of such a block in two dimensions. There are two categories of mesh nodes: *physical nodes* (blue filled circles) and *ghost nodes* (blue unfilled circles). The electromagnetic fields are calculated on physical nodes while the ghost nodes are exclusively required to ensure an efficient calculation and communication, but have no physical denotation.

We define a *physical cell* to be the volume between four mesh nodes (eight in three dimensions) where the upper left corner is a physical node (green square). If the upper left corner is a ghost node, this volume is labeled *ghost cell* (red square). The *physical volume* associated with the entire block is the set of all physical cells (blue square). Within this volume particles move freely in between the mesh nodes (yellow dots). As can be seen, the physical volume is not symmetrical arranged within the block, but it is shifted by $\Delta_x/2$ and $\Delta_y/2$, where Δ_x and Δ_y define the distance between two adjacent mesh nodes in x and y direction, respectively. Compared to the symmetric definition, as indicated via the dashed magenta square, the asymmetric definition turns out to exhibit several advantages for both, refined and unrefined meshes. In particular, only the physical cells are assigned particles while the ghost cells are exclusively assigned particles for an optimized inter block communication as will be explained in section 4.3.

The number of physical mesh nodes and the block length may be chosen independently for each direction x, y, z, where e.g. the block length $L_{Block,x}$ is the edge length of the physical volume in x direction (black bar). The block origin refers to the physical node with the lowest (x, y, z) value, respectively (patterned blue circle). To clarify how the domain

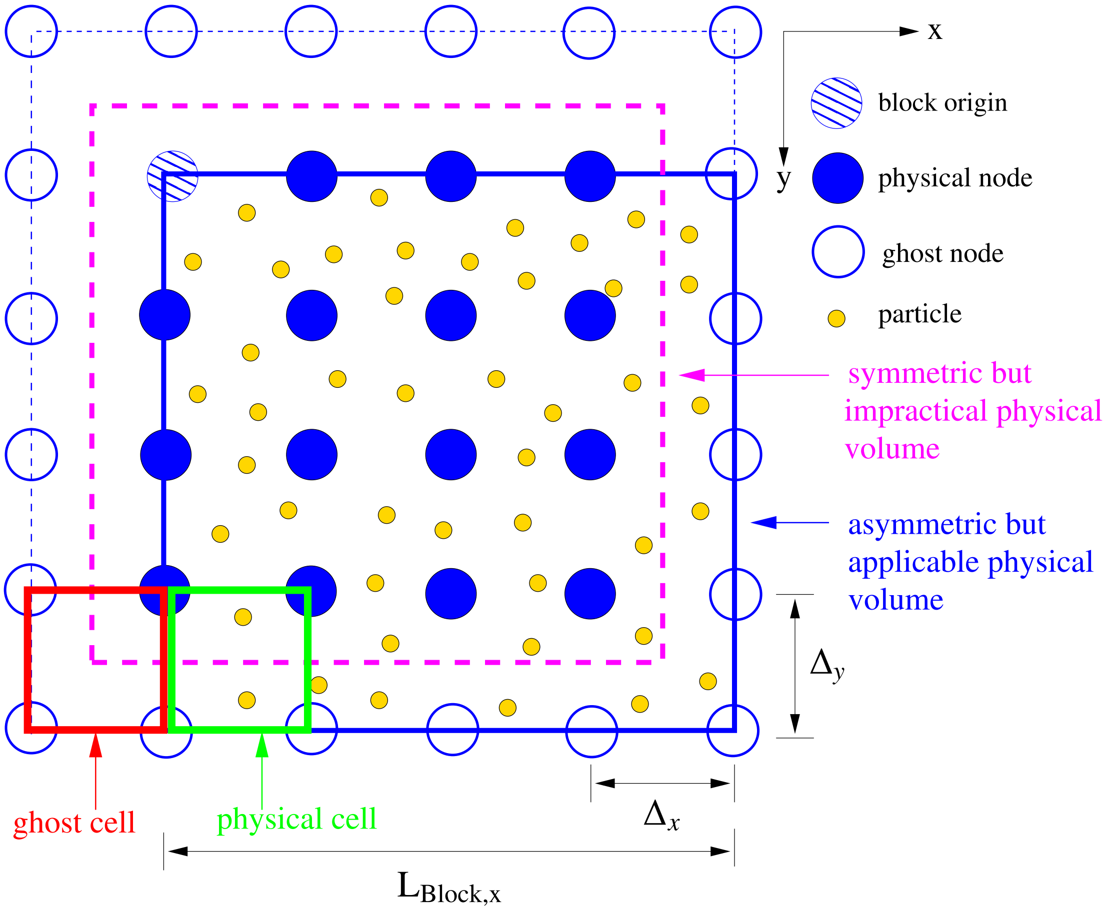

Figure 4.1: The Sketch illustrates the numerical mesh of a block in two dimensions. The mesh nodes are distinguished into physical nodes (blue filled circles) and ghost nodes (blue unfilled circles). The electromagnetic fields are calculated on physical nodes while the ghost nodes are exclusively specified to ensure an efficient calculation and communication, but have no physical meaning.

is decomposed into blocks, figure 4.2(a) displays two neighboring blocks that border on each other. As can be seen the physical block volumes directly match such that no empty space is left in between. The ghost nodes of the blue block coincide with the outer physical nodes of the red block and vice versa. The reason for the application of ghost nodes is explained in the next section 4.2.

4.2 Field Update

As argued in section 3.4, central finite differences are used to solve the hybrid equations introduced in section 2.1. Hence, for the field calculation at a given mesh node the field values at the adjacent mesh nodes are needed. Due to the mixed second derivatives in Faraday's law (cf. equation 2.3) the values of 26 surrounding mesh nodes are required. If an adjacent mesh node is inside the same block, its value can be accessed very quickly.

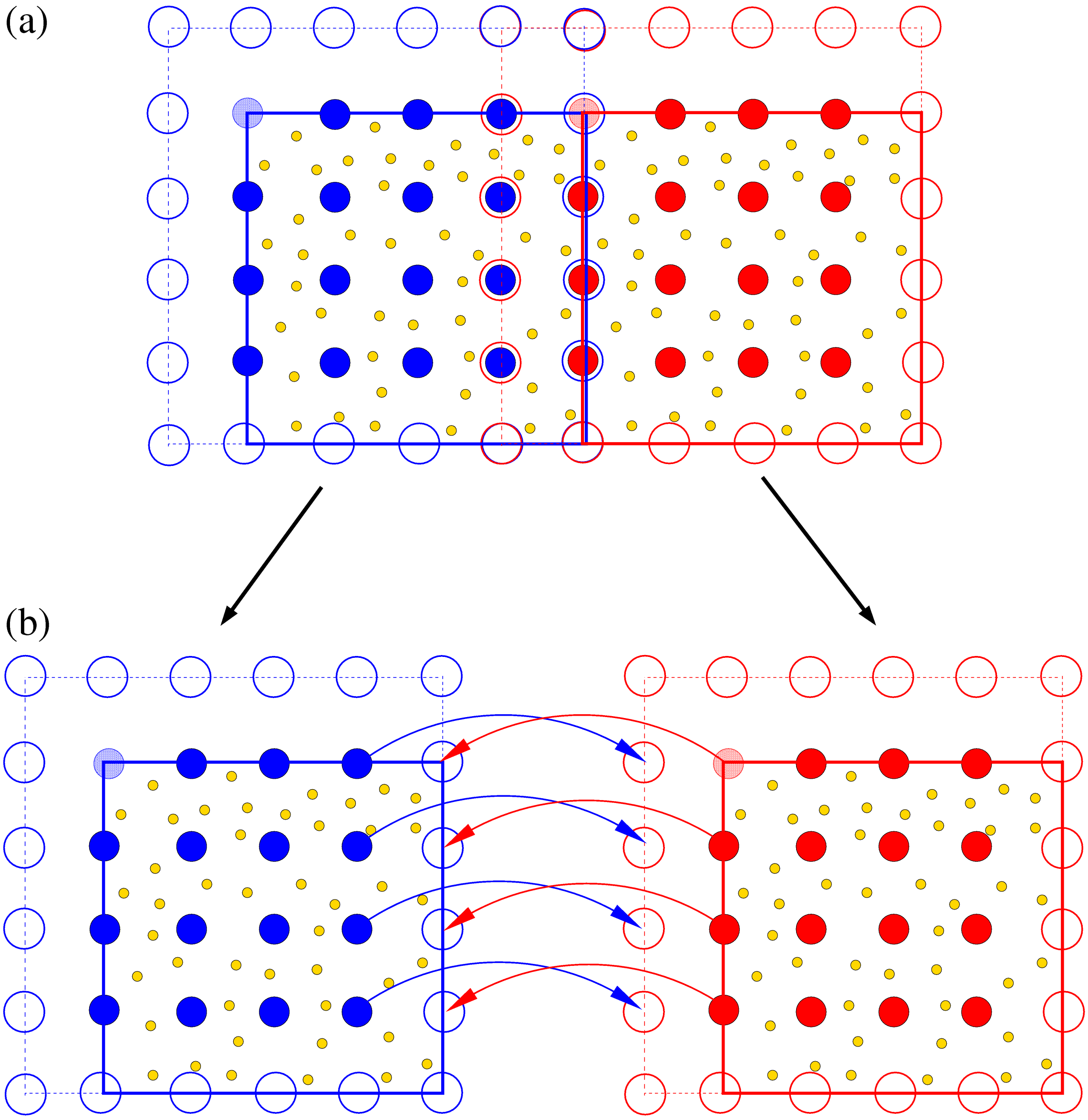

Figure 4.2: To clarify how the domain is composed of blocks, the sketch (a) shows two neighboring blocks that are located adjacent to each other. As can be seen the physical block volumes directly adjoin such that no empty space is left in between. In coordinate space the positions of the blue block's ghost nodes are identical with the outside physical nodes of the red block. However, in memory these values belong to distinct data structures (b). Thus, they have to be synchronized prior to each field update (blue and red arrows).

The reason is that all values of a given block are allocated in the same sequence of memory. However, if the adjacent mesh node is located inside a neighboring block, its field value cannot be accessed likewise quickly. Thus, the field update is decomposed into two steps. In a first step, the physical values at the blue block's edge are copied to the ghost nodes of the red block and vice versa (see arrows in Figure 4.2). In a second step the equations are solved within the respective blocks without requiring further communica-

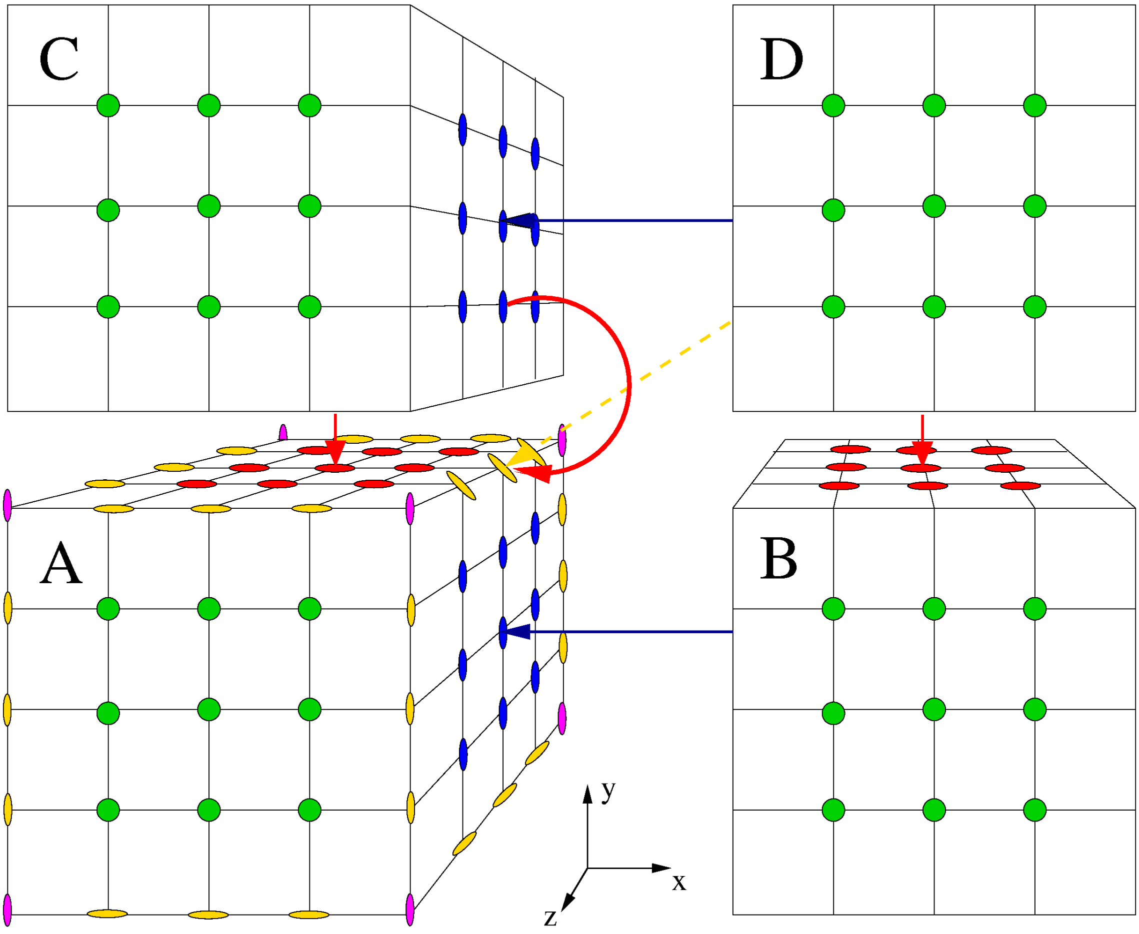

Figure 4.3: Block A requires values from block B in x-direction (blue dots), from block C in y-direction (red dots) and in z-direction (green dots). In addition block A requires the values for eight corners (magenta dots) and twelve edges (yellow). In a first step, the ghost values in positive and negative x-direction are updated (blue arrows). In a second step, all ghost values in positive and negative y-direction are updated (red arrows). Consequently, all edge ghost values that are parallel to the z-axis are updated at the same time (red bended arrow). Obviously the direct path, as sketched by the dashed yellow arrow, is not required. Finally, in a third step, all ghost values in positive and negative z-direction are updated (not shown here). This automatically updates all residual edge and corner ghost values.

tion. In the following, the values at ghost nodes are referred to as *ghost values*.

The gain in efficiency is in particular significant when the blocks are processed in parallel. Then neighboring blocks might be handled by different processors and consequently network communication is required. As network communication is carried out by the Message Passing Interface (MPI) in A.I.K.E.F., values are send via MPI-messages. Each message may include as many values as needed. By using the ghost node method only two MPI messages are needed to exchange the ghost values between the blue and red block (see Figure 4.2). In contrast, when not using ghost nodes at least one message for each node would be required. Since the communication time mainly depends on the number of messages rather than their size, it is much more efficient to send all values combined within a single large message rather than using one message for each value. The performance advantage becomes in particular significant for typical hybrid simulations in which blocks include hundreds of ghost nodes in each direction rather than six, as indicated in sketch 4.2.

Within an uniform mesh each block is surrounded by $3^{dim} - 1$ neighboring blocks. Thus, in three dimensions each block requires the ghost values from 26 adjacent blocks. For clarification the ghost value exchange is sketched in figure 4.3. As can be seen, block A requires face-ghost values from block B in x-direction (blue dots), from block C in y-direction (red dots) as well as in z-direction (green dots). In addition it requires the ghost values for twelve edges (yellow) and eight corners (magenta dots). In this example the right upper edge has to be obtained from block D (yellow dashed arrow). Obviously one way to exchange the ghost values would be to send and receive 26 messages for each block to update all faces, edges and corners. However, as will be explained in the following six messaged are sufficient. In a first step, the ghost values in positive and negative x-direction are updated (blue arrows). In a second step, all ghost values in positive and negative y-direction are updated (red arrows). Consequently, all edge ghost values that are parallel to the z-coordinate are updated as well (red bended arrow). Obviously the direct path as sketched by the dashed yellow arrow is not required. Finally in a third step, all ghost values in positive and negative z-direction are updated (not shown here). This automatically updates all residual edge and corner ghost values. Hence, performing the ghost values update this way requires only six messages instead of 26 are which reduces the communication by more than a factor of four.

4.3 Particle Update

Not only values at ghost nodes but also particle positions have to be updated: during their propagation particles may leave the physical volume of a given block, as sketched in Figure 4.4. The new positions of the green particles that leave the blue block are located within the red block. On the other hand, the new positions of the light blue particles that leave the red block are located within the blue block. Obviously one solution would be to send each particle to the respective block immediately when it leaves this block. However, this would result in a huge number of MPI messages and thus drastically decrease the code's performance.

Hence, in a first step all particles are moved. If the new positions for certain particles are outside the physical volume of the given block, these particles temporary accumulate within ghost cells. In a second step, when the movement of all particles is completed, all particles are reassigned to the new corresponding block and cell. This procedure is very similar to the field update as argued in section 4.2: one step includes block-local calculation and the next step inter-block-communication. The only difference is that twelve

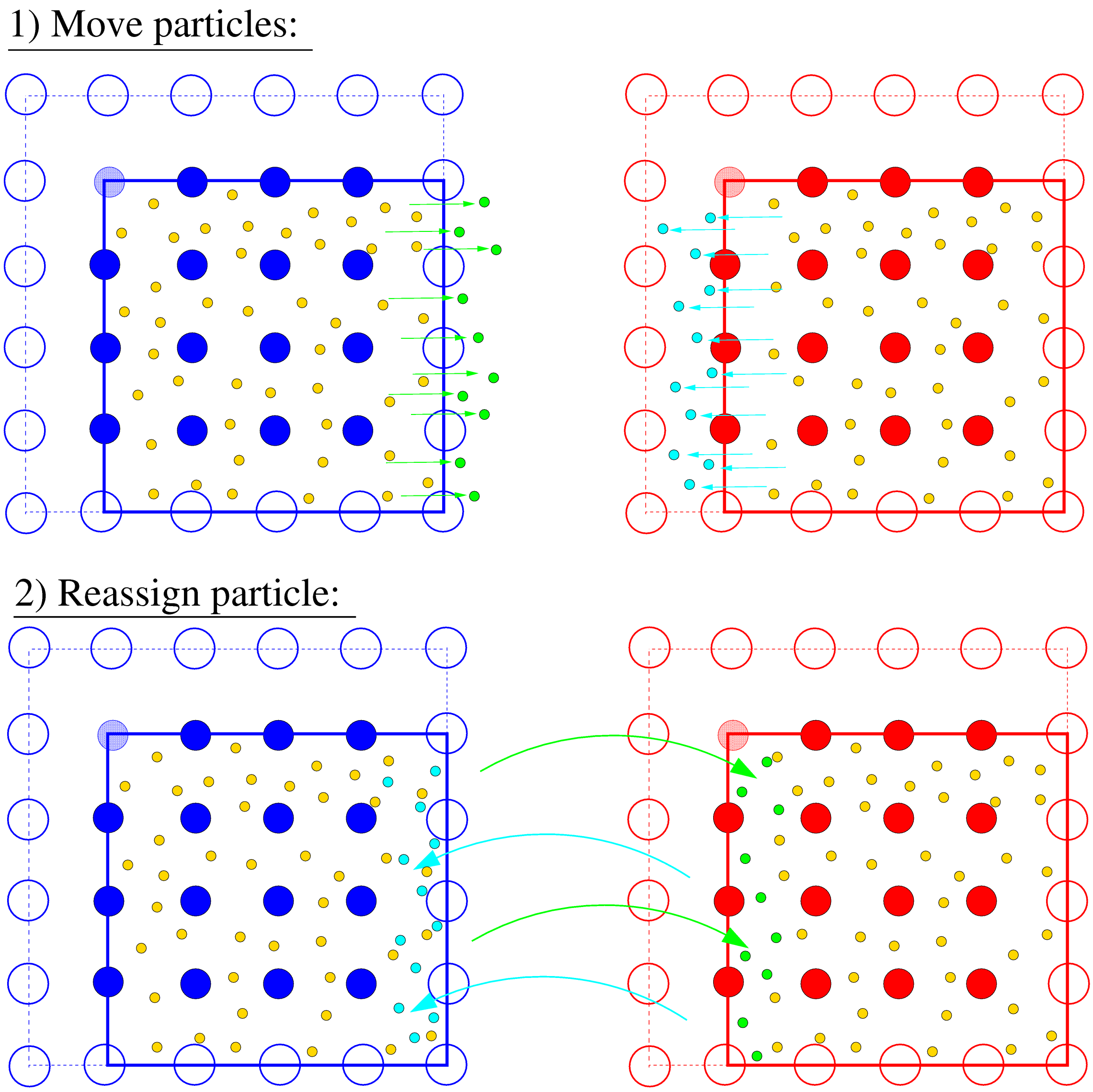

Figure 4.4: In a first step all particles are moved. In case their new positions are outside the physical block-volume their position are temporary stored in ghost cells. In a second step, all particles are reassigned to the corresponding block and cell. This procedure is very similar to the field and ghost value update shown in figure 4.3.

messages are send instead of six, i.e. two in each direction: as the number of particles that leave each block varies from time step to time step, the first set of messages includes the information on how many particles will arrive in each cell of the new block. The second set of messages includes the actual properties of the arriving particles.

As each block is surrounded by only a single layer of ghost cells, even the fastest particle within the simulation may not cross more than one cell within one time step. Otherwise the particle may overjump the ghost cell layer which will cause the simulation to exit. However, in order to correctly model the involved physics the Courant-Friedichs-Lewy

(CFL) condition requires that no particle crosses a cell faster than within one time step and hence, no additional restriction is introduced.

In the following we shall comment on the particle's memory layout within the A.I.K.E.F. simulation code: particles are allocated in arrays, i.e. entire memory blocks rather than linked lists as e.g. implemented its predecessor code. The advantage of particles arrays over linked lists is that today's computer do access the main memory in cache-lines rather than byte by byte. Cache-lines are blocks of bytes and typically several hundred bytes in size. When using arrays, commonly the entire cache-line will be filled with particles that are subsequently processed. In contrast, when using linked lists each particle structure includes a pointer that references the next particle. Particles are allocated randomly distributed across the main memory resulting in significant memory fragmentation ("pointer chasing problem"). Thus, cache-lines will commonly include only a single particle while the other information remains unused. This will cause a drastic increase in cache-misses, i.e. information that shall be processed is not found in CPU-cache and must be accessed in main memory which is slow. As the trend in computer architecture shows the gap between processing speed and memory access rate to widen, the advantage of arrays will even increase likewise in the future.

The improved memory layout is one reason why the A.I.K.E.F. simulation code outperforms its predecessor code by a factor of six even for uniform and serial simulations (see section 5.1). A nice side effect of particle arrays is that the memory required for each particle decreases by about 30%: as each cell is assigned one particle array for each species, the particle structure does neither require information on the particle species nor a pointer to the next particle. Furthermore both, the gathering and particle acceleration method benefit from the improved memory layout.

4.4 Gather Update

Like the field calculation and particle movement the gather method of section 3.5 is decomposed into a block-local gathering step and communication step as well. In the fist step, plasma moments such as currents and densities are gathered within each block according to section 3.5. As sketched in Figure 4.5, particles may only be located inside the blue shaded physical volume (cf. Figure 4.1). Due to the asymmetric definition of the volume (see section 4.1), ghost nodes in positive x,y and z direction will be non-zero (blue circles) while the ghost nodes in negative x,y and z direction will always be zero and therefore remain unused (indicated via red crosses).

Assuming an undisturbed background density of one, each edge node in positive x,y and z direction is assigned 1/2 while each corner node is assigned 1/4 after the gather step (see Figure 4.5). Nodes inside the physical volume are assigned one and therefore do not require further treatment. In order to complete the edge values as well, the edge ghost values are successively added to the outside physical nodes of the neighboring block in positive x, y and z direction (green arrows). As can be seen in Figure 4.5 the values at the corners are assigned one after this procedure as well. Thus, only three messages have

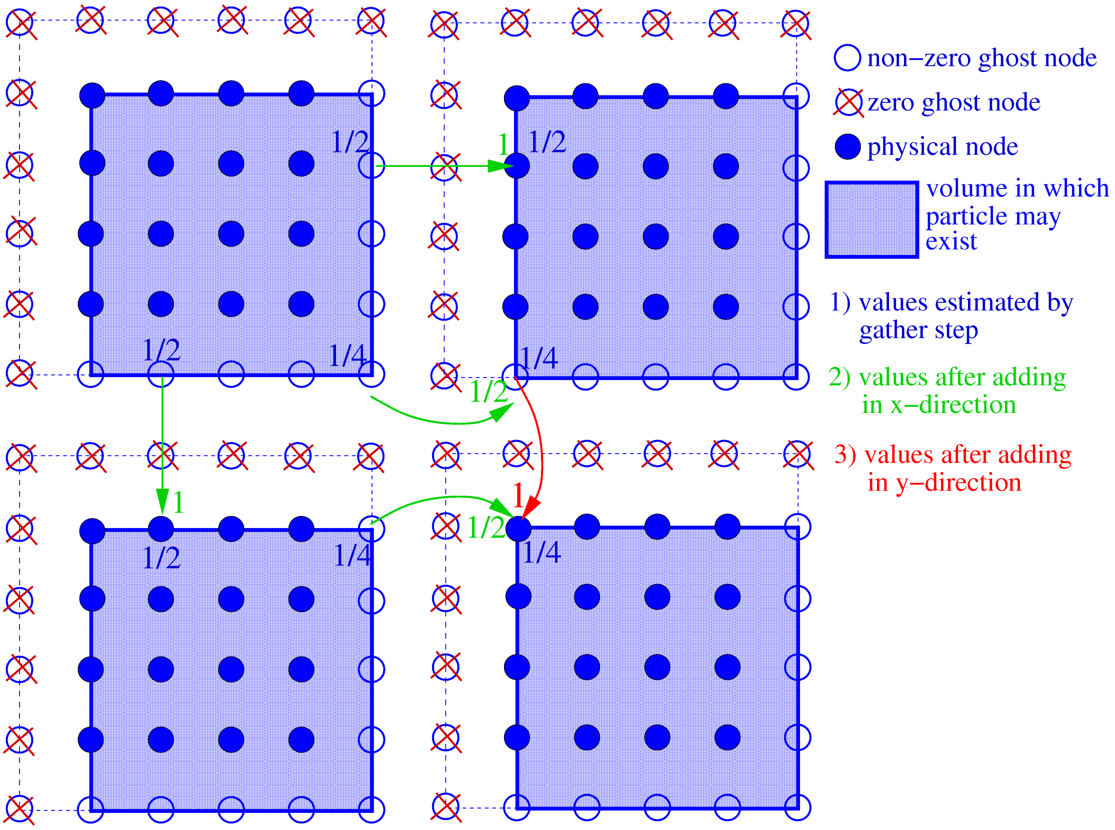

Figure 4.5: The sketch illustrates the particle gathering for a homogeneous background density of one in two dimensions. As was shown in section 4.1, particles may exclusively exist inside the blue shaded physical volume. Thus, ghost nodes in positive x and y direction are assigned non-zero values (blue circles). In contrast, the ghost nodes in negative x and y direction are always zero and therefore remain unused (red crosses). After the gathering inside the block is finished, ghost values at the edges equal half the background density while those at the corners equal one quarter of the background density. To complete the gathering, edge ghost values are added to the corresponding block in x direction (green arrows). In a second step, ghost values are added in y direction (red arrows) which automatically completes the values at the block corners.

to be sent by each block. However, an ordinary ghost node update has to be carried out afterwards in order to allow the electromagnetic field calculation, as described in section 4.2. Hence, in total nine messages are required for each block for completing the gather method.

We shall point out that the number of messages is independent of the number of ion species involved, as A.I.K.E.F. is designed such that all macroscopic ion densities and the total ion current are stored within the same message.

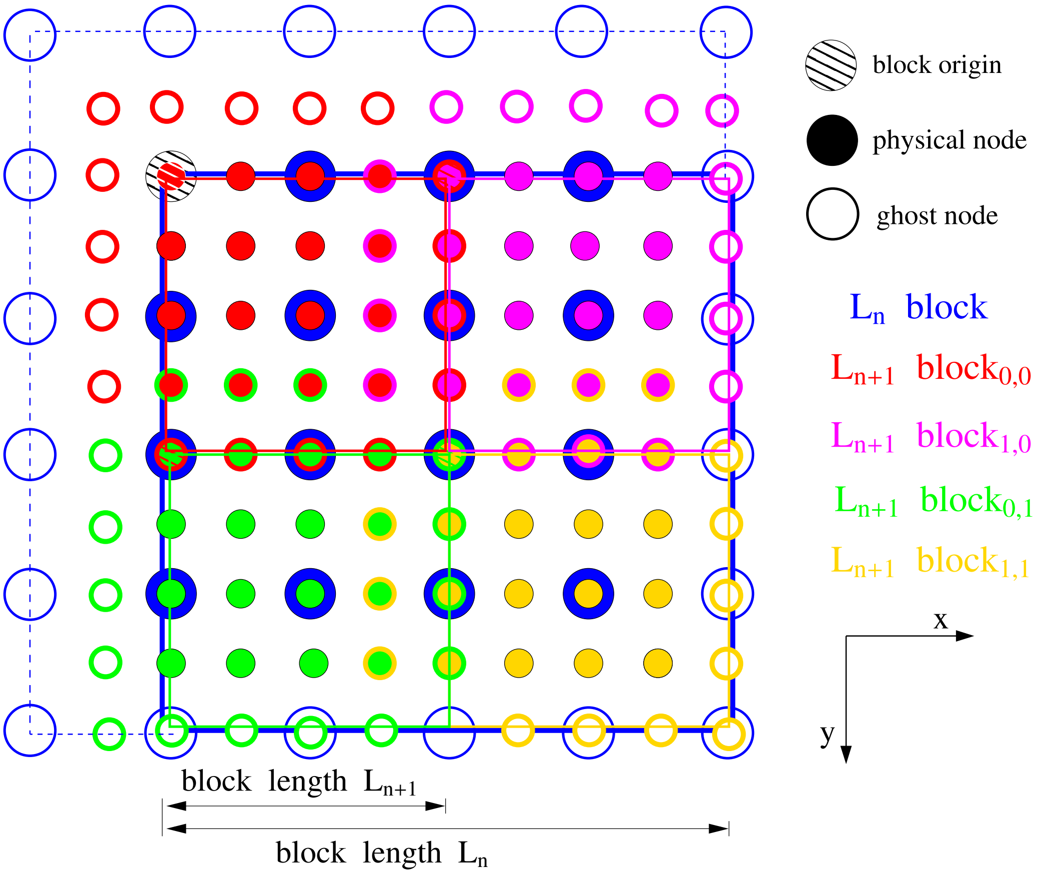

Figure 4.6: The Sketch illustrates how each block can be refined in up to 2^{dim} children blocks, i.e. four in this two dimensional sketch. Physical nodes are indicated by means of filled circles, ghost nodes are denoted via unfilled circles. The large block (blue) is of refinement level L_n, the smaller blocks that cover the blue block are from refinement levels L_{n+1}, (where n=0,1,2,...). The block nesting is chosen such that the combined physical volume of the four refined L_{n+1} blocks covers exactly the original volume of the L_n block. Consequently, the edge length of L_{n+1} blocks is half the edge length of the L_n block. As the number of mesh nodes is the same in every block, the resolution doubles each level increment.

4.5 Treatment of Refined Blocks

So far we have discussed the block decomposition of an uniform mesh. In the following we will explain the implementation of block adaptive mesh refinement (Block-AMR). As sketched in Figure 4.6, each block may be refined in up to 2^{dim} children blocks, i.e. four in this two-dimensional sketch. The sketch is an extension of Figure 4.1, the labeling is basically the same. The large block (blue) is of refinement level L_n, where n=0,1,2,... . The smaller red, yellow, magenta and green blocks are from higher refinement level L_{n+1} and thus cover the blue block. These blocks are referred to as the *children* of the L_n block. On the other hand, the L_n block is referred to as the *parent* of the L_{n+1}-blocks.

(a) Particle inside ghost cells:

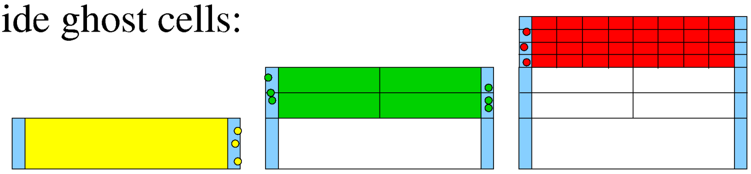

(b) Step 1: particle to parent−block

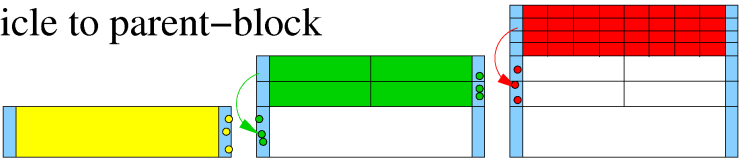

(c) Step 2: exchange particle in equal level

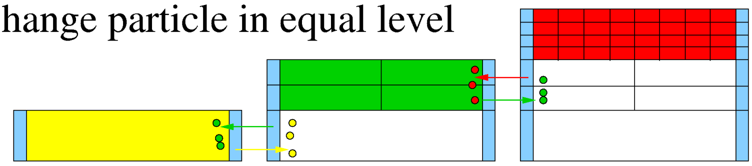

(d) Step 3: particle to children−blocks

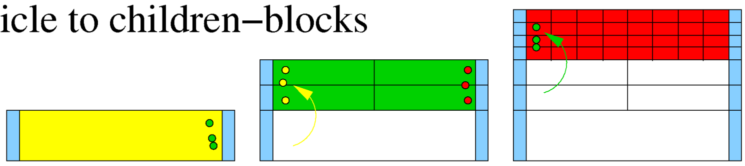

Figure 4.7: The yellow cuboid indicates an L_n block, the green cuboids indicate L_{n+1} blocks and the red cuboids L_{n+2} blocks. When particles are moved, they may be temporary located inside ghost cells (light blue stripes (a)). Afterwards, particles inside ghost cells of blocks that are located adjacent to refinement boundaries are sent to the ghost cells of their parent blocks (b). In a second step, an ordinary particle reassignment is applied as explained in section 4.3, i.e. particles are exclusively exchanged within the same refinement level (c). Finally, particles which are located inside a block that possesses a child block at the respective position are sent to the respective child block (d).

The block nesting is chosen such that the combined physical volume of the four refined L_{n+1} blocks covers exactly the original volume of the L_n block. Consequently, the edge length of L_{n+1} blocks is half the edge length of the L_n block. As the number of mesh nodes is the same in every block independent of its refinement level, the resolution doubles each incrementing level. Due to this choice the origin of the upper left L_{n+1} block (red) coincides with the origin of the L_n block. In order to keep the interpolation between blocks of levels n and n+1 simple, we claim that each mesh node of the L_n block has to coincide with a mesh node of an L_{n+1}-block. This requires the number of mesh nodes in each block to be a multiple of two, i.e. an even number. After each field update the values calculated within L_{n+1}-blocks are projected to the L_n-blocks following equation 3.10 to avoid aliasing. On the other hand, ghost nodes of L_{n+1}-blocks at refinement boundaries receive there values via interpolation from subjacent L_n-blocks.

The particle motion and reassignment might not be as straight forward as L_n-blocks can be surrounded by up to $4^{dim} - 2^{dim}$ L_{n+1} blocks, i.e. 56 blocks in three dimensions. To keep the particle reassignment as simple and fast as possible, the following method is applied as sketched in Figure 4.7. The yellow cuboid denotes a L_n block, the green cuboids denote L_{n+1} blocks and the red cuboids L_{n+2} blocks. Only the topmost blocks are colored as particles are always assigned to the topmost refinement level. The subjacent blocks (white) are only kept allocated to simplify the communication. The light blue stripes indicate ghost cells.

Like in the unrefined case, particles are moved and may leave the physical volume of the respective blocks. Immediately after the movement step these particles are temporary located inside ghost cells, as explained in section 4.3 and sketched in Figure 4.7(a). Starting from this initial state, three successive steps are required to reassign the particles to their designated blocks. In a first step particles inside ghost cells of blocks that are located adjacent to refinement boundaries are sent to the ghost cells of their parent blocks (see 4.7(b)). In a second step, an ordinary particle reassignment is applied as explained in section 4.3, i.e. particles are exclusively exchanged within the same refinement level rather than in between refinement levels (see 4.7(c)). Finally, the particles which are located inside a block that is not the topmost block at its location are send to the respective child block (see 4.7(d)). Consequently, all particles have arrived at their designated blocks.

4.6 Tree Data Structure

Lastly, we shall comment on how the blocks logically connect. As described in section 3.2, each block in refinement level zero is the root of an oct-tree (quad-tree in two dimensions, see Figure 4.8). Every block possesses a pointer to its parent and eight pointers to its children. If the block is not or only partially refined, the respective pointers are assigned zero. In principal these information are sufficient to access every block. However, to perform a ghost node update within a certain level one would have to climb up all oct-trees starting from level zero to instruct the blocks of the respective level to complete the ghost node update. This would be quite circuitous and inefficient. To selectively access exclusively all blocks of certain refinement level, blocks that belong to the same refinement level are sorted in a linked list as is sketched in Figure 4.8.

After a block has been created, it is assigned an integer number which is unique in the respective refinement level. The number depends only on the block position in coordinate space (cf. red numbers in Figure 4.8). The transformation we use to map the block coordinate to an integer number is a Hilbert space-filling-curve (SFC) which for this purpose can be considered a bijective transformation between the $\mathbb{N}^3$ and $\mathbb{N}^1$. After the number has been estimated, the block is inserted at the respective position within the linked list. While every possible position within refinement level zero is used, many blocks in higher levels will usually remain unrefined and their numbers unused (see L_1-SFC in Figure 4.8). Besides the advantage of an optimized parallelization (see section 3.8) the linked list allows to selectively access all blocks of a certain level for instance to perform a ghost node update. In addition, it allows to store the entire refinement tree on hard disk in a data structure that requires only one byte per block.

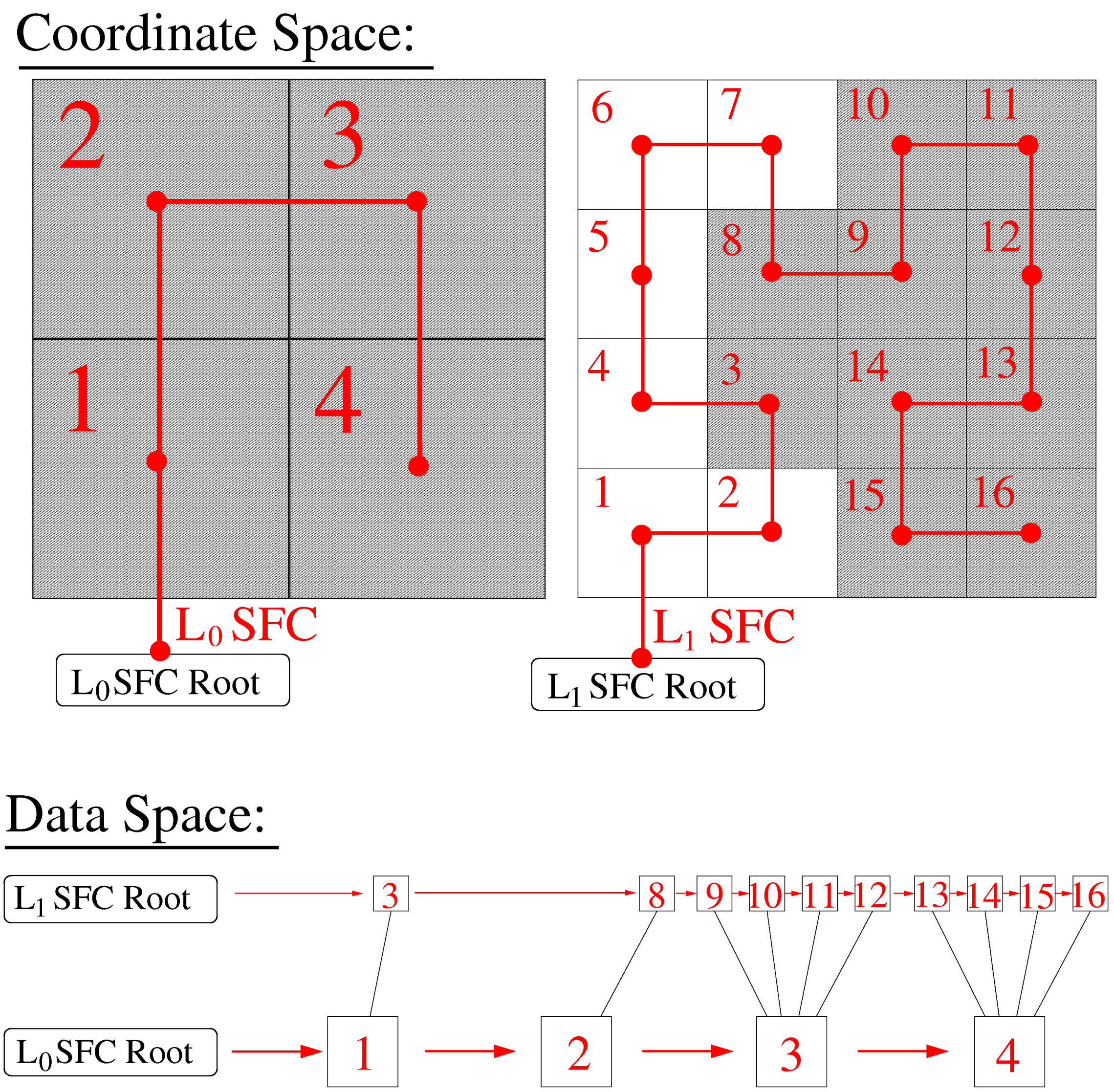

Figure 4.8: The sketch illustrates the coordinate and data space of a two-dimensional mesh that includes four root blocks and one refinement level. Each block in refinement level zero is the root of a quad tree (oct tree in three dimensions). Every block of a given refinement level is assigned a unique number that depends on the block position in coordinate space and defines the location within a linked list. The number is estimated via a space filling curve (SFC) transformation. The linked list allows the selective access of all blocks within a given refinement level (e.g. to perform a ghost node update). While the linked list of refinement level zero is a continuous sequence of integer values, many numbers in higher refinement levels remain unused as not all blocks are refined (cf. L_1-SFC). The use of a linked list is not performance critical when dealing with large objects like blocks.

As the blocks require to communicate with their direct six neighbours in coordinate space, each block additionally possesses pointers to its six direct neighboring blocks in the same refinement level. Even though linked list do perform less well than arrays (see section 4.3) the application of linked lists is more simple and not performance critical here. The reason is that the time required to complete one cycle through the linked list is negligible compared to the time required to carry out the work related to one block.

5 Test Simulations

During and after development, the A.I.K.E.F. simulation code has been constantly tested for correct physical behavior. In this section several tests are presented and sorted by means of increasing complexity. In section 5.1 results of the A.I.K.E.F. simulation code are compared with results of its predecessor, the Bag2002 code. The conservation of several quantities during splitting and merging is tested in section 5.2. In section 5.3 the dispersion relation of high frequency whistler waves is estimated. In addition it is tested via Fourier analysis in space and time whether wave reflexion occurs at refinement boundaries. In section 5.4 a standing fast wave is excited and observed whether it propagates at correct velocity and whether it is modified as it travels across refinement boundaries. In section 5.5 results of an adaptive simulation are compared with a reference uniform mesh simulation and the speedup of the adaptive simulation is estimated. For the final test in section 5.6 we chose a real scenario and compare MESSENGER measurements with simulation results of Mercury's plasma environment.

5.1 Comparison of the A.I.K.E.F. Simulation Code with its Predecessor

As described in section 3, the A.I.K.E.F. simulation code and the Bag2002 code are based on the identical numerical schema by Matthews (1994). The only difference is that the Bag2002 code uses static curvilinear meshes while A.I.K.E.F. uses adaptive Cartesian meshes. The Bag2002 code was tested for several physical properties such as conservation of energy and momentum or correct modeling of wave propagation and dispersion relation on Cartesian meshes (Bagdonat and Motschmann 2002). Beyond that, it has been successfully applied to a large number scenarios, such as comets (Bagdonat 2005), asteroids (Simon et al. 2006a), Mars (Bößwetter et al. 2004) and several Saturnian moons such as Titan (Simon et al. 2006b), Rhea (Roussos et al. 2008) and Enceladus (Kriegel et al. 2009).

Since the application of block AMR requires a complete redesign in terms of data structures, the A.I.K.E.F. code is not based on its predecessor code but rewritten from scratch. Hence, the first obvious test is to check whether the results of both codes are identical when Cartesian meshes are applied, which can be handled by both simulation codes. As a test scenario we choose the interaction of a strong comet with the solar wind that includes many key processes such as wave excitation, heavy ion pick-up and wave particle interaction. However, it is not our intention to analyze the physical processes. A detailed analysis

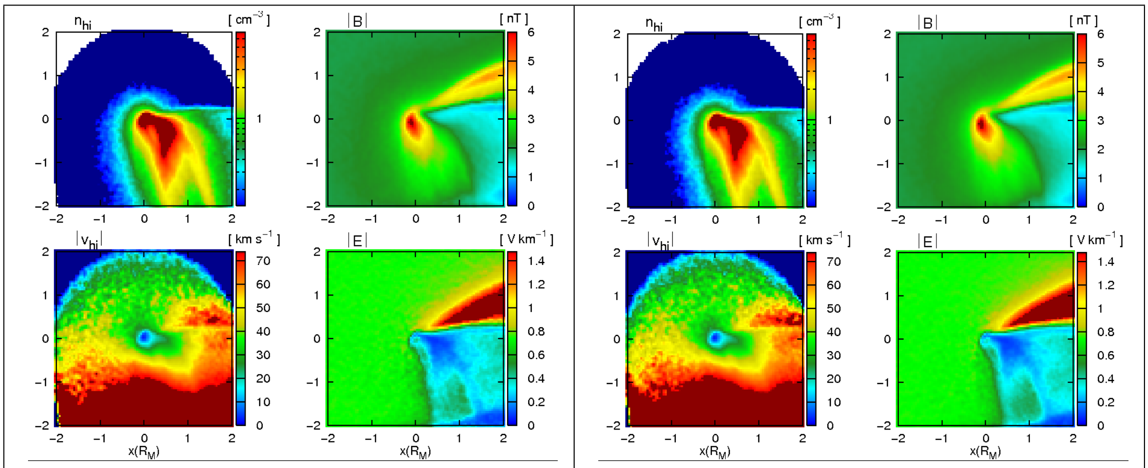

(a) Bag2002 code

(b) A.I.K.E.F. code

Figure 5.1: Cometary uniform mesh simulation of the Bag2002 simulation code (a) and A.I.K.E.F. simulation code (b) are compared. The color coded physical quantities are the heavy ion density n_{hi}, heavy ion velocity v_{hi}, the magnetic field $\underline{B}$ and the electric field $\underline{E}$. The physical structures are qualitatively and quantitatively identical. Due to optimization the A.I.K.E.F. code performs six times faster.

of the physics and description of the simulation setup is given by Bagdonat (2005). The only purpose of this comparison is to proof that both simulation models yield identical results.

Figure 5.1 shows results of the three-dimensional cometary simulation by means of the y-cross-section. The color coded physical quantities are the heavy ion density n_{hi}, heavy ion velocity v_{hi}, the magnetic field $\underline{B}$ and the electric field $\underline{E}$. As can be seen the physical structures are both, qualitatively and quantitatively identical. A close view reveals that the noise, which is due to the finite number of particles, is not exactly the same (eg. in the heavy ion velocity). The reason is that the A.I.K.E.F. code uses the GSL[1] random generators, while the Bag2002 code includes standard C random generators in combination with less sophisticated methods to generate Maxwellian particle distributions in velocity space.

Both simulations have been carried out on an Intel Core2 Duo at 2.4GHz. In both cases only one core had been active. However, due to strong optimization, redesign of particle administration, memory layout and inclusion of GSL functions the A.I.K.E.F. simulation code performed six times faster than its predecessor code.

---

[1] Gnu Scientific Library: http://www.gnu.org/software/gsl/

5.2 Particle Refinement

When dealing with spatially varying mesh resolution, particle refinement is a key technique to obtain a sufficiently accurate representation of the phase function at reasonable computational resources. Many schemas for particle refinement are discussed in the literature (Kallio and Janhunen 2003, Lapenta 2002, Fujimoto and Machida 2006b). However, the usual discussion provided in these studies is about *how* to split up and merge particles. Even though this must be considered, we find that it is at least likewise important *where* particle refinement should be initiated.

Three strategies of particle refinement will be compared in the first part of this section. It will be shown that particles should be refined *before* entering regions of increased resolution. The second part deals with the conservation of mass, momentum and kinetic energy during particle refinement. In order to exclude the effect of any other energy sinks or sources such as particle wave scattering, the electromagnetic fields are deactivated for this particular test. The third part will deal with the conservation of magnetic and particle energy in the presence of electromagnetic fields. Finally the fourth part will show the conservation of the plasma temperature and it will be explained, how accuracy can be treated against performance.

5.2.1 Activation of Particle Refinement

A sufficient number of particles must be present in each cell for mainly two reasons: First, to accurately model the velocity space distribution function and second, to reduce numerical noise, where we define the latter one as follows: ideally the collected density of an undisturbed solar wind flow should exactly equal the background density. However, depending on the number of particles in each cell, fluctuations of even several times the background density may be present. These fluctuations are purely of numerical origin and labeled *numerical noise* in the following.

Numerical noise due to the finite number of particles is a serious issue in particle-mesh simulation codes. This noise maps to all other physical quantities, such as the electromagnetic fields, currents, velocities, etc. Even if the mesh resolution is sufficiently high to resolve magnetic fine structures (eg. fossil fields, shocklets, thin current layers), it is likely that the algorithm fails to capture these structures as their intensity is below background noise. Even worse, the numerical noise may cause the finite differencing schema during field integration (see section 3.3) to become unstable, causing the numerical value of the magnetic field to diverge. To stabilize the magnetic field integrator, numerical diffusion has to be increased (see equation 3.3) which in turn eliminates magnetic fine structures. The bottom line is that reduction of numerical noise must be considered a key objective in particle-mesh simulation codes. In particular, the application of adaptive mesh refinement becomes pointless if this objective is not achieved as even meshes of higher resolution will fail to resolve magnetic fine structures.

We will show below that particle splitting by itself does not necessarily decrease numerical noise. Even more important is where to initiate particle refinement and how the splitted particles should be distributed within the cell. In the following we will introduce three concepts on particle refinement.

As explained in section 3.6, by default particles are refined before entering regions of higher resolution and the splitting and merging procedures do not exactly conserve the center of mass for each individual event, but a small random deviation is allowed. This might seem inscrutable since the center of mass conservation during particle refinement is used in other particle simulations codes (Fujimoto and Machida 2006b, Kallio and Janhunen 2003, Lapenta 2002). In order to establish our choice, we shall compare three concepts for particle refinement:

A) - center of mass conserved,
- refine particles inside meshes of increased resolution

B) - center of mass conserved,
- refine particles *before* entering meshes of increased resolution

C) - center of mass not conserved,
- refine particles *before* entering meshes of increased resolution

The methods are compared by means of the following setup: A three-dimensional simulation domain is used where its size is chosen to be $L_x = 32x_0$ and $L_y = L_z = 16x_0$. Periodic boundaries are applied, i.e. plasma that leaves the domain at any boundary re-enters the simulation domain from the opposite site. The region $|x| \leq 8x_0$ is refined into level 1, the region $|x| \leq 4x_0$ is refined into level 2 (see fig. 5.5). The mesh spacing is $\Delta_{L0} = 1x_0, \Delta_{L1} = 0.5x_0$ and $\Delta_{L2} = 0.25x_0$, respectively. We choose a single-species solar wind, consisting exclusively of hydrogen. The plasma velocity is super-alfvénic, $v_{plasma} = (8v_A, 0, 0)$ and both, the electron and ion plasma betas are set to $\beta_i = \beta_e = 0.4$. The time step is set to $dt = 0.01$, thereby fulfilling the Courant Criterion at every refinement level. As can easily be estimated, the plasma requires 400 time steps to transit the entire simulation domain in x-direction. The optimal number of particles in each cell (oPiC) is set to 80.

At the current stage we are in particular interested in the intersection between refinement level one and two as shown in Figure 5.2. The mesh of the entire domain can be seen in Figure 5.5(c). Figure 5.2(d) illustrates the number density immediately after initialization of the simulation. Ideally the density would be exactly one within the entire geometry. However, due to the finite number of particles a certain noise level is always present. Consequently, the maximal density is about 20% above the background value. Yet, it must be regarded as a “best possible approximation” when 80 particles each cell are used.

In a next step, the simulation is run until the plasma has traversed the entire domain twice. Particles are refined as they cross between meshes of different resolution. Figure 5.2(a) shows the corresponding state where the particle splitting concept (A) has been utilized. As can be seen, the numerical noise has dramatically increased. The maximum density exceeds the background values by nearly 130%. In order to improve the particle refinement we shall address the question, why the numerical noise significantly increases

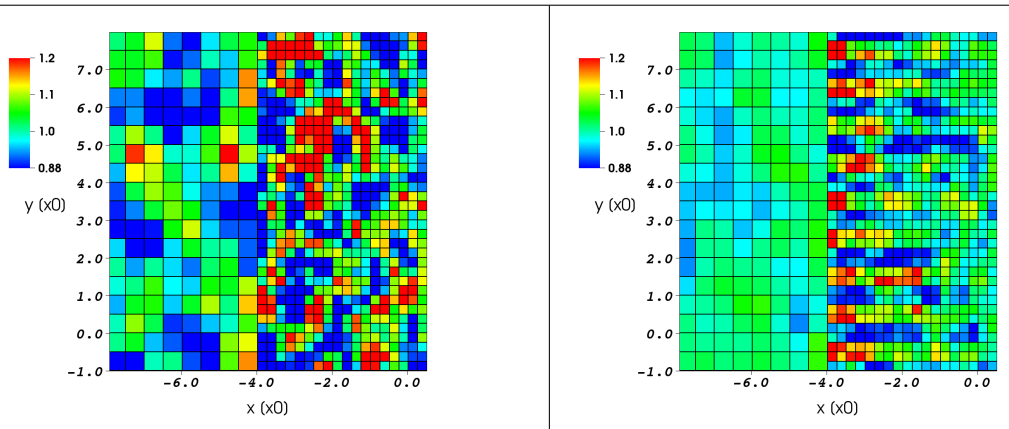

(a) plama density - concept (A)

(b) plama density - concept (B)

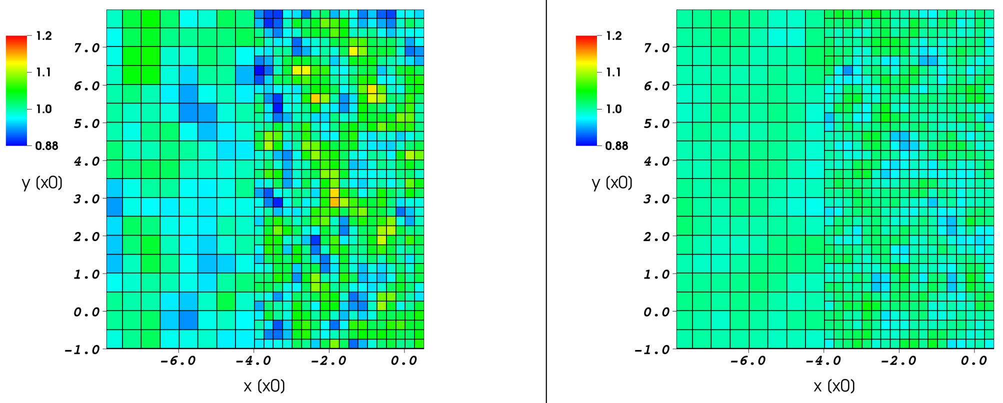

(c) plama density - concept (C)

(d) plama density - reference (initial state)

Figure 5.2: The Figure shows the plasma density after two domain crossings for three different concepts for the particle splitting: While concept A and B do conserve the center of mass during each split event, concept C allows a small deviation. In concept A the particles are split up *after* entering regions of enhanced resolution, while the particles are split up *before* entering regions of enhanced resolution in concept B and C. For comparison the initial state is shown in figure (d).

even though particles are split up as they enter meshes of increased resolution.

The splitting process for simulation of type (A) and particles that travel from refinement level L_0 to refinement level L_2 is sketched in the left-hand column of Figure 5.3. For this simple sketch, the number of particles in each cell is set to three. The initial state is shown in Figure 5.3(a). Particles before being split up are labelled *parent* particle. The newly created particles after the splitting process are labelled the corresponding *children* particle. The cell of refinement level L_0 is filled with three particles that are randomly distributed (blue). All particles are of equal weight, which we define to be $w_0 = 16$, the total weight is thus $w_{total} = 48$. As the plasma flows in positive x direction, two of these particles enter the upper L_1-cells and one enters the lower L_1-cell (see Figure 5.3(b)).

In a next step the particles are split up until each cell is filled with three children particles (see Figure 5.3(e)). For this concept (A) three rules are considered:

1. Each parent particle is split up into two children particles of half size each.
2. The children particles are shifted by a random vector $\pm\Delta\underline{r}$ from the parent particle position, where the vector $\Delta\underline{r}$ is chosen perpendicular to the particle velocity $\underline{v}$. The parent particle is removed after the splitting process.
3. The process is canceled if one of the children particles is located outside the cell.

After the particles are split, each cell is filled with three particles (see Figure 5.3(c)). The total weight in each cell remains unaffected, since the particles cannot leave the cells while being split up. As the particles move into refinement level L_2, they are distributed as sketched in Figure 5.3(d). Since the number of particles in each cell underruns three, they are split up again, which is shown in Figure 5.3(e). After the splitting process, each cell is filled with three particles. Yet, the particle weight is poorly distributed. Even though the total weight $w_{total} = 48$ is conserved, the weight inside the lower cell adds up to four, while the weight inside the cell immediately above adds up to 24. As the weight inside the respective cell translates into the macroscopic moments, the particle density will be distributed in a similar way. This explains the strong density fluctuations generated by concept (A) (see Figure 5.2(a)).

One reason for the poor weight distribution obviously results from the rule that particles may not leave the cell when being split up: if the total weight inside a given cell equals $w_{cell} = 4$ before the splitting procedure is applied (eg. see Figure 5.3(d)/(e)), it will remain the same after the splitting as well. Hence, the next step to improve the weight distribution could be to allow the particle splitting across cell boundaries. However, this introduces two major drawbacks, both theoretically and practically:

On the one hand, Lapenta (2002) pointed out that the splitting must be carried out within a given cell rather than across its boundaries. Otherwise the macroscopic moments will be unphysically affected. On the other hand, expanding the splitting process over several cells destroys the data locality and requires communication between different processes which will significantly slow down the splitting algorithm. However, both of these drawbacks can be avoided while keeping the advantage of improved weight distribution. This will become clear when considering concept (B). This concept uses the same rules as concept (A) except that particles are split up before entering meshes of increased resolution.

Concept (B) is explained by means of the middle column in Figure 5.3. As can be seen in Figure 5.3(f)/(g) the three particles are split up into six children particles inside L_0 and before entering L_1. In doing so, it becomes possible that the weight in both level one cells equals $w_{cell} = 24$ after the particles have entered L_1 (see Figure 5.3(h)). In contrast, by using concept (A) it is impossible to achieve such an equally balanced distribution: the optimal case when using concept (A) is already shown in figure 5.3(b), i.e. the weight inside one cell is twice the weight inside the other cell. Even though in common simulations at least 20 particles are used rather than three (cf. Figure 5.4) we shall point out that Figure 5.3 is a one-dimensional sketch. Thus, each parent particle is split up into two

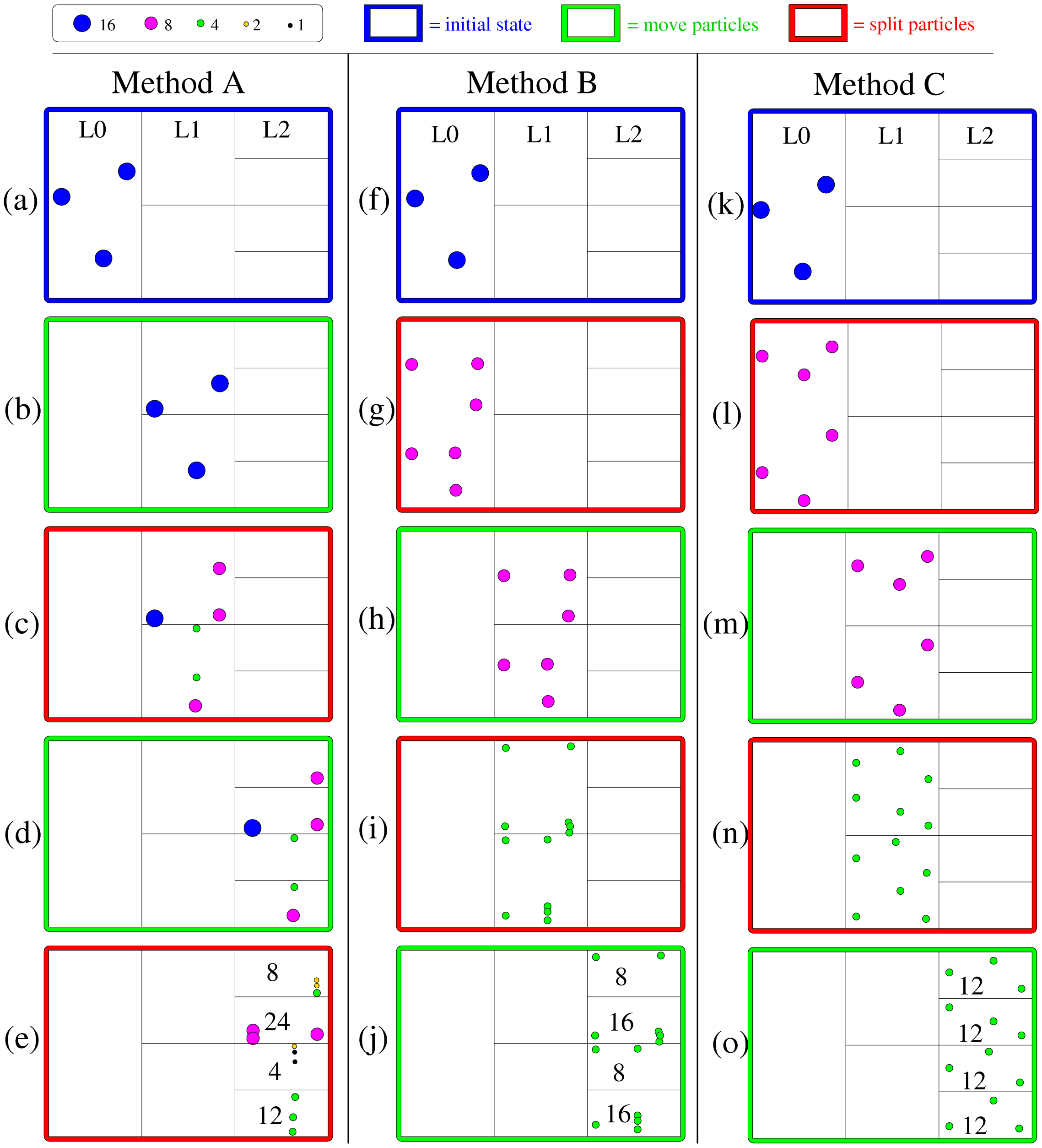

Figure 5.3: The sketch illustrates column-wise three concepts for particle-splitting which are intended to reduce numerical noise: in concept (A) particles are split up after entering higher refinement levels and the center of mass is conserved during each individual split event. In concept (B) the center of mass is conserved but particles are split immediately before entering higher refinement levels. The latter applies to concept (C) as well, but the center of mass is not strictly conserved during each splitting event. The initial state is chosen identical for all three concepts (cf. (a),(f),(k)). However, the final state after the particles have propagated into the highest refinement level differs significantly (cf. (e),(j),(o)). The most homogeneous particle weight distribution is achieved by concept (C). In contrast to concept (B), artificial density accumulations at the cell edges are not introduced. Neither particle splitting nor merging is required in the highest refinement level.

children particles whereas in real three dimensional simulations each particle has to be split up into eight children particles. Beyond this, we found that the distribution achieved when using concept (A) still turns out to be poor when 80 or more particles are initially placed in each cell.

However, the drawback of concept (B) becomes obvious when considering the splitting in level L_1 (see Figure 5.3(h)/(i)). If parent particles that are close to the cell edges are split up the children particles are very close to each other and to the cell edge (see Figure 5.3(i)). The reason simply is that firstly the center of mass is conserved and secondly the children particles must be placed inside the same cell. The only solution to fulfill both conditions is to shift the new particles by a very small $\pm\Delta\underline{r}$, where $\Delta\underline{r}$ is perpendicular to the particle velocity. Unfortunately using a very small $\pm\Delta\underline{r}$ does not significantly reduce the numerical noise. In contrast, if the parent particle is approximately located at the cell's center the $\pm\Delta\underline{r}$ may be chosen somewhat larger as shown in Figure 5.3(i). However, the corresponding children particles will be placed closer towards the cell edges. In summary, the children of particles that are split up near the cell edges will remain there while the children of particles that are split up near the cell centers will be shifted towards the cell edges.

This tendency causes the children particles to accumulate near the cell edges. Yet, due to the cloud-in-cell method (see section 3.5) this tendency is not visible in the macroscopic moments, unless the children particles propagate into the next refinement level (cf. Figure 5.2(b)). There, each cell is halved and a new cell edge is present where in the lower refinement level had been a devoid cell center. Consequently, this new cell edge is hardly assigned any density by the cloud in cell method which is indicated by Figure 5.3(j)) and is well visible in the test simulation in Figure 5.2(b). In contrast, the bulk of the macroscopic density is assigned to the cell edges that coincide with the edges of refinement level L_1. As a consequence artificial "stripes" appear within the macroscopic density. Mathematically spoken these stripes are plane waves with a wave length of $\lambda = 4\Delta_{L2}$.

Interestingly these stripes may only exist in a plane perpendicular to the magnetic field, as shown in Figure 5.3(b). The stripes disappear in a plane parallel to the magnetic field (not shown). The reason is that particles may move force-free only parallel to the magnetic field. Thus, devoid regions parallel to the magnetic field become rapidly refilled and the density accumulations vanish. However, they cannot move freely perpendicular to the magnetic field which maintains the stripes for quite a distance within the perpendicular plane.

In order to maintain the advantage of improved weight distribution, but remove the artificial stripes we intermit the center of mass conservation for concept (C). Instead, the children particles are placed at arbitrary positions on a plane perpendicular to the particles' velocity vector and inside the same cell. However, even though the center of mass is not conserved for every individual splitting event we found that the millions of splitting events statistically ensure the conservation of the total center of mass. Besides we shall point out the common center of mass conservation as described by Lapenta (2002) only refers to the infinitesimal time during the splitting event. However, as the electromagnetic fields are usually different at the children particle positions, these particles will move differently compared to the parent particle from the splitting event forth without conserving the center of mass any longer. We therefore conclude that the importance of strictly conserving the center of mass for an infinitesimal time is commonly overestimated.

The splitting of concept (C) is sketched in the right column of Figures 5.3. As the center of mass is not conserved any longer, parent particles that are close to the cell edges may be split without the drawback that their children particles reside at the cell edges as well (see Figure 5.3(n)). As indicated by sketch 5.3(o) the particle weight may be completely equal distributed in the highest refinement level. This is consistent with the test simulation results in Figure 5.3(c) that show the by far most homogeneous macroscopic densities without introducing numerical artifacts. The maximal numerical noise is 34% above background density and therefore by nearly four times smaller than in the simulation that uses concept (A). In fact, it is only slightly higher than the initial noise which was estimated to be about 20% above the background density.

However, the most important advantage of concept (C) is that a sufficient number of particles already arrives at the highest refinement level. There, neither particle splitting nor merging are required and consequently the particle distribution is not unphysically modified at all. This is in particular important since features of interest usually reside in the highest refinement level where any numerical rooted influence should be avoided. Yet, the impression could arise that method (C) works well in the simple test scenario of a homogeneous density, as described above, but will fail in global plasma simulations with a realistic obstacle to the flow. In order to proof that the advantages described above hold for global plasma simulations with inhomogeneous plasma density as well, we applied all three concepts to the simulations of Mercury's plasma environment. As explained in section 3.6 the splitting of particles before entering higher refinement levels is forced by setting the optimal number of particles in each cell (oPiC) to $oPiC_{local} = 8 \cdot oPiC_{global}$ inside blocks that are located adjacent to refinement boundaries of higher levels.

The simulation results are shown in Figure 5.4 after the quasi-stationary state has been reached. The different concepts are shown column-wise: concept (A) left column, concept (B) middle column and concept (C) right column. For each concept, the macroscopic density (first row), the macroscopic velocity (second row) and current density (third row) are illustrated. The current density acts as the refinement criterion, i.e. if a given current magnitude is exceeded the mesh becomes refined at the respective position. The quantities are shown within the equatorial cross-section, i.e. perpendicular to the dipole and background magnetic field.

These simulations confirm the conclusions that were drawn based on the homogeneous simulations in Figure 5.2. The numerical noise of the macroscopic density in simulation (A) is significantly increased compared to simulation (B) (see Figure 5.4(a)/(b)). However, in simulation (B) artificial stripes are visible near the intersection between the refinement levels which could already be observed in the homogeneous test simulation in Figure 5.2. The lowest level of numerical noise is present in simulation (C). The same observations apply to the macroscopic velocity which is shown in the second row. As

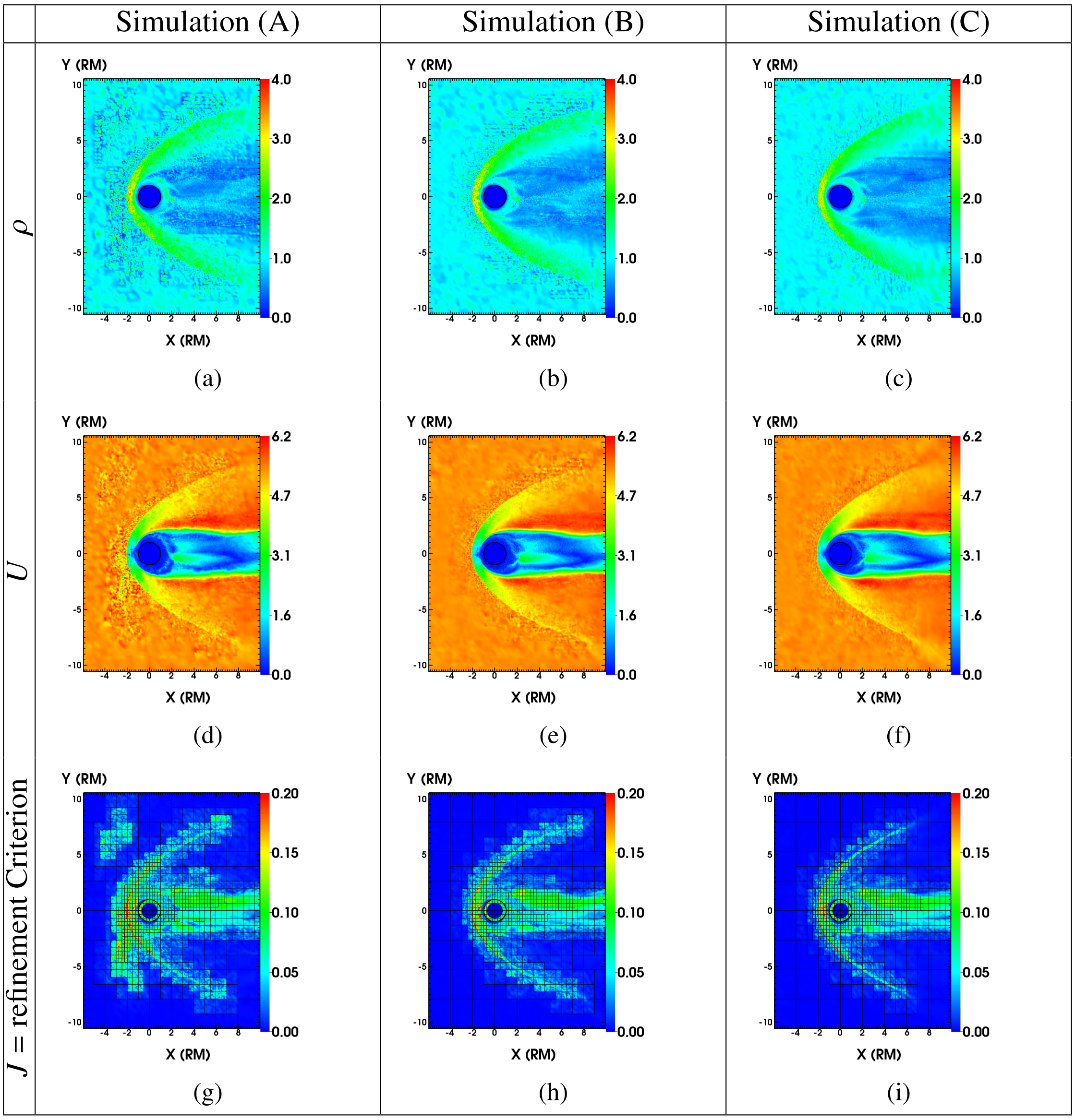

(a) (b) (c)

(d) (e) (f)

(g) (h) (i)

Figure 5.4: Three simulations of Mercury's plasma environment are carried out to compare the concepts of particle refinement (A), (B) and (C) for a realistic hybrid simulation scenario. The results are shown for the equatorial cross section by means of the macroscopic density (first row), velocity (middle row) and current density (bottom row). The numerical noise is strongest for concept (A) and smallest for concept (C). Artificial stripes appear within the plasma moments of concept (B). Even though concept (C) does not exactly conserve the center of mass during each individual split event, no unphysical behavior can be observed.

can be seen in simulation (A) in Figure 5.4(d), in some regions even upstream to the bow shock the undisturbed solar wind velocity drops to half the background speed at the intersection between refinement levels L_2 and L_3. This feature is obviously completely of numerical origin and a typical phenomenon when too less or poorly distributed particles are present. This does neither happen in simulation (B) nor (C) (see Figures 5.4(e)/(f)). However, artificial stripes are visible in the velocity pattern of simulation (B).

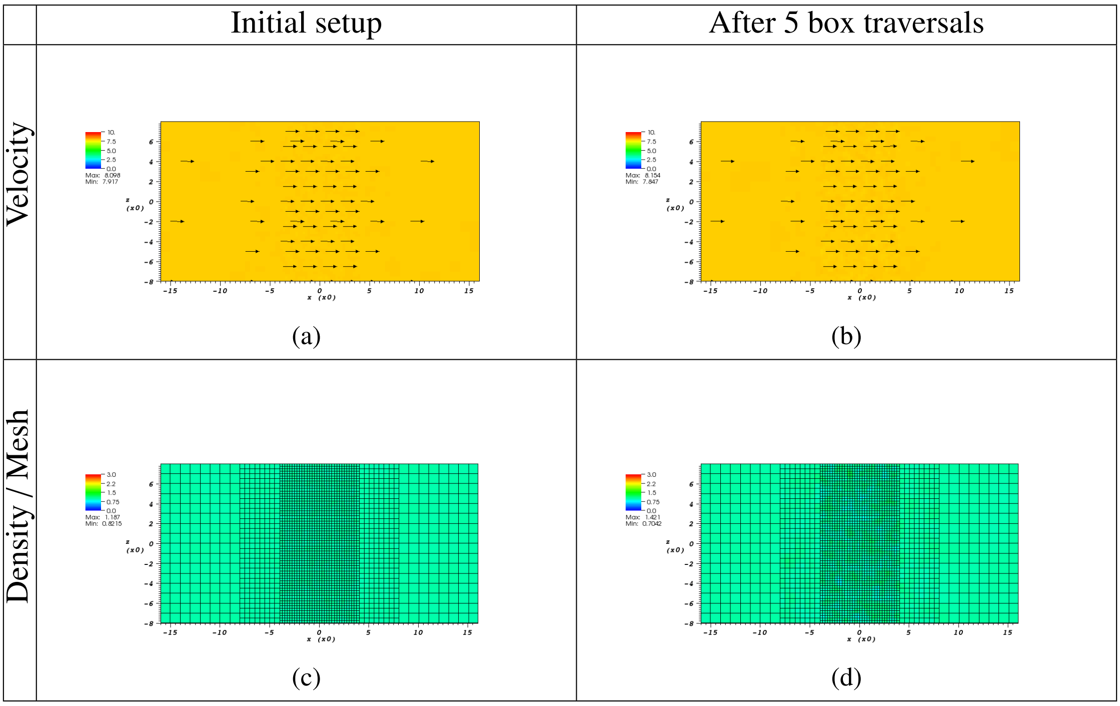

Figure 5.5: The Figure shows the plasma velocity (top row) and density (bottom row) immediately after initialization (left column) and after five simulation domain traversals (right column). The numerical mesh is visualized on top the density plots. As can be seen the noise level remains small in every level of refinement. The macroscopic quantities are not affected by the splitting and merging processes, even after five simulation domain traversals.

As the solar wind speed decreases at the intersection of refinement boundaries in simulation (A), the magnetic field piles up at this intersection forming a current sheet whose magnitude is comparable to the bow shock current magnitude. As the current magnitude is used as a refinement criterion, the mesh becomes further refined in this region which is visible in Figure 5.4(g). This in turn causes even less or no particles to reside inside several cells thereby further increasing the numerical noise. The drastically increase in numerical noise usually cracks the magnetic field integration causing the simulation to exit.

The lowest level of numerical noise is visible in simulation (C). As shown in Figure 5.4(i), the mesh refinement is exclusively triggered in regions of interest like the bow shock or magnetopause rather than in the undisturbed solar wind flow as in simulation (A). In particular, no unphysical behavior can be observed even though the center of mass is not exactly conserved during each individual splitting event. In summary we conclude that the particle refinement concept (C) is the by far most suitable choice for hybrid simulations. Even though all three concepts are included in the A.I.K.E.F. simulation code and can be activated as favored, we recommend to use concept (C).

Crossing	Mass	Momentum	Energy	Splits [Mio]	Merges [Mio]
0	100%	100%	100%	0	0
1	100%	100%	99.9%	18,6	23,8
2	100%	100%	99.9%	36,2	41,7
3	100%	100%	99.8%	54,3	60,0
4	100%	100%	99.8%	72,5	78,0
5	100%	100%	99.7%	90,7	96,3

Table 5.1: The table illustrates the conservation of particle mass, momentum and energy for a simulation within the absence of electromagnetic fields.

5.2.2 Conservation of Particle Properties

As stated in section 3.6, both the splitting and merging procedures are designed to conserve mass, momentum and energy. The following test is meant to reveal how well this is fulfilled for the newly developed adaptive simulation code. As was shown by Bagdonat and Motschmann (2002) the hybrid schema tends to dissipate particle energy. Due to the finite number of particles a certain noise level in the macroscopic densities is always present which in turn can excite waves. Therefore a certain amount of particle energy is transferred into field energy which in turn is partially dissipated by physical or numerical diffusion. In addition the particle acceleration method only acts energy-conserving in the absence of electric fields, which in general is not the case (for details see Bagdonat and Motschmann (2002) and references therein). Hence, the only way to quantify the conservation properties of the splitting and merging procedures is to use a simulation setup in which the particles stream freely through the simulation domain with spatially refined mesh. This setup is achieved by setting the electromagnetic fields to zero.

Each component of momentum, mass and energy are recorded for each time level. Besides the merging and splitting events since simulation start are counted. To test whether the number of macroparticles in each cell impacts on the conservation properties, two simulations are carried out that use 20 and 80 particle in each cell, respectively. Since the results for both simulations are identical to the fourth decimal place, we conclude that the conservation of mass, momentum and energy is independent of the number of macroparticles. Table 5.1 lists the results for the simulation that uses 80 particles each cell. Figure 5.5 shows the plasma velocity (top row) and density (bottom row) immediately after initialization (left column) and after five simulation domain crossings (right column). The numerical mesh is visualized on top the density plots. As can be seen the noise level remains small in every level of refinement. The macroscopic quantities are not affected by the splitting and merging processes, even after five simulation domain crossings.

As can be seen from table 5.1, the total particle mass and momentum are conserved nearly exactly (tested up to fourth decimal place). In contrast, a small loss in total particle energy can be observed. After each simulation domain crossing the total particle energy is decreased by about 0.05%.

5.2.3 Conservation of Macroscopic Properties

The above described test was repeated with activated electromagnetic fields including the full hybrid cycle that is described in section 3.3. Again, the above listed quantities and in addition the electromagnetic energy have been recorded. For five domain crossings, the time evolution of electromagnetic energy, total particle mass, energy and momentum is visualized in figure 5.6. Each quantity is normalized to its initial value. As can be seen, neither particle mass nor particle momentum are affected. However, the total particle energy decreases while the electromagnetic energy slightly increases. Hence, a small fraction of particle energy is converted into electromagnetic energy while another fraction of the particle energy is lost due to the splitting and merging process, as argued above. However it should be pointed out that the change in either energy is below 1% per domain crossing.

Not considered in the analysis shown above is the thermal energy, measured by the temperature which needs a more detailed investigation. We compute the kinetic temperature as defined by Baumjohann and Treumann (1999):

$$T = \frac{m}{3k_B n} \int (\underline{v}_p - \underline{u})^2 f(\underline{v}_p) d^3 v_p \quad , \tag{5.1}$$

where m is the mass of the respective ion species, n the mean density, $\underline{u}$ the mean bulk velocity, $\underline{v}_p$ the individual particle velocity and $f(\underline{v}_p)$ the distribution function. In order to

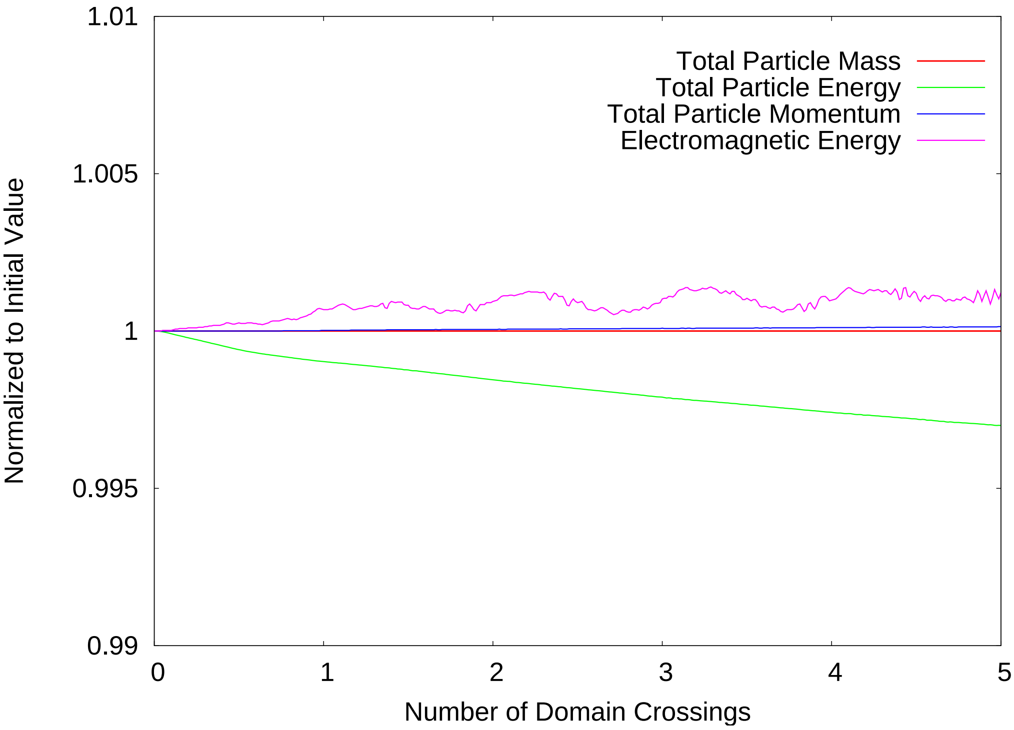

Figure 5.6: The figure illustrates the evolution of particle mass, momentum, energy and electromagnetic energy during five domain crossings.

estimate how the particle refinement influences the temperature the above described test is redone for 5 different refinement parameters. During five domain crossings the mean temperature evolution is calculated according to equation 5.1 and normalized to its initial value. To estimate the influence of particle refinement a reference simulation with deactivated splitting and merging is carried out.

The temperature evolution of this reference simulation is shown by means of the red line in Figure 5.7. Mainly two effects can be observed: firstly the average temperature decreases by about $\Delta T = 2\%$ during each domain crossing. This is comparable with the findings of Bagdonat (2005). Secondly an oscillation is superimposed on this decrease with a period that equals the time of one domain crossing. The oscillation's amplitude is about 3.5% of the initial temperature. The origin of this oscillation can be understood as follow: initially each cell is filled with 80 particles. After half a domain crossing the particles that originate from refinement level L_0 will be located inside refinement level L_2 and vise versa. As the particles are neither split nor merged in this reference simulation and we set $oPiC_{local} = oPiC_{global} = 80$ everywhere, the number of particles inside L_2 will be $80/(8 \cdot 8) = 1.25$ in average, thereby significantly too small to provide a reasonable velocity phase function distribution.

As a consequence, the temperature is underestimated which is the reason for the overall temperature decrease. In addition, strong numerical noise is introduced that generates small-scale electromagnetic field fluctuations. These in turn are dissipated by numerical diffusion which acts as another energy sink. However, after one complete domain crossing and due to the application of periodic boundaries, the particles that originate from refinement level L_2 have again arrived at approximately their original position in level L_2. Thus, the velocity phase function is again accurately modeled which improves the temperature estimation. This yields a local maximum of the temperature oscillation.

In a next step, the simulation is repeated with activated particle splitting. Particles are split up before entering higher refinement levels. This is achieved by setting $oPiC_{local} = 8 \cdot oPiC_{global}$ in blocks adjacent to refinement boundaries. This ensures that a sufficient number of particles is always present in each refinement level. The blue line illustrates the temperature evolution for this simulation. As can be seen the oscillation has vanished. The temperature decreases by about $\Delta T = 0.2\%$ during each domain crossing, that is ten times smaller compared to the simulation without particle splitting. The reason is that the total particle number continuously increases which improves the phase function representation.

Due to the small simulation domain the number of particles has approximately doubled after five domain crossings. However, when dealing with larger simulation domains and more refinement levels the number may easily increase by more than one order of magnitude which is numerically too expensive. Hence, this concept is more of theoretical interest rather than of practical use. The key finding of this test is that particle splitting improves the conservation of temperature.

The opposite applies for particle merging. As described in section 3.6, three particles are

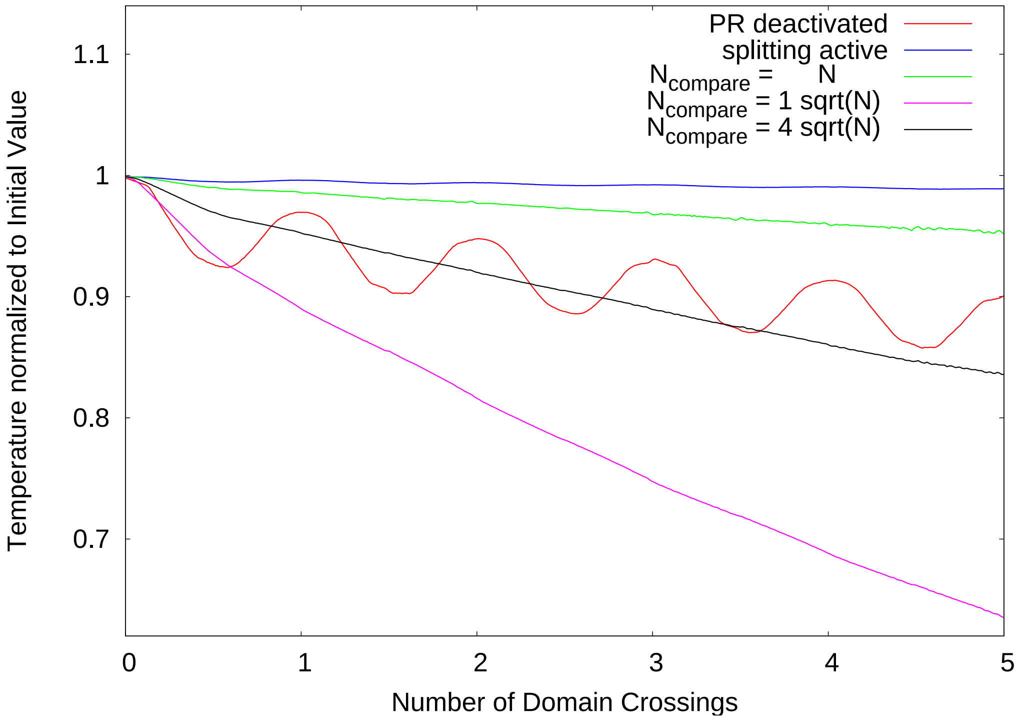

Figure 5.7: The figure illustrates the temperature evolution during five domain crossings for a simulation with deactivated particle refinement (red line) and activated splitting (blue line). Three further simulations show the temperature decay with activated splitting and merging: on the one hand all N particles of a given cell are considered to estimate three particles that have preferably similar velocity vectors for the merging process (green line). Secondly this number is limited to $\sqrt{N}$ (magenta line) and finally to $4\sqrt{N}$ (black line).

merged together that firstly have a small weight and secondly are close in velocity space. If the velocity vectors of the three particles differ too strongly from each other, particle merging tends to reduce the deviation from the mean velocity. In other words merging reduces the thermal speed which is nothing but a temperature decrease. The green line in Figure 5.7 shows the temperature evolution for a simulation that is set up as the previous one, but with activated particle merging. All N particles of a given cell are considered to estimate an optimal triplet of particles. As can be seen the temperature decreases by less than $\Delta T = 1\%$ during each domain crossing. For common hybrid simulations $\Delta T = 1\%$ temperature fluctuation is below the background noise and therefore can be considered negligible.

Yet, as was explained in section 3.6, the computational cost required to find the optimal particle triplet is of the order $O(N^2)$. For this test simulation the global optimal number of particles is set to $oPiC_{global} = 80$. Consequently, the local particle number for blocks adjacent to refinement boundaries equals $oPiC_{local} = 8 \cdot 80 = 640$. Thus, $640^2 \approx 410{,}000$ comparisons have to be carried out in these cells for each merging process. This translates into an immense computational effort. In fact more than 99% of the execution time is spent for the merging procedure. Furthermore, an algorithm that is of order $O(N^2)$ cannot be efficiently parallelized (see section 3.8).

To achieve a convenient performance we limit the number of particles that shall be compared in each cell to $N_{compare} = \sqrt{N}$, where N is the individual number of particles in the respective cell. This choice ensures that the merging algorithm performs with $O(N)$ operations and consequently may be efficiently parallelized. As was explained in section 3.6 the particles within one cell are sorted by increasing weight. Since only the particles within the interval $[0; N_{compare}]$ are considered to find the optimal triplet in velocity space, only particles with low weight are merged.

The gain in speedup is huge: the merging algorithm performs about 350 times faster compared to the simulation where we set $N_{compare} = N$. However, as indicated by the magenta line in Figure 5.7, the temperature decays by 7% during each domain crossing. This might seem to introduce a rather large error. However, whether or not this error is acceptable depends on the scenario that shall be investigated: in most plasma-obstacle interactions scenarios the actual obstacle is located within the maximal refinement level. While streaming towards the obstacle, particles enter meshes of increased refinement and consequently are split up but never merged. Hence, the temperature is conserved. Usually particles are exclusively merged in the downstream region when moving to lower refinement levels and therefore leaving the region of interest. In most cases a cooling of 7% will be acceptable. In particular this will not affect the highest refinement level which is the region of interest.

Yet, in some scenarios a temperature decay in the downstream region of $\Delta T = 7\%$ might be considered too large. For such a case we suggest to set $N_{compare} = \alpha \cdot \sqrt{N}$, with a real number $\alpha > 1$. Consequently, the algorithm still performs with $O(\alpha^2 \cdot N) = O(N)$ and the parallelization remains likewise efficient. Still, one would expect the merging procedure to slow down by a factor α^2. However, we rather find that the merging procedure slows down by about a factor of α. The reason is that finding the optimal triplet is only one part of the merging procedure. The time required to the merging itself, memory access and memory administration remains basically unchanged.

In usual simulations such as the Mercury simulations in chapter 6 the merging algorithm requires about 2.7% of the total computational cycle. As we set $\alpha = 4$ the merging execution time increases by approximately a factor of 4 as well. This causes the total hybrid cycle execution time to increase by about 8%. As will be shown in the discussion on speedup in section 5.5, an increase of 8% execution time can be considered negligible compared to the gain in speedup due to the use of adaptive meshes and particle refinement.

The results of a simulation with $\alpha = 4$ is shown by means of the black line in Figure 5.7. The temperature decay during each domain crossing is $\Delta T = 3.3\%$ which is an improvement compared to the simulation with $\alpha = 1$. However, it is not as good the result of $\Delta T = 1\%$ when setting $N_{compare} = N$. The bottom line is that the user of the A.I.K.E.F. simulation code has to chose an appropriate value of α for the particular scenario that shall be investigated.

5.3 Whistler Waves Dispersion Relation

The Bag2002 simulation code has proven to correctly reproduce Alfvén waves, slow/fast magnetosonic waves and ion whistler waves on a static Cartesian mesh (see Bagdonat and Motschmann (2002) and Bagdonat (2005)). As was shown in section 5.1, the results of the A.I.K.E.F. simulation code and Bag2002 are identical for static Cartesian meshes. It is therefore not required to repeat these tests for the A.I.K.E.F. simulation code.

However, the question remains whether waves travel properly across refinement boundaries and whether their dispersion relation $\omega(k)$ is still modeled in a correct way. Due to the finite mesh resolution of numerical models, there are always small deviations between the analytical and numerical $\omega(k)$-relation and wave propagation velocity. Since the accuracy depends on the mesh resolution and therefore on the level of refinement, wave reflections might occur in case waves are traveling from highly resolved regions into coarser regions and vice versa (see eg. Fujimoto and Machida (2006b)). In order to show that no relevant reflections occur in our model, we chose to carry out simulations on high frequency ion whistler waves which have very short wave lengths and therefore should be most sensitive to generate wave reflection.

Any quantity or equation below is presented in normalized units (see sec. 2.2). After some straightforward algebra the dispersion relation of ion whistler waves in normalized units can be expressed as:

$$\omega^* = (k^*)^2 \quad . \tag{5.2}$$

The following one-dimensional test setup is applied: The simulation domain is periodic with size $L_z = 10x_0$ and refined within the interval $x = [3x_0; 7x_0]$. The resolution at the coarse level is $\Delta_{x0} = 0.1x_0$ and $\Delta_{x1} = 0.05x_0$ in the refined region. The magnetic background field is set to $B_0 = (0, 0, 1)$. Initially a disturbance is superimposed that is consistent with a right-hand polarized whistler wave:

$$\underline{B}_x^*(t_0) = +A \cdot \cos(-kz) \tag{5.3}$$

$$\underline{B}_y^*(t_0) = -A \cdot \sin(-kz) \quad , \tag{5.4}$$

where we choose $A = 0.3$ and k in such a way that an integer number of wave length fits inside the simulation domain:

$$k_i = \frac{2\pi i}{L_z} \tag{5.5}$$

$$i = 1, 2, 3, ..., 18 \tag{5.6}$$

The simulation is run for $N_t = 2000$ time steps with $\Delta t = 0.001$ resulting in a total time of $T = 2$. For each time step the magnetic field is recorded at $N_z = 200$ equidistant positions along the z-direction. That is the same resolution as within the highly refined region. After the simulation has finished, a two-dimensional FFT is carried out, i.e. the data are transferred from $z - t$ into $k - \omega -$ space. The Fourier space for the $i = 11$ simulation is displayed in fig. 5.8(a). The mesh accounts for the finite resolution in Fourier space:

$$\Delta_\omega = \frac{2\pi}{T} = \pi \tag{5.7}$$

$$\Delta_k = \frac{2\pi}{L_z} = \frac{\pi}{5} \tag{5.8}$$

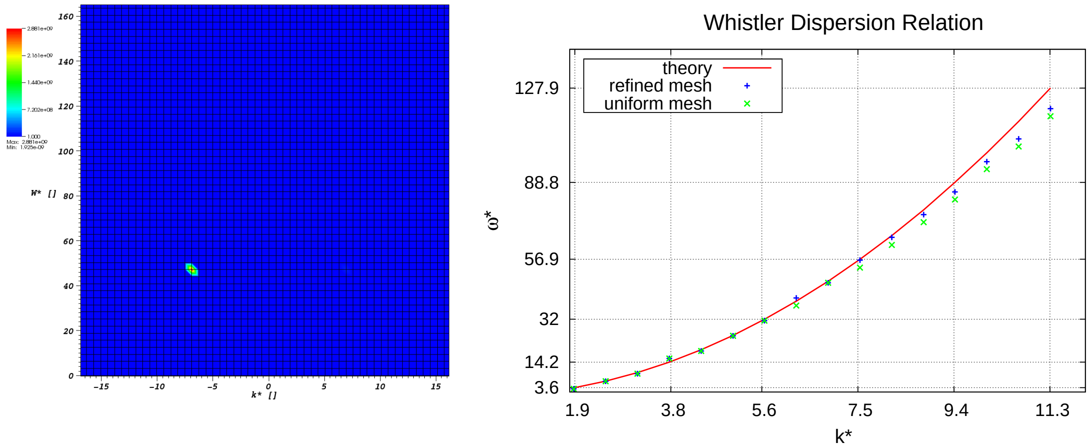

(a) (b)

Figure 5.8: The Fourier space for the $i = 11$ whistler wave simulation is shown in (a), where the mesh accounts for the finite resolution in Fourier space. If waves were reflected at refinement boundaries, the FFT power spectrum would yield two maxima at $(+k, \omega)$ and $(-k, \omega)$, respectively. However, the single sharply focused maximum indicates that no relevant wave reflexion at refinement boundaries occurs. The whistler dispersion relation in (b) is estimated by means of a uniform (green) and adaptive mesh (blue) and compared with the analytical relation (red).

Inserting equation (5.7) into equation (5.5) yields the more convenient form $k_i = i\Delta_k$. This means that the k value used for initializing the simulation is always exactly on a mesh node in discreet Fourier space. However, since the $\omega(k)$ relation is nonlinear, it is not possible to place the resulting values for ω on nodes of the discrete Fourier space. Hence, the Fourier analyzed values for ω should considered to be accurate up to $\pm\Delta_\omega/2$. This limits the minimal and maximal ω and k to

$$\omega_{min} = \Delta_\omega = \pi \tag{5.9}$$

$$\omega_{max} = \frac{N_t \Delta_\omega}{2} = 1000\pi \tag{5.10}$$

$$k_{min} = \Delta_k = \frac{\pi}{5} \tag{5.11}$$

$$k_{max} = \frac{N_z \Delta_k}{2} = 20\pi \tag{5.12}$$

The value of $k_{11} = 11\Delta_k$ applied in fig. 5.8(a) yields a frequency of $\omega = 15\pi$ which is in agreement with the analytical value $k_{11}^2 = 15.2\pi$ within the accuracy of FFT. The simulation is repeated for $i = 1...18$ and the dispersion relation is visualized in fig. 5.8(b) (blue). For comparison the analytical relation is plotted (red). As can be seen both solutions are in good agreement. In addition the simulations are repeated for a mesh without refinement (green). Still the agreement is good, yet the deviation from the analytical relation is slightly higher, in particular for large k. However, most important is that waves can travel across refinement boundaries without falsifying the dispersion relation.

Furthermore fig. 5.8(a) illustrates that no relevant wave reflexion occurs at refinement boundaries: The sign of k yields the direction of wave propagation. If the wave was reflected partially at refinement boundaries, a wave of equal frequency but opposite sign would be excited. The FFT power spectrum in turn would yield two maxima at $(+k, \omega)$ and $(-k, \omega)$, respectively (see Fujimoto and Machida (2006b)). However, since only a single maximum is visible in fig. 5.8(a), we conclude that no relevant wave reflexion occurs at refinement boundaries.

5.4 Mach Cones - Standing Fast Waves

The following three-dimensional setup is applied to test whether waves propagate across refinement boundaries without being refracted, i.e. without changing their direction of propagation. This property could not be tested in the one-dimensional setup described in section 5.3. We choose a simulation domain of size $L = (72, 48, 48)\, x_0$ with a hydrogen plasma of speed $v_{plasma} = 5 v_A \underline{e}_x$ and place an immobile ion population at the simulation box origin. This immobile ion population acts as an obstacle to the flow, exciting a standing fast magnetosonic wave forming a mach cone (for details see Bagdonat and Motschmann (2002)).

The fast wave velocity perpendicular to the magnetic field in normalized units reads

$$v^*_{wave} = \sqrt{(v^*_A)^2 + (v^*_s)^2} \tag{5.13}$$

where $v^*_A = 1$ is the Alfvén velocity and v^*_s the sound velocity. When using an adiabatic exponent of $\kappa = 2$, the sound velocity in normalized units results in:

$$v^*_s = \sqrt{\beta_i + \beta_e} \tag{5.14}$$

We choose $\beta_i = \beta_e = 0.4$ resulting in a wave velocity of $v^*_{wave} = 1.34$. The opening angle α of the Mach cone yields

$$\alpha = \arcsin \frac{v_{wave}}{v_{plasma}} = \arcsin \frac{1.34}{5.0} = 15.6^\circ \tag{5.15}$$

Two simulation runs are carried out. For simulation (A) in fig. 5.9(a) a uniform Cartesian mesh is specified while for simulation (B) (see fig. 5.9(b)) a hierarchical mesh is used. The figures show the total magnetic field strength in the y-cross-section, that is perpendicular to the background magnetic field $\underline{B}_0 \propto -\underline{e}_y$. In both cases a linear Mach cone forms behind the immobile ion population, similar to the gas-dynamical case. The obstacle is too weak to produce a bow shock. The opening angle in simulation (A) can be estimated to be $\alpha \approx 15^\circ$, which is in good agreement with the calculated value of $\alpha = 15.6^\circ$.

In the hierarchical simulation (B), the immobile ion population is placed exclusively within the highest level of refinement L_2. Hence the excited fast magnetosonic wave has to cross two refinement boundaries as it moves downstream with the flow. No refraction at the refinement boundaries is visible. The direction of the wave remains unchanged as it propagates from regions of high to regions of low resolution. The opening angle measured at the $x = x_{max}$ domain boundary in refinement level 0 equals the angle of the

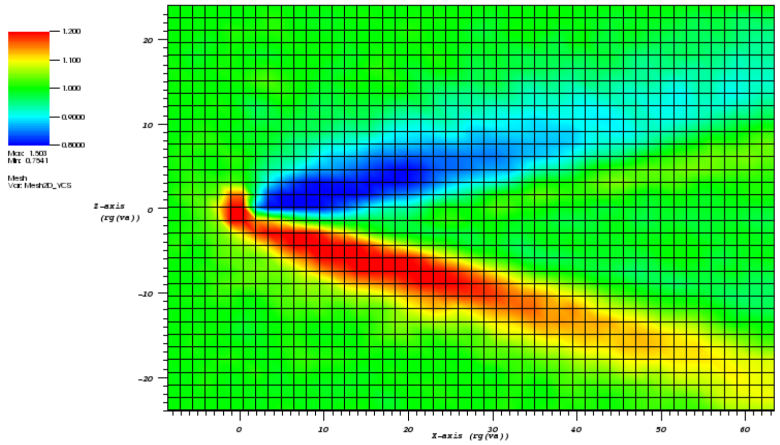

(a) mach cone - uniform mesh

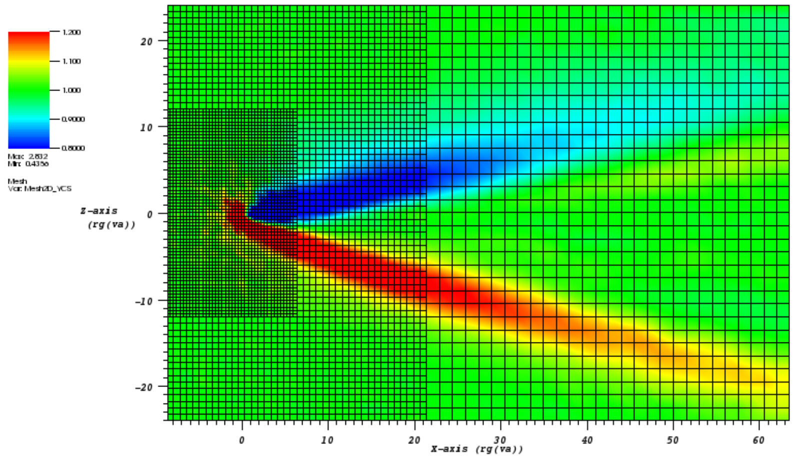

(b) mach cone - hierarchical mesh

Figure 5.9: The images show the excitation of a standing fast wave due to an immobile heavy ion population. The simulations have been carried out by using an uniform mesh (a) and a hierarchical mesh (b). In the latter simulation the wave crosses two refinement boundaries as it moves downstream with the flow. No refraction at the refinement boundaries is visible. The opening angle of the mach-cone reproduces the analytically estimated value.

unrefined case $\alpha \approx 15^\circ$. In general both results are very similar, yet in the hierarchical mesh simulation the mach cone is slightly more focused. In summary we conclude that refinement boundaries do not influence the direction of wave propagation.

5.5 Static versus Adaptive Mesh: Mercury

Due to the ongoing MESSENGER and upcoming Bepi-Colombo Mission, in particular planet Mercury is currently subject of interest (Slavin et al. 2008). In order to resolve small-scale features, a local high resolution is required. On the other hand a large simulation domain of many Mercury radii size is desirable in order to investigate possible substorm activity in Mercury's magnetotail. Thus, significantly different scales are involved in Mercury's interaction with the solar wind which is why we choose Mercury's plasma environment for the following test.

The test is meant to measure the speedup and quality of the adaptive Mercury simulation. In particular it shall be tested whether the mesh refinement influences any of the various physical structures in Mercury's plasma environment. In order to distinguish physical structures from potential mesh artifacts, a static mesh simulation is carried out in a first step. The simulation's coordinate frame is identical to the one of section 3.8 and is sketched in fig. 3.5(a).

The resolution in the entire simulation domain is $\Delta_{static} = 2.5x_0$ in each dimension. We refer to this simulation as *reference simulation*. Secondly an adaptive simulation was carried out that uses a coarse base resolution of $\Delta_{L0} = 8\Delta_{static} = 20x_0$ in each dimension. Four levels of refinement are used: L_0, L_1, L_2 and L_3. Hence, the resolution at the highest level of refinement L_3 is $\Delta_{L3} = \Delta_{L0}/8 = \Delta_{static}$ and thereby equal to the global resolution of the static mesh simulation. The self-refinement within L_0, L_1 and L_2 is guided by the current density while it is fixed to $|\underline{r}| < 1.8R_M$ in L_3.

The plasma upstream parameters for both simulations are listed in table 2.1. Apart from the parameters related to mesh refinement, all physical and numerical parameters are identical in both simulations. Hence, except for some random noise the simulation results should be identical.

5.5.1 Simulation Results

The following discussion does not aim to provide a detailed explanation of the physical structures, but to compare the two simulations from the numerical point of view. Figure 5.10 shows a comparison of the static and adaptive simulation for the polar cross-section while fig. 5.11 provides an overview of the equatorial cross-section (the alignment of polar- and equatorial crossection are sketched in fig. 3.5(a)). The first row illustrates the results for the static (reference) simulation and the second row for the adaptive simulation, respectively. Since the mesh refinement is guided by the current density, i.e. regions of higher current are refined into higher levels, the block refinement is visualized on top the current density in figs. 5.10(h) and 5.11(h).

By comparing figs. 5.10(a) and 5.10(e) it can be seen that the global image is basically the same. In particular the shape of the bow-shock and the magnetopause, the position of the neutral sheet and the cusp region are qualitatively identical. However, a closer look reveals that two features differ quantitatively. In the adaptive simulation the neutral

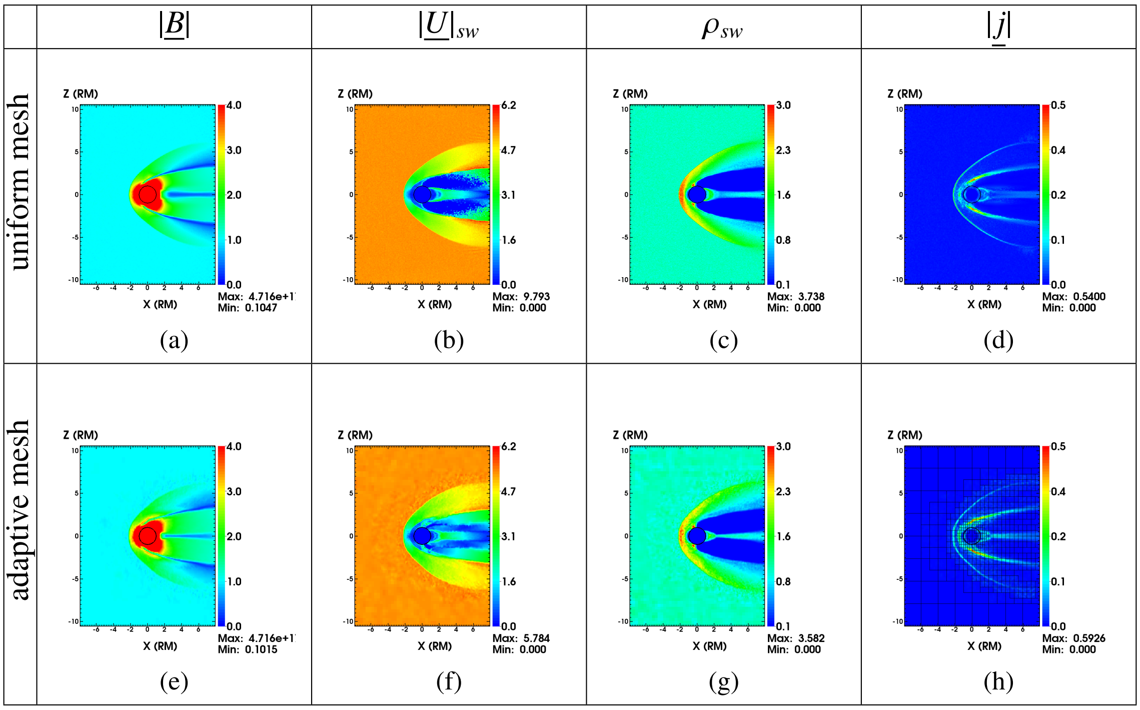

(a) (b) (c) (d)

(e) (f) (g) (h)

Figure 5.10: The figure shows a comparison of uniform mesh simulation (top row) with adaptive mesh simulation (bottom row) by means of the polar cross-section. The color coded physical quantities are the magnetic field $|\underline{B}|$, plasma velocity $|\underline{U}|_{sw}$, plasma density ρ_{sw} and current $|\underline{j}|$. The block topology is visualized on top the current for the adaptive simulation (h).

sheet and the magnetopause boundary are sharper focused compared to the static mesh simulation. This observation is in agreement with a slightly higher current density at the magnetopause and neutral sheet in fig. 5.10(h), compared to the static mesh simulation in fig. 5.10(d). The increased neutral sheet current density is even better visible within the equatorial cross-section figs. 5.11(d) and 5.11(h).

At first glance this seems incomprehensible, since both these features are embedded within refinement level L_2 which is coarser than the static mesh resolution. Hence, one would expect to observe sharper focused features and increased current densities within the highly resolved static mesh simulation.

In order to understand this observation, we shall point out that in the static mesh simulation a certain amount of numerical diffusion has to be added in order to guarantee numerical stability (see equation (3.3)). The amount has to be based on the most critical region, which in the mercury scenario is the strong intrinsic magnetic field near the planetary surface. For the static mesh simulation we use $\alpha_s = 0.08$. In the adaptive simulation the immediate vicinity of Mercury is embedded in refinement level L_3, where we choose numerical diffusion equal to the static mesh simulation $\alpha_{s,L_3} = 0.08$. However, it is sufficient to choose a smaller value of $\alpha_{s,L_2} = 0.012$ for refinement level L_2 since (a) coarser meshes require less diffusion and (b) the magnetopause and neutral sheet are less critical to model than the high magnetic dipole field close to Mercury's surface. For this reason

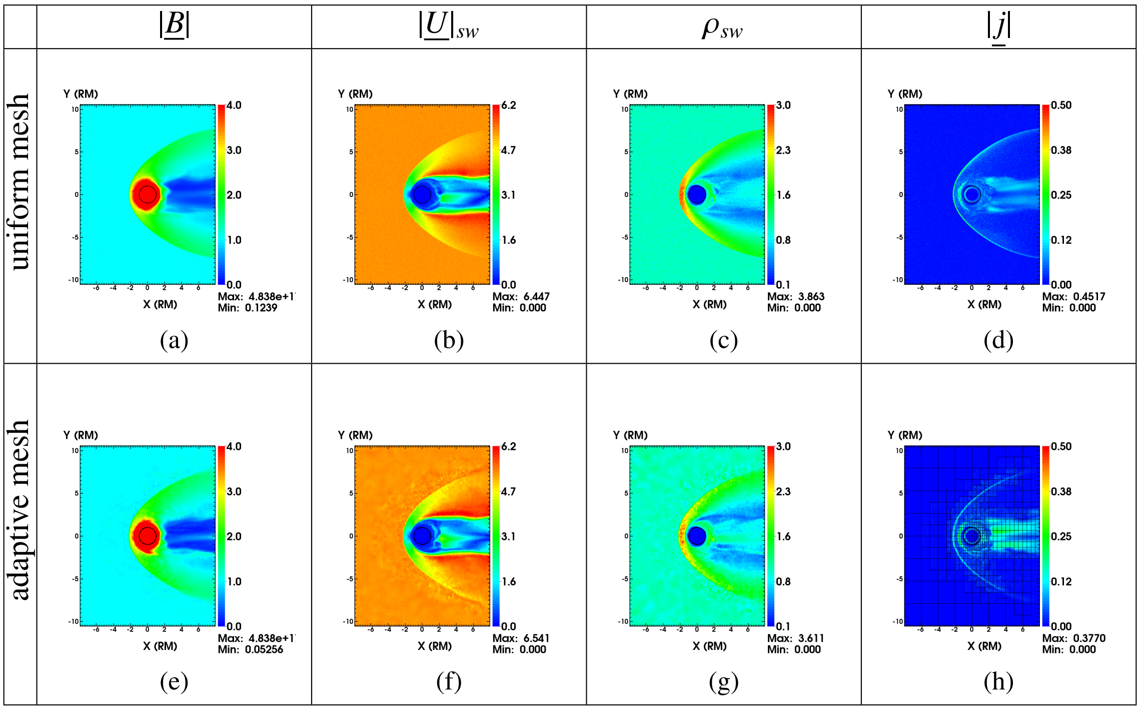

(a) (b) (c) (d)

(e) (f) (g) (h)

Figure 5.11: The figure shows a comparison of uniform mesh simulation (top row) with adaptive mesh simulation (bottom row) by means of the equatorial cross-section. The color coded physical quantities are the magnetic field $|\underline{B}|$, plasma velocity $|\underline{U}|_{sw}$, plasma density ρ_{sw} and current $|\underline{j}|$. The block topology is visualized on top the current for the adaptive simulation (h).

the magnetopause and neutral sheet are sharper focused in the adaptive simulation, even though the mesh resolution in this region is lower than the static mesh simulation.

The plasma velocities in figs. 5.10(b) and 5.10(f) are very similar as well. The most noticeable difference is the fine grained noise within the magnetosphere in the static mesh simulation (light green dots). In the adaptive simulation this region is smeared out because of the coarser mesh resolution at this region. However, the plasma density in this region is close to zero which is why this region is not particularly interesting from the plasma-physical point of view. Having a look at the undisturbed upstream solar wind flow it can be seen that in general, the noise within the adaptive simulation is higher (see figs. 5.10(f) and 5.11(f)). This is due to the fact that adaptive mesh simulations inherently include significantly fewer macroparticles than the static mesh simulation. Even though particles are split several times as they move from level L_0 to level L_3, smooth bulk distributions as smooth as in the reference simulation cannot be achieved. Since the plasma velocity is directly derived from the particles (see sec. 3.5), its noise level reflects the lower resolution in particle phase space. However, since this higher noise level apparently does not influence further plasma quantities, we conclude that the impact on the simulation results can be considered negligible. Still we shall point out that the number of macroparticles (MPiC=30) that was used in this simulation should be regarded as a lower limit for adaptive runs.

Since the plasma density is directly derived from the particle positions similar to the plasma velocity, the noise level is also increased compared to the reference simulation (see figs. 5.10(c) and 5.10(g)). However, apart from that the results are in good agreement. The shapes of bow shock, magnetopause and cusp regions are nearly identical. In particular the stable plasma ring around Mercury within the equatorial cross-section (see figs. 5.11(c) and 5.11(g)) exhibits the same shape in both simulations.

In summary we conclude that the adaptive and the reference simulation are qualitatively identical within the entire simulation domain. Furthermore the results are quantitatively identical everywhere, except for the slightly increased noise level in the adaptive simulation which is expected, but negligible as it does not affect the shape of any physical structure. Despite the coarser resolution the magnetopause and current sheet are even more accurately modeled in the adaptive simulation, since reduced numerical diffusion can be applied within these regions.

5.5.2 Speedup

In the following we shall explain how the speedup of the adaptive simulation is estimated. For its rather small memory requirements the adaptive simulation was run in serial on a personal computer at 2.83 GHz. The quasi stationary state (see figs. 5.10 and 5.11) was reached after 30.85 CPU-hours. In contrast, because of its huge memory requirements the static mesh simulation had to be carried out in parallel on 128 CPUs at 2.4GHz each. The quasi-stationary state was reached after $128 \cdot 20,43\text{h} = 2615.22$ CPU-hours, which is 85 times more than the adaptive simulation. However, if we account for the faster CPU of the adaptive simulation, we shall multiply the speed by 2.4GHz / 2.83GHz = 0.848. Since the static mesh simulation does not scale ideal (see section 3.8), we correct the speedup corresponding to fig. 3.5(d) by multiplying with 0.98. This still results in a speedup of 71 or in other words: a static mesh simulation that takes 10 weeks requires less than one day on an adaptive mesh while yielding essentially the same results.

5.6 Comparison of MESSENGER and Simulation Data

As introduced in section 5.5, planet Mercury is target of the MESSENGER spacecraft mission (Slavin et al. 2008). At the time of this writing three flybys had been carried out, where magnetic field measurements are available for flyby I and II. By chance the interplanetary magnetic field (IMF) conditions in both Flybys have been very different. While during flyby I the IMF and dipole field were basically aligned, they have been anti-parallel during flyby II. This offers the unique opportunity to compare the case of a closed and an open magnetosphere, respectively.

In the following we shall test whether the A.I.K.E.F. simulation code is able to model the configuration of both cases: a closed and an open magnetosphere at Mercury. However, we shall point out that the results shown below are not meant to explain the involved physics. A detailled physical analysis is carried out throughout chapter 6. Here, the sim-

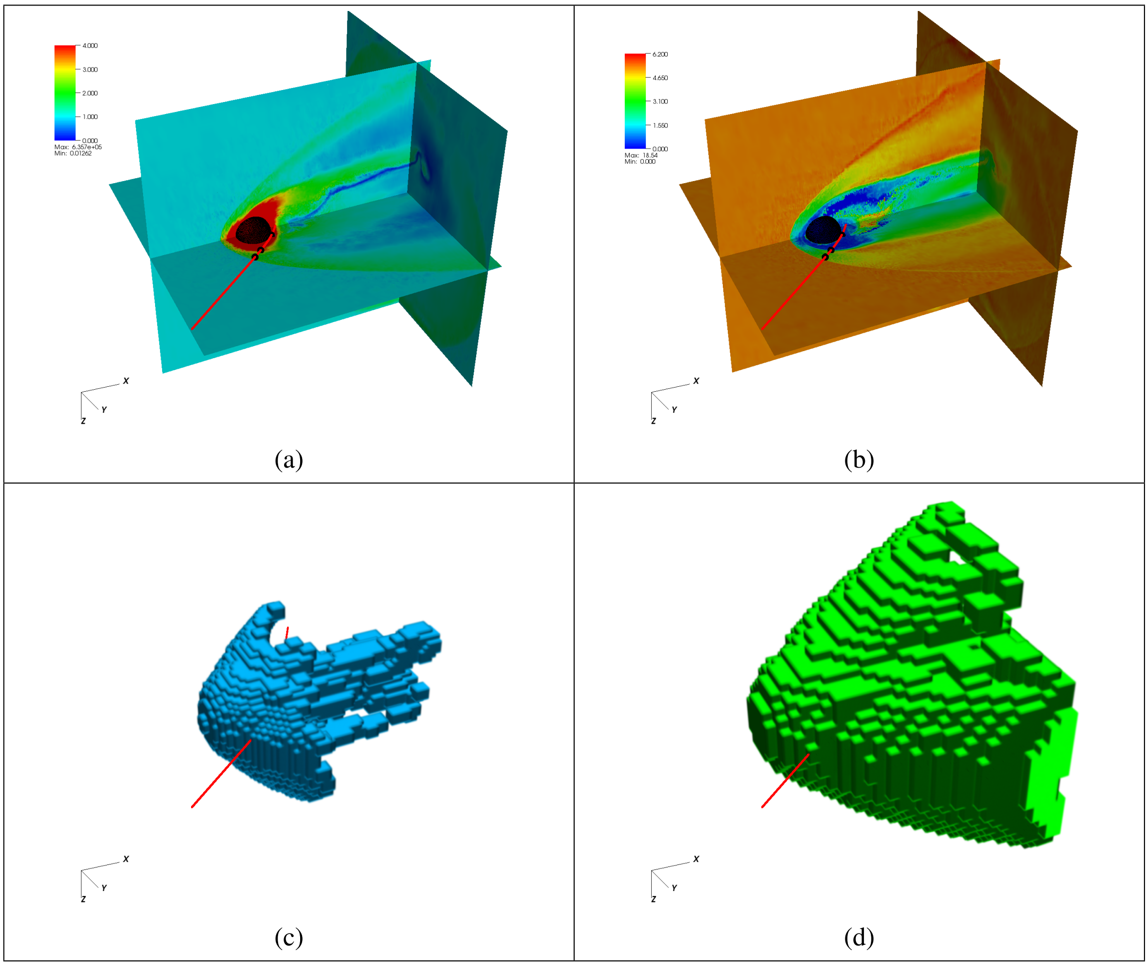

(a) (b) (c) (d)

Figure 5.12: The figure shows the magnetic field (a) and plasma velocity (b) of the three dimensional MESSENGER I simulation geometry. Mercury is indicated by means of a black sphere. The red line shows the MESSENGER trajectory where the three black marks indicate the bow-shock, magnetopause and C/A, respectively. The block topology of refinement level three (c) and two (d) show that the refinement follows the shape of bow-shock and magnetopause. Animations are available online at www.tu-braunschweig.de/theophys/people/jmueller.

ulations should rather be considered a benchmark for the quality of the results. Therefore two simulations were carried out that use the IMF configuration of MESSENGER flybys I and II, respectively. Unfortunately neither plasma densities nor velocities are available. However, we assume that the values of table (2.1) are a reasonable estimate. During both flybys the magnetic field strength has been 21nT. While the IMF direction in flyby I has been $\Theta_{flybyI} = 53°$ with a Parker spiral angle of $\phi_{flybyI} = 27°$, it has been $\Theta_{flybyII} = 118°$ with a Parker spiral angle of $\phi_{flybyII} = 37°$ during flyby II (Wang et al. 2010).

Another source of uncertainty is Mercury's intrinsic magnetic dipole field: the few Mercury flybys of MESSENGER and Mariner 10 have not been sufficient to derive a reliable fit of Mercury's intrinsic magnetic field. It is usually assumed to be dipolar. The values for the dipole strength range from 196 nTR_M^3 (Alexeev et al. 2010) to 340nTR_M^3 (Glassmeier

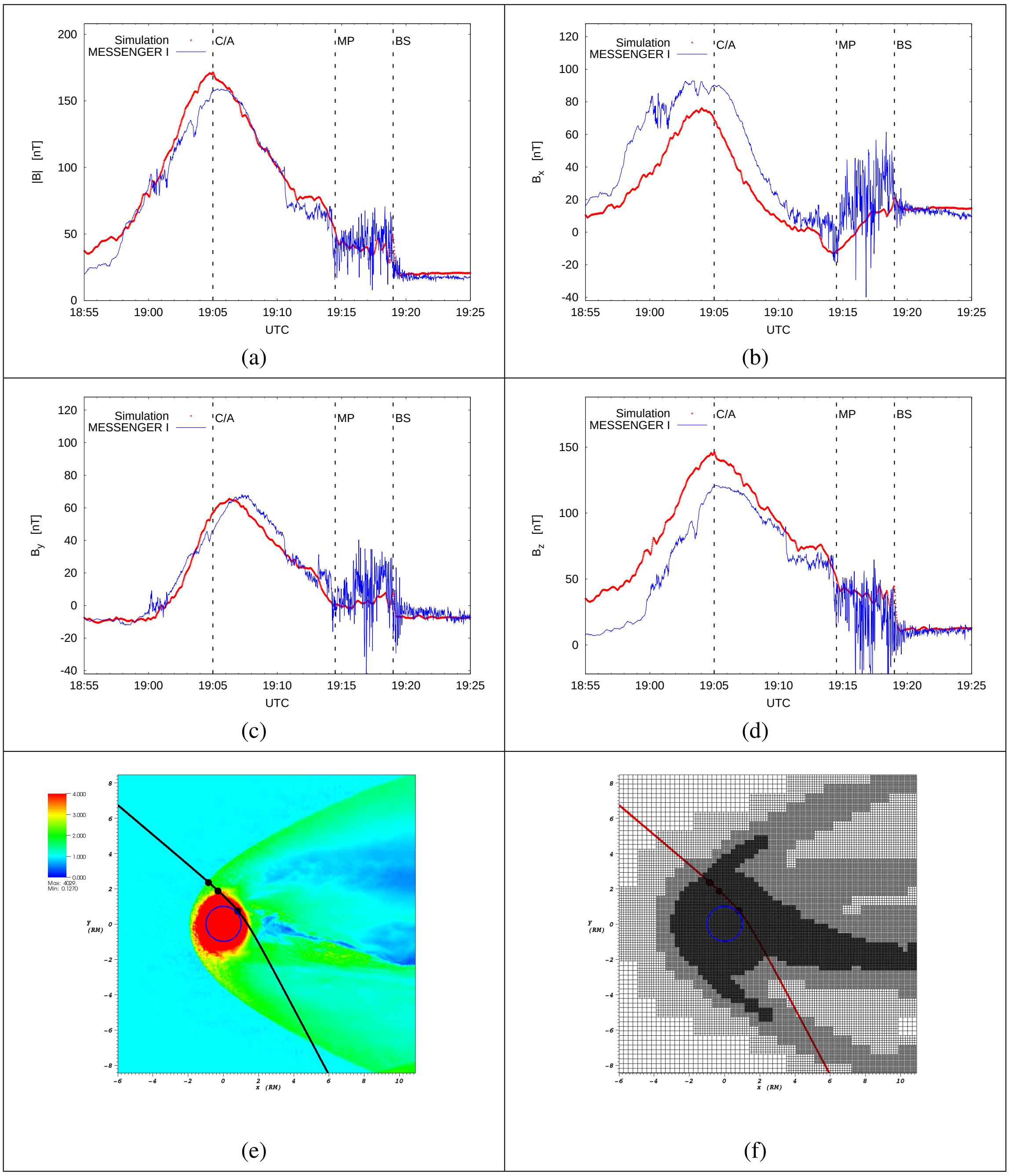

(a) (b) (c) (d) (e) (f)

Figure 5.13: Figures (a) to (d) show the magnetic field and its components for the MESSENGER I flyby. Fig (e) and (f) show the magnetic field and adaptive mesh of the equatorial cross-section. The three marks on MESSENGER's trajectory indicate bow-shock, magnetopause and C/A, respectively. See text for details. Animations are available online at www.tu-braunschweig.de/theophys/people/jmueller.

2000). Corresponding to Anderson et al. (2008) Mercury's dipole moment may exhibit an inclination of 5° to 12° from the rotational axis. The most recent dipole fit has been carried out by Alexeev et al. (2010) who estimates a dipole strength of 196 nTR_M^3, where the dipole centre is shifted 405km in northern direction. The inclination is estimated to be 4° with an eastern longitude of 193° for the dipole northern pole. However, improved models are subject to the orbital phase of MESSENGER.

Because of the large uncertainties we shall use a “simplified dipole model” of Mercury’s intrinsic field. For the present simulations we assume the dipole strength to be $200nTR_M^3$ and apply a shift of the dipole’s center of 405km in northern direction. However, any inclination is neglected. Due to the uncertainties in plasma upstream parameters and intrinsic dipole field we do not expect to observe perfect quantitative agreement between model and spacecraft data, however physical structures should match up qualitatively. Again the simulation coordinate frame is identical to the one of section 3.8 and is sketched in fig. 3.5(a).

A magnetic field and plasma velocity of the three dimensional MESSENGER I simulation geometry are visualized in figs. 5.12(a) and 5.12(b). Mercury is indicated by means of a black sphere. The red line shows the MESSENGER trajectory, where the three black marks indicate the bow-shock, magnetopause and C/A, respectively. The block topology of refinement level three and two are shown figs. 5.12(c) and 5.12(d). As can be seen the refinement follows the shape of bow-shock and magnetopause. To obtain a better understanding on how the physical quantities and numerical mesh develop in time we recommend to view the associated animations that are available online at *www.tu-braunschweig.de/theophys/people/jmueller*

The simulation results are visualized in figs 5.13 and 5.14. Magnetic field data along MESSENGER’s orbit are displayed in figs (a)-(d): $|\underline{B}|$, B_x, B_y and B_z, respectively. The equatorial cross-section that includes MESSENGER’s trajectory (black line) is shown in fig (e). The dark blue circle indicates the planetary surface. Figure (f) shows the mesh refinement at quasi-stationary state. As can be seen in fig. 5.13 the magnetic field magnitude of simulation and observation are in qualitative and quantitative agreement. In particular the bow-shock and magnetopause position are virtually identical. While the B_y component is in very good agreement as well, the simulation’s B_x component is slightly to small at C/A while the B_z component is slightly to large. This quite likely is due to the negligence of the dipole’s inclination within the simulation. However, both the B_x and B_z component show very good agreement at magnetopause and bow-shock position which is why we conclude that physics are correctly modeled.

In particular we shall point out that in both, spacecraft measurements and simulation results, a region of decreased magnetic field can be observed between 19:11 and 19:14 UTC (see Figure 5.13(a)/(d)). This feature is not expected to be observed in common planetary magnetosphere and was labeled Mercury’s “dayside boundary layer”. It is confined by a double current sheet which is referred to as Mercury’s “double magnetosphere” (Slavin et al. 2008). A trusted explanation for both these structures is missing to the present day. However, for the time being we conclude that the A.I.K.E.F. simulation model is capable of modeling the case of a closed magnetosphere and dedicate the next chapter to an in-depth analysis of the involved physics.

The MESSENGER II results in fig. 5.14 show very good qualitative agreement in ev-

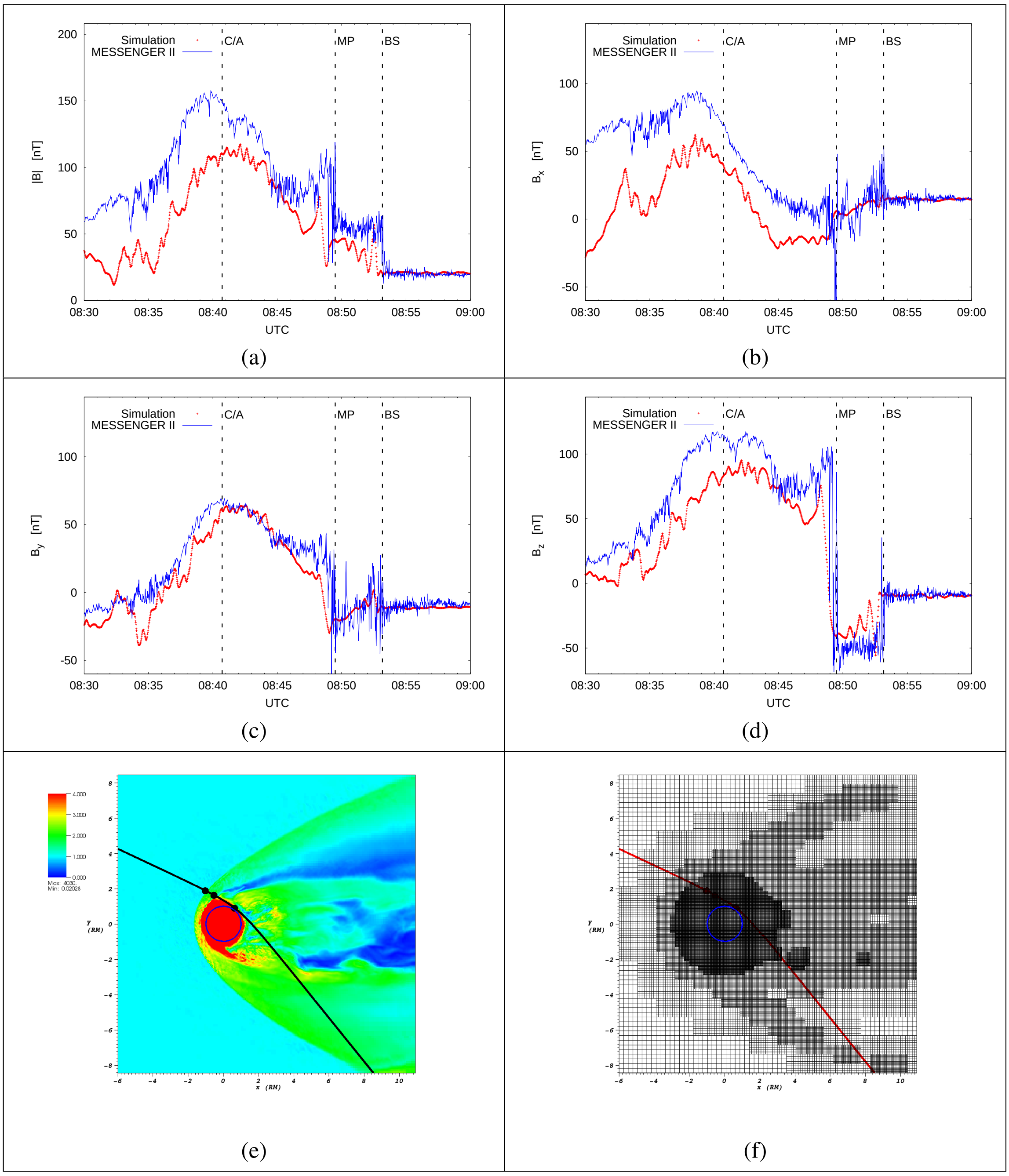

(a) (b) (c) (d) (e) (f)

Figure 5.14: Figures (a) to (d) show the magnetic field and its components for the MESSENGER II flyby. Fig (e) and (f) show the magnetic field and adaptive mesh of the equatorial cross-section. The three marks on MESSENGER's trajectory indicate bow-shock, magnetopause and C/A, respectively. See text for details.

ery component as well, in particular at bow-shock and magnetopause position. However, the total magnetic field strength appears to be under estimated. We cannot state with certainty whether this is due to the negligence of the dipole's inclination, under estimation of dipole strength or a shift of the dipole origin. This must be investigated by means of different dipole setups which is beyond the scope of this chapter. However we shall point out that sharp discontinuities are correctly modeled, which can be best seen in the B_z component at magnetopause and bow-shock position. In summary we conclude that in consideration of several unknowns in both, dipole and plasma parameters, simulation results and observations are in excellent agreement.

6 Potential Origin of Mercury's Double Magnetopause

As was shown at the end of the previous chapter a region of decreased magnetic field has been observed inside Mercury's magnetosphere during the MESSENGER flybys. Since a trusted explanation for this feature is missing to the present day, we carry out an in-depth analysis of the involved physical processes throughout this chapter. In section 6.1 we describe the MESSENGER flyby geometry and the discovery of the "dayside boundary layer" and "double magnetopause" before we summarize the corresponding magnetic field and plasma observations that were available at the time of this writing in section 6.2. We substantiate the application of a simplified magnetic field topology and dipole moment in section 6.3 followed by listing the input parameter in section 6.4. Section 6.5 includes an elaborate presentation of the simulation results which are in detail discussed in section 6.6. The results have been submitted for publication (Müller et al. 2011b).

6.1 MESSENGER Encounters in the Year 2008

On 14 January 2008 the MESSENGER spacecraft detected a wide region of decreased magnetic field inside Mercury's dawn magnetosphere (see Figure 6.1) that was confined in between a double current sheet. Such a double current sheet had never been observed before, neither in Mercury's nor in any other planetary magnetosphere. Slavin et al. (2008) pointed out that both current layers are very similar in orientation and thickness, only the intensity of the inner current sheet is weaker. Consequently, the authors called this double current sheet Mercury's "double magnetopause". Slavin et al. (2008) concluded that the outer current sheet separates the magnetosheath and magnetosphere and that the region of decreased magnetic field in between the double sheet originates from enhanced plasma pressure. This region in between both current sheets was labeled Mercury's "dayside boundary layer" (Anderson et al. 2011). The boundary layer could be observed in both flybys that are abbreviated M1 and M2 in the following (Anderson et al. 2010). During the third flyby the spacecraft had been in secure mode and neither magnetic field nor plasma data has been recorded for the respective region. MESSENGER's orbital phase was successfully initiated on 18 March 2011, but no measurements had been available at the time of this writing.

Since both flybys M1 and M2 suggest the existence of the boundary layer and solar wind conditions have been very quiet during M1, it is very likely that the boundary layer is a stable and stationary region. Up to the present day the boundary layer itself and the

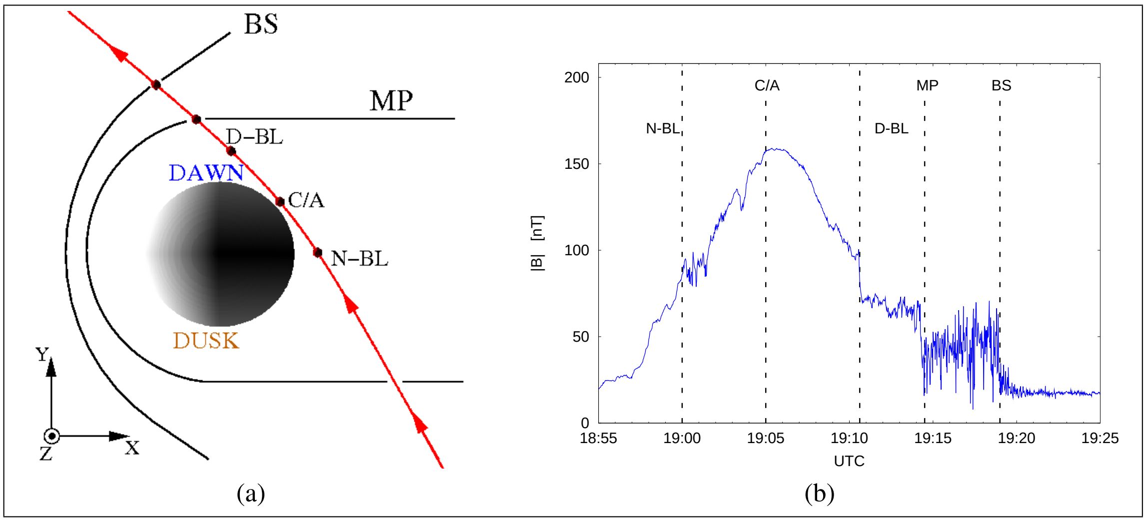

Figure 6.1: The sketch (a) illustrates the MESSENGER trajectory of the first flyby where the arrows indicate the spacecraft’s flight direction (red). The black dots mark from top to bottom the positions of outbound bow shock (BS), outbound magnetopause (MP), dayside boundary layer’s (D-BL) edge, closest approach (C/A) and nightside boundary layer’s (N-BL) edge. The corresponding magnetic field measurements are shown in (b).

key processes of its formation are not well understood. Slavin et al. (2008) pointed out that different processes could cause the layer’s formation: one explanation would be the diamagnetic effect of solar wind plasma that enters Mercury’s magnetosphere along open flux tubes. Alternatively exospheric ions that enter the magnetosphere after being picked up by the solar wind and accelerated in the magnetosheath could produce the diamagnetic decrease.

The study presented throughout this chapter intends to advance the understanding of the boundary layer and its formation. Since ion kinetic processes are believed to play an important role within Mercury’s magnetosphere (Glassmeier et al. 2003, Slavin et al. 2008), the A.I.K.E.F. simulation code is well suited for the investigation. Plasma quantities and magnetic field results will be compared to the measurements that have been provided in the initial, pre-orbital phase of the MESSENEGER mission.

6.2 On Mercury’s Dayside Boundary Layer

Based on Slavin et al. (2008), Anderson et al. (2011), Raines et al. (2011) we will summarize the available knowledge about Mercury’s boundary layer. A more detailed overview can be found in the respective articles and references therein. During both, M1 and M2, a region of depressed magnetic field and increased proton flux adjacent to it could be observed immediately after entrance into Mercury’s dawn magnetosphere. This region of depressed magnetic field was labeled the “dayside boundary layer” (D-BL). The M1 trajectory and corresponding magnetic field are shown in Figure 6.1. While interplanetary magnetic field (IMF) and Mercury’s dipole field were basically parallel at the sub-solar point during M1, they had been anti-parallel during M2, resulting in notedly increased sub-solar reconnection (Anderson et al. 2011). Since the existence of the D-BL does not seem to depend on the IMF direction, Anderson et al. (2011) concluded that sub-solar reconnection is unlikely to be responsible for the D-BL formation at Mercury. In contrast, the low latitude boundary layer (LLBL) at Earth significantly depends on the rate of sub-solar reconnection (Fuselier et al. 1999). Hence, it is unlikely that both layers are formed by the same process. Furthermore, the D-BL at Mercury occupies a significant fraction of Mercury's magnetosphere and is much larger than the LLBL at Earth, at least on scales comparable to respective magnetospheric dimensions.

During M1 the width of the D-BL was estimated to be 1000 - 1100 km and the magnetic field magnitude inside varied between 60nT and 70nT (see Figure 6.1(b)). According to Raines et al. (2011) the proton density was 16cm^{-3}, resulting in a proton inertia length of about 57km. Hence, the D-BL itself is a macro scale phenomenon for the protons. The width of the D-BL's inner edge, on the other hand, is comparable to proton gyration scale (see Figure 6.1(b) at 19:10:37 UTC). While the magnetic field intensity showed a sudden decrease from 101nT to 79nT when crossing the inner edge of the D-BL during M1, the direction of the magnetic field remained basically unchanged. This is consistent with a plasma pressure gradient that is directed outward and perpendicular to the magnetic field, as pointed out by Anderson et al. (2011). The magnetic field decrease inside the boundary layer was accompanied by an increased thermal pressure. The proton pressure inside the D-BL during M1 was estimated to be 0.4nPa with a proton temperature of $2 \cdot 10^6$K during M1, whereas the values were 1.0nPa and $10 \cdot 10^6$K during M2. A second magnetic field decrease, at Mercury's nightside, was observed during M1 at 19:00 UTC and went along with an increased proton density of about 4-5 cm^{-3}, during both M1 and M2 (Raines et al. 2011). The corresponding temperatures were measured to $4 - 8 \cdot 10^6$K during M1 and $8 \cdot 10^6$K during M2. This region was labeled the "nightside boundary-layer" (N-BL). Hence, solar wind protons should be considered to significantly impact on the boundary layer formation, even though heavy exospheric ions could play a role as well (Slavin et al. 2008, Anderson et al. 2011). In particular, the results show that both flybys yielded qualitatively the same results in terms of magnetic field and plasma observations, despite the significant difference in IMF direction.

6.3 Simulations Setup

As was shown in section 5.6, simulations using the A.I.K.E.F. code have already been successfully applied to model the magnetic field for the M1 and M2 flybys. However, these simulation were not addressed to discuss the boundary layer formation. The analysis of Mercury's magnetosphere and boundary layer formation is subject to this chapter. Even though the results are in very good agreement with the magnetic field that was recorded by MESSENGER, the simulations are not well suited for the analysis of the physics involved in the boundary layer formation because the shifted dipole and M1 IMF direction considerably complicate the analysis. Hence, we redid the simulations using a slightly simplified geometry and suggest that the corresponding physical processes are valid for the real M1 case as well.

Quantity	Symbol	(Müller et al. 2011a)	present study
Solar wind density	n	$32/\mathrm{cm}^3$	$32/\mathrm{cm}^3$
Solar wind velocity	v	$430\mathrm{km/s}$	$430\mathrm{km/s}$
ion temperature	$\mathrm{T}_{\mathrm{ion}}$	$2 \cdot 10^5$ K	$2 \cdot 10^5$ K
electron temperature	$\mathrm{T}_{\mathrm{electron}}$	$2 \cdot 10^5$ K	$2 \cdot 10^5$ K
planetary radius	R_{M}	2440 km	2440 km
magnetic moment	M	$200\ \mathrm{nTR}_{\mathrm{M}}^3$	$200\ \mathrm{nTR}_{\mathrm{M}}^3$
magnetic moment offset	$\Delta_{M,z}$	405 km	0 km
IMF magnitude	B	21.0 nT	12.6 nT
IMF longitude angle	ϕ_B	$-53°$	$90°$
IMF latitude angle	λ_B	$63°$	$0°$

Table 6.1: The table compares the physical parameter of the simulaton in section 5.6 with the simulation presented throughout this chapter. The values for Mercury's plasma environment are chosen corresponding to Wang et al. (2010).

For the simulation presented in this chapter we will focus on the M1 flyby since Mercury's dipole field and IMF were basically parallel in the sub-solar region, resulting in negligible dayside reconnection. As the simulations of Müller et al. (2011a) did show the dayside diamagnetic decrease even in a pure hydrogen plasma, we concluded that all physics seen in the data can be completely explained without the inclusion of sodium or any other exospheric species. Hence, at the current stage we decided to continue our modeling by using single species hydrogen plasma that is exclusively injected at the domain boundaries. The influence of exospheric ion species on the boundary layer will be subject to future studies. Compared to the input parameters of Müller et al. (2011a) we introduce the following modifications that are also listed in table 6.1:

1. Centered planetary dipole moment.
2. M1 trajectory mapped to equatorial plane.
3. IMF in y-direction, ie. perpendicular to Mercury's magnetic moment
4. Improved model of Mercuries interior.

Each of the listed rearrangements is explained below:

1. According to Alexeev et al. (2010) the center of Mercury's magnetic moment is shifted about 405km in northern direction. Figure 6.2 shows the magnetic field of such a dipole along the M1 trajectory (red). As can be seen, both B_x and B_y are non-zero. However, we cannot see any physical reason why the existence of the boundary layer should depend on this shift. Hence, we use a planetary centered magnetic moment in order to simplify the analysis. The green line in Figure 6.2 shows the magnetic dipole field along the M1 trajectory that results from a centered magnetic moment.

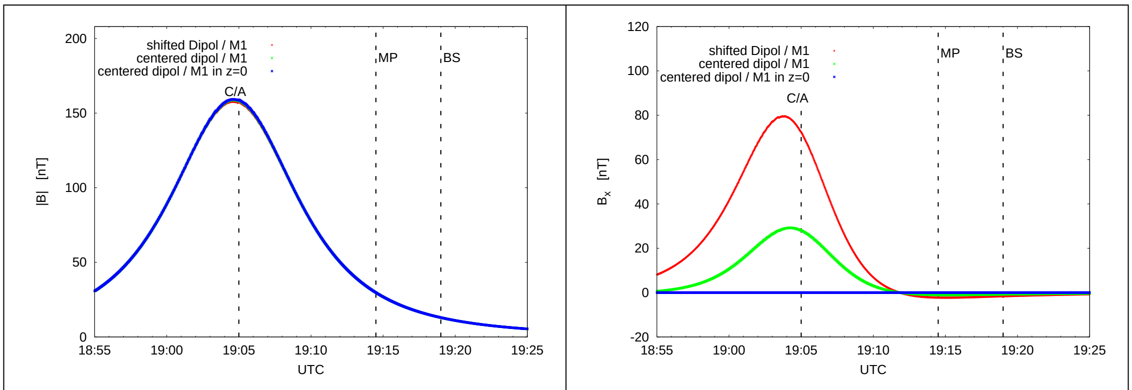

(a) $|\underline{B}|$ [nT]

(b) B_x [nT]

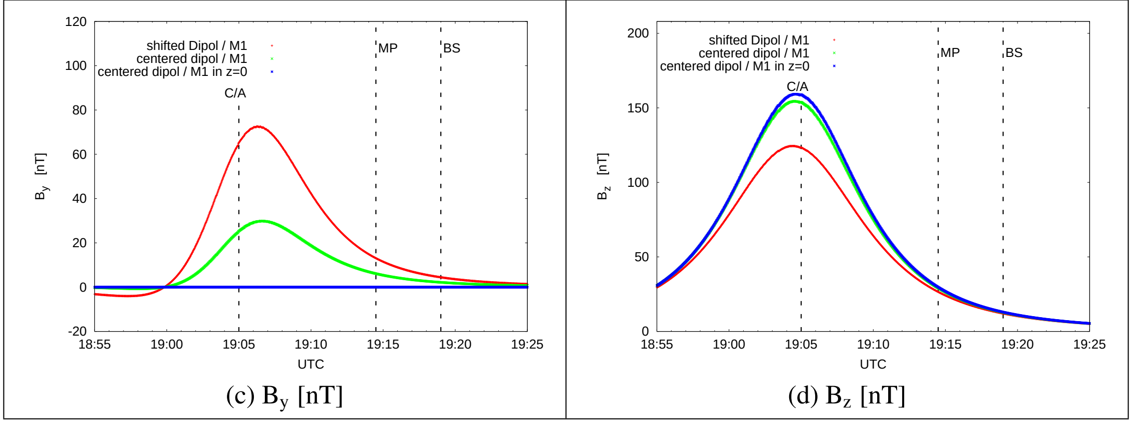

(c) B_y [nT]

(d) B_z [nT]

Figure 6.2: The images show the magnetic field and its components for an offset dipole (Alexeev et al. 2010) along the M1 trajectory (red). Both B_x and B_y are non-zero. As we do not see any physical reason why the boundary layer should depend on this shift we use a planetary centered dipole in order to simplify the analysis. The green line shows the magnetic field for a centered dipole along the M1 trajectory. Finally the blue line shows the field of a centered dipole along the M1 trajectory that is projected on the equatorial cross-section, i.e. the z-component of each coordinate is set to zero. We shall point out that any of the modifications barely affects the magnetic field magnitude in plot (a).

2. The M1 Orbit is not exactly located inside the equatorial cross-section, but shows a rather small inclination. For the present simulation we neglect this inclination, i.e. we set $z = 0$ for each position while the x- and y-coordinates remain unchanged. Figure 6.2 shows the corresponding magnetic field (blue). As can be seen, both the B_x and B_y components vanish everywhere along the trajectory. However, we shall point out that this simplification barely impacts the total magnetic field strength: all three configurations show nearly the same magnetic magnitude along the entire trajectory (see Figure 6.2(a).)

3. In contrast to the simulations of Müller et al. (2011a) that use the real M1 and M2 magnetic field configurations, a simulation with simplified IMF is carried out for the present study. The IMF is set to $B_{\mathrm{IMF}} = (0, 12.6, 0)$nT, therefore being entirely directed in y-direction. Like the Parker spiral field at Mercury the latitude angle of this IMF is zero, i.e. the field is perpendicular to Mercury's magnetic moment. Furthermore this choice simplifies the differentiation between Mercury's intrinsic field and the IMF: within the

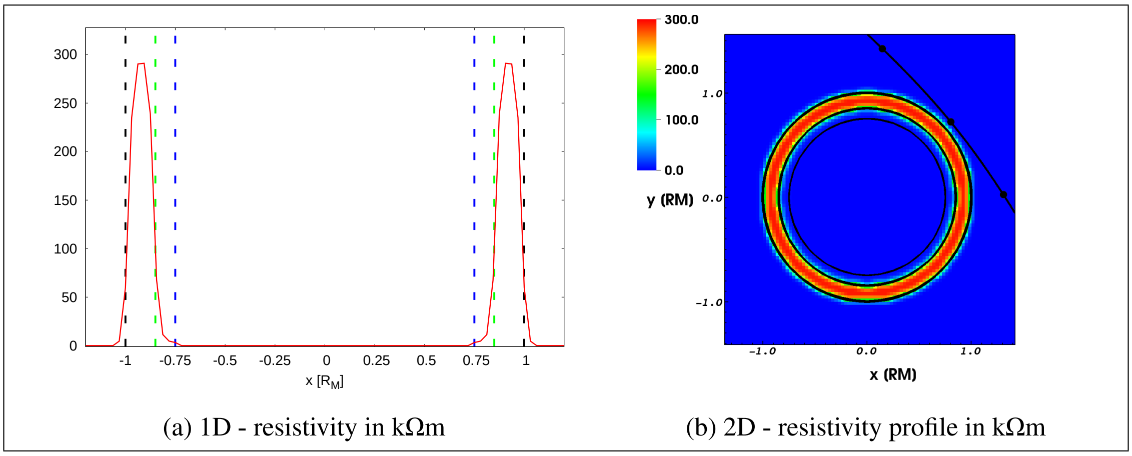

(a) 1D - resistivity in kΩm

(b) 2D - resistivity profile in kΩm

Figure 6.3: The plot (a) shows the resistivity profile by means of a one-dimensional cut along the x-axis. Within a radius of $0.75R_M$ that is marked by blue dashed vertical line a zero resistivity is specified, i.e. in this region Mercury's intrinsic dipole field remains unaffected during the entire simulation. Mercury's mantle is divided into an inner region of lower resistivity $\eta_\mathrm{i} \approx 4\mathrm{k}\Omega\mathrm{m}$ between the blue and green vertical line. An outer region of higher resistivity $\eta_\mathrm{o} \approx 300\mathrm{k}\Omega\mathrm{m}$ is located between the green and black vertical line. The black line coincides with Mercury's surface. Plot (b) shows the resistivity profile in the equatorial cross-section.

equatorial cross section we expect to observe a zero B_z component within the magnetosheath while inside the inner magnetosphere B_x and B_y are expected to be zero. Hence, for the dayside boundary layer that resides in between these regions it will be easy to distinguish whether Mercury's intrinsic dipole field or the IMF dominates.

4. Due to the small stand-off distance at Mercury that is about $0.5R_M$ above Mercury's surface (where R_M=2440km is the planetary radius), current generation inside Mercury may play an important role (Glassmeier et al. 2007, Grosser et al. 2004, Hood and Schubert 1979, Suess and Goldstein 1979). The A.I.K.E.F. simulation model self-consistently incorporates obstacles of arbitrary conductivity profile into the plasma environment (Müller et al. 2011a). This method has already been successfully applied to model fossil fields at Titan (Müller et al. 2010) and several other Saturnian moons (Roussos et al. 2008, Kriegel et al. 2009). For the Mercury simulations the resistivity profile of the planetary body is setup as visualized in Figure 6.3.

Within a radius of $0.75R_M$ that is marked by blue dashed vertical lines a zero resistivity is specified, i.e. in this region Mercury's intrinsic dipole field remains unaffected during the entire simulation, accounting for Mercury's highly conducting ion core (Milillo et al. 2005) and therefore diffusion times of many thousand years. Formally this region can be referred to be the simulation's "inner boundary". Assuming that electric properties of Mercury's mantle are similar to those of moon, Glassmeier (2000) concludes that values of 10^{-2}S/m to 10^{-9} S/m are reasonable to describe the mantle region. In terms of resistivity these values correspond to 0.1kΩm to 10^6kΩm. In our simulation we use values that are in between these estimates. We divide Mercury's mantle into an inner region of lower resistivity $\eta_\mathrm{i} \approx 4\mathrm{k}\Omega\mathrm{m}$ that resides in between the blue and green vertical line (see Figure 6.3(a)). An outer region of higher resistivity $\eta_\mathrm{o} \approx 300\mathrm{k}\Omega\mathrm{m}$ is located in between the green and black vertical line. The black line coincides with Mercury's surface. The highly resistive outer region accounts for an isolating crust which confines any currents that are generated inside the mantle region from Mercury's surface. Figure 6.3(b) illustrates the resistivity profile in the equatorial cross section. To guarantee numerical stability the resistivity profile is slightly smoothed, which is visible at the smeared out edges near the surface. However, at C/A the resistivity has already decayed to zero.

6.4 Numerical Parameters

The numerical parameters for the simulation presented in this chapter are listed in table 6.2. The simulation domain is visualized in Figure 6.4(a). A large simulation Box of L=(12,20,20)R_M is used in order to avoid any boundary effects. As argued before, the M1 trajectory is projected into the equatorial cross-section, which is shown by means of a blue frame. The trajectory is depicted in red where the arrows indicate the flight direction of the MESSENGER spacecraft.

Quantity	symbol	value
Domain size	L	(12,20,20)$\mathrm{R_M}$
Origin	O	(4,10,10)$\mathrm{R_M}$
Mesh Spacing L2	Δ_x	(1.8,1.8,3.6)$\mathrm{x_0}$
Time Step	Δ_t	0.1 $\Omega_{\mathrm{p,100nT}}$
Particles each Cell	PPC	80
Minimal Proton Density	MPD	1.6/cm^3

Table 6.2: The table lists the numerical parameters for the simulation presented in this chapter.

The simulation is carried out on 128 CPUs, the numerical mesh includes three levels of refinement: L_0, L_1 and L_2. Figure 6.4(b) illustrates an enlarged view on the plasma environment that is close to Mercury and embedded inside refinement levels L_1 and L_2. The spatial resolution within the highest level of refinement is Δ_x = (1.8, 1.8, 3.6)x_0, where x_0 = 40km is the proton inertia length, i.e. the gyro radius at Alfvén speed with respect to the background parameter of table 6.1. Hence, the proton gyration is spatially resolved inside the solar wind. Yet, the gyration of a proton that travels at background Alfvén speed is spatially not yet resolved in a 100nT magnetic field as at D-BL's inner edge. However, as will be seen later the thermal velocity at the D-BL's inner edge reaches three to four times the background Alfvén speed. Hence, the local gyration radius in this region is about 1.2 times Δ_x in the equatorial cross section and therefore a reasonable spatial resolution is guaranteed. Even more important, the kinetic treatment of the ions allows to accurately capture the proton temperature distribution which will show to be an important quantity for the boundary layer formation (cf. section 6.6).

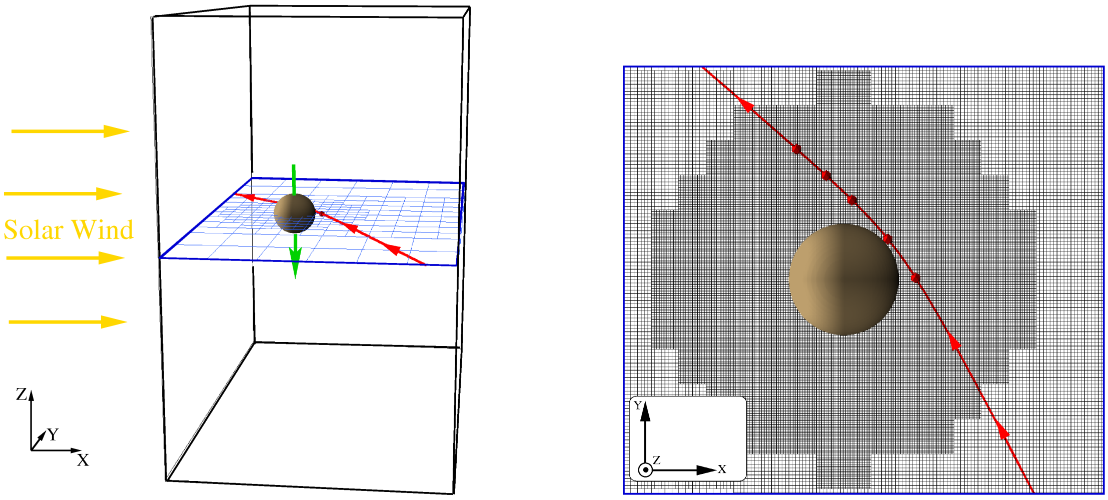

(a) (b)

Figure 6.4: The entire simulation domain is shown by means of the black cuboid in (a). All results discussed in this chapter have been taken from the equatorial cross section, that is indicated by the blue frame. The brown sphere represents Mercury where the green arrow illustrates the direction of its magnetic moment. The red line illustrates the MESSENGER trajectory where the red arrows indicate the direction of flight. An enlarged view on the numerical mesh is shown in Figure (b) for the equatorial cross-section. As can be seen the locations of interest from outbound bow shock (topmost red dot) to nightside boundary layer (lowermost red dot) are located within the highest level of refinement.

Even though the code supports meshes that are also adaptive in time and may resolve dynamical features, we use a mesh that is static in time and fix the level of highest resolution within a spherical region of $3.5R_M$ from the planetary center. In doing so, we reside to highly resolve the far downstream region and bow shock flanks. This saves computational resources that in turn are used to increase the number of particles and resolution within the immediate vicinity of Mercury. We shall point out that in particular the following positions along the trajectory are embedded within this highest level of refinement L_2: Outbound bow shock crossing (BS), outbound magnetopause crossing (MP), dayside boundary layer crossing (D-BL), closed approach (C/A) and nightside boundary layer crossing (N-BL) (see Figure 6.4(b)). Thus, we can exclude that any of these positions are influenced by refinement boundaries. Also we shall point out that the A.I.K.E.F. model is designed such that particle refinement is not required within the highest level of refinement and therefore the phase space distribution is not modified at all (Müller et al. 2011a). However, as we do not employ a time adaptive mesh the inbound bow-shock and inbound magnetopause reside in coarse refinement levels. For this reason we focus our analysis on the outbound passage between 18:55 and 19:25 UTC that is entirely embedded in the highest level of refinement.

The time step is chosen to be $\Delta_t = 0.1\Omega_{\mathrm{p,100nT}}$, where $\Omega_{\mathrm{p,100nT}} = 0.1s$ is the proton gyration period inside a 100nT field. This ensures that the proton kinetic motion is well resolved in time, even near the planetary surface where the magnetic field is strongest. In some regions like the neutral sheet the proton density might drop to zero which cannot be handled within the hybrid approximation. We therefore set a lower threshold for the proton density to $1.6/\text{cm}^3$, that is 20 times below the solar wind density. The total number of macro particles involved in this simulation is about 10^9.

6.5 Results

The simulation reaches the quasi stationary state after 3 domain traversals, i.e. after the solar wind has traveled a distance of 36 R_M. We shall point out that the physical quantities are *quasi*-stationary, i.e. they are still subject to fluctuations. In order to eliminate high frequency and numerical noise, the visualized magnetic fields and currents are averaged over 20 time steps. In order to exclude any start-up-effect, we let the simulation continue until the solar wind has travelled a distance of 108 R_M. The magnetic field data along the M1 Orbit is recorded in regular time intervals and compared against the M1 measurements.

Figure 6.5 shows the magnetic field magnitude of the simulation along the M1 orbit at simulation times $t_1 \approx$ 3min (a), $t_2 \approx$ 5min (b), $t_3 \approx$ 8min (c) and $t_4 \approx$ 10min (d) in red. For comparison the M1 measurements are visualized in blue. The five dashed vertical lines indicate the outbound bow-shock (BS), outbound magnetopause (MP), inner edge of the boundary layer (D-BL), closest approach (C/A) and inner edge of the nightside boundary layer (N-BL). As can be seen the overall shape remains the same, even though the magnetic field jump at the D-BL's inner edge does not show a sharp step in each snapshot. Hence, we resign to state a value for the magnetic field jump. However, a region of decreased magnetic field strength between MP and the D-BL's inner edge is clearly visible and in agreement with the measured dayside boundary layer. The width of the D-BL is about 1100km, which is within the range estimated by Anderson et al. (2011). In contrast to this, the nightside diamagnetic decrease is a rather transient structure that dis- and reappears with time (see Figure 6.5(d)). However, we have reason to assume that this is due to numerical limitations and will comment this behavior at the end of this section.

In order to gain an improved understanding of the magnetic field topology, the magnetic field magnitude and its components are visualized in Figure 6.6(a)-(h). The left column shows an enlarged two dimensional view of Mercury's magnetosphere for the equatorial cross-section while the right column shows the corresponding one-dimensional field along the M1 trajectory. Black dots within the 2D plots correspond to the vertical lines in the 1D plots, that are from top to bottom: bow shock (BS), magnetopause (MP), inner edge of the dayside boundary layer (D-BL), closest approach (C/A) and nightside boundary layer (N-BL).

The magnetic field magnitude along the M1 trajectory in plot (a) shows the existence of four qualitative distinct regions: 1. undisturbed solar wind field (dark blue), 2. magnetosheath (light blue), 3. dayside boundary layer (green) and 4. inner magnetosphere (red). These regions are separated by sudden increases in magnetic field intensity. While bow-shock and magnetopause are well understood and have been observed in all magnetospheres within the solar system, the differentiation between boundary layer and inner magnetosphere is a feature exclusively related to the Hermean magnetosphere. To the authors' knowledge, the boundary layer has not been captured by any numerical model before. Again we shall point out that the dayside boundary layer even exists in the absence of any exospheric ions like sodium.

The usage of a simple B_y IMF offers the unique opportunity to distinguish the regions by means of their magnetic field component. It is instructive to follow the simulation results from undisturbed solar wind at outbound 19:25 UTC to the N-BL at 19:00 UTC, that is the *reverse direction* of the MESSENGER1 spacecraft and from right to left within the 1D plots. The B_x component in Figure 6.6(c)/(d) vanishes within the undisturbed solar wind. At the BS it exhibits a sudden increase, which is due to the draped and piled-up

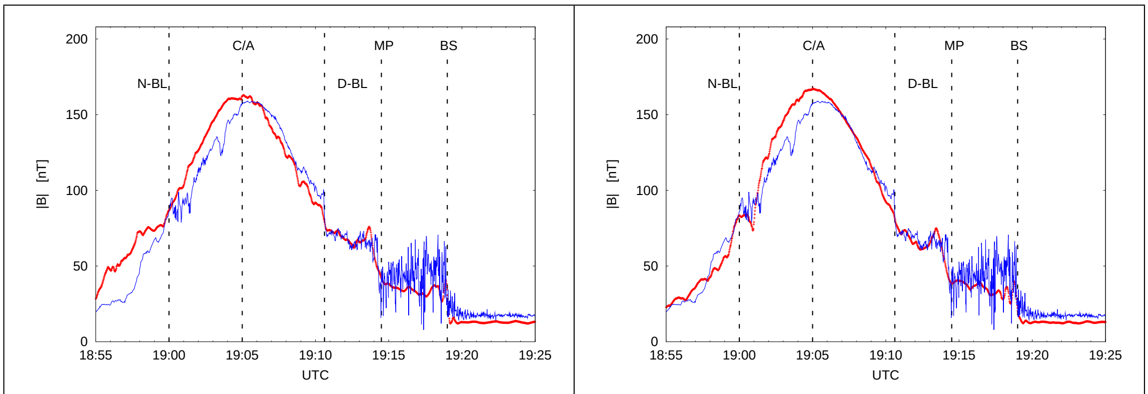

(a) $|\underline{B}|$ at $t_1 \approx 3$min (b) $|\underline{B}|$ at $t_2 \approx 5$min

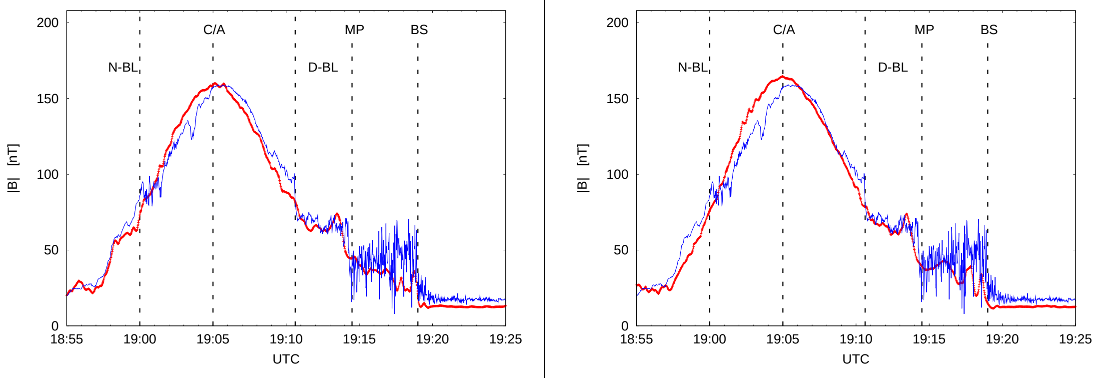

(c) $|\underline{B}|$ at $t_3 \approx 8$min (d) $|\underline{B}|$ at $t_4 \approx 10$min

Figure 6.5: The images show the magnetic field magnitude along the MESSENGER1 trajectory (red) after the quasi-stationary state has been reached. The field is compared with the MESSENGER measurements in blue for the simulation times $t_1 \approx 3$min (a), $t_2 \approx 5$min (b), $t_3 \approx 8$min (c) and $t_4 \approx 10$min (d). After 10 minutes the solar wind has traveled a distance of more than 100 R_M. As can be seen the magnetic field is stationary, yet not static. Several features such as the bow shock (BS), magnetopause (MP) and the dayside boundary layer (D-BL) are well visible at every time. However, the inbound diamagnetic decrease at 19:00 UTC is a rather transient structure. Over the observed time of 10 minutes it dis- and reappears.

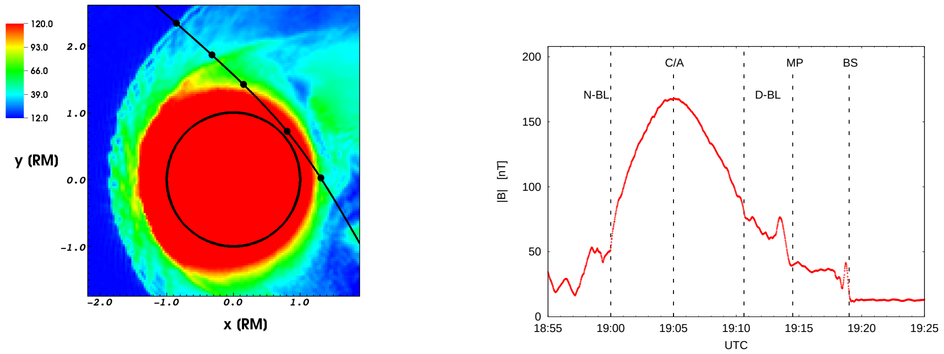

(a) $|\underline{B}|$ in nT (b) $|\underline{B}|$ in nT

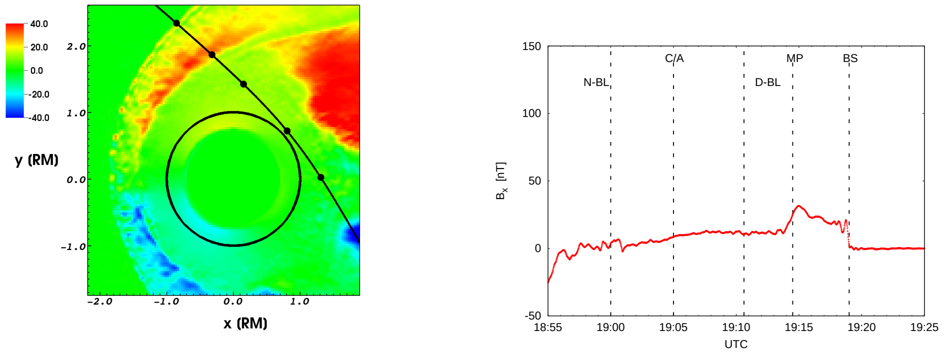

(c) B_x in nT (d) B_x in nT

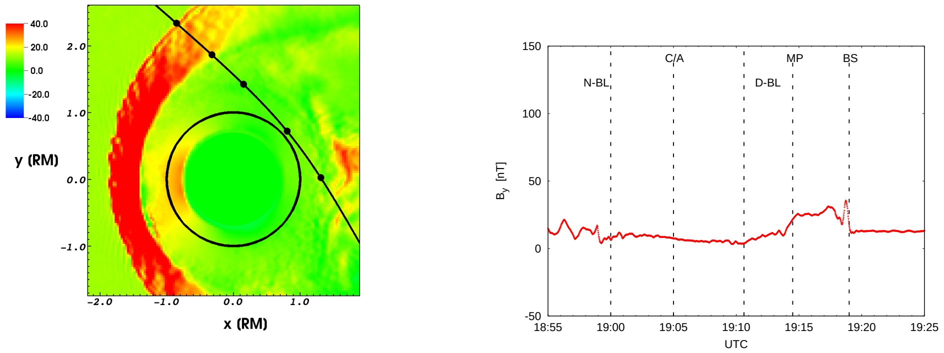

(e) B_y in nT (f) B_y in nT

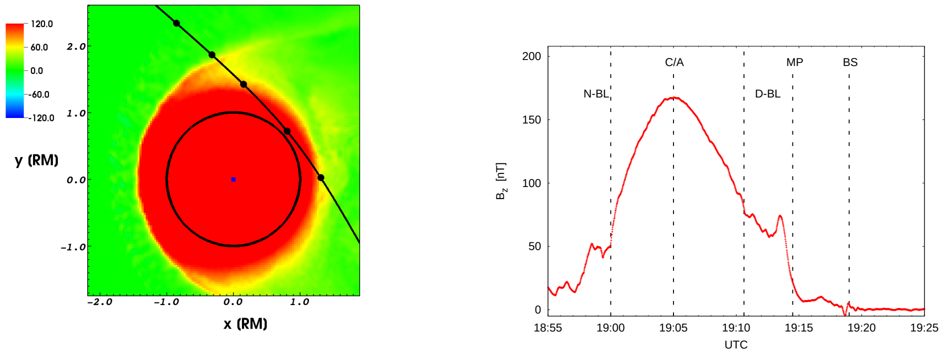

(g) B_z in nT (h) B_z in nT

Figure 6.6: Illustrated are the magnetic field and its components in the equatorial cross-section (left column) and along the MESSENGER trajectory (right column). Plot (a) shows the existence of four qualitatively different regions: 1. IMF (dark blue), 2. magnetosheath (light blue), 3. boundary layer (green) and 4. inner magnetosphere (red).

IMF within the magnetosheath. When crossing the MP it decays to values close to zero, i.e. it almost vanishes within the boundary layer. The fact that it is not exactly zero might account for the slightly draped dipole field within the magnetopause. However, when crossing the inner edge of the D-BL and moving into the inner magnetosphere, B_x remains unaffected. Obviously, the boundary layer formation is controlled by Mercury's intrinsic field, rather than by the IMF.

This conclusion is supported by the view on the B_y-component in Figure 6.6(e)/(f): At BS, a sudden increase in field intensity can be observed, but when moving from the magnetosheath into the boundary layer the field strength decays below IMF intensity. The edge of the boundary layer is hardly visible within the B_y component.

A different behavior can be observed within B_z in Figures 6.6(g)/(h), which is zero within the undisturbed solar wind flow. It experiences some fluctuations in the magnetosheath, but remains basically zero outside the magnetosphere. The reason is, that, in contrast to the B_x component, it does not contribute to the draped magnetosheath field. However, when crossing the MP into the dayside boundary-layer a sudden increase can be observed, i.e. Mercury's intrinsic dipole field clearly dominates the boundary layer region. Crossing the inner edge of the boundary layer into the inner magnetosphere, the B_z component experiences another sudden increase. Continuing to C/A, the B_z component exhibits a dipolar behavior. In the inbound region of the trajectory, a sudden decrease can be observed denoting the nightside boundary-layer.

The magnetic field in Figure 6.6 is consistent with a current density $\underline{j} = \nabla \times \underline{B}/\mu_0$ that is visualized in Figure 6.7. Even though the current density is quite noisy (which is inherent to particle mesh simulation codes), the basic current systems can be nevertheless identified. Besides the current magnitude in Figure 6.7(a)/(b) the j_x and j_y components are visualized in Figures 6.7(c) to (f). The color scale of the j_x and j_y components in Figures 6.7(c)/(e) is arranged such that red indicates positive, blue negative and green zero values. We resign to visualize the j_z component that shows a single local maximum at the bow shock and therefore is only of minor interest for our discussion.

The magnitude of the current density in Figure 6.7(a)/(b) shows at least four local maxima above background noise: the maximum at 19:19 UTC is consistent with the magnetic field jump at the bow shock while the peak at the MP accounts for the magnetopause current. As can be seen in Figures 6.7(d) and (f), this current is negative in j_x and j_y which is obvious if one follows the MP geometry in the 2D Figures 6.7(c) and (e).

A third local maximum can be identified at 19:10:30 UTC in Figure 6.7(b) which coincides with the D-BL's inner edge. This current mainly points in negative x-direction and connects to the dayside magnetopause current, which can be seen in Figure 6.7(a) and (c). The orientation is very similar to the orientation of the MP current even though its intensity is weaker. The current extends to the nightside where the fourth local maximum at 19:00 UTC can be observed in consistency with the presence of the nightside boundary layer. Obviously, both, the inbound and outbound diamagnetic decreases, are caused by the same current layer, which we will label *boundary layer current* in the fol-

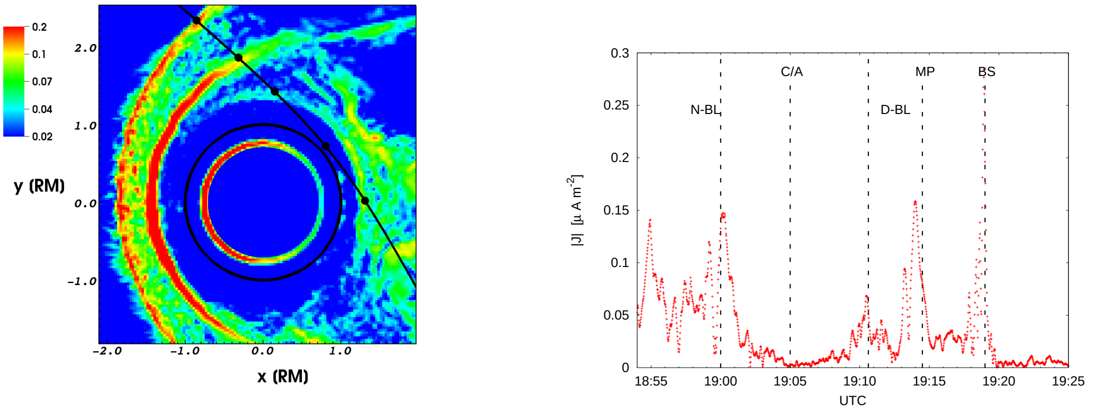

(a) $|\underline{j}|$ in μAm^{-2} (b) $|\underline{j}|$ in μAm^{-2}

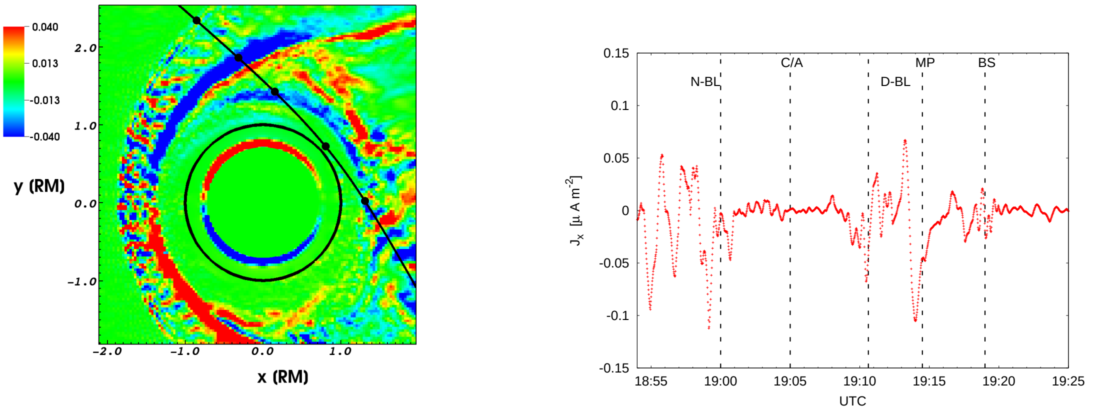

(c) j_x in μAm^{-2} (d) j_x in μAm^{-2}

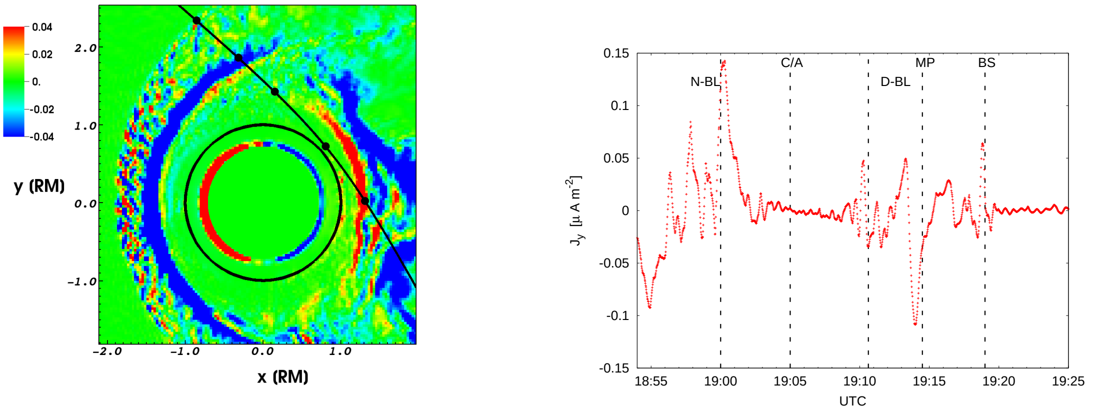

(e) j_y in μAm^{-2} (f) j_y in μAm^{-2}

Figure 6.7: The Figure illustrates the current density in μAm^{-2} in the equatorial cross-section (left column) and along the MESSENGER trajectory (right column). The first row shows the magnitude while the second illustrates the j_x and the third the j_y component, respectively. The current magnitude clearly shows four local maxima above background noise that are located at the bow shock, magnetopause, inner edge of the dayside and nightside boundary layer.

lowing. Since the boundary layer current exhibits a semi-circle shape, it is mainly directed in positive y-direction at the nightside that can be seen well in Figure 6.7(e).

At about 18:55 UTC, close to the N-BL, the current's direction is reversed into negative y-direction. This region can be clearly identified with the neutral sheet current that extends from the dawn to the dusk flank of Mercury's magnetopause. It resides at about 0.4 R_M above Mercury's nightside surface.

As will be shown below, the regions and boundaries described above can be observed in the simulated plasma quantities as well. Since a single species hydrogen plasma is used, any quantity shown below relates to protons. Their velocity is visualized in Figures 6.8(a)/(b). The plasma is diverted at the bow shock and its velocity decreases from 430km/s in solar wind to about 280km/s inside the magnetosheath. At the magnetopause, the plasma velocity decreases to nearly zero within the magnetosphere. In contrast to the terrestrial magnetosphere, the plasma does not co-rotate within Mercury's magnetosphere. The reason is that Mercury itself does not rotate (at least not on time scales discussed here). Furthermore, neither curvature nor gradient drift play a noteworthy role near Mercury (cf. section 6.6).

As we follow the direction from the magnetopause towards C/A, the velocity exhibits a sudden increase to about 80km/s adjacent to the D-BL's inner edge. However, the arrows in Figure 6.8(a) and the U_x-component in Figures 6.8(c)/(d) show that the velocity is not directed downstream, but sun-ward. The color scale of the U_x component in Figure 6.8(c) is arranged in such way that red indicates down-stream, blue sun-ward and green zero velocity. The sun-ward stream at the D-BL's inner edge coincides with the sun-ward directed current that was shown in Figure 6.7(c)/(d).

The U_y-component at the N-BL in Figure 6.8(e)/(f) shows a similar behavior as the j_y-component that was shown in Figure 6.7(e)/(f). The nightside diamagnetic decrease resides between two opposing streams where the planet-ward plasma stream is directed in positive y direction at 60km/s, while the flow points in negative y-direction at 160km/s on the downstream side. Hence, the latter one accounts for the neutral sheet current while the planet-ward stream constitutes for the boundary layer current. The fact that two opposing plasma streams exist adjacent to each other at the N-BL within a narrow region results in a rather unstable configuration. This is why we observe strong fluctuations at the N-BL as mentioned at the beginning of this section. However, following the flow magnitude in Figure 6.8(a) reveals that the flows at D-BL and N-BL are part of the same plasma stream.

While velocity measurements were not available at the time of this writing, density and temperature estimates have been published by Raines et al. (2011). In the following, we will compare our findings with these measurements. The proton number density is visualized in Figures 6.9(a)/(b). In the two-dimensional plot 6.9(a), the density is shown color coded on a logarithmic scale. The regions map to the colors in orange (solar wind), magnetosheath (red), boundary layer (yellow) and inner magnetosphere (green). Quantitative results along the M1 trajectory can be seen in Figure 6.9(b): At BS the density

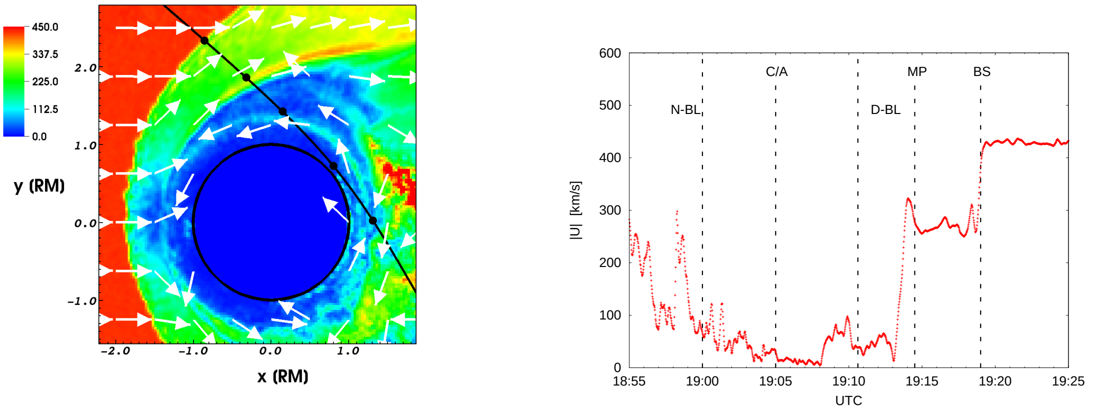

(a) $|\underline{U}|$ in km/s (b) $|\underline{U}|$ in km/s

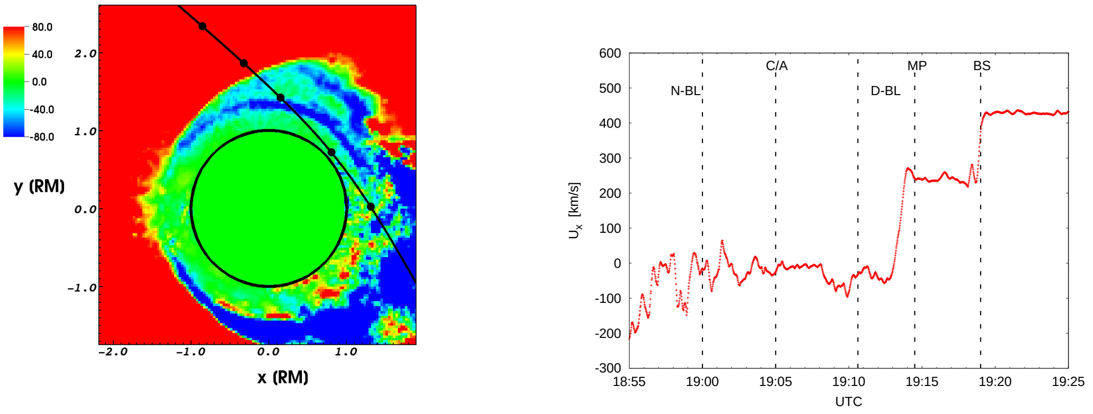

(c) U_x in km/s (d) U_x in km/s

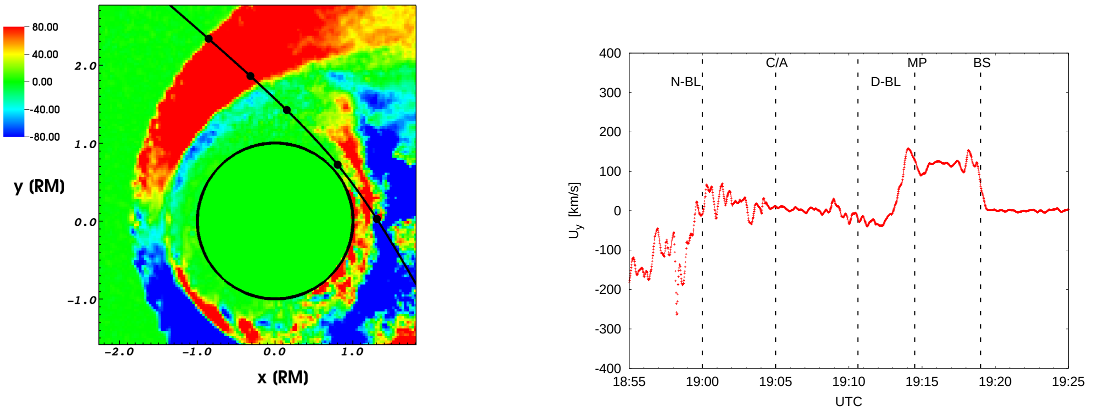

(e) U_y in km/s (f) U_y in km/s

Figure 6.8: The Figure illustrates the proton velocity in km/s in the equatorial cross-section (left column) and along the MESSENGER trajectory (right column). The first row shows the magnitude while the second illustrates the U_x and the third the U_y component, respectively. A local maximum of about 80 km/s can be observed at the inner edge of the dayside boundary layer. As can be seen in Figures (c) and (d) the flow is not directed downstream but sunward in this region.

Quantity	simulation	observations M1
width	1100 km	1000-1400 km
$\lvert \underline{B} \rvert$	60-70 nT	60-70 nT
n_{proton}	$20/\text{cm}^3$	$16/\text{cm}^3$
T_{proton}	$2.9 \cdot 10^6$K	$2 \cdot 10^6$K
p_{proton}	1nPa	0.4nPa

Table 6.3: The table shows a comparison of simulation results (left column) and MESSENGER observations during the M1 flyby (right column) for the dayside boundary layer region. The observations correspond to Anderson et al. (2011) and Raines et al. (2011).

experiences a jump from 32cm^{-3} background value to 118cm^{-3}, that is nearly a factor of four. Within the magnetosheath it undergoes strong oscillations with an average density of about 80cm^{-3}. At the MP the density decays to about 20cm^{-3}, which is comparable to the 16cm^{-3} that have been estimated by Raines et al. (2011) for the density inside the D-BL. At the inner edge of the D-BL the density experiences a further decrease to about 5cm^{-3}. After 19:08 UTC it finally decreases to nearly zero.

A small local maximum of about 10cm^{-3} can be observed at 19:01 UTC, coinciding with the N-BL. A comparable density increase of about 5cm^{-3} at the N-BL has been estimated by Raines et al. (2011). Inside the plasma sheet the density resides at about 2cm^{-3} which is within the range of 1-10/cm^3 that was estimated by Raines et al. (2011) for this region.

Raines et al. (2011) estimated the proton pressure inside the boundary to be 0.4nPa during M1 and 1nPa during M2. This is comparable to the proton pressure in our simulation (see Figures 6.9(a)/(b)) that is slightly above 1nPa inside the D-BL. When crossing the D-BL's inner edge into the magnetosphere the pressure drops to nearly zero, which is expected for a classical magnetosphere. At 19:01 UTC the proton pressure increases for a short interval, thereby causing the inbound diamagnetic decrease. As can be seen in Figure 6.9(a), the origin of this pressure increase is hot plasma that drifts towards the dusk side in the direction of the neutral sheet current. We reside to discuss the electron pressure which is $p_e = 5 \cdot 10^{-3}$nPa in our simulation inside the BL and therefore negligible compared to the proton pressure.

By comparing Figures 6.9(b) and 6.9(d), it can be seen that the proton pressure $p_p = n_p k_B T_p$ inside the D-BL is only slightly smaller than inside the magnetosheath, even though the density drops by nearly a factor of four. The reason is the temperature increase inside the D-BL by more than a factor of three compared to the magnetosheath. However, while the parallel temperature $T_{p,\parallel} = 9{\cdot}10^5$K remains about the same in in both, magnetosheath and layer (see Figure 6.9(f)), the perpendicular temperature increases to an average value of about $T_{p,\perp} = 2{\cdot}10^6$K inside the boundary layer. A significantly increased perpendicular temperature near Mercury has already been predicted by the hybrid simulations of Trávníček et al. (2009, 2010). Their results indicate that the perpendicular temperature near Mercury may be one order of magnitude above the solar wind temperature. The maximal perpendicular temperature inside the D-BL of $T_{p,\perp} = 2.5{\cdot}10^6$K is reached at its inner

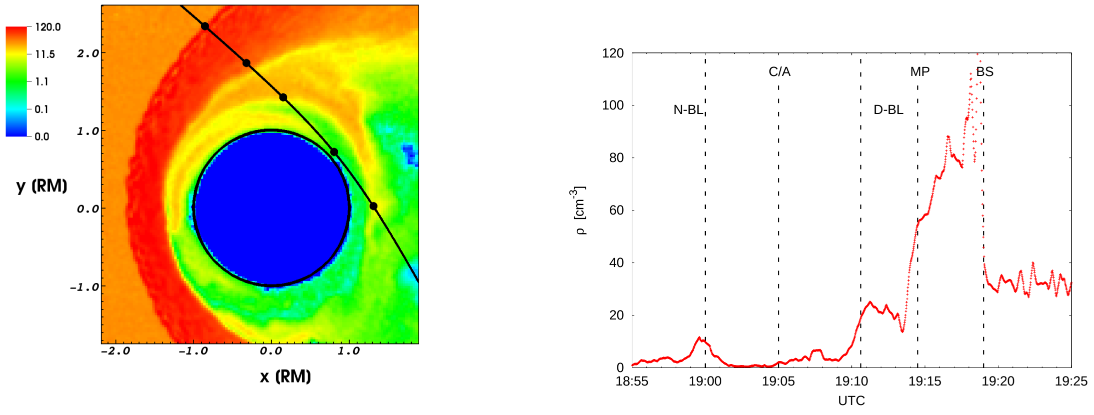

(a) n in 1/cm^3 (b) n in 1/cm^3

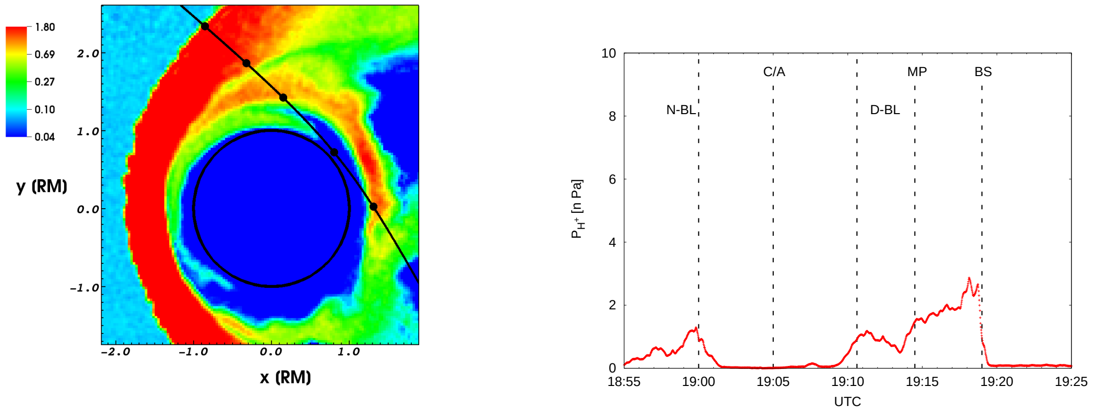

(c) p in nPa (d) p in nPa

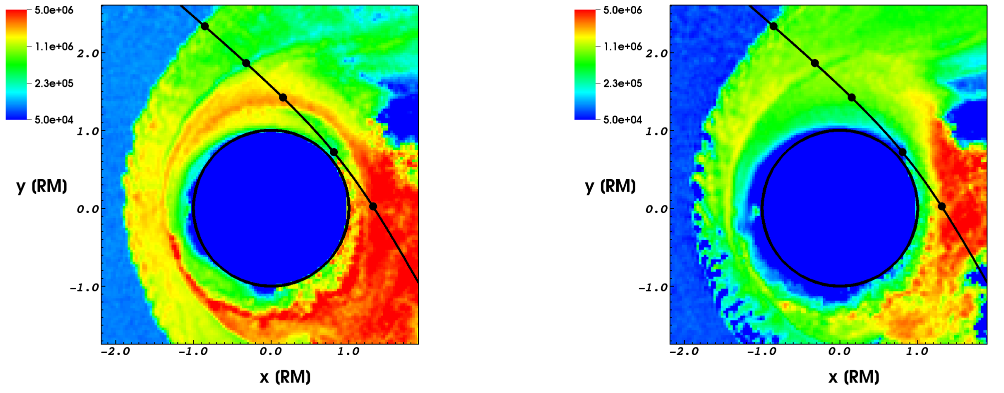

(e) $T_\perp$ in K (f) $T_{||}$ in K

Figure 6.9: The Figure illustrates the proton density in cm^{-3} (top row) and the proton pressure in nPa (second row). The third row shows the perpendicular proton temperature (left plot) and the parallel proton temperature (right plot) in K. Even though the plasma density inside the dayside boundary layer is about four times smaller than in the magnetosheath (see Figure (b)), the pressure in both regions is comparable (see Figure (d)). The reason is the increased perpendicular temperature

edge. The values are comparable to the temperature of $T_p = 2\cdot10^6$K that was estimated by Raines et al. (2011) for the boundary layer.

At the N-BL the temperature increases to $T_p = 7\cdot10^6$K, which is within the range of $T_p = 4$-$8\cdot10^6$K that was estimated by Raines et al. (2011) for this region. The key findings of our simulation for the dayside boundary layer region are summarized in table 6.3 and compared to the M1 observations. We choose the M1 observations rather than the M2 observations for comparison since the former configuration shows a sub-solar closed magnetosphere which resembles the case in our simulations. Yet, both configurations are not identical and therefore differences are expected.

6.6 Discussion

In the following we will explain the physical processes that produce the signatures shown above. In particular the boundary filling, the origin of the temperature asymmetry and the formation of the boundary layer current will be discussed.

6.6.1 Boundary Layer Filling

At first we shall explore from the simulation where the plasma that populates the boundary layer enters Mercury's magnetosphere. In order to understand this process, a volume of particles that enter the simulation geometry is marked at the inflow boundary and traced during its propagation. The initial size of this volume is chosen to be $V = (0.5R_M, L_Y, L_Z)$. Similar to a flip-book, Figure 6.10 shows in real-time the motion of the marked protons by means of their normalized macroscopic density within the equatorial cross-section. In order to understand the particle motion it is instructive to account for the magnetic field topology, which is shown in Figure 6.11. As the situation needs to be considered three dimensional, Figures 6.12(a)/(b) illustrates the three dimensional shape of the proton density that drifts through the boundary layer. The gray plane in both Figures is the equatorial cross-section of Figure 6.10. In addition, we show a 3D view of the total plasma density in Figure 6.12(c)/(d) to explain how the marked particles are distributed within the magnetosphere.

We define $t_1 = 0s$ in Figure 6.10(a) to be the time when the marked particles reach the bow-shock position of the M1 trajectory. As they enter the magnetosheath they are strongly compressed, heated and decelerated. The width of the magnetosheath at this position is 1700km. At $t_2 = 20s$ the protons arrive at the magnetopause (see Figure 6.10(b)). In the sub-solar region, the population is compressed to a narrow layer and deflected around the magnetopause. We did not observe a single proton that entered the magnetosphere in the sub-solar region, which confirms the magnetosphere to be closed sub-solar. At $t_3 = 36$s the very first protons enter the magnetosphere in the equatorial cross-section along the dawn flanks, see Figure 6.10(c). Figures 6.10(d) and 6.10(e) reveal that the downstream dawn flank of Mercury's magnetosphere is to some extent open to solar wind particles, as will be explained in the following:

Figure 6.11 shows magnetic field lines that originate from both, Mercury and the IMF. The color indicates the B_x component: blue is negative ie. pointing sun ward, red is positive ie. pointing downstream and green indicates zero. As the draped IMF exhibits a positive B_x component at Mercury's dawn side, IMF and closed field lines are directed antiparallel in this region (see 6.11(a), black arrow). This topology is likely to trigger reconnection. Hence, Mercury's magnetic field lines may connect to the IMF as can be seen in Figures 6.11(b) and (c). Figure 6.11(d) shows the identical topology of Figure 6.11(c) from Mercury's dawn side. The field line that is marked by means of a black arrow connects to both, IMF and Mercury's south pole. This type of reconnection where one end of a flux tube connects to the solar wind while the other roots in the planet has alredy been reported by Slavin et al. (2009) for the Hermean system. Figure 6.11(f) shows by means of the density of the marked particle population that solar wind protons enter Mercury's

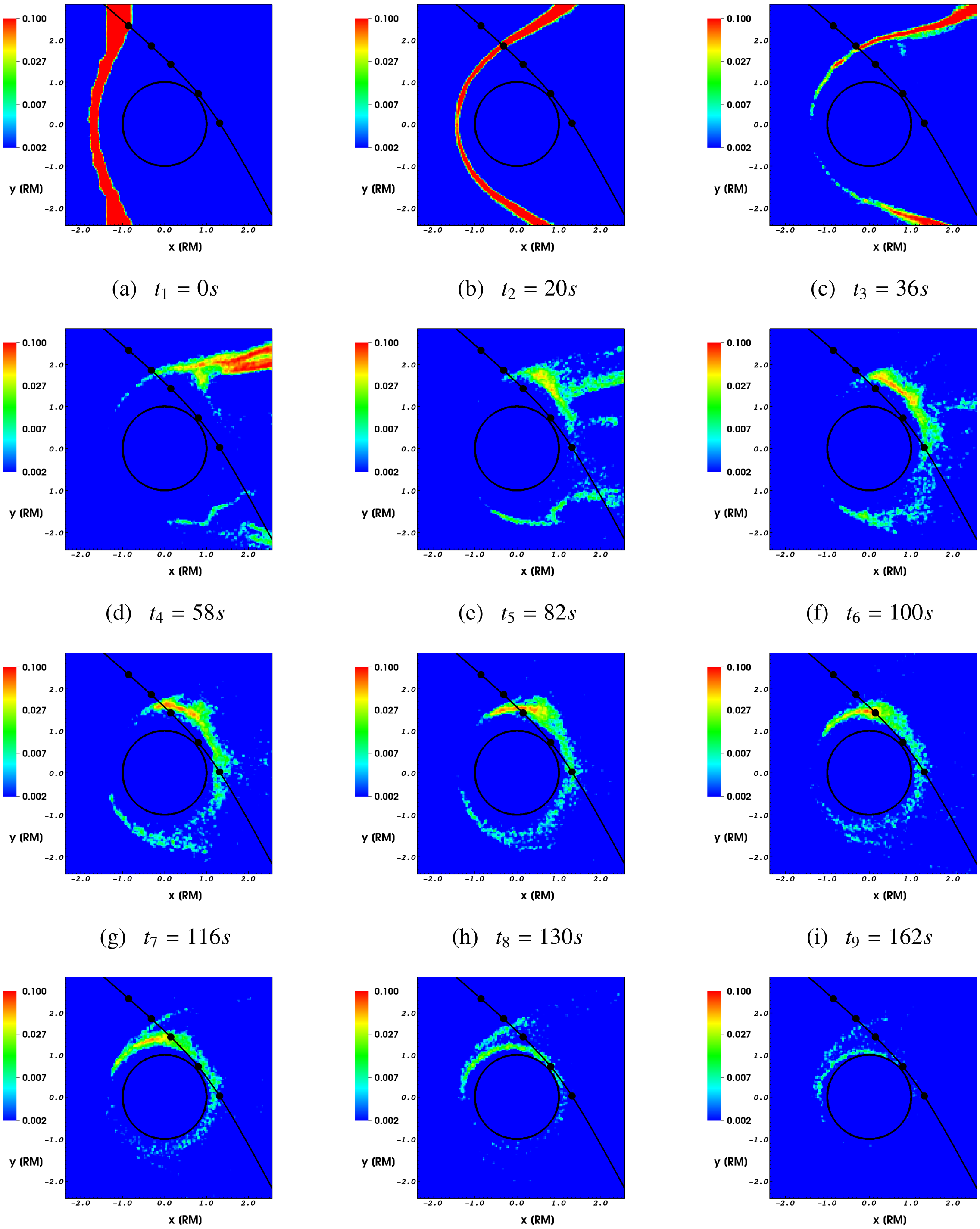

(a) $t_1 = 0s$ (b) $t_2 = 20s$ (c) $t_3 = 36s$

(d) $t_4 = 58s$ (e) $t_5 = 82s$ (f) $t_6 = 100s$

(g) $t_7 = 116s$ (h) $t_8 = 130s$ (i) $t_9 = 162s$

(j) $t_{10} = 192s$ (k) $t_{11} = 290s$ (l) $t_{12} = 436s$

Figure 6.10: The Figure shows a time sequence of solar wind protons that are marked immediately after being injected at the inflow boundary. This time sequence reveals where the solar wind protons enter the Hermean magnetosphere and how the boundary layer is populated.

magnetosphere in regions of exactly such open field lines. The yellow arrow indicates the direction of motion that is planet-ward. The entire process can be observed best by means of animations that are available at:
http://www.tu-braunschweig.de/theophys/people/jmueller/aikef/mercurybl

However, additional mechanisms may likewise promote the entrance of solar wind particles into the Hermean magnetosphere, such as the protons' gyro-kinetic motion as predicted by Trávníček et al. (2007, 2010). Another prominent candidate to transfer solar wind plasma into the Hermean magnetosphere might be the Kelvin Helmholtz instability, which most likely is excited at Mercury's magnetospheric flanks (Glassmeier and Espley 2006). As pointed out by Sundberg et al. (2010), Mercury's dawn magnetospheric flank is shown to be less stable than the dusk flank. This could explain the asymmetric entrance of solar wind protons into the magnetosphere as observed in our simulation in Figure 6.10.

After having shown that solar wind protons may enter Mercury's magnetosphere at the downstream dawn flank we shall explain why they drift planet-ward rather than downstream. At the dawn flank the neutral sheet current is present that flows from dawn to dusk, i.e. basically in negative y-direction. However, it exhibits a positive x-component as well. For clarification this configuration is sketched in Figure 6.13(c) by means of magenta arrows. In consequence, protons experience a Lorentz force that is:

$$\underline{F} = q_p \left(\underline{E} + \underline{v}_p \times \underline{B} \right) \quad , \tag{6.1}$$

where the electric field for a proton plasma in the hybrid approximation reads:

$$\underline{E} = -\underline{u}_p \times \underline{B} + \frac{\underline{j} \times \underline{B}}{\mu_0 e n_p} - \frac{\nabla p_e}{\mu_0 e n_p} \quad , \tag{6.2}$$

where $\underline{u}_p$ is the mean proton velocity, n_p the mean proton density and p_e the electron pressure. According to our simulations the electron pressure gradient within the neutral sheet is significantly smaller than the Hall term and may be neglected in the following. If we furthermore consider the drift direction of the particles to resemble the local bulk velocity (ie. fluid behavior) we can assume $\underline{v}_p \approx \underline{u}_p$. The resulting force on the guiding center of solar wind protons then reads:

$$\underline{F} = \frac{\underline{j} \times \underline{B}}{\mu_0 n_p} \quad , \tag{6.3}$$

which is the $\underline{j} \times \underline{B}$ force known from MHD.

As the magnetic field in this region exhibits a positive z component (yellow circles in 6.13(c)), the resulting force points in negative x and negative y direction (red arrows). Hence, protons are accelerated sunward and towards the planet. Plots 6.10(d) to 6.10(f) show that the particle population splits up as it approaches Mercury: The larger fraction moves in negative x-direction populating the D-BL. The smaller fraction propagates in negative y direction populating the N-BL and finally re-unites with plasma at the dusk flank of the magnetopause. We shall point out that the sequence described above indicates that D-BL and N-BL are part of the same boundary layer that extends from Mercury's

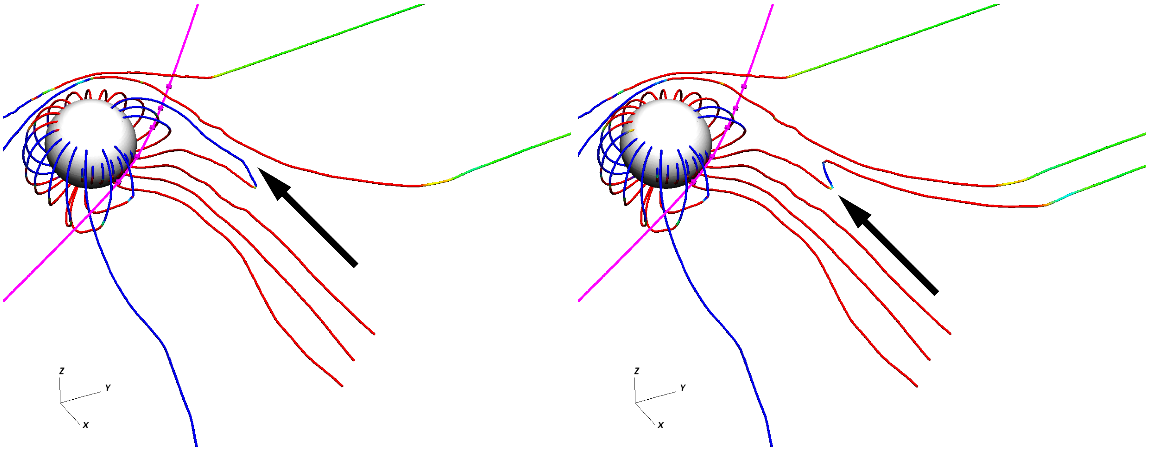

(a) anti-parallel planetary and IMF field lines

(b) planetary field line reconnecting to the IMF

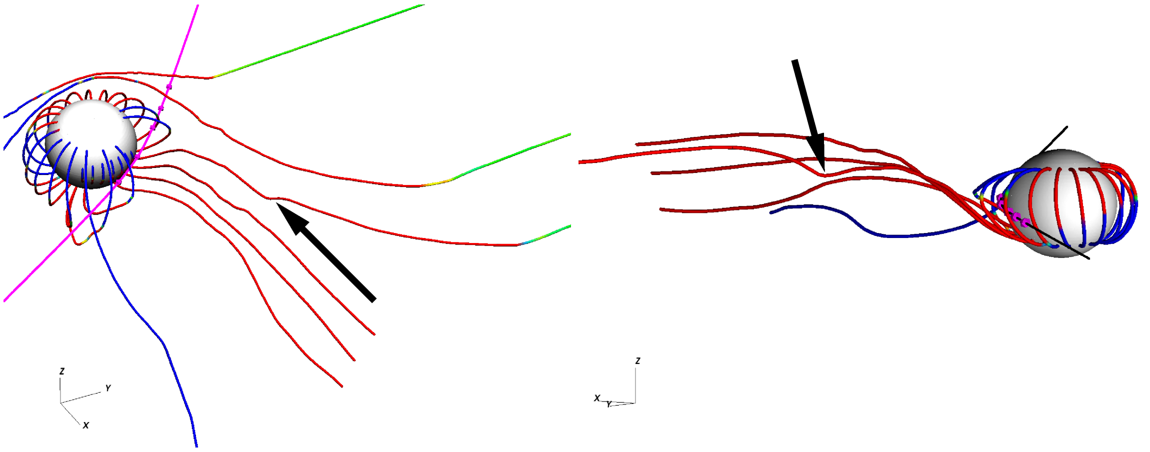

(c) planetary field line connected to the IMF

(d) same field as in (b), view from dawn side

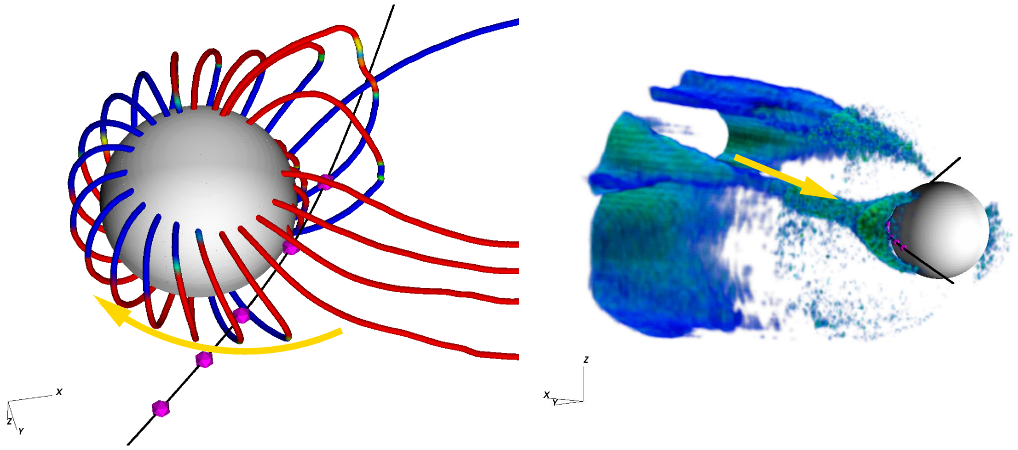

(e) same field as in (b), view from south pole

(f) proton motion along open field lines

Figure 6.11: Shown are magnetic field lines that originate from Mercury and the solar wind. The M1 trajectory is the magenta line. The color indicates the B_x component: blue is negative ie. pointing sun ward, red is positive i.e. pointing downstream and green indicates zero. As the draped IMF exhibits a positive B_x component at Mercury’s dawn side, IMF and closed field lines are directed antiparallel in this region (see (a), black arrow). This topology is likely to trigger reconnection (b) and Mercury’s magnetic field lines may connect to the solar wind (c). Protons that enter Mercury’s magnetosphere along such open field lines will arrive at the poles. Subsequently, they are trapped on closed planetary field lines thereby populating the boundary layer (f).

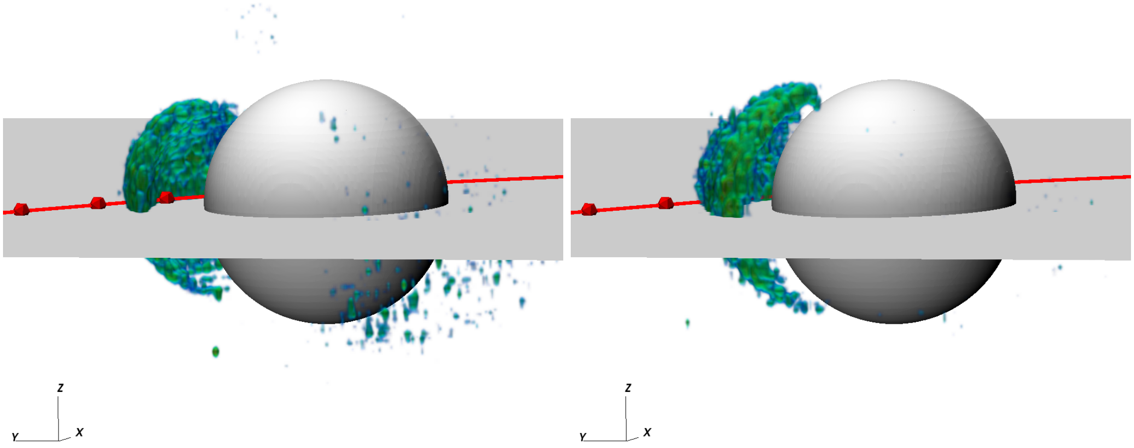

(a) $t_8 = 130s$ (b) $t_9 = 162s$

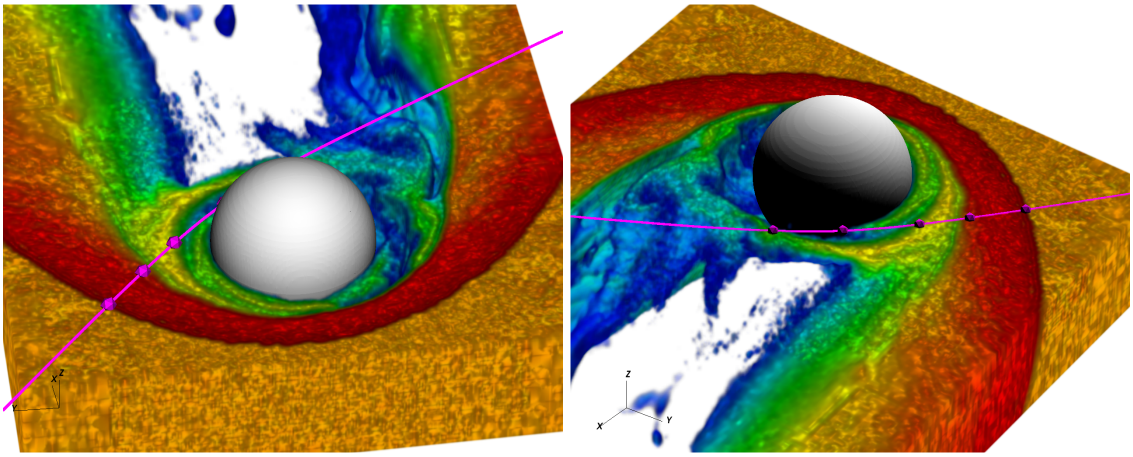

(c) **total density - front view** (d) **total density - back view**

Figure 6.12: Three dimensional view on the ions that populate the boundary layer at times $t_8 = 130s$ in (a) and $t_9 = 162s$ in (b). Mercury is illustrated by means of the white sphere. Also shown is the MESSENGER trajectory where the dots indicate from left to right outbound BS, MP and inner edge of the D-BL. The protons move in sun-ward direction but remain inside the DB-L. The number of protons that arrive inside the inner magnetosphere i.e. below the DB-L's inner edge is negligible. Images (c) and (d) show the total plasma density in front and back view, respectively. A logarithmic color scale is used. The yellow boundary layer region can be clearly distinguished from the red magnetosheath and green inner magnetosphere. Animations are available online at: *www.tu-braunschweig.de/theophys/people/jmueller*

dawn-dayside over the nightside to the dusk-dayside.

The sequence of Figures 6.10(f) to (i) shows how the proton population slowly drifts through the D-BL in sun-ward direction. By comparing Figures 6.10(f) and 6.10(i) the drift velocity of the ions at the BL's inner edge can be estimated to $\mathrm{v_{drift}} = 1.2\mathrm{R_M}/62\mathrm{s}$

$\approx 50km/s$. The density's maximum is close to the boundary layer's inner edge. Figures 6.12(a) and (b) reveal that the motion must be considered 3-dimensional: While drifting through the boundary layer the protons are mirrored between north and south pole on closed magnetic field lines. Hence, the boundary layer itself is a three dimensional region. As sketched in Figure 6.13(a) that shows an enlarged view on the boundary layer, the proton gyration coincides with the equatorial plane.

Furthermore, the time sequence Figure 6.10 reveals that only a negligible fraction of the protons enters the inner magnetosphere. The inner magnetosphere is mainly devoid of protons (also sketched in 6.13(a)). One reason for this behavior is that solar wind protons mainly arrive at high latitudes at the poles before being trapped on closed field lines. Neighboring closed field lines extend to an altitude of about $0.4R_M$ above Mercury's surface in the equatorial cross-section (see Figure 6.11(e)). Hence, protons that enter these closed field lines near the poles will not underrun an altitude of $0.4R_M$ while bouncing from pole to pole and drifting sunward. This drift motion is indicated by means of an yellow arrow in 6.11(e).

However, protons still could drift planet-ward due to an $\underline{j} \times \underline{B}$-force as stated to be the case near the magnetospheric flank. A $\underline{j} \times \underline{B}$-force exist at the boundary layer's inner edge indeed but is oppositely directed: As sketched in Figure 6.13(c) by means of green arrows and shown in the simulation results in Figures 6.7(c)/(d), a current forms at the inner edge of the dayside boundary layer at about $0.4R_M$ above Mercury's surface. This current is directed sunward. As the magnetic field in this region strictly points in positive z-direction (yellow circles in sketch 6.13(c)), the resulting $\underline{j}\times\underline{B}$-force is directed outwards in positive y-direction (light blue arrows) thereby hindering protons from entering the inner magnetosphere. This configuration sustains and enhances the devoid state of the inner magnetosphere and explains the rather steep density decay that can be observed in Figure 6.9(b) at the D-BL's inner edge.

More than 3 minutes after entrance into the D-BL the proton population arrives close to the sub-solar point. The drift velocity is nearly reduced to stagnation. Several ions that are close to the magnetopause are picked up and convected downstream, thereby completing their 4 minute-visit in the Hermean magnetopause (see Figure 6.10(k)). The drift velocity of other ions is reversed and they drift back downstream again into the inner magnetosphere while their altitude is constantly decreased until they finally impact on Mercury's surface. At $t_{12} = 436s$, i.e. about 5.5 minutes after the population had reached the boundary layer, the density is reduced to less 1% of the initial density and can be considered negligible. During the same time protons with background solar wind speed would have passed a distance of 60 R_M.

From the three-dimensional view in Figures 6.12(a)/(b) it can be well seen that the location of the marked particles coincides with the location of the boundary layer that is visible in the total plasma density in Figures 6.12(c) and (d), i.e. the yellow layer that resides in between the magnetosheath (red) and inner magnetosphere (green). Animations for both, the marked and total density are available online at:
www.tu-braunschweig.de/theophys/people/jmueller

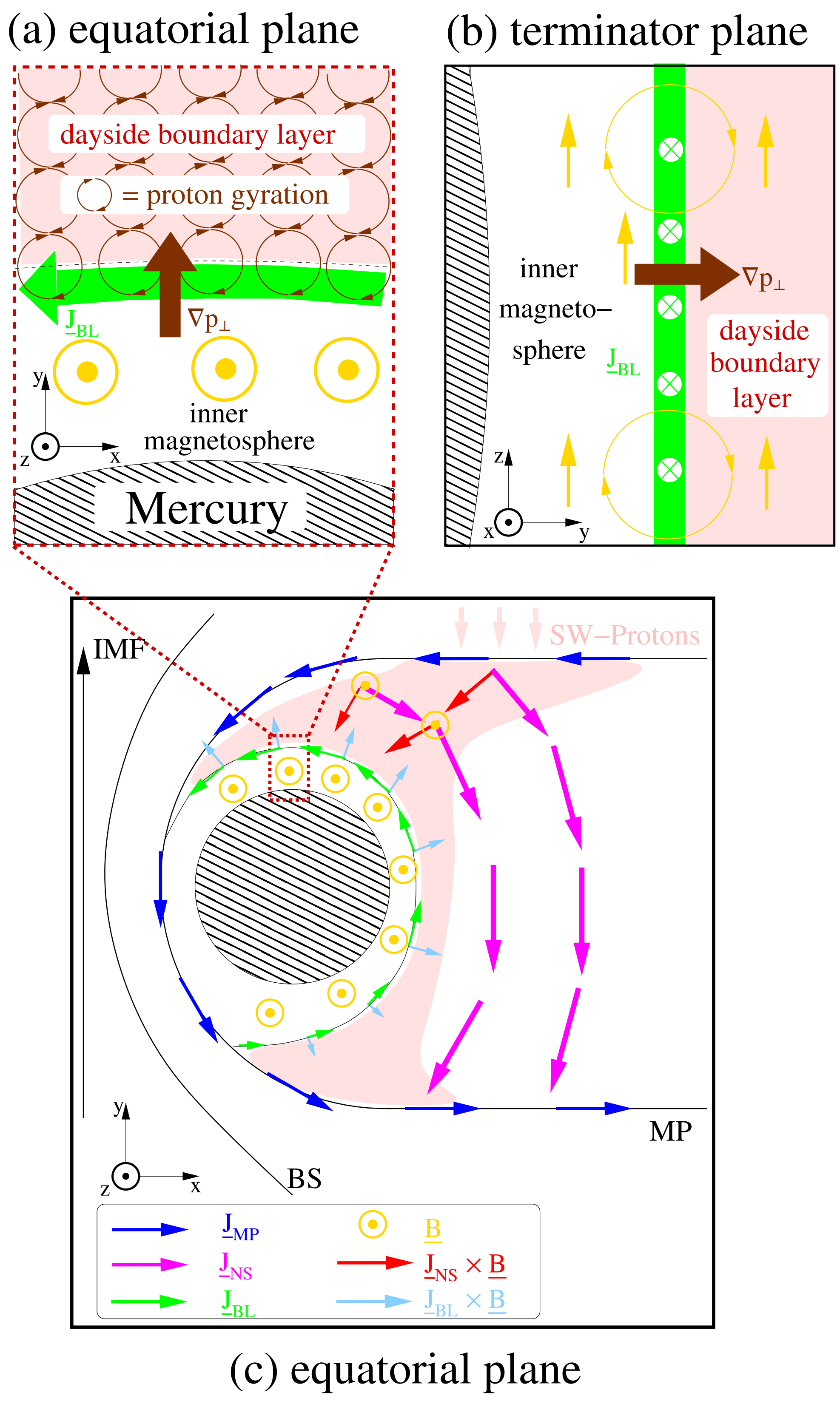

Figure 6.13: The sketch (c) illustrates the locations of several current layers. The enlarged view (a) explains the origin of the bondary-layer-current by means of the proton gyration. Sketch (b) shows that the magnetic field related to the boundary-layer-current.

6.6.2 Proton Trajectories

In order to clarify the kinetic motion of the protons, the trajectories of three representative protons that enter the boundary layer are shown in Figure 6.14. While the particles **A** and **B** impact on Mercury's surface, particle **C** may escape the Hermean magnetosphere after having crossed the boundary layer.

Figure 6.14 is arranged such that the left column illustrates the top view of the trajectories (from above Mercury's north pole) while the right column shows the trajectories from the dawn side. Mercury is shown by means of a white sphere, the M1 trajectory is visualized in magenta and the positions of BS, MP, D-BL, C/A and N-BL are marked by means of small magenta spheres from top to button. The z=const cross-section shows the color-coded magnetic field. The particle trajectories are colored in black. In addition closed magnetic field lines are shown.

Particle **A** in Figures 6.14(a)/(b) enters the magnetosheath in the sub-solar region, is subsequently deflected along the dawn-side magnetopause but enters the magnetosphere downstream at $x = 1.7R_M$. As was shown in sketch 6.13(c) by means of red arrows, it experiences a $\underline{j} \times \underline{B}$- force in this region that is directed planet-ward. The particle drifts towards Mercury and is trapped on closed magnetic field lines. While it is trapped inside the magnetic mirror configuration and bounces between north and south pole, it slowly drifts in sun-ward direction. Again we shall point out that this drift is neither a gradient nor a curvature drift which firstly is negligible in terms of magnitude and secondly would cause the particles to drift clockwise within the D-BL region, which is the contrary direction. Particles like particle **A** account for the sun-ward plasma motion that was shown by means of the macroscopic density in the previous section (see Figure 6.10). In the equatorial cross-section it stays off from Mercury's surface at a distance of about $0.4R_M$, i.e. at the inner edge of the boundary layer. The magnetic field increases as it drifts further in sub-solar direction. Hence, while the gyro-frequency increases the gyro-radius decreases and the mirror points move to lower latitudes since they depend on the particles pitch angle.

If the particle's magnetic moment is conserved, the motion into regions of increased field strength goes along with a gain in perpendicular energy. This process is referred to as "adiabatic heating", i.e. drift energy is converted into perpendicular energy. As a consequence the perpendicular temperature increases while the parallel energy and temperature remain unaffected. This conclusion is in agreement with the temperature profile in Figures 6.9(e)/(f) where the perpendicular temperature increases inside the D-BL and experiences a local maximum at the D-BL's inner edge. In contrast to this the parallel temperature remains unaffected and is hardly showing any change, neither inside the D-BL nor at its inner edge. Another reason for a strong temperature asymmetry could arise as argued by Trávníček et al. (2009), who observed a significantly increased perpendicular temperature near Mercury as well: the mirror points of protons that are heated parallel to the magnetic field may be located below Mercury's surface. As a consequence, these protons will be lost by impacting on the planetary surface. In contrast, an increased perpendicular velocity enhances the proton's pitch angle and thus the probability to be trapped without impact.

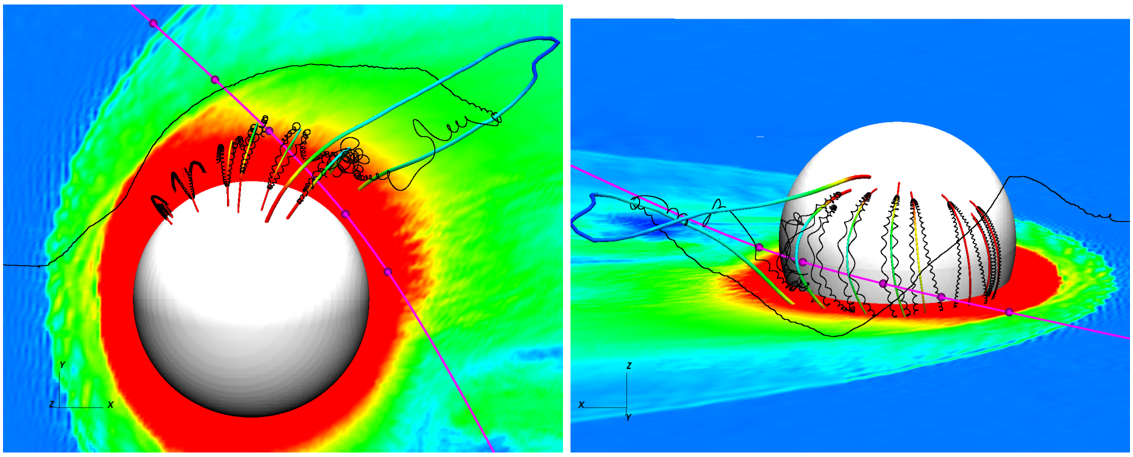

(a) **particle A - top view** (b) **particle A - side view**

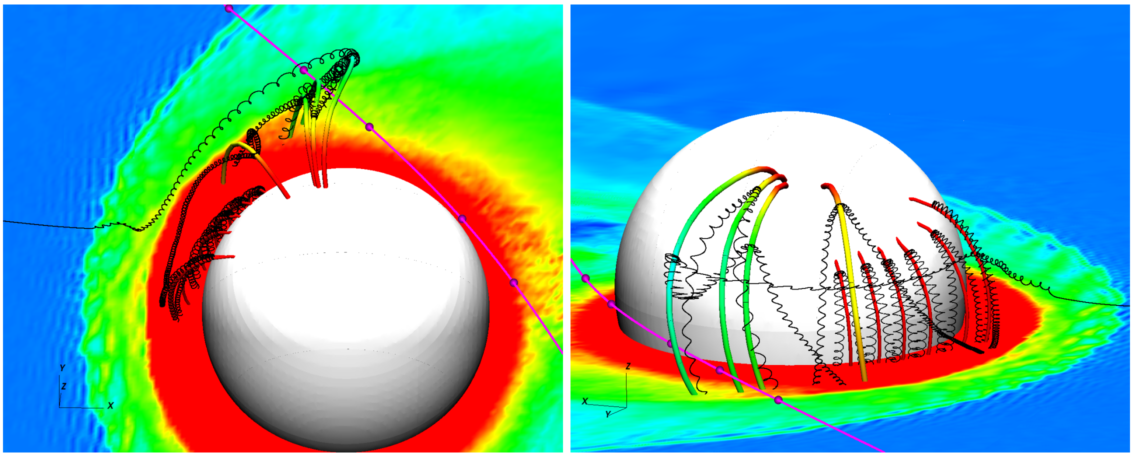

(c) **particle B - top view** (d) **particle B - side view**

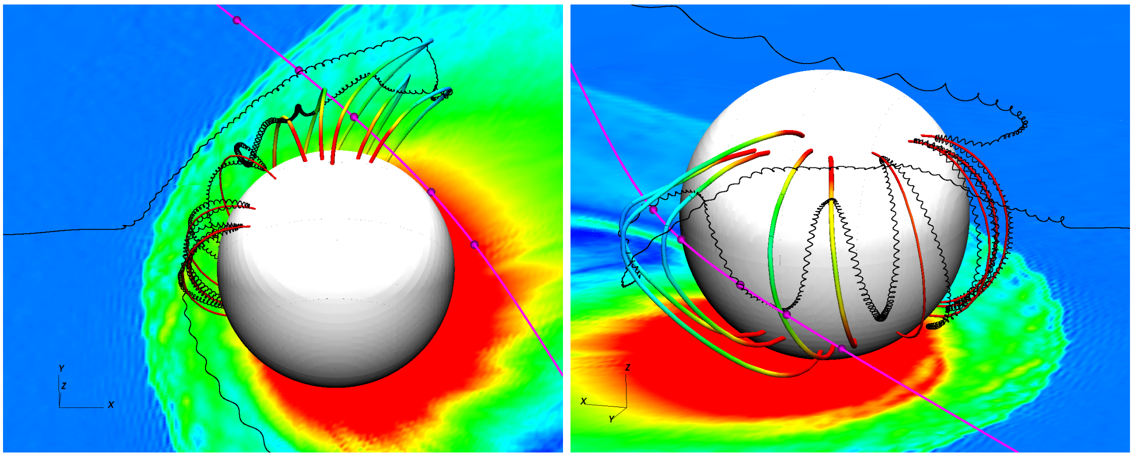

(e) **particle C - top view** (f) **particle C - side view**

Figure 6.14: The Figure is arranged such that the left column illustrates the particle trajectories by means of a top view (from above Mercury's north pole) while the right column shows the trajectories from the dawnside view. The top row illustrates the trajectory of particle **A**, the second particle **B** and the third row particle **C**. See text for details.

The second particle **B** in Figures 6.14(c)/(d) enters the magnetosphere further upstream compared to particle **A**. It is accelerate sun-ward and traverses the D-BL at higher initial altitudes than **A**. Simultaneously its altitude continuously decreases. Its guiding center motion is reversed near the sub-solar point and for a short time the particle drifts downstream again before it finally impacts on the planetary surface. A close view on the density in Figures 6.9(a)/(b) reveals that this type of particle is responsible for the small density enhancement observed at 19:08 UTC.

The third particle **C** that is shown in Figures 6.14(e)/(f) enters Mercury's magnetosphere downstream at about 1 R_M. Like particle **B** it traverses the D-BL at rather high altitudes. Its guiding center motion is decelerated while it drifts in sun-ward direction. However, in contrast to particle **B** its drift velocity is not reversed in the sub-solar region. Instead, it is reflected at high latitudes and may escape the Hermean magnetosphere into the dusk magnetosheath where it is picked up and convected downstream. We could observe many particles that are picked up into the dawn magnetosphere as well (not shown here). This behavior is consistent with the macroscopic density in Figures 6.10(j)-(l).

6.6.3 Origin of the Boundary Layer Current

So far we have shown the existence of the boundary layer current in Figure 6.7 and have argued that it gives rise to a $\underline{j} \times \underline{B}$-force, preventing solar wind protons from entering the inner magnetosphere (see Figure 6.13(c)). The density decrease in Figure 6.9(a)/(b) is a direct consequence of this force. We will discuss the formation of the boundary layer current below.

A first hint towards the current formation can be observed when comparing the macroscopic particle motion in Figure 6.10 with the macroscopic velocity in Figure 6.8. As was argued above, the sun-ward drift velocity of the ion population was estimated to be $\mathrm{v}_{\mathrm{drift}} \approx 50\mathrm{km/s}$. In contrast to this, Figure 6.8(c) showed the macroscopic ion velocity in sun-ward direction to be about 80 km/s at the boundary layer's inner edge. This might seem conflicting since the average drift velocity of the ion's guiding centers should directly translate into the macroscopic velocity. Hence the the macroscopic velocity appears to be overestimated by $\Delta\mathrm{u} \approx 30\mathrm{km/s}$.

However, the macroscopic velocity includes any particle and fluid drifts, where the latter does not necessarily require guiding center motion. In particular the diamagnetic drift is solely a result of density and temperature gradients of a particle distribution that gyrates with guiding centers at rest:

$$\underline{v}_{dia} = \frac{\underline{B} \times \nabla_\perp p_\perp}{qnB^2} \quad , \tag{6.4}$$

where $p_\perp$, q and n are the perpendicular thermal pressure, charge and number density of the respective particle population. Since the drift direction depends on the sign of charge, the diamagnetic drift of an proton-electron plasma results into the current:

$$\underline{j}_{dia} = \frac{\underline{B} \times \nabla_\perp p_\perp}{B^2} \quad , \tag{6.5}$$

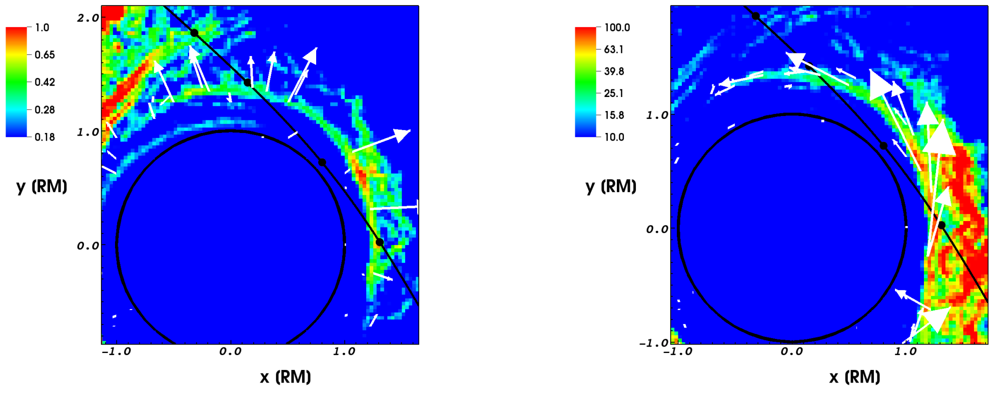

(a) $\nabla_\perp p_\perp$ [] (b) $v_{\text{diamagnetic}}$ **[km/s]**

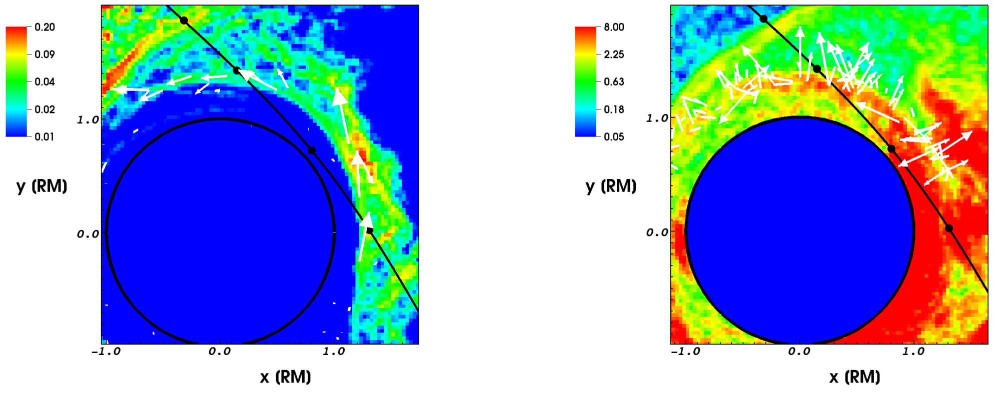

(c) $\underline{J}_{\text{diamagnetic}}$ [μA/m^2] (d) $\underline{E}_{\text{Hall}}$ [mV/m]

Figure 6.15: Shown is the perpendicular gradient of the perpendicular proton pressure (a). As the magnetic field points in z-direction at the location of this pressure gradient, a significant diamagnetic drift velocity results of about 30km/s that is shown in (b). The corresponding diamagnetic current is shown in (c). As the diamagnetic current is perpendicular to the magnetic field as well, this configuration yields a strong Hall electric field pointing radially outward. This field prevents protons from entering the inner magnetosphere and consequently maintains the pressure gradient.

where $p_\perp = p_{\perp h^+} + p_{\perp e^-}$. As was argued above the electron pressure turned out to be negligible as it is at least one order of magnitude smaller than the proton pressure inside the D-BL. Hence, the following analysis will be carried out solely for the proton population.

As was shown in Figure 6.9(c)/(d), the proton pressure experiences a sudden decrease inside the inner magnetosphere at the D-BL's inner edge. Figures 6.9(a) and (e) reveal that this results from the decrease in density and perpendicular temperature. Hence, mainly the perpendicular pressure is affected rather than the parallel pressure. The perpendicular gradient of the perpendicular pressure is shown in Figure 6.15(a). For technical reasons we assume $\nabla_\perp = (\partial_x, \partial_y, 0)$ which can be justified by the observation $B_x \approx B_y \approx 0$ and $B_z \gg 0$ inside the boundary layer region (see Figure 6.6). However, this condition is not met in other regions and the results of Figure 6.15 may be considered valid exclusively inside the boundary layer region. The direction of the respective quantity within the boundary layer region is indicated by means of white arrows.

As has already been stated by Anderson et al. (2011) an outward directed plasma pressure gradient is expected at the D-BL's inner edge in consistency with the change in magnetic field intensity. This conclusion is clearly confirmed by our simulation results, as can be seen in 6.15(a). Since the proton pressure gradient is perpendicular to the magnetic field in this region, this yields a significant proton diamagnetic drift velocity in negative x-direction at the D-BL and positive y-direction at the N-BL, see Figure 6.15(b). In particular the drift velocity at the D-BL is about 30km/s that is superimposed on the guiding center motion. This would explain the deviation between macroscopic velocity and ion motion, as revealed at the beginning of this section.

The current related to the diamagnetic drift is shown in Figure 6.15(c). At the D-BL's inner edge its magnitude can be estimated to about 0.03 - 0.04 μA/m^2, which is consistent with the current at the D-BL that was shown in Figure 6.7. This in turn causes an increased Hall electric field $\underline{E}_{Hall} = \underline{j} \times \underline{B}/\mu_0 e n_p$ that is directed outward (see Figure 6.15(d)), thereby preventing the drifting protons from entering the inner magnetosphere.

For clarification the situation is sketched in the enlarged view on the boundary layer in Figure 6.13(a). While protons populate the boundary layer (pink region) the inner magnetosphere is mainly devoid of protons. This translates into a pressure gradient that is directed outwards (brown arrow). For protons with guiding centers at rest the macroscopic velocity cancels to zero inside the boundary layer. However, Figure 6.13(a) illustrates that this is not valid at the boundary layer's inner edge. The consequence is an enhanced proton velocity in negative x-direction at the boundary layer's inner edge that superimposes with the proton drift motion and is referred to as "diamagnetic drift". This conclusion is in agreement with the simulation results in Figure 6.8(c). As the direction of the diamagnetic drift depends on the rotational direction of the involved gyrating particles, the diamagnetic drift of protons and electrons occurs counterwards (compare equation 6.5). Hence, a current forms that in the case discussed here is the "boundary layer current" which is sketched by means of a green arrow in Figure 6.13(a). The magnetic field which is consistent with the boundary layer current enhances the inner magnetospheric field while it causes the diamagnetic decreases inside the boundary layer (see yellow circles in Figure 6.13(b)).

In summary we conclude that the dayside boundary layer forms by means of the following sequence:

1. Protons enter the Hermean magnetosphere at its downstream flank on open magnetic field lines. They are accelerated planet-wards and their perpendicular energy increases as they move into regions of increased field strength.

2. Most open magnetic field lines connect to the planet at high latitudes, i.e. near the poles.

3. Adjacent closed field lines extent to high altitudes within the equatorial cross sec-

tion.

4. Hence, protons tend to complete their bounce motion at similar altitudes rather than immediately above Mercury's surface.
5. This causes an outward directed density gradient.
6. In combination with the increased perpendicular energy an outward directed perpendicular pressure gradient results.
7. The conjunction of perpendicular pressure gradient and dipole field initiates a diamagnetic current.
8. The conjunction of diamagnetic current and dipole field causes an outward directed $\underline{j} \times \underline{B}$-force.
9. This force enhances the initial state and steepens the pressure gradient as protons are hindered to enter low altitudes, i.e. the inner magnetosphere.
10. Finally a self consistent quasi-stationary state is established with the current being located at about $0.4 R_M$ above Mercury's surface, thereby forming the inner edge of the dayside boundary layer.

Obviously the equatorial altitude of closed magnetic field lines that connect to the poles seems to be an important property. In this regard Mercury's magnetic field very much differs from that of Earth or any other planet within the solar system. From initial test runs that are still in progress we can derive information on the boundary layer's distance to Mercury's surface: As we increase the strength of Mercury's dipole field the size of the inner magnetosphere increases and the boundary layer moves to higher altitudes. This might seem intuitively clear since closed magnetic field lines extend to higher altitudes. Hence, protons complete there bounce motion at higher altitudes.

However, the influence of different core-mantle conductivities might be less intuitive: As can be seen in Figures 6.7(c)/(e), the core-mantle current is directed such that it enhances the inner magnetospheric field. The magnitude of the corresponding generated magnetic field at the equatorial surface is about 13nT and at the D-BL it is still 6nT. The effect is similar to an increased dipole field: closed magnetic field lines extend to higher altitudes as without this field enhancement. As we decrease the core-mantle conductivity the core-mantle current is suppressed. Consequently the inner magnetospheric field diminishes and the boundary layer moves towards Mercury's surface. Hence, current closure through Mercury's interior might play an important role, which has already been proposed by Janhunen and Kallio (2004). However, quantitatively deriving the influence of different core-mantle conductivities or dipole strengths is beyond the scope of this thesis and will be subject to future studies.

7 Magnetopause Passage of Titan

After having studied the solar wind interaction of Mercury's planetary magnetosphere throughout the previous chapters, we now turn to Saturn's largest moon Titan whose plasma interaction is of fundamental difference. We therefore provide a detailed introduction in section 7.1 and substantiate our motivation to model a magnetopause passage which enables the observation of so called "fossil fields". Before deriving the time scale for their life time by means of self-consistent hybrid simulation, a rough analytical estimation is given in section 7.2. Physical and numerical input parameter are shown in section 7.3 and 7.4, respectively. We describe the rather complex simulation geometry in section 7.5 before providing a detailed analysis of the simulation results in section 7.6. All results of this chapter have been published by Müller et al. (2010).

7.1 Field Fossilization in Titan's Ionosphere

Titan, Saturn's largest satellite, orbits its parent body in the outer magnetosphere at a distance of about $20.3 R_S$ (radius of Saturn: $R_S = 60268\,\mathrm{km}$). Since Titan does not possess a noteworthy intrinsic magnetic field (Ness et al. 1982, Neubauer et al. 1984, Backes et al. 2005), the moon's atmosphere and ionosphere are directly exposed to the at least partially corotating magnetospheric plasma. The resulting plasma interaction process is to some extent analogous to the situation at Venus, Mars or comets. Of course, due to the submagnetosonic speed of the magnetospheric plasma, no bow shock is formed in front of Titan. However, the magnetic field lines are strongly draped around the obstacle, giving rise to a magnetic pile-up region at Titan's ramside and a bipolar induced magnetotail in the wake region. Newly generated ionospheric particles are picked up by the ambient magnetospheric fields, with their gyroradii exceeding the radius of Titan ($R_T = 2575\,\mathrm{km}$) by a large factor (see e.g. Simon et al. (2007) for details). The large gyroradii of the involved ion species yield a pronounced asymmetry of the interaction region with respect to the direction of the convective electric field (see e.g. Simon et al. (2006b), Luhmann (1996), Wahlund et al. (2005) for details).

In the past years, a large number of numerical models have been applied to study Titan's interaction with Saturn's magnetospheric plasma. While single-fluid magnetohydrodynamic codes (e.g. Nagy et al. (2001), Ma et al. (2006)) are able to account for complex chemical processes in the moon's ionosphere, they do not include effects associated with the large gyroradii of the involved pick-up species, such as non-Maxwellian distribution functions or velocity differences between light and heavy plasma constituents. On the other hand, hybrid codes are able to cover these effects in a self-consistent way (cf. Brecht et al. (2000), Kallio et al. (2004), Modolo and Chanteur (2008), Simon and Motschmann (2009) and references therein). However, the grid resolution applied by the hybrid models has so far been too coarse to provide a sophisticated description of ionospheric processes, such as ion-neutral collisions. A compromise between hybrid and magnetohydrodynamic (MHD) codes is represented by the multi-fluid approximation of Snowden et al. (2007) and Winglee et al. (2009).

Apart from its proximity to Saturn's warped and highly dynamic magnetodisk current sheet (Arridge et al. 2008, Bertucci et al. 2009), a major source of variability in Titan's plasma environment is its proximity to Saturn's magnetopause. As reported by Achilleos et al. (2008), the average stand-off distance ranges between $22R_S$ and $27R_S$. However, when the magnetosphere is compressed during times of high solar wind dynamic pressure, Titan might be able to leave the magnetosphere near local noon and enter the hot, dense plasma in Saturn's magnetosheath. The first in-situ observations of such a scenario were made during the T32 encounter on 13 June 2007 (Bertucci et al. 2008). A passage from the magnetosphere into the magnetosheath typically goes along with a significant change in the ambient plasma and magnetic field conditions near Titan. During T32, the magnetic fields inside and outside the magnetosphere were found to be nearly antiparallel. Plasma density, temperature and composition also changed drastically during the pass (Coates et al. 2007, Garnier et al. 2009).

As suggested by Neubauer et al. (2006), this kind of variability in the ambient magnetic field conditions leaves a long-time imprint in Titan's ionosphere. Below altitudes of 1600 km, the plasma mainly consists of a dense and slow heavy ion population with a bulk speed of only a few 100 m/s. This value is about three orders of magnitude smaller than the speed at which the rotating magnetospheric plasma impinges on Titan's ionosphere (Neubauer et al. 1984). These small flow speeds yield a drastic increase in the convection times of magnetic flux tubes through the near-Titan region: The findings of Neubauer et al. (2006) imply that a flux tube which has entered the near-Titan region may remain trapped there for about several hours. In other words, even after a strong change in the ambient magnetic field conditions near Titan (e.g. due to a magnetopause passage or current sheet oscillations (Arridge et al. 2007, Khurana et al. 2009)), magnetic flux tubes "collected" in previously encountered field regimes may still be present in Titan's ionosphere. Neubauer et al. (2006) refer to these trapped magnetic field lines as *fossil fields*. These authors suggest that fossil magnetic fields may be responsible for discrepancies between Cassini magnetometer data (Dougherty et al. 2004) and results from their global MHD model for the first series of Titan encounters in 2004 and early 2005 of Cassini's first Titan encounter in 2004 (see also Backes et al. (2005) and Backes (2005)). We shall point out that fossil magnetic fields should be detectable at any obstacle that is surrounded by slow heavy ion plasma and exposed to varying upstream conditions. For instance Raeder et al. (1987) did observe layers of opposite magnetic field polarity inside the pile up region of comet P/Halley. These layers arose from IMF field reversals that had been convected into the pile up region and had not been destroyed by diffusial effects nor magnetic field reconnection.

The first in-situ confirmation for the existence of fossil magnetic fields at Titan was made possible through magnetometer data collected during the T32 flyby. During this encounter, Cassini crossed to a bundle of trapped magnetic field lines that had been carried from Saturn's magnetosphere into the magnetosheath only a few minutes before closest approach (Bertucci et al. 2008). Recently, Wei et al. (2009) suggested that Titan itself may exert a certain level of control on the position of Saturn's magnetopause. Near noon, the magnetopause seems to be more frequently located inside Titan's orbit with the moon absent than with it present. Wei et al. (2009) suggest that due to mass-loading at Titan the total pressure may locally be enhanced which would reduce the magnetospheric compressibility (see also Glassmeier et al. (2004)).

The purpose of this study is to investigate the characteristic time scales upon which Titan's plasma environment is reconfigured during a magnetopause passage. Especially, we are interested in the lifetime of fossil fields after a change in the ambient magnetic field conditions. Our study is based on a newly developed hybrid simulation model.

So far, only very few codes have been applied to study Titan's plasma interaction in a non-stationary magnetic environment. Simon et al. (2008) carried out a real-time simulation study of Titan's plasma interaction when a simple periodic distortion is imposed on the background electromagnetic fields. They found that to a certain degree, the moon's pick-up tail can shield itself against the ambient field perturbations. These authors also investigated the dynamics of the pick-up tail during a magnetopause passage and found that crossing the tangential discontinuity does not go along with a detachment of the pick-up tail from the satellite. Applications of this real-time model to the T32 magnetosheath excursion and to Titan's plasma interaction during an entry into the supersonic solar wind have been presented in two subsequent works (Simon et al. 2009a, Simon 2009). It has been shown that during a reversal of the ambient magnetic field, the large-scale structure of Titan's induced magnetotail is reconfigured due to reconnection, with the characteristic time scale being prescribed by the convection time of the plasma flow through the interaction region. In this model, the tail reconfiguration is completed within a time window of about 10 minutes.

However, the grid resolution in the Simon et al. (2009a) model was too coarse and numerical diffusion too large to resolve any fossil fields trapped in the ionosphere, i.e. only the rather short reconfiguration of the large-scale features of the magnetotail was reproduced. So far, the only numerical model that could reproduce fossil magnetic field signatures in Titan's ionosphere is the MHD code applied by Ma et al. (2009). In Titan's ionosphere, this model achieves a mesh spacing of 0.01 R_T, which is about a factor of 10 smaller than the resolution reached in the preceding hybrid simulation studies. Ma et al. (2009) predict the lifetime of trapped magnetic fields in Titan's ionosphere to be of the order of $2 - 3$ h. However, the Ma et al. (2009) model does not contain a realistic description of magnetic field diffusion through Titan's interior. It is not clear to what degree the lifetime of fossil magnetic field lines is affected by the inner boundary condition in their model. Furthermore, the approach by Ma et al. (2009) cannot consider the large-scale asymmetry of the interaction region due to ion kinetic effects nor the strong velocity shear between magnetospheric upstream plasma and slow ionospheric pick-up ions. For this reason, the model predictions for the dynamics of the pick-up tail are in contradiction to the hybrid model by

Simon et al. (2009a): the MHD results show a tail detachment during the passage through the discontinuity, whereas the hybrid results suggest the tail to remain connected to the moon.

Our study intends to fill the following gaps in our understanding of fossil magnetic field signatures at Titan:

- The grid resolution in the hybrid code developed for this study is comparable to the resolution in preceding MHD studies of Titan's plasma interaction. Thus, for the first time, a self-consistent description of the important ion kinetic effects and a high-resolution ionosphere region are combined within the same model.

- In contrast to any other existing global simulation code, our model permits a self-consistent computation of the magnetic fields in Titan's interior. Therefore, we can separate the influence of long convection times in the ionosphere on the lifetime of fossil magnetic fields from the impact of possible induction effects inside the moon's interior.

- The previous models of Titan's plasma interaction during a magnetopause passage did not consider a realistic flow geometry, since the bulk speed $\underline{u}_0$ of the ambient plasma was assumed to point in the same direction during the entire duration of the real-time simulation. More important, the bulk speed was aligned with the speed of the magnetopause. In contrast to this, our newly developed model permits the inclusion of different flow speeds on both sides of the tangential discontinuity.

7.2 Time Scales for the Survival of Fossil Magnetic Fields

The magnetic memory effect arises from low plasma convection speeds in the dense ionospheric heavy ion plasma and a sufficiently large electric conductivity, allowing strong coupling between flow and magnetic field. In such a situation magnetic diffusion is a minor effect only. The conductivity must be sufficiently large to keep the plasma and the magnetic field lines from decoupling, i.e. to prevent diffusion from becoming the predominant process. According to earlier simulation studies (e.g. Simon et al. (2007), Neubauer et al. (2006)), the plasma flow speed drops to values of a few 100 m/s below altitudes of $h_1 = 1600\,\mathrm{km}$. For the following scaling, we consider the fossil field region to be bounded by two concentric spheres, with the upper one being located at the altitude h_1. The lower boundary of the fossil field region is located at an altitude h_2 where collisions start to become dominant, i.e. the conductivity decreases and the magnetic field lines remain no longer connected to plasma motion. In a collision-dominated plasma, the Hall conductivity vanishes, whereas the Pedersen conductivity becomes equal to the parallel conductivity. As recently shown by Rosenqvist et al. (2009) and Garnier et al. (2009), this typically happens below altitudes of $h_2 = 800\,\mathrm{km}$. In order to pass from the upper to the lower sphere, a convection time of the order of

$$T_1 \approx \frac{800\,\mathrm{km}}{0.1\,\mathrm{km/s}} = 8 \cdot 10^4\,\mathrm{s} \tag{7.1}$$

is required when the convection speed is entirely radial directed. Since in general the velocity is not directed radially, the estimated time must be regarded as a lower limit. Within the region between h_1 and h_2, the plasma conductivity is always larger than $\sigma = 10^{-2}\,\mathrm{S/m}$ (Garnier et al. 2009, Rosenqvist et al. 2009). Thus, a lower limit for the magnetic diffusion time is given by

$$T_2 \approx \mu_0 \sigma (h_1 - h_2)^2 \approx 10^{-6} \cdot 10^{-2} \cdot \left(10^6\right)^2\,\mathrm{s} \approx 10^4\,\mathrm{s} \quad . \tag{7.2}$$

Hence, in the region where the magnetic memory effect will occur, magnetic convection and diffusion times are of the same order. If the conductivity in this region is larger than $10^{-2}\,\mathrm{S/m}$ by at least by one order of magnitude, the convection time scale is clearly exceeded by the diffusion scale.

However, it is important to notice that the magnetic diffusion time cannot become significantly smaller than the convection times. Otherwise, the motion of the magnetic field lines would no longer be governed by convection, i.e. the field lines could decouple from the slow heavy ion plasma and their velocity would no longer be prescribed by the speed of the slow ion population in Titan's plasma mantle. The above scaling suggests that the lifetimes of fossil magnetic fields should be of the order of 10^4 s, i.e. they should not survive longer than a few hours.

7.3 Physical Parameters

In our model, most of the ambient plasma parameters inside Saturn's magnetosphere correspond to the "classical" upstream conditions for the Titan interaction deduced after the Voyager 1 flyby in 1980 (Neubauer et al. 1984) which are still frequently applied in the Cassini era (e.g. Kallio et al. (2004), Ma et al. (2006), Simon and Motschmann (2009)). The magnetospheric and magnetosheath plasma quantities are listed in Table 7.1. The bulk speed of the impinging magnetospheric flow is assumed at $u_0 = 120\,\mathrm{km/s}$, thereby yielding a superalfvenic, yet subsonic and submagnetosonic upstream situation.

Previous modeling attempts of Titan's plasma environment under non-stationary upstream conditions clearly showed that –as long as the total ram pressure is not altered– the mass of the impinging ion species does not play a noteworthy role for the reconfiguration process (Simon et al. 2009b, Ma et al. 2009). In order to keep the simulation geometry as simple as possible, we therefore assume the particle mass, number density and temperature in Saturn's magnetosheath to be the same as inside the magnetosphere.

Titan's dayside ionosphere is assumed to be generated mainly by solar UV radiation. In analogy to our preceding simulation studies, the applied dayside ionosphere model

Parameter	Magnetosphere	Magnetosheath
Magnetic field $\underline{B}_0$	$-(0, 0, 8\,\text{nT})$	$+(0, 0, 8\,\text{nT})$
Plasma velocity $\underline{u}_0$	$+(120\,\text{km/s}, 0, 0)$	$-(120\,\text{km/s}, 0, 0)$
Plasma density n_0	$0.2\,\text{cm}^{-3}$	$0.2\,\text{cm}^{-3}$
Ion Mass m_i	14 amu	14 amu
Ion beta β_i	1.88	1.88
Electron beta β_e	0	0
Ion gyroradius (N^+) r_g	2193.1 km	2193.1 km
Alfven velocity V_A	104.3 km/s	104.3 km/s
Alfvenic Mach number M_A	1.15	1.15
Sonic Mach number M_S	0.84	0.84
Magnetosonic Mach number M_{MS}	0.68	0.68

Table 7.1: Upstream plasma parameters for the magnetospheric and magnetosheath plasma.

considers functional dependency on both the altitude above Titan's surface and the solar zenith angle. The nightside ion production profile contains only a dependency on the altitude above the surface (see e.g. Simon et al. (2006b) for details). The model considers three ionospheric species of representative masses: molecular nitrogen (N_2^+), methane (CH_4^+) and molecular hydrogen (H_2^+), with the production rate for each of them being set to $2 \cdot 10^{25}\,\text{s}^{-1}$.

Like Ma et al. (2009), we set the inner boundary to 750 km above Titan. Both the inner boundary and Titan are marked by means of black circles within our simulation results in section 7.6. Particles hitting the inner boundary are removed from the simulation. However, unlike any other existing hybrid model of moon-magnetosphere interactions, we do not impose any boundary condition on the electromagnetic fields in the interior of Titan. The electromagnetic fields below the outer boundary are computed in a self-consistent way from Maxwell's equations and Ohm's law for a conductor: since no particles can penetrate into the moon, the computed plasma velocity is zero. The electromagnetic fields inside the moon are exclusively propagated by means of diffusion depending on the conductivity, which we assume to be $1 \cdot 10^{-2} S/m$ for both simulations, as argued in section 7.2. Therefore, the diffusion of magnetic field lines through Titan's interior is not falsified by artificial boundary conditions imposed on the fields. This technique has already been successfully applied to study the plasma interactions of Rhea (Roussos et al. 2008), Tethys (Simon et al. 2009b) and Enceladus (Kriegel et al. 2009).

7.4 Numerical Parameters

The A.I.K.E.F. simulation code supports numerical meshes that are adaptive in both, space and time. However, since we are in particular interested in resolving the immediate vicinity of Titan in order to investigate field fossilization, we apply a numerical mesh that is adaptive in space but static in time. The mesh operates on four levels of refinement:

parameter	symbol	normalized value	si value
mesh spacing L_0	Δ_{L0}	$0.47r_g$	1031km
mesh spacing L_3	Δ_{L3}	$0.059r_g$	129km
time step particle	$\Delta_{t,particle}$	$3 \cdot 10^{-3}\Omega_{N^+}^{-1}$	$5 \cdot 10^{-2}s$
time step BField	$\Delta_{t,BField}$	$6.8e^{-5}\Omega_{N^+}^{-1}$	$10^{-3}s$
macro-particle / cell	MPiC	120	/

Table 7.2: Numerical parameters that have been used in both simulations, (A) and (B). For a detailed discussion see section 7.4

$L_0 \ldots L_3$. Using adaptivity in time, e.g. to trace the reconfiguring heavy ion tail, is possible yet not required: Even in the coarsest level of refinement (L_0) the resolution is as high as $\Delta_{L0} = 0.47r_g$ where $r_g = u_0 m_{N^+}/eB = 2193$km is the gyro radius of the upstream species (N^+). Hence the kinetics of the heaviest ion species N_2^+ that dominates the tail reconfiguration process (see section 7.6) is clearly resolved as well. Also the width of a cycloidal arc $r_{cg} = 2\pi r_g$ that dominate the ion pick-up motion are resolved at even higher accuracy. The resolution in the highest level of refinement is $\Delta_{L3} = \Delta_{L0}/2^3 = 0.059r_g = 129.5$km, i.e. the distance between adjacent mesh nodes is 17 times smaller than the gyro radius of the upstream species and even 212 times smaller than a cycloidal arc of the heavy ion species N_2^+. The total number of mesh nodes accumulated over all levels of refinement is 2.5 millions. A uniform mesh with a resolution equal to the resolution achieved by the adaptive mesh would require $512^3 = 134$ millions mesh nodes, that is 54 times more.

A global timestep Δ_t is used for the time integration, i.e. the timestep is identical at each of the four refinement levels. Even though this is more expensive in terms of computation time, it keeps the propagation of physical quantities exactly synchronized. Interpolation in time at refinement boundaries is not required which is more accurate than a local time stepping schema. We set $\Delta_t = 3 \cdot 10^{-3}\Omega_{N^+}^{-1}$ where $\Omega_{N^+}^{-1} = 18.27$s is the gyration period of the upstream species, which means a full gyration cycle of an N^+ ion is completed after not less than 333 timesteps using an implicit second order accurate leapfrog schema. In order to obtain a highly accurate description of the fossil magnetic field, we use a 44 times subcycled second order accurate leapfrog schema for the magnetic field propagation, i.e. the timestep for the magnetic field is $\Delta_{t,BField} = \Delta_{t,particle}/44 = 6.8e^{-5}\Omega_{N^+}^{-1}$. The numerical values for both simulations are summarized in table 7.2.

In our preceding real-time simulation of Titan's plasma interaction during a magnetopause passage (Simon et al. 2008, 2009a) fossil fields could not be observed due to two limitations in the numerical method: a) inaccurate resolution of $\Delta_g = 0.15R_T$ that is about four times coarser in each direction and b) a rather large amount of numerical diffusion. Both limitations have been overcome within the framework of this study. While the resolution has been increased by using an adaptive mesh, the numerical diffusion could be completely removed. This will be explained below.

First we shall point out that we define numerical diffusion to be any type of non-physical diffusion term which we will refer to as "‘smoothing"’ in the following. In our preceding simulation model this smoothing used to be a 26 point stencil averaging procedure. After each time step the spatial average $\underline{b}$ of the magnetic field $\underline{B}$ at every mesh node i, j, k was calculated:

$$\underline{b}_{ijk} = \sum_{a,b,c=-1}^{1} \underline{B}_{i+a,j+b,k+c} \cdot 2^{-(a^2+b^2+c^2+3)} \tag{7.3}$$

Afterwards the average weighted magnetic field was estimated:

$$\underline{B}_{ijk} = (1-\alpha_s)\underline{B}_{ijk} + \alpha_s \underline{b}_{ijk} \tag{7.4}$$

where we call α_s the “smoothing parameter”. In finite differences this schema is similar to a high order laplace operator and therefor acts similar as diffusion (see section 3.3 for details).

For our previous simulation runs of (Simon et al. 2008, 2009a) the smoothing parameter was set to $\alpha_s = 0.18$. However, we found that this value yields a physical conductivity that is orders of magnitudes below Titan’s ionospheric conductivity and would eliminate any field fossilization within a few seconds. The high smoothing value had been required to reduce divergence of the magnetic field that in turn destabilizes the magnetic field integration schema. This destabilizing nature due to finite divergence had been observed by Uyeshima and Schultz (2000) before.

We chose to apply the same method as Uyeshima and Schultz (2000) in order to maintain the div$\underline{B} = 0$ condition, which is the “projection method” by Brackbill and Barnes (1980). After each time step the magnetic field is corrected in the following way: In a frist step a poisson equation for the potential Φ is solved. In a second step the magnetic field is projected onto the space of divergence-free magnetic fields:

$$0 = \Delta\Phi + \mathrm{div}\underline{B} \tag{7.5}$$

$$\underline{B}_{corrected} = \underline{B} + \mathrm{grad}\Phi \tag{7.6}$$

The poisson equation for the potential Φ is solved by using an iterative multi-grid successive over relaxiation (SOR) algorithm on the adaptive mesh. Since Φ barely changes with time, the solution for Φ at time step $N-1$ is used as an initial guess for time step N therefor convergence is achieved after few iteration cycles.

The application of the projection method in combination with a ionospheric conductivity of $\sigma = 10^{-2}$ S/m guarantied stability of the numerical schema, even after the smoothing parameter α_s was set to zero. Since the value of $\sigma = 10^{-2}$ S/m is in agreement to what was estimated by Garnier et al. (2009) for the ionosphere, it is guaranteed that the fossil fields inside Titan’s ionosphere are modeled in a sufficiently accurate way.

7.5 Simulation Geometry

In this chapter, we study the characteristics of the heavy ion tail reconfiguration and magnetic field memorization process in Titan's ionosphere when the moon leaves Saturn's magnetosphere and enters the magnetosheath, where the magnetopause separates both regions. The major purpose of this study is not to quantitatively reproduce Cassini observations made during the T32 magnetopause passage, but to systematically analyze the dependency of the overall reconfiguration process on the relative magnetospheric and magnetosheath flow directions as well as the relative magnetic field orientation in both plasma regimes. Furthermore we will discuss the heavy ion tail reconfiguration which changes its shape and orientation during the magnetopause passage.

So far, none of the available models has analyzed the impact of different flow directions on the magnetic reconfiguration process during a magnetopause passage. As a first step in this direction, two simulations (A) and (B) have been carried out that consider two different geometries: in simulation (A) the plasma flow in the magnetosheath is assumed to be antiparallel to the corotational magnetospheric flow, whereas in simulation (B) the velocity directions in magnetosheath and magnetosphere are the same. In both simulation geometries, the magnitude of the flow speed in magnetosheath and magnetosphere are identical. This geometry may be somewhat idealized, but at this point we are mainly interested in the overall physics of the reconfiguration process when a finite velocity shear is included.

In the following, we shall provide a detailed description on the coordinate frame for simulation (A). For simulation (B) the same setup is chosen except for the magnetosheath flow direction being the same as inside the magnetosphere. Since this is the only difference, we resign to sketch setup (B). The simulation domain and Titan coordinate frame is sketched in Figure 7.1. Figure 7.2 shows the Titan coordinate frame with respect to Saturn and how the upstream conditions change during the magnetopause passage.

In Figure 7.1 the simulation domain (black cube) and the position of Titan inside the domain (brown sphere) is sketched. The flow inside the magnetosphere (green arrows) is superimposed by the magnetopause velocity (blue arrows). Therefore the simulation is initialized with a plasma that moves in positive x and positive y direction (red shaded arrows). We label the u_y flow component the 'magnetopause velocity' and choose $u_y \approx u_x$. While u_y remains unchanged during the entire simulation, u_x will be reversed after the stationary state is reached thereby representing the magnetosheath flow (not sketched in this figure). The simulation results in section 7.6 are visualized by either the y- or z-cross-section, which are sketched by means of a cyan and magenta frame, respectively.

Figure 7.2 provides an overview of Titan's magnetopause passage. It is subdivided into three columns, each of which illustrates Titan before, during and after the magnetopause crossing. Magnetospheric quantities are denoted in green, magnetosheath quantities in yellow and the magnetopause in blue.

The first column illustrates the global configuration (see Figures 7.2(a), 7.2(d) and 7.2(g)).

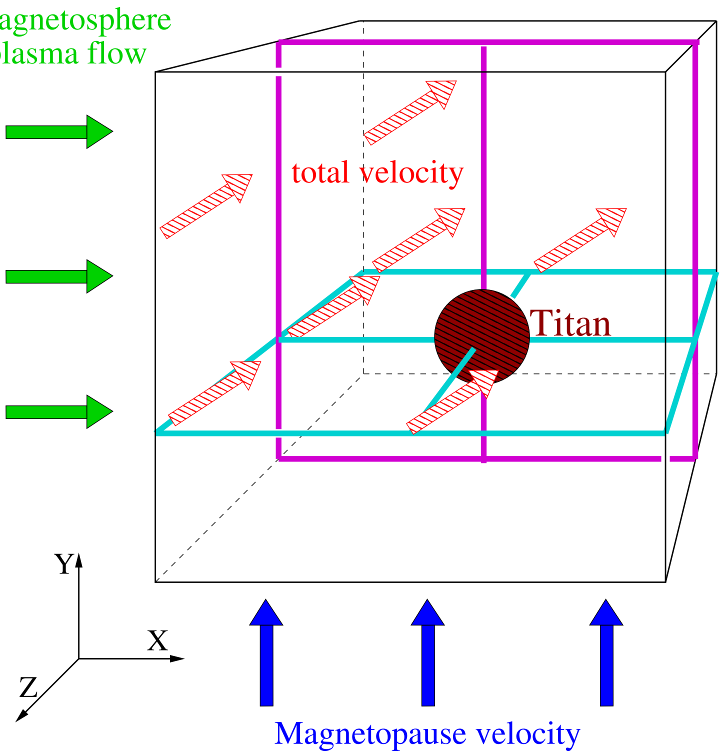

Figure 7.1: The plasma flow direction (red shaded arrows) inside the simulation geometry is a superposition of the magnetospheric flow component in x-direction (green arrows) and the magnetopause flow component in y-direction (blue arrows). Simulation results in section 7.6 are visualized by means of the y-cross-section (cyan frame) and z-cross-section (magenta frame).

In the idealized geometry discussed here, we assume Titan to be located at 12:00 Saturnian Local Time (SLT) and the latitude of the moon's subsolar point to be zero. The applied coordinate frame is the Titan Interaction System (TIIS, cf. Backes et al. (2005) and Backes (2005)) whose origin coincides with the center of Titan. The x-axis is aligned with the direction of ideal corotation (green arrows), whereas the y axis points from Titan to Saturn. The positive z axis is directed perpendicular to the moon's orbital plane, pointing "upward", i.e. it is parallel to Saturn's magnetic moment/ rotation axis. The direction of the impinging solar UV radiation, which is responsible for generating Titan's dayside ionosphere, is therefore aligned with the positive y-axis throughout the entire duration of the simulation. Similar to Neubauer et al. (1984) and Bertucci et al. (2008), the magnetic field inside the magnetosphere is directed anti-parallel to the z-axis (green crosses). The magnetopause (blue boundary) separates the magnetosphere from the magnetosheath where the velocity is aligned with the negative x direction (yellow arrows). The magnetic field points in positive z direction, that is out of the plane (yellow circles). A complete reversal of the ambient magnetic field direction corresponds to Cassini MAG observations during the T32 encounter, as discussed by Bertucci et al. (2008). Superimposed on the magnetospheric and magnetosheath velocity is the magnetopause velocity (blue arrows) in positive y direction (towards Saturn) that makes the discontinuity sweep over Titan.

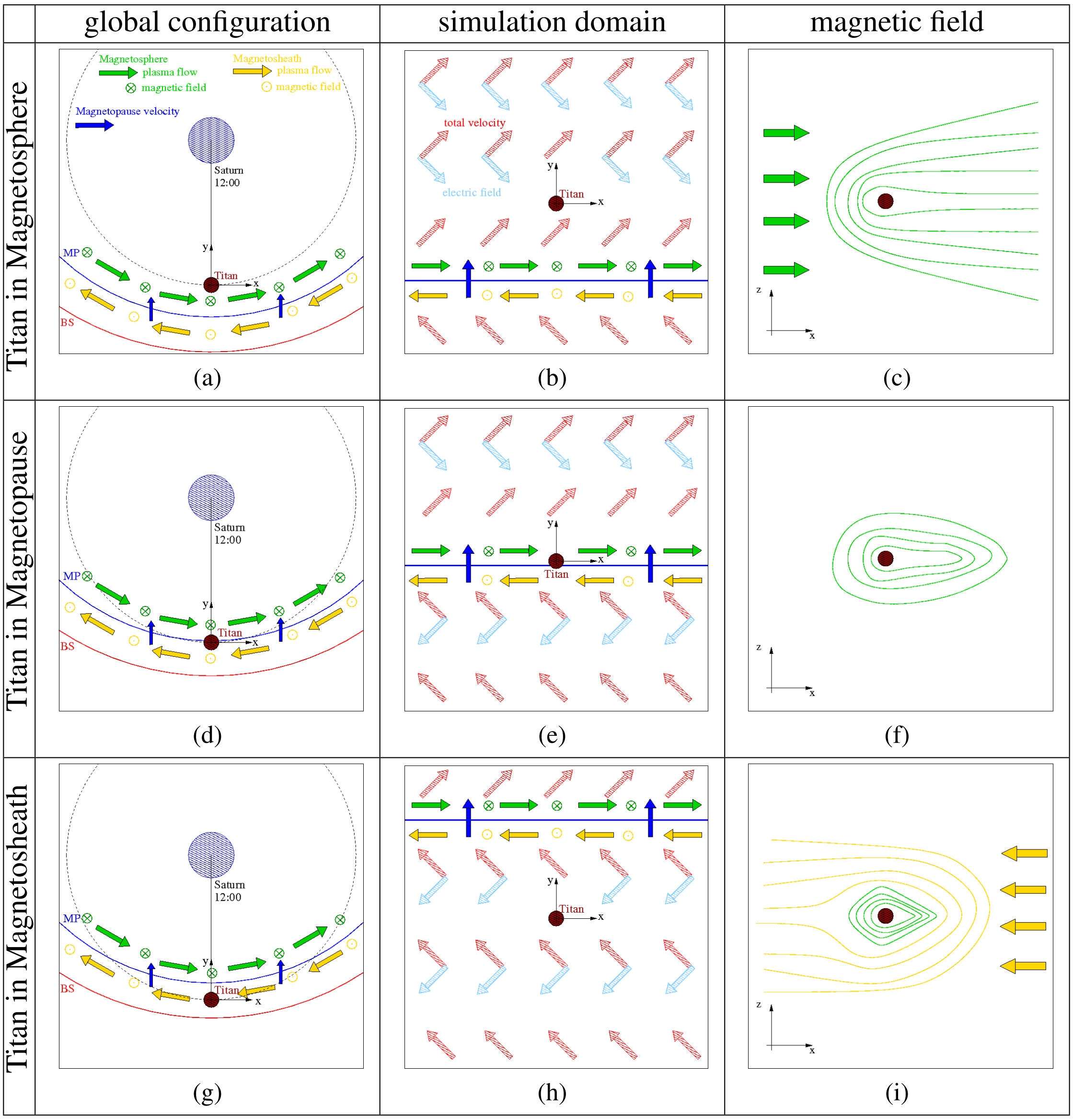

Figure 7.2: Titan before, during, and after the magnetopause crossing: Magnetospheric quantities are sketched in green, magnetosheath quantities in yellow and the magnetopause in blue. The first column demonstrates the global configuration, the second column provides a view on the simulation domain and the third column illustrates the magnetic field configuration during the magnetopause passage.

Therefore both, the magnetosphere and magnetosheath plasma are in addition moving in direction of Saturn, in synchronization with the Magnetopause motion. In other words no flow component perpendicular to the tangential magnetopause discontinuity boundary does exist.

The second column provides a view of the simulation domain within the z-cross-section. It is not convenient for todays computers to model the entire Saturnian magnetosphere by means of hybrid simulations. Fortunately this is not needed, therefore we constrain our simulation domain to 25 R_{Titan} length. The time of one simulation run can be subdivided into three steps: (1) magnetoshperic stationary state (see Figure 7.2(b)), (2) magnetopause passage at Titan (see Figure 7.2(e)) and (3) magnetosheath stationary state (see Figure 7.2(h)). These three subsequent steps are described in detail below.

In step (1) where Titan is located inside Saturn's magnetosphere the total flow is directed towards the Saturn facing right corner within the z=const cross-Section (red shaded arrows). The background magnetospheric field is antiparallel to the z axis, hence the convective electric field points towards the Saturn averted right corner of the simulation domain (light blue arrows). By keeping the upstream parameters constant, the simulation is continued until a quasi-stationary state is reached. After the quasi-stationary state has been reached step (2) commences, which means the u_x component of the plasma flow is reversed now pointing in negative x-direction. The u_y component, on the other hand remains unchanged. Consequently, the resulting velocity points towards the Saturn facing left corner of the simulation domain. At the same time, the magnetic field is rotated into positive z-direction at the lower y-boundary. This goes along with a reversal in the convective electric field now pointing towards the Saturn averted left corner of the simulation domain. These new flow and magnetic field conditions are convected into the simulation domain by means of the u_y flow component. Moving boundary conditions are applied to the left $x = -12.5R_T$ and right $x = +12.5R_T$ domain boundary, i.e. inflow and outflow conditions are used in synchronization with the magnetopause motion. We would like to emphasize that in this way, no flow component perpendicular to the magnetopause is introduced, as it moves with the flow. Again the simulation is continued until a quasi-stationary state is reached long after the magnetopause has left the simulation domain (step (3)).

The third column provides a schematic sketch of the expected magnetic field configuration (see Figures 7.2(c), 7.2(f) and 7.2(i)). These sketches provide a view on the magnetic field draping within the y-cross-section that is perpendicular to the magnetopause motion. For this reason, the projection of the plasma velocity is directed straight in positive or negative x-direction respectively, and does not appear to be diagonal. After the simulation is driven into quasi-stationary state in the magnetosphere, the magnetic draping pattern is fully developed. This configuration is identical to the steady-state scenario discussed by Simon et al. (2007). Figure 7.2(f) illustrates the point in time when the magnetopause sweeps over Titan. Even though the magnetic field and u_x flow component are zero at the magnetopause center, the magnetospheric field is still maintained inside Titan's ionosphere for it is frozen in the slow heavy ion plasma near Titan. After the magnetopause has left the near-Titan region the magnetosheath flow arrives streaming into negative x direction. At this point, the third step of our simulation commences. The magnetopause has left the simulation domain at the Saturn facing $y = 19.2R_T$ domain boundary and we expect to find fossil magnetic fields in the moon's lower atmosphere, i.e. the coexistence of a magnetosheath draping which encloses the magnetospheric draping that has been trapped in the slow and dense heavy ion plasma. In other words, we expect to find a residual bundle of draped field lines that has "survived" the transition from the magnetosphere into the magnetosheath. As the direction of any fossil field line should be antiparallel to the ambient (magnetosheath) field, the fossil fields will be eroded by the impinging magnetosheath fields due to reconnection. For the duration of the third simulation step, the ambient plasma conditions are therefore again kept constant until the fossil field lines have been completely eroded from Titan's ionosphere.

7.6 Simulation Results

Since the geometry of antiparallel magnetospheric and magnetosheath plasma flow has never been modeled before, we will analyze simulation (A) in great detail. Afterwards we will provide a brief discussion of the parallel flow scenario (B). In order to illustrate the key features of Titan's plasma wake under stationary upstream conditions, the structure of the moon's plasma environment when being located inside Saturn's magnetosphere is shown in fig. 7.3. This scenario represents the initial configuration that is exposed to the retracting magnetopause in the real-time simulations. The time-dependent behavior during simulation (A) is illustrated by means of seven subsequent points in time which are illustrated in Figures 7.4 to 7.10, similar to a series of snap-shots forming a flip-book. The points in time are chosen in such a way that two figures show Titan before the magnetopause crossing (see Figures 7.4 and 7.5), Figure 7.6 illustrates the moment when the magnetopause sweeps over Titan and four additional figures show the evolution of the moon's plasma environment after the magnetopause crossing (see Figures 7.7 to 7.10). We define the moment when the magnetopause is in the $y = 0$ plane (i.e. Titan's terminator plane) to be $t = 0$ minutes. Hence any point in time before the magnetopause crossing is negative, while any point in time after the magnetopause crossing is assigned a positive sign. The exact time values for each of the plots are listed in table 7.3.

Time step	Real time	Figures Run (A)	Figures Run (B)
t_1	-5min 00s	7.4	N/A
t_2	-1min 50s	7.5	N/A
t_3	0min 00s	7.6	7.11
t_4	+4min 35s	7.7	7.11
t_5	+7min 30s	7.8	7.11
t_6	+16min 15s	7.9	N/A
t_7	+24min 07s	7.10	7.11

Table 7.3: For each of the seven subsequent time steps the table shows the corresponding real time and figure number for both simulations (A) and (B).

7.6.1 Stationary State: Global View

All physical quantities within the result section 7.6 are either visualized for the $y = 0$ or $z = 0$-cross-sections, i.e. for the planes containing either B_0 or $E_0 = -u_0 \times B_0$. In order to clarify how these cross-sections are positioned wtih respect to Titan and its heavy ion tail, Figure 7.3 provides a three dimensional view on the magnetospheric stationary state, immediately before the magnetopause sweeps over Titan. Figure 7.3(a) illustrates the B_z-component and field line draping at $t = t_2$. The yellow layer indicates the arriving magnetosheath field, the green to light blue transition is around zero field strength, thereby representing the magnetopause. Dark blue denotes negative values, i.e. the magnetospheric field. Values below -3 nT. are set invisible, therefore most of the Saturn facing part of the simulation domain appears empty, except for the neutral sheet downstream of Titan. Magnetic field lines drape around Titan forming a bipolar induced magnetotail at the wakeside and the neutral sheet inbetween.

The actual obstacle to the plasma flow is not Titan's solid body but its ionosphere and heavy ion tail. These are illustrated in Figure 7.3(b) in addition to the B_z-component. The red arrow indicates the total plasma flow direction and the light blue arrow marks the convective electric field. As can be seen in Figure 7.3(d) both of these quantities are aligned inside the z-cross-section while in the y-cross-section only their projection on the x-axis is visible (see Figure 7.3(c)). We would emphasize that the heavy ion tail extents out of the y-cross-section and therefore will appear to be shortened within the y-cross-section. This must be considered for a correct interpretation of the simulation results (see section 7.6). In order to obtain a precise idea of the three dimensional structure we advise to view the associated animations that are available online at:
www.tu-braunschweig.de/theophys/people/jmueller.

For both simulations the same numerical mesh is applied. Its hierarchical structure is visible in Figures 7.3(c) and 7.3(d). The mesh resolution at the highest level of refinement is 0.05 R_T. This highly refined region covers a cubic volume of $5R_T$ edge length with Titan being located at its center.

7.6.2 Simulation (A), Anti Parallel Flow

In order to provide an impression of the time-depended magnetopause crossing, the simulation results at the seven different points in time are visualized for the y- and z-cross-sections, respectively. To obtain a complete idea of the time sequence we recommend to view the associated animations that are available online at:
www.tu-braunschweig.de/theophys/people/jmueller.

For each time step the B_y and B_z component and the magnitude of the magnetic field are shown. Additionally the N_2^+-density, N_2^+-velocity and total velocity are visualized, where the total velocity is the density weighted average of all ion species velocities. The quantities are normalized by means of their background values B_0, n_0 and V_a (cf. Tab. 7.1).

Titan in Saturn's Magnetosphere 5 min before the Magnetopause Crossing: $t = t_1$

At $t = t_1$, Titan is completely embedded in the corotating plasma of Saturn's magnetosphere. The simulation was ran until stationary state and the magnetopause is about to enter the simulation domain from the Saturn-averted y-domain boundary and will travel towards Titan in positive y-direction. Within the $z = 0$ cross-section the typical draping pattern is visible in the total magnetic field (see Figure 7.4(a)). The magnetic tail forms an

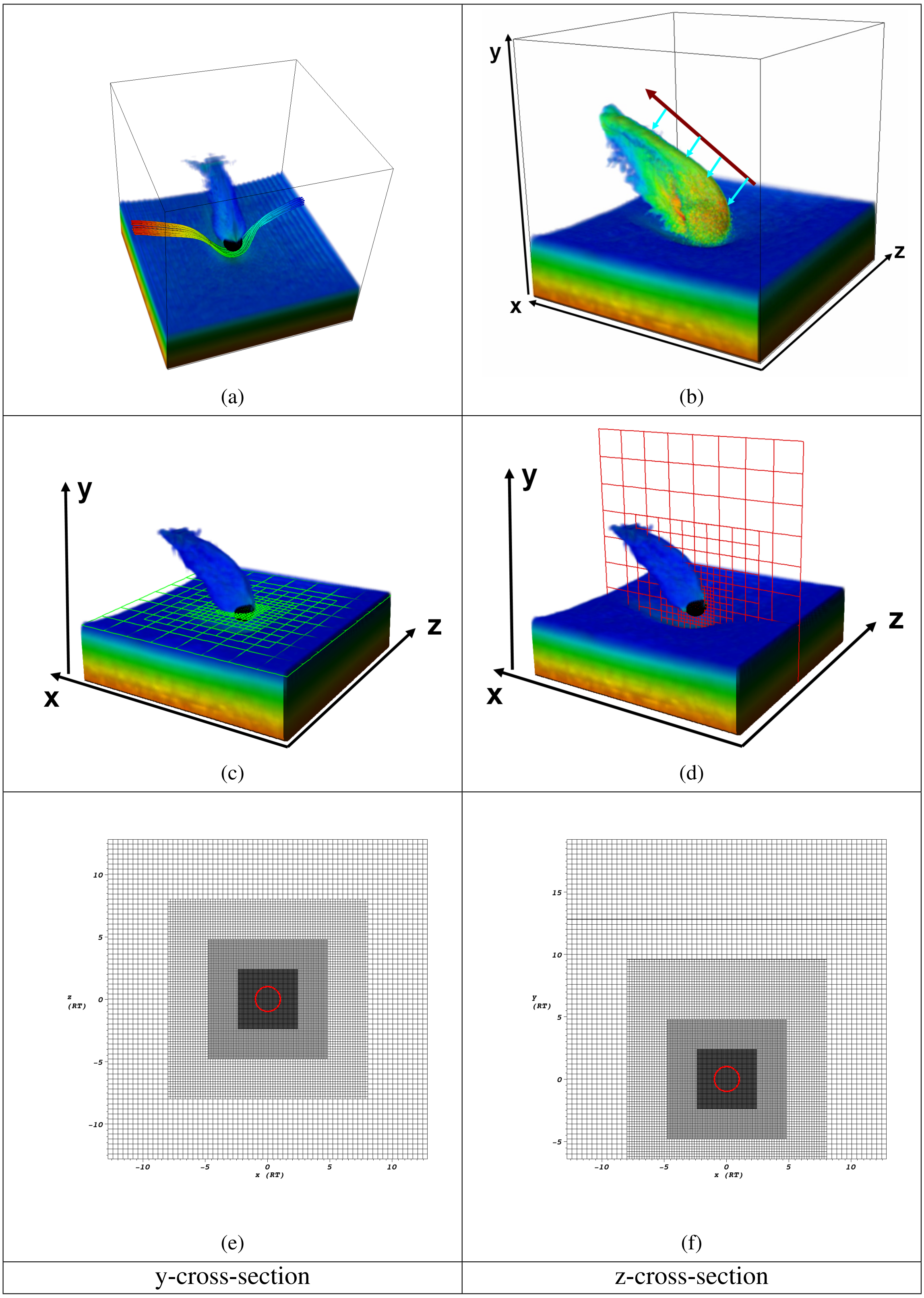

Figure 7.3: Figures 7.3(a) to 7.3(d) show the B_z-component, immediately before the magnetopause sweeps over Titan. Figure 7.3(a) shows draping magnetic field lines around Titan. In fig. 7.3(b) The actual obstacle to the plasma flow is schown that is not Titan's solid body but its ionosphere and heavy ion tail. Figures 7.3(c) and 7.3(d) illustrate the position of the *y*- and *z*-cross-section. Figures 7.3(e) and 7.3(f) provide a 2D view of the numerical mesh of the *y*- and *z*-cross-section, respectively.

angle of $\alpha = 49°$ degree with respect to the y-axis. This means the magnetic tail is aligned with the direction of the impinging magnetospheric plasma flow (see Figure 7.4(i)). It is enclosed by the wake-side lobes of enhanced magnetic field strength (see Figure 7.4(d)). While the B_y component is zero within the entire cross-section (see Figure 7.4(b)), the B_z component is at -8nT background value everywhere except for the tail region where the B_z component is zero (see Figure 7.4(c)).

The convective electric field is aligned inside the z-cross-section (see Figure 7.2(b) and 7.3(b)). Hence within the y-cross-section, we expect to observe a symmetry with respect to the x-axis in all quantities which is in agreement with the results (see Figure 7.4(d)-7.4(f)). The neutral sheet is compressed down to a narrow layer and appears to be cut off about $x = 3R_T$ (see Figure 7.4(d)). This impression is due the choice of the coordinate frame in which the magnetic tail is tilted by an angle of $\alpha = 41°$ with respect to this cross-section (compare Figure 7.3(b) and Figure 7.3(c)). For the same reason, the typical magnetotail seen in Figure 7.4(e) appears to be rather short. The negative B_y-component in the northern lobe and positive B_y-component in the southern lobe reflect the typical draping pattern. Note that this orientation will be reversed after the magnetopause crossing, hence we expect the fossilized magnetic field to be visible in this component. The B_z-component in the y-cross-section is at -8nT background value everywhere (except for the induced magnetotail, see Figure 7.4(f)). As the B_z-component will be reversed to +8nT at the magnetopause boundary, we expect to observe fossilized fields within the B_z-component as well. In contrast, the B_x-component will not change its orientation after the magnetopause passage.

In the z-cross-section the convective electric field is oriented perpendicular to the plasma flow. Hence cycloidal heavy pick-up up motion should be visible in this cross-section. On the other hand, in the y-cross-section the heavy ions are trapped in between the magnetic lobes, which is why we expect to observe a narrow heavy ion layer there. Furthermore, as shown by (Simon et al. 2007), the light ionospheric species (H_2^+ and CH_4^+) are shielded by the heaviest one (N_2^+) , therefore not influencing the shape of the magnetic field lines in Titan's wake in a noteworthy way. For this reason we exclusively visualize the heaviest (N_2^+) ionospheric species. The N_2^+ heavy ion tail in Figure 7.4(g) confirms the expectations described above. Furthermore the tail exhibits two different regimes: A first regime can be identified close to Titan's geometric plasma shadow. In this region, the density is orders of magnitude above background values. In this regime the total plasma velocity (see Figure 7.4(i)) is strongly reduced. Hence, the convective electric field drops to values close to zero which is why the diameters of the cycloidal arcs of the ion's pick-up motion become very small. For this reason the heavy ion's individual trajectories in this region appear to be straight lines in direction of the $E \times B$ - drift motion. This type of slow heavy ion outflow has been observed at several other ionospheric obstacles (Bößwetter et al. 2004).

A second regime can be identified about one R_T above Titan's surface: when approaching the outer flank of the tail, the heavy ion density steadily decreases and finally becomes much lower than the magnetospheric background plasma density, thereby hardly affecting the average flow speed of magnetospheric plasma and heavy ions (see Figure 7.4(i)). The

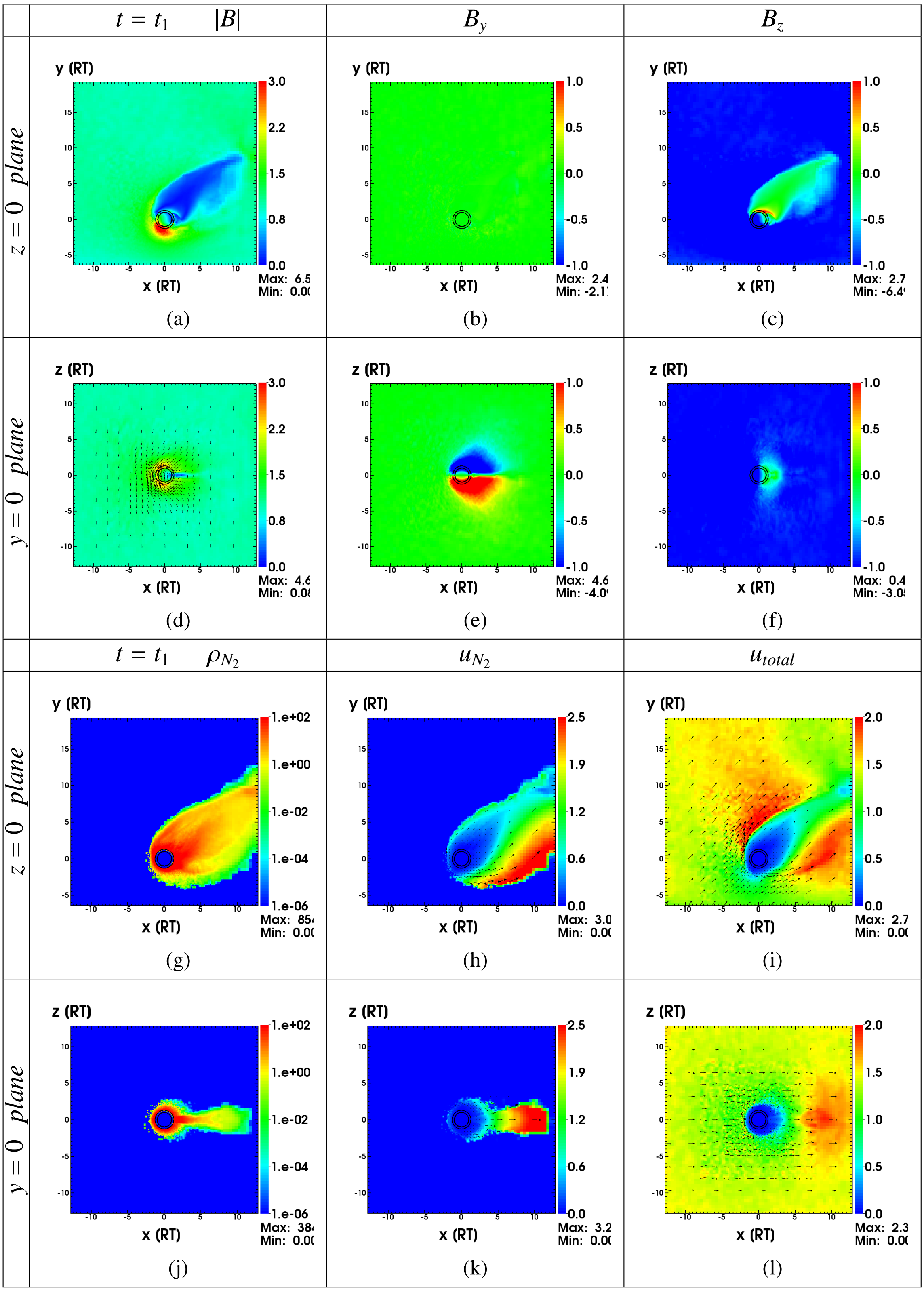

(a) (b) (c) (d) (e) (f) (g) (h) (i) (j) (k) (l)

Figure 7.4: $|B|$, B_y, B_z, $\rho_{N_2^+}$, $u_{N_2^+}$ **and** u_{total} **at** t_1

convective electric field is barely decreased which is why the heavy ions are picked up on large cycloids. In this region, the heavy ions are accelerated above background velocity (see Figures 7.4(h) and 7.4(k)). The y-cross-section clearly reveals the two-dimensional shape of the heavy ion pick up tail (see Figures 7.4(j) and 7.4(k)). The heavy ion population is confined in between the magnetic lobes. Furthermore, we would like to point out that the total velocity within one R_T around Titan drops down to values less than 2% of the background velocity therefore resulting in large convection times and being ideal to trap fossil magnetic fields (see Figures 7.4(i) and 7.4(l)).

Titan two Minutes before the Magnetopause Crossing: $t = t_2$

At time $t = t_2$ the inward moving magnetopause has entered the simulation domain and is located at $-5R_T$ upstream of Titan (see Figure 7.5(a)). It can already be seen in the B_z-component at y=$-5R_T$ that the presence of Titan and its highly conducting ionosphere shields the magnetospheric field against the magnetosheath field (see Figure 7.5(c)). The magnetic field at $y = 0$ is hardly influenced by the magnetopause yet (see Figures 7.5(a) - 7.5(c)).

Magnetopause at Titan's Center: $t = t_3$

At $t = t_3$ the magnetopause has arrived at $y = 0$ and therefore coincides with Titan's terminator plane. Hence, the background magnetic field in the y-cross-section vanishes (see Figure 7.6(d)). The region of enhanced magnetic field in the immediate vicinity of Titan has hardly changed its shape compared with $t = t_2$. The reason clearly is the highly conducting ionosphere and slow plasma velocity that conserve the magnetospheric conditions due to large diffusion and convection time scales as argued in the analytical estimation in section 7.2. This can be observed in both, the magnetic field (see Figures 7.6(d) - 7.6(f)) and plasma quantities (see Figures 7.6(j) - 7.6(l)). The anti-parallel magnetospheric and magnetosheath field barely reconnect and a thin neutral sheet layer forms inbetween both field regimes (see Figure 7.6(a)).

While the plasma flow is parallel to the y-axis at $y = 0$, the flow is already fully tilted by $\alpha = -49°$ with respect to the y-axis at $y = -5R_T$ (see Figure 7.6(i)). In other words the u_x-component has reversed its sign. The heavy ion velocity is slightly decreased below Titan but remains unaffected elsewhere (see Figure 7.6(h)).

While the high heavy ion density is not effected at all by the approaching magnetopause, the thin regime at the Saturn averted flank of the pick-up tail is slightly compressed towards Titan (see Figure 7.5(g)). The u_x-component at y=$-5R_T$ is decreased to zero, hence the total velocity is parallel to the y-axis at the magnetopause center (see Figure 7.5(i)). The decrease of the total velocity in the y-cross-section reveals that the outer edge of the magnetopause already arrived at Titan. However, the heavy ion density and velocity are barely influenced at this time (see Figures 7.5(j) and 7.5(k)).

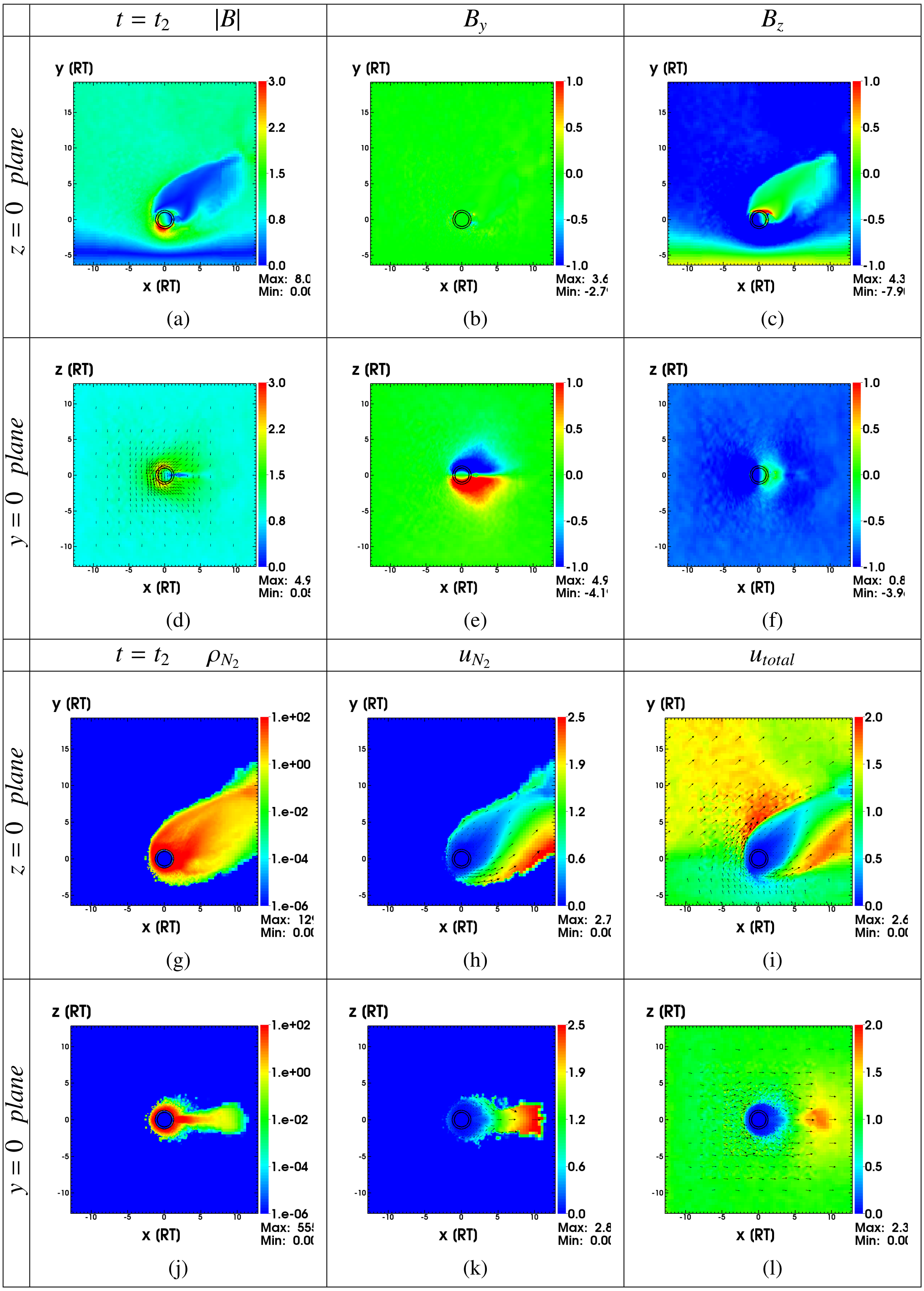

(a) (b) (c)

(d) (e) (f)

(g) (h) (i)

(j) (k) (l)

Figure 7.5: $|B|$**,** B_y**,** B_z**,** $\rho_{N_2^+}$**,** $u_{N_2^+}$ **and** u_{total} **at** t_2

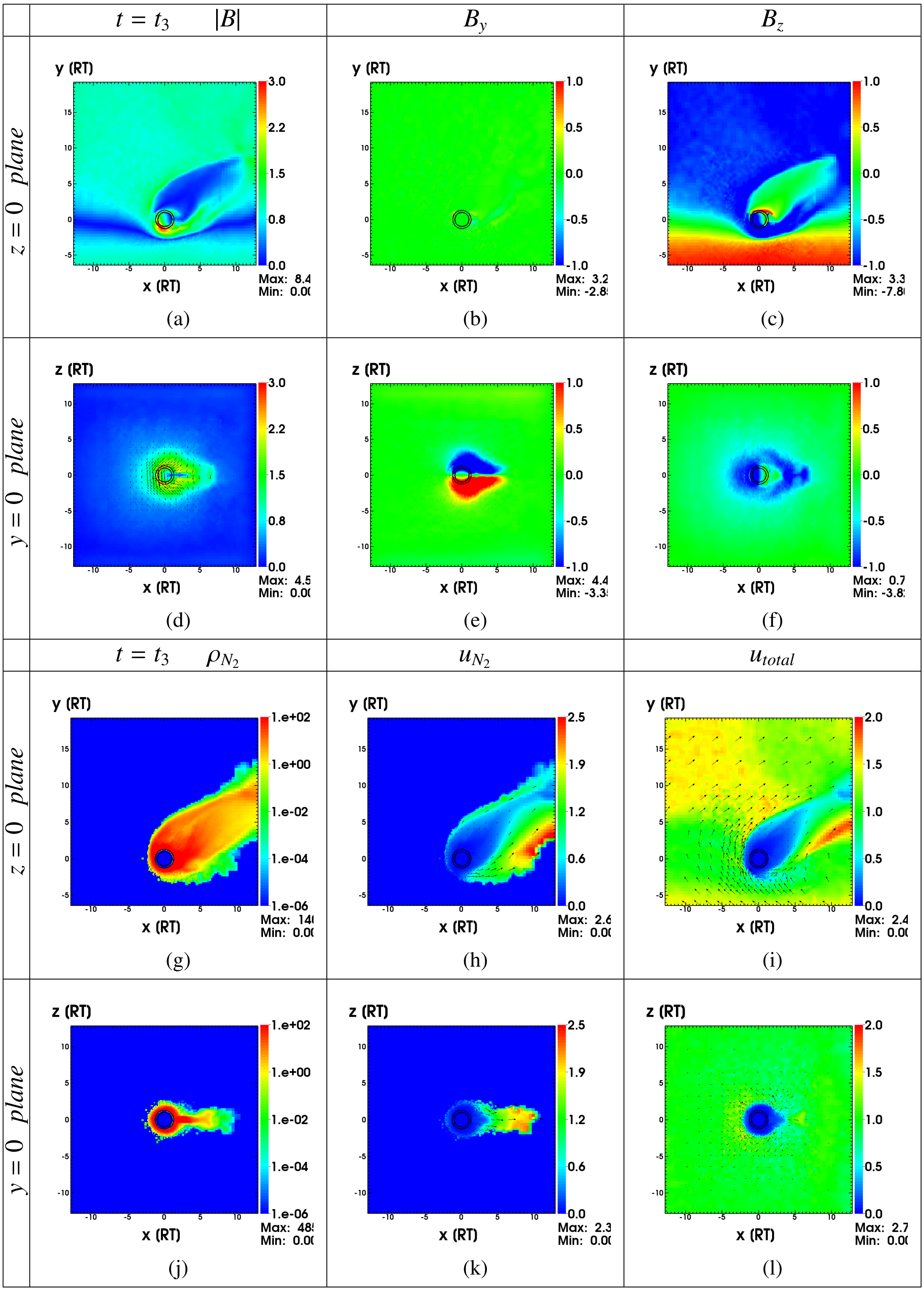

Figure 7.6: $|B|$, B_y, B_z, $\rho_{N_2^+}$, $u_{N_2^+}$ **and** u_{total} **at** t_3

Titan's plasma environment at $t_4 = 4.5$ minutes

At $t = t_4$ the center of the magnetopause has traveled to $y = 12R_T$ and Titan is completely located inside Saturn's magnetosheath. Therefore the background magnetic field is at +8nT, now pointing northward (see Figure 7.7(f)). The u_x-component has reversed its direction as well (see Figure 7.7(l)). Still the magnetosheath field cannot enter Titan's ionosphere or heavy ion tail. Instead the magnetosheath field piles up in front of the tail and ionosphere, forming a region of enhanced magnetic field strength that extends up to $10R_T$ downstream of Titan which is several times larger than the original magnetic barrier (see Figure 7.7(a)). Because of the reversed magnetic field direction and the unchanged flow component in y-direction, the polarity of the draping pattern of the B_y-component is reversed. As the time since the magnetopause passage is shorter than the high diffusion- and convection times within Titan's ionosphere both, the magnetospheric- and magnetosheath-draping coexist (see Figure 7.7(e)). The B_z component is still at magnetospheric values near Titan (see Figure 7.7(c)). As opposed to the B_y draping the the perturbation of the B_x-component will remain unaffected since both, the B_z and u_x direction are reversed, thereby canceling out the change in sign.

Due to the reversed u_x-component the plasma flow now enters from the right-hand boundary of the simulation domain. As a consequence the dense heavy ion regime is slowly rotated towards the direction of the magnetosheath plasma flow. In the regions where the heavy ion density is of the same order as the background density, the newly generated heavy ions are immediately picked up. This difference in the involved time scales leads to the interesting case that a dense tail aligned with the original flow direction and a cycloidal pick up tail coexist, but in different hemispheres (see Figure 7.7(g)). While the straight tail still points in magnetospheric plasma flow direction and is hardly accelerated because of its high density, the cycloidal tail is already fully rotated in direction of the magnetosheath plasma. This reconfiguration of the cycloidal tail is completed about 4 minutes after the magnetopause passage. As will be shown later, the reconfiguration of the dense heavy ion regime will last 24 minutes. Again the total velocity is hardly affected by the thin ion population that moves on cycloidal trajectories (see Figure 7.7(i)). Since the magnetic lobes in $-x$ direction are not fully developed yet, the rotated thin heavy ion tail is not trapped in between magnetic lobes and therefore loses its two dimensional nature for a few minutes (see Figure 7.7(j) and Figure 7.7(k)). However, we shall point out that this relates exclusively to the thin heavy ion regime that is three orders of magnitude below background density therefore not at all impacting on the total plasma velocity (see Figure 7.7(l)).

Titan's plasma environment at $t_5 = 7.5$ minutes

At time $t = t_5$ the magnetopause center has arrived at the upper ($y = 20R_T$) boundary of the simulation box. Yet the presence of Titan prevents the magnetosheath field from entering the large triangle-shaped area at the Saturn facing side of Titan (see Figure 7.8(c)). The magnetic field enhancement that arises in front of the slowly rotating heavy ion tail splits up into smaller islands (see Figure 7.8(a)), filling up voids within the inhomogeneous heavy ion plasma density, thereby ensuring total pressure balance (see Figure

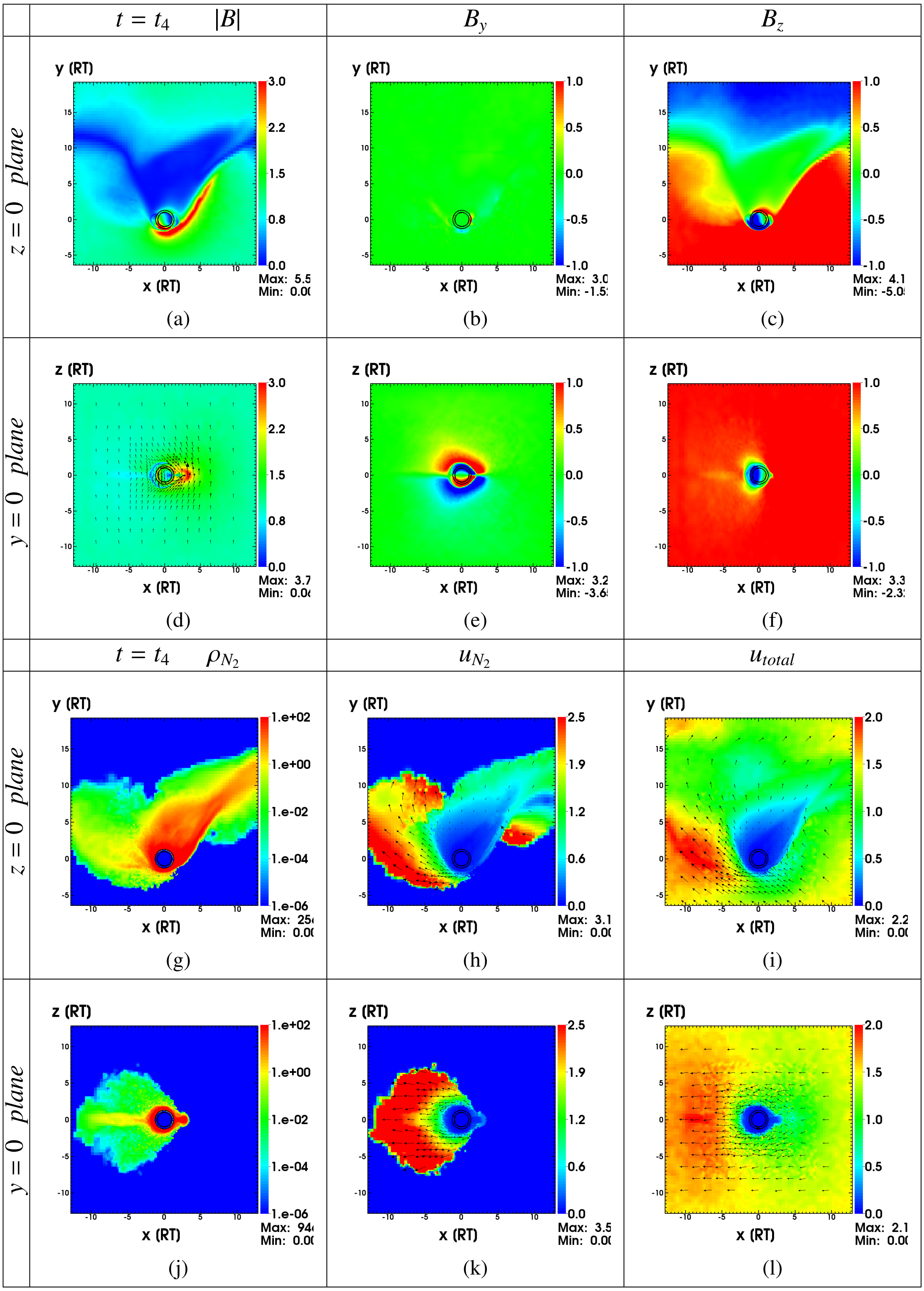

(a) (b) (c)

(d) (e) (f)

(g) (h) (i)

(j) (k) (l)

Figure 7.7: $|B|$, B_y, B_z, $\rho_{N_2^+}$, $u_{N_2^+}$ **and** u_{total} **at** t_4

7.8(g)). The coexisting magnetosheath and magnetosphere draping are still clearly visible (see Figure 7.8(e)) and fossilized magnetic fields can be identified in the B_y and B_z component close to Titan's surface (see Figure 7.8(f)). However, meanwhile the magnetic lobes that started to form after entry into the magnetosheath plasma flow are fully developed (see Figure 7.8(d)) which is why the downstream heavy ion population is re-trapped and forced to return into its previous two-dimensional confinement (see Figure 7.8(j) and 7.8(k)). Hence, the time scale upon which the magnetic lobes are reversed is less than seven minutes and therefore much shorter than the lifetime of the fossil fields. This is the first time that the complex tail reversal as well as the field fossilization occurring on much larger scales are resolved simultaneously within a single simulation model.

The total velocity in the y-cross-section (see Figure 7.8(l)) already appears to be nearly the complement of the stationary magnetospheric state (see Figure 7.4(l)), yet a wide region of accelerated plasma downstream of Titan is visible since in this region, the dilute heavy ion population experiences the nearly unperturbed background fields of the ambient magnetospheric plasma. Also, a decrease in velocity upstream of Titan can be seen which forms due to the dense and slow heavy ion population (see Figure 7.8(j)). This decrease in the total velocity causes an enhanced pile up in the magnetic field in front of Titan (see Figure 7.8(d)).

Titan's plasma environment at t_6 = 16.25 minutes

The magnetopause has left the simulation domain and would now be located at $y = 54R_T$ inside Titan's orbit. Meanwhile the ion tail has been rotated towards the magnetosheath downstream direction. During this process, the magnetic field pile up in front of the heavy ion tail has split up into many isolated magnetic field islands that fill up voids in the heavy ion density. Due to the shear between heavy ion and magnetosheath velocity kelvin helmholtz instabilities are excited (see Figure 7.9(i)), resulting in periodic amplifications of density fluctuations at the Saturn facing flank of the heavy ion tail (see Figure 7.9(g)). These fluctuations in turn grow into huge heavy ion clouds to the extent of three Titan radii and travel alongside the heavy ion tail at reduced velocity (see Figure 7.9(h)).

Compared to $t = t_5$, little changes are visible in the $y = 0$-cross-section. The amplitude of the fossilized fields has slightly diminished. (see Figures 7.9(e) and 7.9(f)). The broad region of enhanced magnetic field strength above the ionosphere has vanished (see Figure 7.9(d)) and the total velocity (see Figure 7.9(l)) meanwhile is the exact complement of that in the magnetospheric flow (see Figure 7.4(l)).

Titan's plasma environment at t_7 = 24.1 minutes

The magnetopause resides at $y = 67R_T$ distance to Titan and 24.1 minutes have passed since it has swept over Titan. A quasi-stationary state is reached, representing the complement of the magnetospheric stationary state at $t = t_1$. Compared to $t = t_1$, all quantities are mirrored with respect to the x-cross-section. However we would like to point out that the magnetosheath magnetic field has not yet entered the immediate vicinity of Titan which is visible in the B_z-component at Titan's north pole above the inner boundary

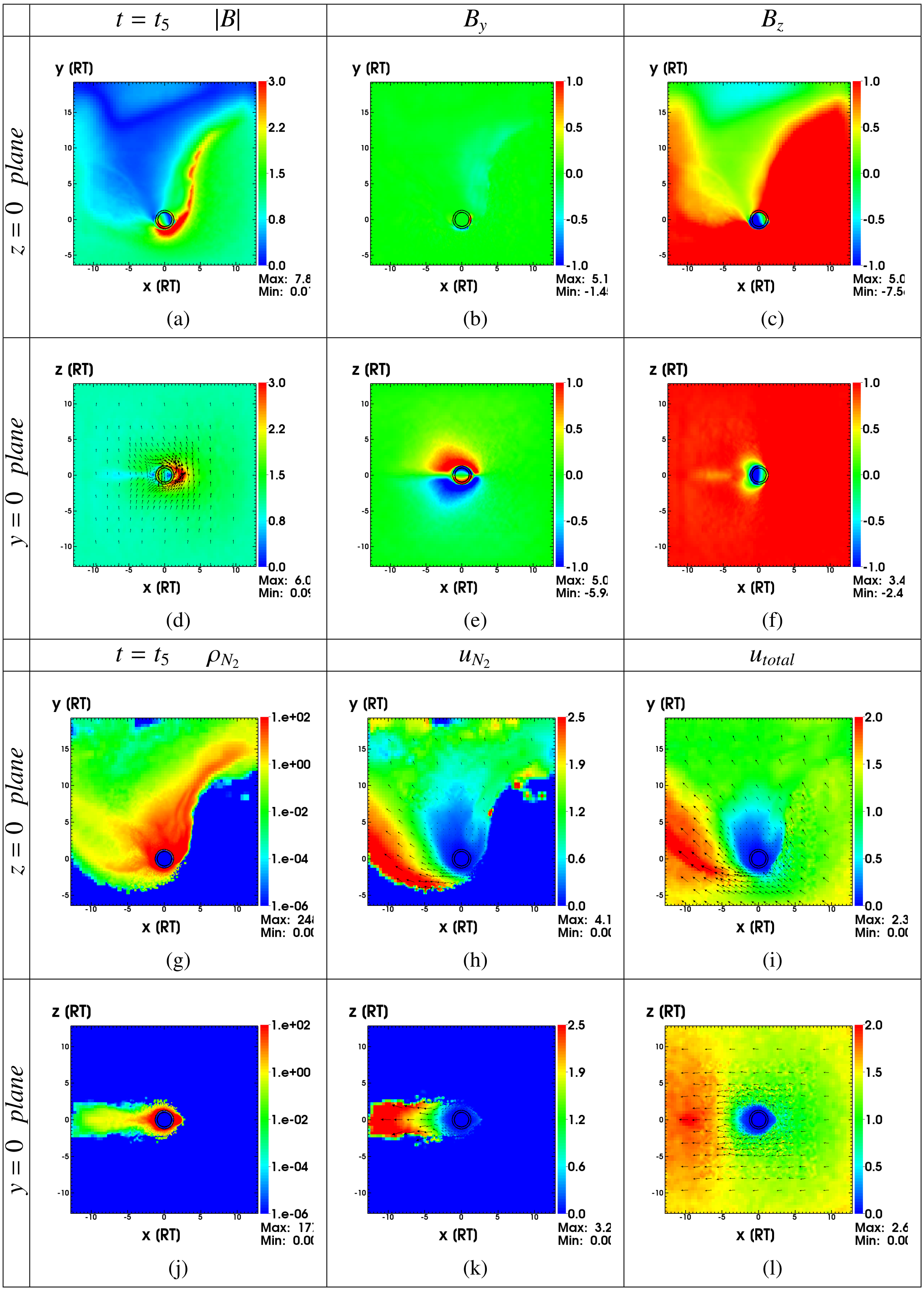

Figure 7.8: $|B|$**,** B_y**,** B_z**,** $\rho_{N_2^+}$**,** $u_{N_2^+}$ **and** u_{total} **at** t_5

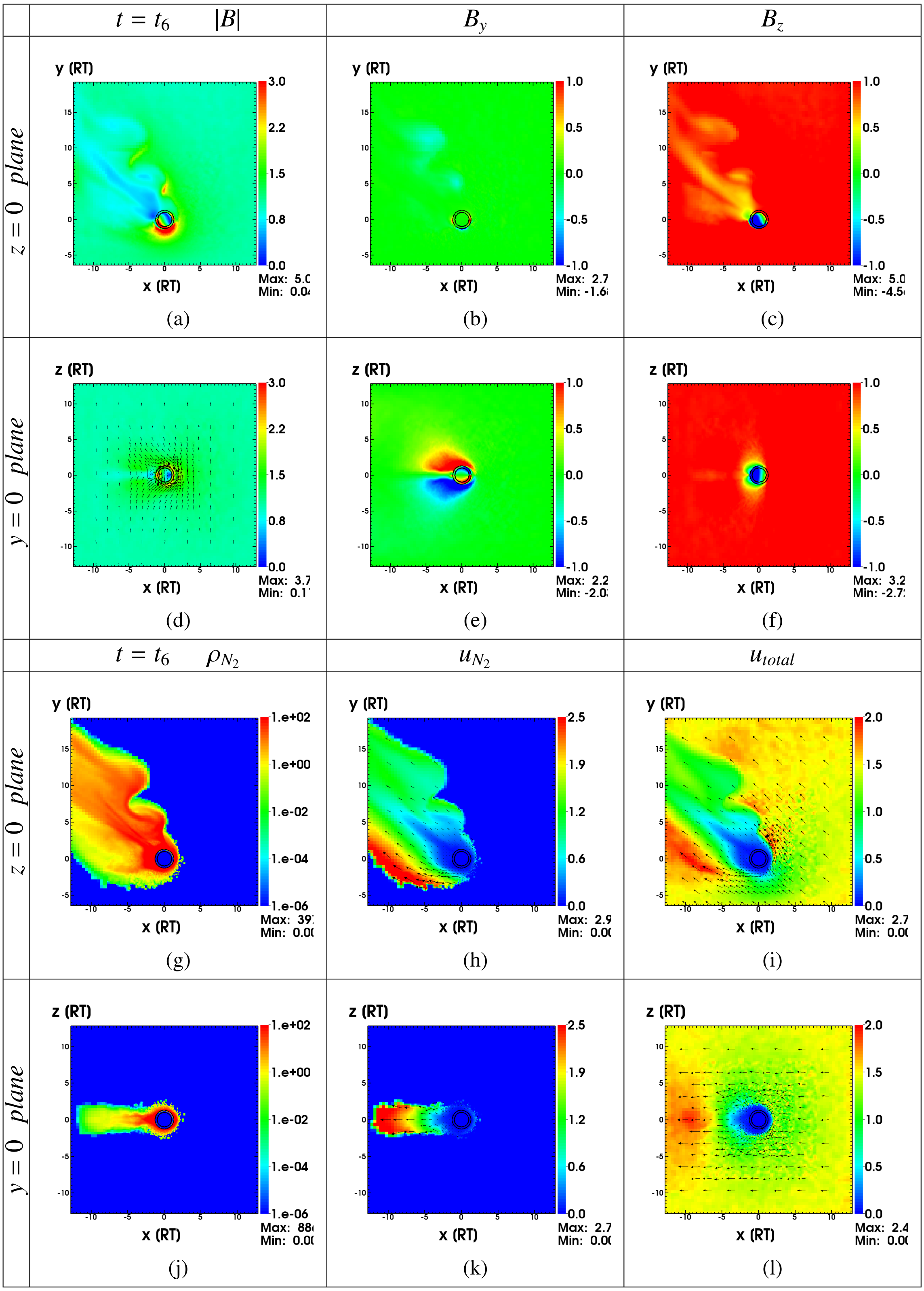

(a) (b) (c)

(d) (e) (f)

(g) (h) (i)

(j) (k) (l)

Figure 7.9: $|B|$, B_y, B_z, $\rho_{N_2^+}$, $u_{N_2^+}$ **and** u_{total} **at** t_6

(see Figure 7.10(f)): since in the stationary magnetospheric case the B_z-component is at $-8nT$, we consequently would expect to find the B_z-component at $+8nT$ in the stationary magnetosheath state. However, its value is still close to zero which originates from the magnetopause crossing and therefore can be categorized as fossilized field.

Furthermore, the magnetospheric draping is still persistent above Titan's north pole and is enclosed by the magnetosheath draping (see Figure 7.10(e)). During the T32 encounter Cassini did observe the fossilized fields above Titan's north pole as well (Bertucci et al. 2008, 2009). A lower limit for their lifetime could estimated to be 20 minutes which is in excellent agreement with our simulation results.

7.6.3 Simulation (B), Parallel Flow

The plasma processes in the simulations with parallel flows (B) will now be compared to the antiparallel flow simulation (A). We like to point out the core differences of both simulations and therefore resign to illustrate every time step and just show time steps t_3, t_4, t_5 and t_7 instead (see Figure 7.11), which are the same moments in time that have been shown for the antiparallel simulation (cf. Tab. 7.3). The image is divided into three columns where the first one shows the heavy ion N_2^+ density, the second one the total magnetic field and the third one the B_y component. The heavy ion density and the total magnetic field are visualized for the z-cross-section, the B_y component for the y-cross-section.

The first row for $t = t_3$ illustrates the point in time when the magnetopause arrives at Titan. The total magnetic field in Figure 7.11(b) and the B_y-component in Figure 7.11(c) are nearly identical to their respective state in antiparallel flow simulation (cf. Figures 7.6(a) and 7.6(e)). The heavy ion density in contrast is less confined (see Figure 7.11(a)) compared to the antiparallel case in Figure 7.6(g) where the heavy ions have been compressed into the tail by the reversed upstream velocity.

At time $t = t_4$ there are several differences between the results of both simulation runs. While in simulation (A) the thin heavy ion regime was separated from the dense heavy ion regime (see Figure 7.7(g)), the heavy ion tail of the parallel simulation remains as a whole. Nevertheless several fluctuation at its Saturn facing flank are present. These differences are due to the reversed convective electric field that points towards the Saturn facing left corner of the simulation domain. Hence, the cycloidal shape of the heavy ion tail develops at the Saturn facing flank while the dense heavy ion regime is located at the Saturn averted tail flank inside the magnetosheath. The magnetic field pile-up in figure 7.11(e) is rotated by 90° towards the $-x$ direction. However, in contrast to the magnetic field of simulation (A) (see Figure 7.7(a)) the pile-up is confined to the immediate vicinity of Titan, i.e. here is no field enhancement along the entire flank of the heavy ion tail. Like in simulation (A), the B_y-component of the draping signature is reversed and encloses the magnetospheric draping (see Figure 7.11(f)), yet the transition from magnetospheric to magnetosheath draping is more continuous (cf. Figure 7.7(e)). The reason is that the downstream direction remains unchanged, hence the newly developing draping is less strongly compressed towards Titan.

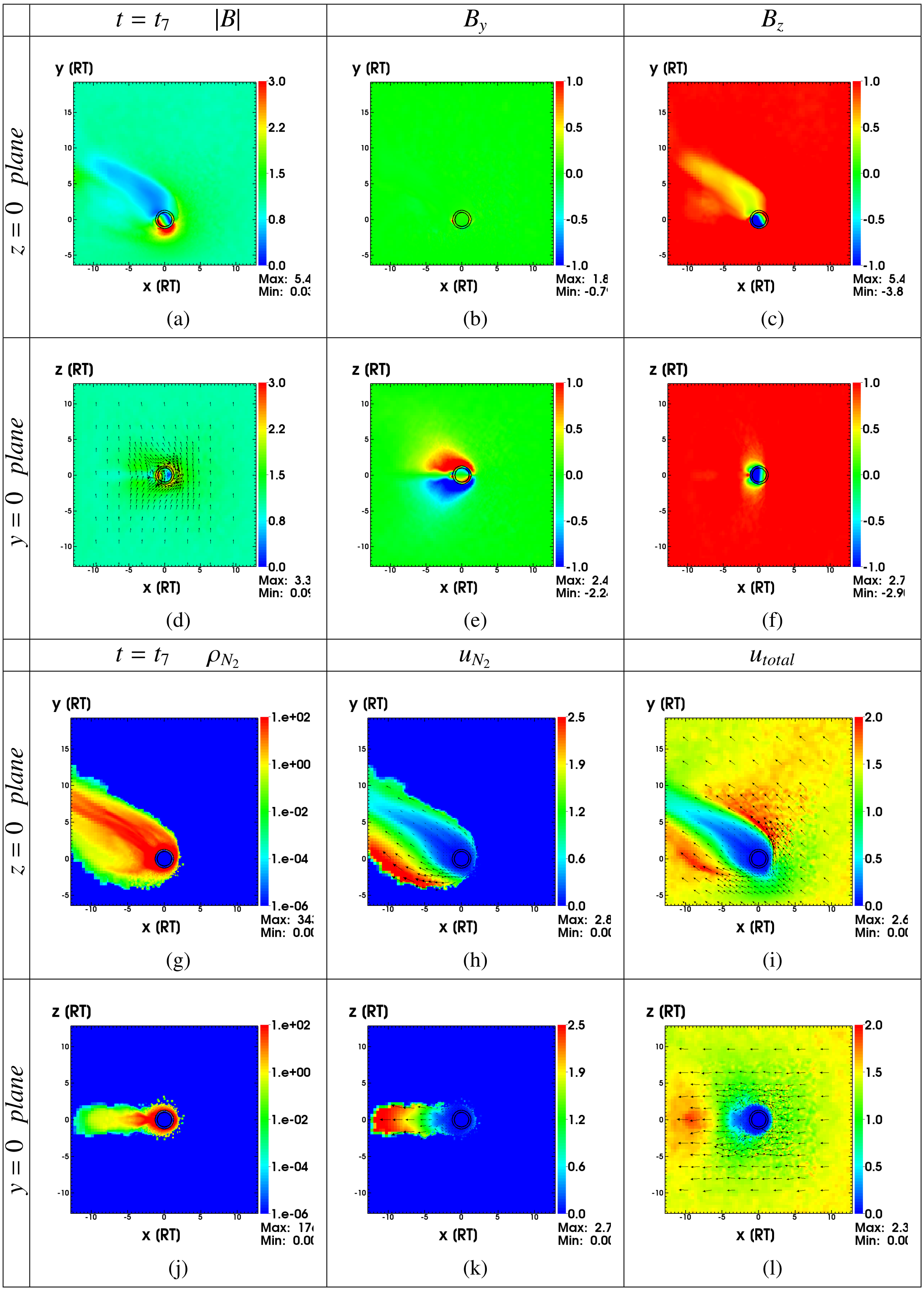

Figure 7.10: $|B|$, B_y, B_z, $\rho_{N_2^+}$, $u_{N_2^+}$ **and** u_{total} **at** t_7

At $t = t_5$ the magnetopause has arrived at the Saturn facing boundary of the simulation domain. Meanwhile the reversal of the ion tail is basically complete: the Saturn facing flank of the tail features a cycloidal shape, while the Saturn averted flank forms a straight boundary of dense heavy ion plasma (see Figure 7.11(g)). Small fluctuations of heavy ion density are still present at the upper domain boundary that slowly stream outwards, hardly influencing the surrounding plasma and therefore these small fluctuations of heavy ion density can be considered negligible. Hence, the time scale of the tail reversal is at least two times smaller compared to the antiparallel flow scenario. In contrast to simulation (A) where the huge triangle-shaped area had been shielded against the magnetosheath field (cf. Figure 7.8(a)), the magnetosheath field now fills the entire Saturn facing part of the simulation domain. The only exception is the stretched neutral sheet that forms a tube of reduced field strength which is still connected to the magnetopause, expanding more than 20 R_T downstream (cf. Figure 7.11(h)). Little changes are visible in the fossilized field draping in Figure 7.11(i), except for the enclosing magnetosheath draping having reached its final state in the meantime.

At $t = t_7$ the final, quasi-stationary state is reached. The heavy ion tail exhibits its typical shape, any fluctuations that were excited during the magnetopause crossing have vanished (see Figure 7.11(j)). The stretched neutral sheet has been cut off the magnetopause. The neutral sheet is not fully developed yet which can be seen in the magnetic field strength that is still larger than zero (see Figure 7.11(k)). Like in the antiparallel flow simulation, the fossil fields inside Titan's ionosphere have almost completely vanished. Even though the fossil contributions in Figure 7.11(l) appears to be somewhat stronger compared to Figure 7.10(e), we shall point out that this effect is limited to Titan's interior. Hence, the lifetime of fossil magnetic fields inside Titan's ionosphere is not influenced by the change in flow direction in a significant way. The high ionospheric density shields the magnetic field from the rapidly changing flow conditions that were specified in the presented simulation, regardless of whether parallel or anti parallel flow conditions are applied.

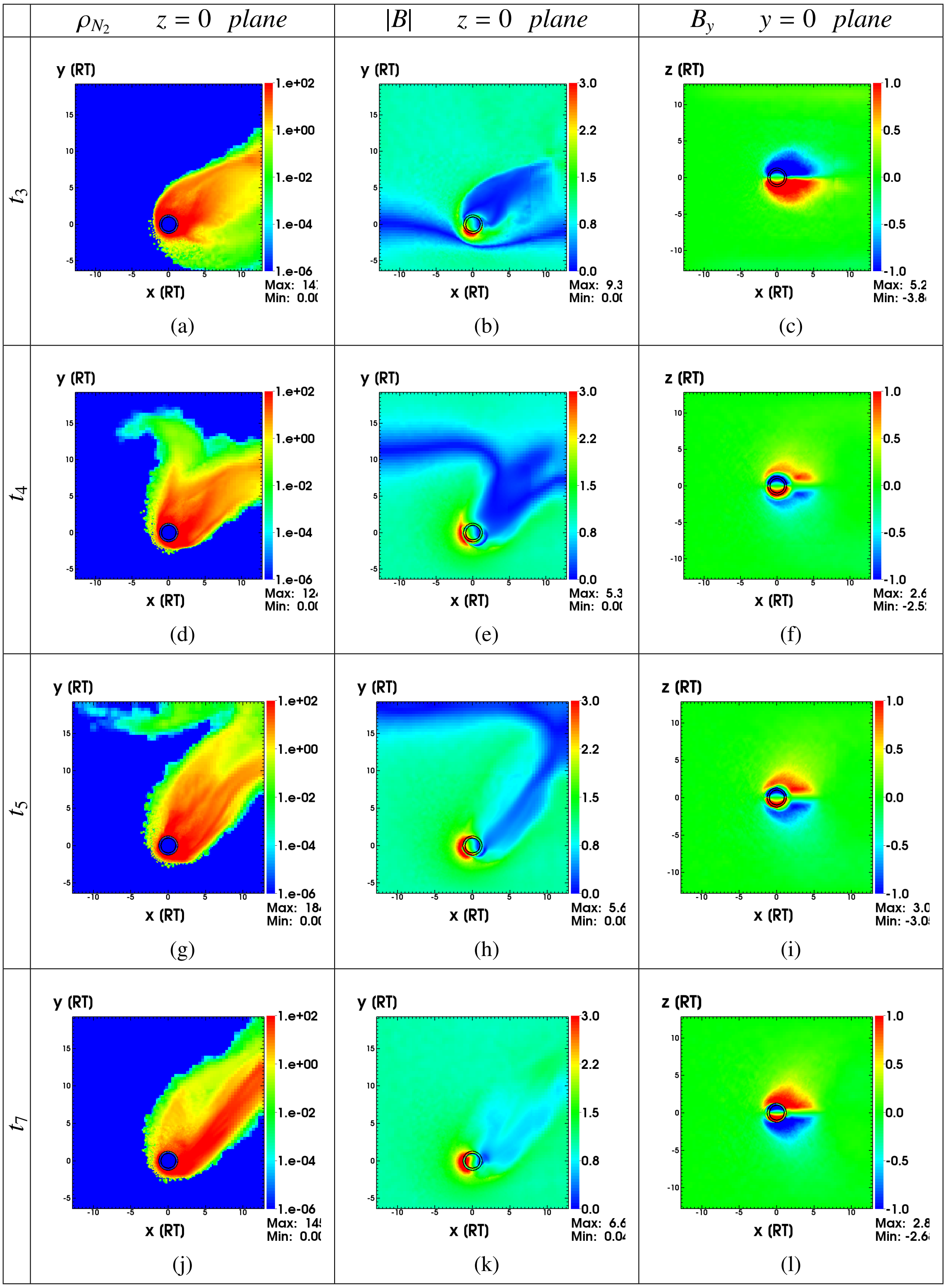

(a) (b) (c) (d) (e) (f) (g) (h) (i) (j) (k) (l)

Figure 7.11: $\rho_{N_2^+}$, $|B|$ **and** B_y **at** t_3, t_4, t_5 **and** t_7

8 Summary and Outlook

8.1 A.I.K.E.F.

The world's first adaptive hybrid simulation code for planetary plasma interactions is presented throughout this thesis, which we label A.I.K.E.F. *(Adaptive **I**on-**K**inetic **E**lectron-**F**luid)*. Adaptivity in space and time is implemented by means of Hybrid-Block-AMR, that is individual octs are refined rather than entire blocks, where an oct is one eighth of a block. This enables a significant improved mesh flexibility, compared to the ordinary block-AMR approach. The code is efficiently parallelized for distributed systems by means of the Message Passing Interface (MPI). The application of Space Filling Curves ensures optimal load balancing while communication between different CPUs is minimized. The code has been demonstrated to scale nearly linearly on up to 256 CPUs.

To the present day the code has been successfully applied to study the plasma environments of Mercury (Müller et al. 2011a,b, Wang et al. 2010), the Saturnian moons Titan (Müller et al. 2010) and Enceladus (Kriegel et al. 2009, 2011), the terrestrial moon (Wiehle et al. 2011b, Wang et al. 2011), comets (Wiehle et al. 2011a), asteroid Lutetia (Richter et al. 2011), exoplanets (Johansson et al. 2011) and nonlinear wave particle interaction (Verscharen et al. 2011).

In order to account for a reasonable number of particles in each cell, particles are refined by means of splitting and merging. Even though both methods are based on well established schemas, they have been strongly optimized for a better reduction of numerical noise and enhanced performance. In particular the workload related to particle merging is reduced such, that an efficient parallelization is possible. Both, splitting and merging, conserve total mass, momentum and energy. As particles are refined before entering meshes of higher resolution, neither splitting nor merging of particles is required within the highest level of refinement. This ensures a high accurate description of features of interest.

A broad variety of test scenarios has been considered to validate the accuracy of the code. The dispersion relation of ion whistler waves has been reproduced on both, uniform and refined meshes. By carrying out a Fourier transformation in both space and time, it has been demonstrated that waves are not reflected as they travel across refinement boundaries. By exciting a standing fast wave a sharp Mach-cone forms that reproduces the analytical opening angle and remains unaffected as it propagates from finer to coarser meshes. We furthermore verify that the results obtained on a high resolution uniform mesh are nearly identical to the results from an adaptive mesh simulation that is initialized by means of a coarse base resolution but includes various levels of refinement. An estimation of speedup shows that the adaptive simulation performs 71 times faster than the uniform mesh simulation. Simulations of the MESSENGER I and II flybys have been carried out. Under consideration of several uncertainties in plasma and dipole parameters, space-craft observations and simulation results are in very good qualitative and quantitative agreement.

From the technical point of view we regard the A.I.K.E.F. simulation model as completed with the exception of further optimizing the parallelization. As was mentioned in section 3.8, the code distributes blocks across CPUs by accounting for workload related to particles. This is in general not the ideal load distribution with respect to electromagnetic field propagation. A further improvement would be to use two independent block distributions, accounting for field computation and particle propagation, respectively. Another range for further optimization offers the combinations of several messages into a single one. If, for instance, a simulation is carried out on two CPUs and includes ten blocks that require inter CPU communication, ten messages are send per CPU whereas a single combined message would be sufficient. The more blocks and CPUs are involved, the higher the gain of a further optimized CPU communication. However, as the code scales well on the CPU number that is available to us nowadays (about 128), the above mentioned concepts will become by far more important for future simulations that might be carried out on many ten thousand CPUs.

In general the A.I.K.E.F. simulation model can be used to model scenarios that involve plasma processes on different spatial scales. For instance it enables the possibility of modeling the fine structures of the Enceladus plasma interaction by resolving the individual jets emerging from the moons surface (Kriegel et al. 2009). However, apart from the ability to model scenarios at high accuracy, the application of AMR offers the great opportunity to execute simulations that took weeks or even months before within a few hours. When comparing the execution speed of the A.I.K.E.F. simulation code the Bagdonat2002 code, we measure a gain of six in speedup due to optimization even on uniform and serial simulation runs(see section 5.1). A further gain of 71 due to the application of AMR (see section 5.5). Additionally a gain of 40 in speed up is achieved when executed on 64 CPUs (see section 3.8), resulting in the remarkable total speedup of larger than 17000, compared to a serial simulation of our successor code version.

8.2 Mercury

After having shown in chapter 5 that the simulation results of Mercury's plasma environment represent well the MESSENGER measurements, we have carried out hybrid simulations in order to advance the understanding of Mercury's dayside boundary layer and "double magnetopause". An idealized IMF and dipole field configuration has been used to simplify the analysis but referring to the preceding simulations we are confident that the physical processes involved are valid for the real configuration as well. The major findings are summarized below:

- The simulation shows a region of decreased magnetic field strength that is consistent with the pre-orbital-phase MESSENGER observations for the dayside boundary layer in both, width and field magnitude as discussed by Slavin et al. (2008) and Anderson et al. (2011). The proton plasma quantities such as density, pressure and temperature inside the dayside boundary layer are very similar to what has been estimated by Raines et al. (2011) for the dayside boundary layer during the MESSENGER flybys.

- As a single species hydrogen plasma is used that is exclusively injected at the domain boundaries, the simulation suggest that the dayside boundary layer may exist even in the absence of any exospheric ions like sodium. The boundary layer is populated by solar wind protons that enter Mercury's magnetosphere downstream and subsequently are accelerated planet-wards. The planet-ward acceleration is a consequence of the $\underline{j} \times \underline{B}$-force that results from the configuration of neutral sheet current and dipole field.

- The dayside boundary layer region is confined by a double current sheet. Both current sheets are similar in orientation, but the outer one is stronger in intensity. The occurrence of this "double magnetopause" configuration is in agreement with the MESSENGER observations discussed by Slavin et al. (2008).

- While the outer current sheet can be considered the classical magnetopause, the inner "boundary layer current" turns out to be a diamagnetic current sustained by solar wind protons that are mirrored between north and south pole. This boundary layer current extends to Mercury's nightside and dusk-side causing the nightside diamagnetic decrease. It exhibits a semi-circle shape and closes with the magnetopause current.

- The conjunction of boundary layer current and Mercury's dipole field causes a $\underline{j} \times \underline{B}$-force that prevents the protons from entering the inner magnetosphere, thereby enhancing the outward directed proton pressure gradient at the boundary layer's inner edge.

One next step to further improve the quantitative results of the boundary layer is to increase the spatial resolution of the numerical mesh. In particular for quantitative comparison of the magnetic field jump at the boundary layer's inner edge an increased resolution is desirable. The same applies for the nightside boundary layer which is still a rather transient structure in our simulations, most likely due to the limited resolution.

Secondly the influence of exospheric ions like sodium on the boundary layer formation should be tested for different production rates. Even though our simulations show that the layer may exist in the absence of exospheric ions, the physical processes involved might be different when heavy ions are included.

Finally preliminary simulation results suggest that different conductivity profiles for Mercury's interior may influence the boundary layer location. This should be investigated more precisely since in doing so, it might be possible to derive information on Mercury's interior from the boundary layer's shape and distance to the planetary surface.

8.3 Titan

We have carried out two hybrid simulations in order to investigate the plasma environment of Saturn's moon Titan during a magnetopause crossing, comparable to the one observed by Cassini during the T32 flyby. While in simulation (A), a geometry with antiparallel magnetospheric and magnetosheath has been studied, the flows were considered parallel in simulation (B). This study was motivated by the fact that so far, none of the existing simulation models had considered a shear between magnetospheric and magnetosheath flow. This allowed an indepth analysis of the fossilization of magnetic fields in Titan's ionosphere as well as reconfigurations of the heavy ion tail and its feedback onto the Titan plasma environment.

Major findings of our simulations are:

- According to our simulations, the lifetime of fossil magnetic fields in Titan's ionosphere can estimated to be at least 25 minutes, which is in good agreement with observations of the T32 encounter and is well covered by our analytical estimation.
- The change of the ambient flow direction does not influence the lifetime of fossil magnetic fields in Titan's ionosphere in any significant way. The high ionospheric density shields the trapped magnetic field from rapidly changing ambient flow conditions, regardless of whether parallel or antiparallel flow conditions are applied.
- In contrast to the magnetic field configuration, the change in ambient flow direction does strongly influence the timescale of the heavy ion tail reconfiguration. In the parallel flow scenario (B) the direction of the tail remains aligned with the upstream plasma flow throughout the entire simulation. Its cycloidal shape is rotated within 4 minutes. In the antiparallel flow simulation (A), the entire tail is rotated by 90° in direction of the magnetosheath plasma flow. This process takes approximately 24 minutes and is accompanied by the excitation of large scale instabilities.

In both simulations (A) and (B) the lifetime of fossil magnetic fields is limited due to the convection time. Since the simulations do not account for a realistic ionospheric chemistry, the convection speed could be over estimated. Likewise the lifetime of fossil magnetic fields could be larger. For instance we observe an ionospheric velocity which is about 2% of the upstream velocity. However according to Neubauer et al. (2006) the velocity may decrease even down to 0.1% of the upstream velocity which is 20 time smaller than in our simulation. Hence, the time scales of fossil magnetic field survival that is estimated by the presented study should be regarded as a lower limit. The investigation of fossil magnetic fields under the inclusion of a more realistic ionospheric chemistry is one aspect that should be considered in future work.

Bibliography

Achilleos, N., Arridge, C. S., Bertucci, C., Jackman, C. M., Dougherty, M. K., Khurana, K. K., Russell, C. T., 2008, Large-scale dynamics of saturn's magnetopause: Observations by cassini, Journal of Geophysical Research (Space Physics), 113, 11 209–+

Alexeev, I. I., Belenkaya, E. S., Slavin, J. A., Korth, H., Anderson, B. J., Baker, D. N., Boardsen, S. A., Johnson, C. L., Purucker, M. E., Sarantos, M., Solomon, S. C., 2010, Mercury's magnetospheric magnetic field after the first two MESSENGER flybys, Icarus, 209, 23–39

Anderson, B. J., Acuña, M. H., Korth, H., Purucker, M. E., Johnson, C. L., Slavin, J. A., Solomon, S. C., McNutt, R. L., 2008, The Structure of Mercury's Magnetic Field from MESSENGER's First Flyby, Science, 321, 82

Anderson, B. J., Acuña, M. H., Korth, H., Slavin, J. A., Uno, H., Johnson, C. L., Purucker, M. E., Solomon, S. C., Raines, J. M., Zurbuchen, T. H., Gloeckler, G., McNutt, R. L., 2010, The Magnetic Field of Mercury, Space Science Reviews, 152, 307–339

Anderson, M., Slavin, J., Horth, H., 2011, The dayside magnetospheric boundary layer at mercury, Planetary and Space Science

Arridge, C. S., Russell, C. T., Khurana, K. K., Achilleos, N., André, N., Rymer, A. M., Dougherty, M. K., Coates, A. J., 2007, Mass of Saturn's magnetodisc: Cassini observations, Geophys. Res. Lett., 34, L09 108, doi: 10.1029/2006GL028 921

Arridge, C. S., Khurana, K. K., Russell, C. T., Southwood, D. J., Achilleos, N., Dougherty, M. K., Coates, A. J., Leinweber, H. K., 2008, Warping of Saturn's magnetospheric and magnetotail current sheets, J. Geophys. Res., 113, A08 217, doi:10.1029/2007JA012 963

Backes, H., 2005, Titan's Interaction with the Saturnian Magnetospheric Plasma, Ph.D. thesis, Universität zu Köln

Backes, H., Neubauer, F. M., Dougherty, M. K., Achilleos, N., André, N., Arridge, C. S., Bertucci, C., Jones, G. H., Khurana, K. K., Russell, C. T., Wennmacher, A., 2005, Titan's Magnetic Field Signature During the First Cassini Encounter, Science, 308, 992–995

Bagdonat, T., 2005, Hybrid Simulation of Weak Comets, Ph.D. thesis, Technische Universität Braunschweig

Bagdonat, T., Motschmann, U., 2001, 3d hybrid simulation of solar wind interaction with comets, in Space Plasma Simulation - Proceedings of the Sixth International School/ Symposium ISSS-6, (Eds.) J. Büchner, C. Dum, M. Scholer, pp. 80–83

Bagdonat, T., Motschmann, U., 2002, 3D Hybrid Simulation Code Using Curvilinear Coordinates, J. of Computational Physics, 183, 470–485

Baumjohann, W., Treumann, R. A., 1999, Basic space plasma physics, Imperial College Press, London

Berger, M. J., Oliger, J., 1984, Adaptive Mesh Refinement for Hyperbolic Partial Differential Equations, Journal of Computational Physics, 53, 484–+

Bertucci, C., Achilleos, N., Dougherty, M. K., Modolo, R., Coates, A. J., Szego, K., Masters, A., Ma, Y., Neubauer, F. M., Garnier, P., Wahlund, J.-E., Young, D. T., 2008, The Magnetic Memory of Titan's Ionized Atmosphere, Science, 321, 1475–1478

Bertucci, C., Sinclair, B., Achilleos, N., Hunt, P., Dougherty, M. K., Arridge, C. S., 2009, The variability of Titan's magnetic environment, Planet. Space Sci., pp. 1813–1820, doi: 10.1016/j.pss.2009.02.009

Bößwetter, A., Bagdonat, T., Motschmann, U., Sauer, K., 2004, Plasma boundaries at Mars: A 3D simulation study, Ann. Geophys., 22, 4363–4379

Brackbill, J. U., Barnes, J., 1980, The Effect of Nonzero divB on the Numerical Solution of the Magnetohydrodynamic Equations, J. of Computational Physics, 35, 426

Brecht, S. H., Luhmann, J. G., Larson, D. J., 2000, Simulation of the Saturnian magnetospheric interaction with Titan, J. Geophys. Res., 105, 13,119–13,130

Büchner, J., Dum, C., Scholer, M. (Eds.), 2003, Space Plasma Simulation, vol. 615 of Lecture Notes in Physics, Berlin Springer Verlag

Childs, H., Brugger, E., Bonnell, K., Meredith, J., Miller, M., Whitlock, B., Max, N., 2005, A Contract-Based System for Large Data Visualization, Proceedings of IEEE Visualization, pp. 190–198

Coates, A. J., McAndrews, H. J., Arridge, C. S., Jones, G. H., Crary, F. J., Young, D. T., Szego, K., Sittler, E. C., Thomsen, M. F., Tokar, R. L., Bertucci, C., Dougherty, M. K., 2007, Titan at Saturn's magnetopause: CAPS results from T32, AGU Fall Meeting Abstracts, pp. A1021+

Dougherty, M. K., Kellock, S., Southwood, D. J., Balogh, A., Smith, E. J., Tsurutani, B. T., Gerlach, B., Glassmeier, K.-H., Gleim, F., Russell, C. T., Erdos, G., Neubauer, F. M., Cowley, S. W. H., 2004, The Cassini Magnetic Field Investigation, Space Science Reviews, 114, 331–383, doi:10.1007/s11 214–004–1432–2

Dreher, J., Grauer, R., 2005, Racoon: A parallel mesh-adaptive framework for hyperbolic conservation laws, Parallel Computing, 231

Fujimoto, K., Machida, S., 2006a, Full particle simulation of the plasma sheet using adaptive mesh refinement technique, Advances in Space Research, 37, 1348–1353

Fujimoto, K., Machida, S., 2006b, Electromagnetic full particle code with adaptive mesh refinement technique: Application to the current sheet evolution, Journal of Computational Physics, 214, 550–566

Fuselier, S. A., Lockwood, M., Onsager, T. G., Peterson, W. K., 1999, The source population for the cusp and cleft/LLBL for southward IMF, Geophysical Research Letters, 26, 1665–1668

Garnier, P., Wahlund, J., Rosenqvist, L., Modolo, R., Ågren, K., Sergis, N., Canu, P., Andre, M., Gurnett, D. A., Kurth, W. S., Krimigis, S. M., Coates, A., Dougherty, M., Waite, J. H., 2009, Titan's ionosphere in the magnetosheath: Cassini RPWS results during the T32 flyby, Annales Geophysicae, 27, 4257–4272

Glassmeier, K.-H., 2000, Currents in Mercury's Magnetosphere, pp. 371–+, The American Geophysical Union

Glassmeier, K.-H., Espley, J., 2006, ULF Waves in Planetary Magnetospheres, in Magnetospheric ULF Waves: Synthesis and New Directions, vol. 169 of Washington DC American Geophysical Union Geophysical Monograph Series, pp. 341–+

Glassmeier, K.-H., Mager, P. N., Klimushkin, D. Y., 2003, Concerning ULF pulsations in Mercury's magnetosphere, Geophysical Research Letters, 30, 1928

Glassmeier, K.-H., Klimushkin, D., Othmer, C., Mager, P., 2004, Ulf waves at mercury: Earth, the giants, and their little brother compared, Advances in Space Research, 33, 1875–1883

Glassmeier, K.-H., Auster, H.-U., Motschmann, U., 2007, A feedback dynamo generating Mercury's magnetic field, Geophysical Research Letters, 34, L22 201

Gombosi, T. I., De Zeeuw, D. L., Powell, K. G., Ridley, A., Sokolov, I. V., Stout, Q. F., Tóth, G., 2003, Adaptive Mesh Refinement for Global Magnetohydrodynamic Simulation, in Space Plasma Simulation, (Eds.) J. Büchner, C. T. Dum, M. Scholer, pp. 247–274, Springer-Verlag, Berlin/ Heidelberg/ New York

Gortsas, N., Motschmann, U., Kührt, E., Glassmeier, K.-H., Hansen, K. C., Müller, J., Schmidt, A., 2010, Global plasma-parameter simulation of Comet 67P/Churyumov-Gerasimenko approaching the Sun, Astronomy and Astrophysics, 520, A92+

Grosser, J., Glassmeier, K., Stadelmann, A., 2004, Induced magnetic field effects at planet Mercury, Planetary and Space Science, 52, 1251–1260

Hood, L., Schubert, G., 1979, Inhibition of solar wind impingement on Mercury by planetary induction currents, Journal of Geophysical Research, 84, 2641–2647

Janhunen, P., Kallio, E., 2004, Surface conductivity of mercury provides current closure and may affect magnetospheric symmetry, Annales Geophysicae, 22, 1829–1837

Johansson, E. P. G., Mueller, J., Motschmann, U., 2011, Interplanetary magnetic field orientation and the magnetospheres of close-in exoplanets, Astronomy and Astrophysics, 525, 117+

Kallio, E., Janhunen, P., 2003, Modelling the solar wind interaction with Mercury by a quasi-neutral hybrid model, Ann. Geophys., 21, 2133–2145

Kallio, E., Sillanpää, I., Janhunen, P., 2004, Titan in subsonic and supersonic flow, Geophys. Res. Lett., 31, L15 703, doi: 10.1029/2004GL020 344

Keppens, R., Nool, M., Tóth, G., Goedbloed, J. P., 2003, Adaptive Mesh Refinement for conservative systems: multi-dimensional efficiency evaluation, Computer Physics Communications, 153, 317–339, `arXiv:astro-ph/0403124`

Khokhlov, A., 1998, Fully Threaded Tree Algorithms for Adaptive Refinement Fluid Dynamics Simulations, Journal of Computational Physics, 143, 519–543, `arXiv:astro-ph/9701194`

Khurana, K. K., Mitchell, D. G., Arridge, C. S., Dougherty, M. K., Russell, C. T., Paranicas, C., Krupp, N., Coates, A. J., 2009, Sources of rotational signals in saturn's magnetosphere, Journal of Geophysical Research (Space Physics), 114, 2211–+

Kriegel, H., Simon, S., Müller, J., Motschmann, U., Saur, J., Glassmeier, K., Dougherty, M. K., 2009, The plasma interaction of Enceladus: 3D hybrid simulations and comparison with Cassini MAG data, Planet. Space Sci., 57, 2113–2122, doi: 10.1016/j.pss.2009.09.025

Kriegel, H., Simon, S., Motschmann, U., Saur, J., Neubauer, F. M., Persoon, A. M., Dougherty, M. K., Gurnett, D. A., 2011, Influence of negatively charged plume grains on the structure of Enceladus' Alfvén wings: hybrid simulations versus Cassini MAG data, Journal of Geophysical Research (Space Physics), p. in press

Lapenta, G., 2002, Particle rezoning for multidimensional kinetic particle-in-cell simulations, Journal of Computational Physics, 181, 317–337

Leroy, M. M., Winske, D., Goodrich, C. C., Wu, C. S., Papadopoulos, K., 1982, The structure of perpendicular bow shocks, Journal of Geophysical Research, 87, 5081–5094

Lipatov, A. S., 2002, The hybrid multiscale simulation technology: an introduction with application to astrophysical and laboratory plasmas

Luhmann, J. G., 1996, Titan's ion exosphere wake: A natural ion mass spectrometer?, J. Geophys. Res., 101, 29.387–29,393

Ma, Y.-J., Nagy, A. F., Cravens, T. E., Sokolov, I. V., Hansen, K. C., Wahlund, J.-E., Crary, F. J., Coates, A. J., Dougherty, M. K., 2006, Comparisons between MHD model calculations and observations of Cassini flybys of Titan, J. Geophys. Res., 111, A05 207 (doi:10.1029/2005JA011 481)

Ma, Y. J., Russell, C. T., Nagy, A. F., Toth, G., Bertucci, C., Dougherty, M. K., Neubauer, F. M., Wellbrock, A., Coates, A. J., Garnier, P., Wahlund, J.-E., Cravens, T. E., Crary, F. J., 2009, Time-dependent global MHD simulations of Cassini T32 flyby: From magnetosphere to magnetosheath, J. Geophys. Res., 114, A03 204, doi: 10.1029/2008JA013 676

Matthews, A. P., 1994, Current Advance Method and Cyclic Leapfrog for 2D Multispecies Hybrid Plasma Simulations, J. of Computational Physics, 112, 102–116

Milillo, A., Wurz, P., Orsini, S., Delcourt, D., Kallio, E., Killen, R. M., Lammer, H., Massetti, S., Mura, A., Barabash, S., Cremonese, G., Daglis, I. A., Angelis, E., Lellis, A. M., Livi, S., Mangano, V., Torkar, K., 2005, Surface-Exosphere-Magnetosphere System Of Mercury, Space Science Rev., 117, 397–443

Modolo, R., Chanteur, G. M., 2008, A global hybrid model for Titan's interaction with the Kronian plasma: Application to the Cassini Ta flyby, Journal of Geophysical Research (Space Physics), 113, 1317–+, doi:10.1029/2007JA012 453

Motschmann, U., Sauer, K., Roatsch, T., 1992, Simulation of ion acceleration in a charged dust cloud, Geophysical Research Letters, 19, 225–228

Müller, J., Simon, S., Motschmann, U., Glassmeier, K. H., Saur, J., Schuele, J., Pringle, G. J., 2010, Magnetic field fossilization and tail reconfiguration in Titan's plasma environment during a magnetopause passage: 3D adaptive hybrid code simulations , Planet. Space Sci., 58, 1526–1546, doi: 10.1016/j.pss.2010.07.018

Müller, J., Simon, S., Motschmann, U., Schüle, J., Glassmeier, K., Pringle, G. J., 2011a, A.I.K.E.F.: Adaptive hybrid model for space plasma simulations, Computer Physics Communications, 182, 946–966

Müller, J., Simon, S., Wang, Y. C., Motschmann, U., Heyner, D., Schuele, J., Ip, W. H., Kleindienst, G., Pringle, G. J., 2011b, Origin of Mercury's Double Magnetopause: 3D Hybrid Simulation Study with A.I.K.E.F., submitted to ICARUS

Nagy, A. F., Liu, Y., Hansen, K. C., Kabin, K., Gombosi, T. I., Combi, M. R., DeZeeuw, D. L., 2001, The interaction between the magnetosphere of Saturn and Titan's ionosphere, J. Geophys. Res., 106, 6151–6160

Ness, N. F., Acuna, M. H., Behannon, K. W., Neubauer, F. M., 1982, The induced magnetosphere of Titan, J. Geophys. Res., 87, 1369–1381

Neubauer, F. M., Backes, H., Dougherty, M. K., Wennmacher, A., Russell, C. T., Coates, A., Young, D., Achilleos, N., Andre, N., Arridge, C. S., Bertucci, C., Jones, G. H., Khurana, K. K., Knetter, T., Law, A., Lewis, G. R., Saur, J., 2006, Titan's near magnetotail from magnetic field and plasma observations and modelling: Cassini flybys TA, TB and T3, J. Geophys. Res., 111, A10 220, doi:10.1029/2006JA011 676

Neubauer, F. M., Gurnett, D. A., Scudder, J. D., Hartle, R. E., 1984, Titan's magnetospheric interaction, in Saturn, (Eds.) T. Gehrels, M. S. Matthews, pp. 760–787, University of Arizona Press, Tucson, Arizona

Omidi, N., Blanco-Cano, X., Russel, C. T., Karimabadi, H., Acuna, M., 2002, Hybrid simulations of solar wind interaction with magnetized asteroids: General characteristics, J. Geophys. Res., 107, 12,1–12,10

Raeder, J., Neubauer, F. M., Ness, N. F., Burlaga, L. F., 1987, Macroscopic perturbations of the imf by p/ halley as seen by the giotto magnetometer, Astronomy and Astrophys., 187, 61–64

Raines, J. M., Slavin, J. A., Zurbuchen, T. H., Gloeckler, G., Anderson, B. J., Baker, D. N., Korth, H., Krimigis, S. M., Jr, R. L. M., 2011, MESSENGER observations of the plasma environment near Mercury, Planetary and Space Science, In Press, Corrected Proof

Richter, I., Auster, H., Glassmeier, K., Koenders, C., Carr, C., Motschmann, U., Müller, J., McKenna-Lawlor, S., 2011, Magnetic field measurements during the rosetta flyby at asteroid (21)lutetia, Planetary and Space Science, doi:10.1016/j.pss.2011.08.009

Rosenqvist, L., Wahlund, J., Ågren, K., Modolo, R., Opgenoorth, H. J., Strobel, D., Müller-Wodarg, I., Garnier, P., Bertucci, C., 2009, Titan ionospheric conductivities from Cassini measurements, Planet. Space Sci., 57, 1828–1833, doi: 10.1016/j.pss.2009.01.007

Roussos, E., Mueller, J., Simon, S., Boesswetter, A., Motschmann, U., Krupp, N., Fraenz, M., Woch, J., Khurana, K. K., Dougherty, M. K., 2008, Plasma and fields in the wake of Rhea: 3-D hybrid simulation and comparison with Cassini data, Annales Geophysicae, 26, 619–637

Simon, S., 2007a, Titan's highly variable plasma environment: A 3D hybrid simulation study, Ph.D. thesis, Technische Universität Braunschweig

Simon, S., 2007b, Titan's highly variable plasma environment: A 3D hybrid simulation study, Ph.D. thesis, Technische Universität Braunschweig

Simon, S., 2009, Real-time 3D hybrid simulation of Titan's plasma interaction during a solar wind excursion, Annales Geophysicae, (submitted)

Simon, S., Motschmann, U., 2009, Titan's induced magnetosphere under non-ideal upstream conditions: 3D multi-species hybrid simulations, Planet. Space Sci., 57, 2001–2015, doi: 10.1016/j.pss.2009.08.010

Simon, S., Bagdonat, T., Motschmann, U., Glassmeier, K.-H., 2006a, Plasma environment of magnetized asteroids: A 3D hybrid simulation study, Annales Geophysicae, 24, 407–414

Simon, S., Boesswetter, A., Bagdonat, T., Motschmann, U., Glassmeier, K.-H., 2006b, Plasma environment of Titan: a 3-d hybrid simulation study, Ann. Geophys., 24, 1113–1135

Simon, S., Boesswetter, A., Bagdonat, T., Motschmann, U., Schuele, J., 2007, Three-dimensional multispecies hybrid simulation of Titan's highly variable plasma environment, Ann. Geophys., 25, 117–144

Simon, S., Motschmann, U., Glassmeier, K.-H., 2008, Influence of non-stationary electromagnetic field conditions on ion pick-up at Titan: 3-d multispecies hybrid simulations, Ann. Geophys., 26, 599–617

Simon, S., Motschmann, U., Kleindienst, G., Saur, J., Bertucci, C., Dougherty, M., Arridge, C., Coates, A., 2009a, Titan's plasma environment during a magnetosheath excursion: Real-time scenarios for Cassini's T32 flyby from a hybrid simulation, Annales Geophysicae, 27(2), 669–685

Simon, S., Saur, J., Neubauer, F., Motschmann, U., Dougherty, M., 2009b, Plasma wake of Tethys: Hybrid simulations versus Cassini MAG data, Geophys. Res. Lett., Vol. 36, L04 108, doi: 10.1029/2008GL036 943

Simpson, R. B., 1978, Automatic Local Refinement for Irregular Rectangular Meshes, Int. Jour. for numerical methods in engineering, 14, 1665–1678

Slavin, J. A., Acuña, M. H., Anderson, B. J., Baker, D. N., Benna, M., Gloeckler, G., Gold, R. E., Ho, G. C., Killen, R. M., Korth, H., Krimigis, S. M., McNutt, R. L., Nittler, L. R., Raines, J. M., Schriver, D., Solomon, S. C., Starr, R. D., Trávníček, P., Zurbuchen, T. H., 2008, Mercury's Magnetosphere After MESSENGER's First Flyby, Science, 321, 85–

Slavin, J. A., Acuña, M. H., Anderson, B. J., Baker, D. N., Benna, M., Boardsen, S. A., Gloeckler, G., Gold, R. E., Ho, G. C., Korth, H., Krimigis, S. M., McNutt, R. L., Raines, J. M., Sarantos, M., Schriver, D., Solomon, S. C., Trávníček, P., Zurbuchen, T. H., 2009, MESSENGER Observations of Magnetic Reconnection in Mercury's Magnetosphere, Science, 324, 606–

Snowden, D., Winglee, R., Bertucci, C., Dougherty, M., 2007, Three-dimensional multifluid simulation of the plasma interaction at Titan, Journal of Geophysical Research (Space Physics), 112, 12 221–+, doi:10.1029/2007JA012 393

Suess, S. T., Goldstein, B. E., 1979, Compression of the Hermaean magnetosphere by the solar wind, Journal of Geophysical Research, 84, 3306–3312

Sundberg, T., Boardsen, S. A., Slavin, J. A., Blomberg, L. G., Korth, H., 2010, The Kelvin-Helmholtz instability at Mercury: An assessment, Planetary and Space Science, 58, 1434–1441

Trávníček, P. M., Hellinger, P., Schriver, D., 2007, Structure of Mercury's magnetosphere for different pressure of the solar wind: Three dimensional hybrid simulations, Geophys. Res. Lett., 35, L05 104 (1–5), doi: 10.10292 006GL028 518

Trávníček, P. M., Hellinger, P., Schriver, D., Herčík, D., Slavin, J. A., Anderson, B. J., 2009, Kinetic instabilities in Mercury's magnetosphere: Three-dimensional simulation results, Geophys. Res. Lett., 36, L07 104

Trávníček, P. M., Schriver, D., Hellinger, P., Herčík, D., Anderson, B. J., Sarantos, M., Slavin, J. A., 2010, Mercury's magnetosphere-solar wind interaction for northward and southward interplanetary magnetic field: Hybrid simulation results, Icarus, 209, 11–22

Uyeshima, M., Schultz, A., 2000, Geoelectromagnetic induction in a heterogeneous sphere:a new three-dimensional forward solver using a conservative staggered-grid finite difference method, Geophysical Journal International, 140, 636–650

van der Holst, B., Keppens, R., 2007, Hybrid block-AMR in cartesian and curvilinear coordinates: MHD applications, Journal of Computational Physics, 226, 925–946

Verscharen, D., Marsch, E., Motschmann, U., Müller, J., 2011, Cascade of weak solar wind turbulence beyond MHD scales in two-dimensional hybrid simulations, submitted to Physics of Plasmas

Wahlund, J.-E., Boström, R., Gustafsson, G., Gurnett, D. A., Kurth, W. S., Pedersen, A., Averkamp, T. F., Hospodarsky, G. B., Persoon, A. M., Canu, P., Neubauer, F. M., Dougherty, M. K., Eriksson, A. I., Morooka, M. W., Gill, R., André, M., Eliasson, L., Mueller-Wordag, I., 2005, Cassini Measurements of Cold Plasma in the Ionosphere of Titan, Science, 308, 986–989

Wang, Y., Mueller, J., Motschmann, U., Ip, W., 2010, A hybrid simulation of Mercury's magnetosphere for the MESSENGER encounters in year 2008, Icarus, 209, 46–52

Wang, Y. C., Müller, J., Ip, W. H., Motschmann, U., 2011, A 3D Hybrid Simulation Study of the Electromagnetic Field Distributions in the Lunar Wake, submitted to ICARUS

Wei, H. Y., Russell, C. T., Wellbrock, A., Dougherty, M. K., Coates, A. J., 2009, Plasma environment at Titan's orbit with Titan present and absent, Geophys. Res. Lett., 36, L23 202, doi: 10.1029/2009GL041 048

Wiehle, S., Motschmann, U., Gortsas, N., Glassmeier, K.-H., Müller, J., Koenders, C., 2011a, Simulation of cometary jets in interaction with the solar wind, Advances in Space Research, 48, 1108–1113

Wiehle, S., Plaschke, F., Motschmann, U., Glassmeier, K.-H., Auster, H. U., Angelopoulos, V., Mueller, J., Kriegel, H., Georgescu, E., Halekas, J., Sibeck, D. G., McFadden, J. P., 2011b, First lunar wake passage of ARTEMIS: Discrimination of wake effects and solar wind fluctuations by 3D hybrid simulations, Planetary and Space Science, 59, 661–671

Winglee, R., Snowden, D., Kidder, A., 2009, Modification of Titan's ion tail and the Kronian magnetosphere: Coupled magnetospheric simulations, J. Geophys. Res., 114, A05 215, doi: 10.1029/2008JA013 343

Winske, D., Leroy, M. M., 1985, Hybrid simulation techniques applied to the earth's bow shock, in Computer Simulation of Space Plasmas, (Ed.) H. Matsumoto & T. Sato, pp. 255–278

Danksagung

Ich möchte mich vor allem bei Herrn Professor Motschmann bedanken. Zum einen danke ich ihm für die große Freiheit, die er mir in der Bearbeitung meines Themas ließ. Dabei konnte ich mich stets auf seine Unterstützung verlassen. In zahlreichen Gesprächen diskutierten wir die Ergebnisse und deren Interpretation. Außerdem gestand er mir stets genügend Zeit zur Veröffentlichung auch umfangreicher Artikel zu. Aber auch schon vor der Zeit in seiner Arbeitsgruppe profitierte ich in meinem Studium von seinen exzellenten Vorlesungen in der theoretischen Physik. Insbesondere von seinen äußerst verständlich formulierten Skripten habe ich mehr gelernt als aus so manchem Lehrbuch.

Ich möchte mich einerseits bei Herrn Professor Glaßmeier dafür bedanken, dass er diese Arbeit als Zweitgutachter betreut hat. In vielen Diskussionen und Kommentaren zu meinen Veröffentlichungen profitierte ich von seinem umfangreichem Wissen. Darüber hinaus verdanke ich ihm durch seine Vorlesungen meine grundlegenden Kenntnisse in der Plasmaphysik. Ihm gelang es stets, die physikalischen Sachverhalte auf sehr anschauliche und verständliche Weise darzustellen.

Genauso möchte ich mich bei Herrn Dr. Schüle für die Betreuung dieser Arbeit bedanken. Neben vielen Ratschlägen bezüglich effizienter Parallelisierung machte er mich auf das HPC2-Europa Programm aufmerksam und unterstützte mich bei dessen Beantragung. Dieses ermöglichte mir einen äußerst interessanten, zweimonatigen Aufenthalt an der Universität Edinburgh, in dessen Rahmen ich meine Informatik-Kenntnisse deutlich erweitern konnte.

Ein ebenso großer Dank gebührt Sven Simon, mit dem ich seit meiner Diplomarbeit in ständigem Kontakt stehe. Seine Koautorschaft auf jedem meiner Artikel zeigt, dass wir auch nach seinem Wechsel an die Universität von Köln genauso eng zusammen arbeiten, wie während seiner Zeit in Braunschweig. In ungezählten Diskussionen gab er mir viele Impulse und Ideen bezüglich der Interpretation von Ergebnissen und ebenso Hinweise auf entsprechende Literatur. Aber auch schon während meiner Zeit als Student habe ich oft von seiner großen Hilfsbereitschaft bei der Bearbeitung von Aufgaben in der theoretischen Physik profitiert.

Bei meinen Kollegen und Freunden möchte ich mich für die tolle Atmosphäre in unserer Arbeitsgruppe und die schöne Zeit in Braunschweig bedanken. Nicht zuletzt danke ich meinen Eltern und meinem Bruder dafür, dass sie mich in meinem bisherigen Lebensweg zu jedem Zeitpunkt unterstützt haben.

Lebenslauf

Name: Joachim Müller
Geburtsdatum: 25.02.1981
Geburtsort: Oldenburg
Staatsangehörigkeit: deutsch
Familienstand: ledig

03/2007 bis 11/2011: Promotion am Institut für Theoretische Physik der Technischen Universität Braunschweig

02/2007: Diplom der Physik (Abschlußnote: 1,1)
10/2001 bis 02/2007: Studium der Physik an der TU Braunschweig (Diplomarbeit: “Entwicklung eines numerischen Modells zur Untersuchung der Wechselwirkung leitfähiger Objekte mit dem Sonnenwind” Abschlußnote: 1,0)

04/2001 bis 10/2001: Studium der Mathematik, Carl-von-Ossietzky Universität, Oldenburg

07/2000 bis 04/2001: Grundwehrdienst, Luftwaffe, Oldenburg

06/2000: Allgemeine Hochschulreife

1993 bis 2000: Liebfrauenschule, Oldenburg

1991 bis 1993: Paulusschule, Oldenburg

1987 bis 1991: Lerigauschule, Oldenburg

Wissenschaftliche Veröffentlichungen allgemeiner Art

Gortsas, N., Motschmann, U., Kührt, E., Glassmeier, K.-H., Hansen, K. C., Müller, J., Schmidt, A., 2010, Global plasma-parameter simulation of Comet 67P/Churyumov-Gerasimenko approaching the Sun, Astronomy and Astrophysics, 520, A92

Johansson, E. P. G., Mueller, J., Motschmann, U., 2011, Interplanetary magnetic field orientation and the magnetospheres of close-in exoplanets, Astronomy and Astrophysics, 525, 117

Kriegel, H., Simon, S., Müller, J., Motschmann, U., Saur, J., Glassmeier, K., Dougherty, M. K., 2009, The plasma interaction of Enceladus: 3D hybrid simulations and comparison with Cassini MAG data, Planet. Space Sci., 57, 2113–2122

Richter, I., Auster, H., Glassmeier, K., Koenders, C., Carr, C., Motschmann, U., Müller, J., McKenna-Lawlor, S., 2011, Magnetic field measurements during the rosetta flyby at asteroid (21)lutetia, Planetary and Space Science, doi: 10.1016/j.pss.2011.08.009

Roussos, E., Mueller, J., Simon, S., Boesswetter, A., Motschmann, U., Krupp, N., Fraenz, M., Woch, J., Khurana, K. K., Dougherty, M. K., 2008, Plasma and fields in the wake of Rhea: 3-D hybrid simulation and comparison with Cassini data, Annales Geophysicae, 26, 619–637

Verscharen, D., Marsch, E., Motschmann, U., Müller, J., 2011, Kinetic cascade beyond MHD of solar wind turbulence in two-dimensional hybrid simulations, Physics of Plasmas, in press, 2012

Verscharen, D., Marsch, E., Motschmann, U., Müller, J., 2012, Parametric decay of oblique Alfvén waves in two-dimensional hybrid simulations, submitted to Physical Review, 2012

Wang, Y., Mueller, J., Motschmann, U., Ip, W. H., 2010, A hybrid simulation of Mercury's magnetosphere for the MESSENGER encounters in year 2008, Icarus, 209, 46–52

Wang, Y. C., Müller, J., Ip, W. H., Motschmann, U., 2011, A 3D Hybrid Simulation Study of the Electromagnetic Field Distributions in the Lunar Wake, Icarus, 216, 415-425

Wiehle, S., Motschmann, U., Gortsas, N., Glassmeier, K.-H., Müller, J., Koenders, C., 2011a, Simulation of cometary jets in interaction with the solar wind, Advances in Space Research, 48, 1108–1113

Wiehle, S., Plaschke, F., Motschmann, U., Glassmeier, K.-H., Auster, H. U., Angelopoulos, V., Mueller, J., Kriegel, H., Georgescu, E., Halekas, J., Sibeck, D. G., McFadden, J. P., 2011b, First lunar wake passage of ARTEMIS: Discrimination of wake effects and solar wind fluctuations by 3D hybrid simulations, Planetary and Space Science, 59, 661–671